



# Supramolecular electronics : from molecular wires to (semi)conducting materials

Chiara Musumeci

## ► To cite this version:

Chiara Musumeci. Supramolecular electronics : from molecular wires to (semi)conducting materials. Other. Université de Strasbourg, 2014. English. NNT : 2014STRAF004 . tel-01038014

HAL Id: tel-01038014

<https://theses.hal.science/tel-01038014>

Submitted on 23 Jul 2014

**HAL** is a multi-disciplinary open access archive for the deposit and dissemination of scientific research documents, whether they are published or not. The documents may come from teaching and research institutions in France or abroad, or from public or private research centers.

L'archive ouverte pluridisciplinaire **HAL**, est destinée au dépôt et à la diffusion de documents scientifiques de niveau recherche, publiés ou non, émanant des établissements d'enseignement et de recherche français ou étrangers, des laboratoires publics ou privés.

**ÉCOLE DOCTORALE DES SCIENCES CHIMIQUES**  
**Institut de Science et d'Ingénierie Supramoléculaires (I.S.I.S)**  
**UMR7006 Nanochimie**

# THÈSE

présentée par :

**Chiara MUSUMECI**

soutenue le : **16 Avril 2014**

pour obtenir le grade de : **Docteur de l'Université de Strasbourg**

Discipline/ Spécialité : Chimie Physique

## SUPRAMOLECULAR ELECTRONICS : FROM MOLECULAR WIRES TO (SEMI)CONDUCTING MATERIALS

THÈSE dirigée par :

**Prof. SAMORÌ Paolo**

Université de Strasbourg

RAPPORTEURS :

**Dr. CAVALLINI Massimiliano**

CNR- ISMN Bologna

**Dr. SURIN Mathieu**

Université de Mons

AUTRES MEMBRES DU JURY :

**Prof. DOUDIN Bernard**

Université de Strasbourg



---

# Table of Contents

<b>Résumé</b>	<b>V</b>
<b>Abstract</b>	<b>XVII</b>
<b>Abbreviations</b>	<b>XXIX</b>
<b>1. Introduction</b>	<b>1</b>
1.1. Motivation	1
1.2. Charge transport in organic molecules	3
1.3. Self-assembly	6
1.3.1.From self-assembled monolayer to layer-by-layer growth	7
1.3.2.Assembly by Langmuir-Blodgett technique	8
1.3.3.Electric-field assisted assembly	11
1.4. References	13
<b>2. Exploring multiscale structural and electrical properties of materials</b>	<b>17</b>
2.1. Photon-based characterization techniques	17
2.2. Atomic Force Microscopy	21
2.2.1.Conductive Atomic Force Microscopy (C-AFM): state of the art	22
2.3. Organic Thin Film Transistors (OTFTs)	29
2.4. References	33
<b>3. Nanoscale electrical investigation of layer-by-layer grown molecular wires</b>	<b>37</b>
3.1. Introduction	37
3.2. Experimental details	38
3.3. Structural characterization	40
3.3.1.XPS analysis	40
3.3.2.NEXAFS analysis	42
3.3.3.UV-Vis characterization	43
3.3.4.AFM morphological characterization	44
3.4. Electrical nanojunction by C-AFM	45

---

3.5. Theoretical calculation	49
3.6. Conclusions	51
3.7. References	51
<b>4. Tailoring the conductive properties of supramolecular metal-organic polymers by chemical design</b>	<b>55</b>
4.1. Introduction	55
4.2. Experimental details	57
4.3. Morphological and structural characterization	58
4.4. Electrical behavior in two terminal devices and at the nanoscale	64
4.5. Theoretical insights	67
4.6. Conclusions	68
4.7. References	69
<b>5. On the electrical properties of perylenecarboxydiimide-based nanoarchitectures</b>	<b>71</b>
5.1. Introduction	71
5.2. Experimental details	72
5.3. Assembly and structural characterization	73
5.4. Vertical charge transport in the LB monolayer	80
5.5. Horizontal charge transport in the LB monolayer	82
5.6. Vertical charge transport in the ultrathin nanocrystals	87
5.7. Conclusions	91
5.8. References	91
<b>6. Controlling the morphology of conductive PEDOT by in situ electropolymerization</b>	<b>95</b>
6.1. Introduction	95
6.2. Experimental details	96
6.3. Electropolymerization at different electric fields	97
6.4. Insights on the electropolymerization mechanisms: nucleation and growth, electromigration	100
6.5. Electropolymerization of EDOT in propylene carbonate solution	103
6.6. Conclusions	105
6.7. References	105

---

<b>7. Conclusions and perspectives</b>	<b>109</b>
<b>Acknowledgements</b>	<b>115</b>
<b>List of publications</b>	<b>117</b>
<b>Annex A</b> - Further computational method on Fe(II)-bis(terpyridine) molecular system based on 4',4''''-(1,4-phenylene)bis(2,2':6',2''-terpyridine) (TPT) ligand	119
<b>Annex B</b> - Further computational methods on Pd(II)-(terpyridine-antracene-pyridine) (TAP) polymer	123



---

## Résumé

Le domaine de l'électronique organique, ou plastique, fut introduit à la fin des années soixante-dix, quand Alan MacDiarmid, Hideki Shirakawa et Alan Heeger découvrirent la conduction électrique dans les polymères conjugués, montrant également la possibilité de moduler la conductivité par dopage.<sup>1, 2</sup> Dans les polymères conjugués, les orbitales des atomes de carbone sont dans la configuration de type  $sp^2-p_z$ ; les orbitales des atomes de carbone successifs le long de la chaîne du polymère se chevauchent, ce qui conduit à la délocalisation des électrons le long du squelette du polymère. Cette délocalisation électronique établit le chemin pour la mobilité de charge le long de la chaîne polymérique. De même, les oligomères conjugués et les petites

---

molécules peuvent également transporter des charges et présenter des propriétés électriques.<sup>3</sup>

Au cours des dernières décennies, les molécules  $\pi$ -conjuguées ont été employées pour la fabrication de dispositifs électroniques tels que transistors organiques à effet de champ (OTFTs),<sup>4,5</sup> les diodes électroluminescentes organiques (OLEDs),<sup>6</sup> les cellules photovoltaïques organiques (OPVs),<sup>7, 8</sup> les mémoires organiques,<sup>9</sup> les capteurs organiques<sup>10</sup> et les radio-étiquettes (RF-ID)<sup>11</sup> pour l'intégration dans l'électronique grande surface, vers des dispositifs logiques.

Dans les mêmes années Aviram et Ratner, proposé rectification électrique par une seule molécule organique avec asymétrie électronique appropriée,<sup>12</sup> donnant la naissance à l'électronique moléculaire. L'électronique moléculaire concerne les processus électriques et électroniques qui impliquent un ou très peu de molécules.

Entre l'électronique moléculaire et l'électronique plastique, c'est à dire allant de l'échelle de la molécule à la fonction des matériaux organiques, l'électronique supramoléculaires vise à construire et à étudier les propriétés optoélectroniques de nanoarchitectures supramoléculaires.<sup>13</sup>

---

Par rapport à l'électronique inorganique traditionnelle à base de procédés de lithographie, les technologies impliquant des molécules organiques, étant principalement basées sur des procédés en solution qui sont des procédés additifs, sont beaucoup plus simples. Les procédés de fabrication à faible coût et à basse température sont aussi compatibles avec des substrats tels que le plastique, ce qui permet également l'intégration sur des supports flexibles. Toutefois, pour obtenir des performances optimales d'une matière organique, la question clé est d'obtenir une maîtrise complète de sa structure et de son organisation à l'état solide. En fait, les propriétés optoélectroniques des matériaux conjugués sont étroitement liées à leur organisation supramoléculaire.<sup>13</sup> À cet égard, l'objectif de cette thèse est d'obtenir le contrôle de l'organisation des systèmes moléculaires organiques et de corrélérer leur structure avec les propriétés électriques.

Les caractérisations électriques ont été effectuées à la fois à l'échelle microscopique, par la fabrication de dispositifs à deux électrodes et des transistors organiques, et à l'échelle nanométrique en utilisant des techniques de microscopie à force atomique C-(AFM) à sonde conductrice.

---

La microscopie à force atomique à sonde conductrice est un outil particulièrement approprié pour la caractérisation des structures moléculaires mésoscopiques, car il donne une corrélation immédiate entre la morphologie du matériau et sa conductivité locale à l'échelle nanométrique en mesurant le courant circulant entre la pointe et l'échantillon conducteur.

Différentes stratégies ont été utilisées pour l'ingénierie des architectures moléculaires sur une surface. Dans la première partie, nous discuterons d'un assemblage moléculaire guidé par des interactions spécifiques métal-ligand dans des composés supramoléculaires de coordination,<sup>14</sup> c'est à dire un contrôle de l'assemblage réalisé par un design chimique.

Nous exploitons une stratégie basée sur la chimie de coordination pour fabriquer des assemblages moléculaires conducteurs de Fe(II)-bis(terpyridine) au moyen d'une croissance couche par couche sur un substrat d'or, dans le but d'obtenir un aperçu des mécanismes de transport de charge de ces structures ordonnées à nanofils. Les propriétés structurales ont été étudiées en utilisant une grande variété de techniques, telles que NEXAFS, XPS, spectroscopie UV-Vis et AFM. En utilisant la microscopie à force atomique à sonde conductrice (C-AFM) nous avons efficacement construit des

---

jonctions métal-molécule-métal à l'échelle nanométrique et nous avons étudié la dépendance des propriétés électriques de la longueur moléculaire, c'est à dire le nombre d'étapes de coordination. Toutes les données expérimentales fournissent sans équivoque des preuves de l'existence d'un mécanisme de transport de charge par saut (*hopping*), caractérisé par une très faible atténuation du courant. Des calculs théoriques ont montré que l'énergie de réorganisation due à l'ajout d'un trou d'électron sur le centre fer est beaucoup plus grande que le couplage électronique entre les sites de fer, ce qui indique clairement que le processus de transport d'électrons ne peut être gouverné par effet tunnel résonnant, mais plutôt par sauts entre sites adjacents. Les caractéristiques électriques remarquables de ces jonctions moléculaires en font non seulement des systèmes idéaux pour des études fondamentales sur transport de charge à longue distance dans les fils organométalliques à l'état solide, mais aussi ouvrent la voie à leur exploitation pour des applications électroniques moléculaires et/ou organiques.

Des systèmes moléculaires similaires où le ligand est basé sur un noyau anthracène portant deux groupes éthynyle équipés d'un groupe pyridine et un terpyridine aux pôles ont également été étudiés. Lorsque la complexation de ce ligand

---

est effectuée en utilisant des ions Co(II) et Pd(II), des structures de polymère sont formées sous forme de suspension dans le solvant des deux réactifs. Cette suspension peut être déposée par goutte sur des substrats et étudiée dans la phase solide. La caractérisation morphologique des polymères ayant deux métaux différents a montré que l'assemblage à l'échelle nanométrique est régi par la géométrie de coordination. Le complexe à base de Co octaédrique donne en effet des structures polycristallines globulaires, comme on le voit par microscopie à force atomique et des techniques de diffraction des rayons X. A l'inverse, la coordination plane carrée des ions Pd produit des structures fibrillaires où les domaines cristallins ont tendance à avoir une orientation préférée spécifique dans le sens de la direction hors-plan. Systématiquement, les structures polymériques avec des morphologies différentes présentent également un comportement électrique différent. Bien qu'aucune conductivité ne soit détectée sur un dispositif à deux électrodes lorsque le complexe de Co est utilisé comme couche active, la conduction est représentée par le complexe Pd. La conduction des structures semblables à des fibres est également sondée à l'échelle nanométrique par C-AFM. Les calculs théoriques sont également utilisés ici pour

---

obtenir un aperçu de la structure cristalline de polymère Pd et de ses propriétés conductrices.

Dans la seconde partie de la thèse un exemple d'assemblage guidé est montré, où un film monomoléculaire d'un semi-conducteur organique est formé grâce à la technique de Langmuir-Blodgett (LB), c'est à dire que le contrôle de l'assemblage est donné par une force mécanique extérieure, qui est la pression exercée par deux barrières sur les molécules réparties sur une couche d'eau. Un film monocouche LB d'une molécule à base de pérylène a été obtenu à l'interface air-eau et transféré sur des substrats solides tels que l'or, l'oxyde de silicium et le verre. Le transport électrique a pu être testé dans une jonction verticale nanoscopique C-AFM lorsque le film a été déposé sur l'or, montrant des propriétés de rectification. Le transport horizontal a été testé dans des dispositifs transistor organiques à effet de champ et de hautes performances ont été obtenues pour les transistors à couches minces de différentes longueurs de chaînes.

Sur ces films minces monomoléculaires des procédés après-dépôt ont également été réalisés. Ceux-ci ont largement été utilisés pour modifier la microstructure des matériaux organiques.

---

Un traitement thermique a favorisé la réorganisation du film monocouche LB en fines structures cristallines micrométriques multicouches de quelques nm d'épaisseur. La structure en couches minces de ces nanocristaux ressemblait à la structure des cristaux micrométriques obtenus par la méthode de précipitation induite du solvant,<sup>16</sup> comme démontré par analyses AFM et C-AFM et également corroborée par la caractérisation photophysique. La caractérisation électrique de ces structures cristalline d'épaisseurs différentes a été réalisée par C-AFM donnant un aperçu du transport de charge vertical.

Enfin, nous montrons comment des structures organisées peuvent également être obtenues par l'exploitation du champ électrique externe par des processus électrochimiques *in situ*.

Nous avons employé un système de polymère modèle, le poly (3,4-éthylènedioxythiophène) (PEDOT), qui est largement utilisé comme polymère conducteur pour la fabrication de dispositifs électroniques organiques, en raison de sa bonne conductivité électrique, d'une excellente transparence dans le domaine visible et de sa stabilité vis-à-vis de l'environnement.<sup>18,19</sup> Il peut être obtenu par la polymérisation de 3,4- éthylènedioxythiophène à la fois par oxydation chimique et par des procédés

---

électrochimiques. Ici, nous avons utilisé une procédure d'électropolymérisation *in situ*,<sup>20</sup> dans le but d'étudier la possibilité d'obtenir un polymère fonctionnel déposé directement sur un dispositif de fente de micromètre. Nous avons trouvé<sup>21</sup> que la morphologie du PEDOT synthétisé par voie électrochimique peut être finement réglée directement dans un dispositif, en guidant soigneusement les processus de nucléation et de croissance ainsi que des phénomènes d'électromigration. En particulier, les intensités de champ électrique élevées favorisent la formation de fils alignés qui traversent la fente, qui sont dus à la nucléation instantanée, la croissance limitée par diffusion et un processus d'électromigration. Inversement, les valeurs de champ électrique plus faibles conduisent à la formation de couches minces par l'intermédiaire de la nucléation et de la croissance progressive en 2D. De manière significative, la fonction électrique de la matière électropolymérisée s'est trouvée fortement affectée par la morphologie, comme le montre la différence de comportement résistif.

En conclusion, ce travail de thèse montre que l'ingénierie des matériaux nanostructurés organisés est fondamentale pour affiner les propriétés électriques des matériaux organiques  $\pi$  - conjugués. Les stratégies utilisées nécessitent simultanément le réglage du design moléculaire et un plein contrôle sur les interactions (molécule-

---

molécule, molécule-sous-strat, molécule-solvant), la cinétique des processus d'auto-assemblage (auto-assemblage contre auto-organisation) et la présence de forces extérieures. En particulier, nous avons conçu des architectures moléculaires par conception moléculaire exploitant des interactions spécifiques et directionnelles de coordination métal-ligand, nous avons guidé l'assemblage d'un semi-conducteur organique très performant à l'interface air-eau par des approches Langmuir-Blodgett, et fait des modifications de l'architecture de la monocouche par traitement thermique post-dépôt. Enfin, nous avons forcé l'assemblage d'un polymère exploitant un champ électrique.

Les résultats présentés ont montré que les processus basés sur des solutions sont simples, polyvalents et efficaces, permettant l'étude des matériaux à l'échelle supramoléculaire et la création de dispositifs fonctionnels pour les applications dans les nanotechnologies, les matériaux intelligents, l'électronique organique et les biocapteurs.

## References

1. Shirakawa, H.; Louis, E. J.; MacDiarmid, A. G.; Chiang, C. K.; Heeger, A. J. *J. Chem. Soc., Chem. Commun.* **1977**, 578.

- 
2. Heeger, A. *Angew. Chem. Int. Ed.* **2001**, *40*, 2591
  3. Fichou, D.; Horowitz, G.; Nishikitani, Y.; Garnier, F. *Synth. Met.* **1989**, *28*, C723.
  4. Zaumseil, J.; Sirringhaus, H. *Chem. Rev.* **2007**, *107*, 1296.
  5. Zhao, Y.; Guo, Y.; Liu, Y. *Adv. Mater.* **2013**, *25*, 5372.
  6. Friend, R. H.; Gymer, R. W.; Holmes, A. B.; Burroughes, J. H.; Marks, R. N.; Taliani, C.; Bradley, D. D. C.; Santos, D. A. D.; Brédas, J. L.; Lögdlund, M.; Salaneck, W. R. *Nature* **1999**, *397*, 121.
  7. Thompson, B. C.; Frechet, J. M. *Angew. Chem. Int. Ed. Engl.* **2008**, *47*, 58.
  8. Mishra, A.; Bauerle, P. *Angew. Chem. Int. Ed.* **2012**, *51*, 2020.
  9. Scott, J. C.; Bozano, L. D. *Adv. Mater.* **2007**, *19*, 1452.
  10. Mabeck, J. T.; Malliaras, G. G. *Anal. Bioanal. Chem.* **2006**, *384*, 343.
  11. Baude, P. F.; Ender, D. A.; Haase, M. A.; Kelley, T. W.; Muyres, D. V.; Theiss, S. D. *Appl. Phys. Lett.* **2003**, *82*, 3964.
  12. Aviram, A.; Ratner, M. A. *Chem. Phys. Lett.* **1974**, *29*, 277.
  13. Lèclere, P.; Surin, M.; Brocorens, P.; Cavallini, M.; Biscarini, F.; Lazzaroni, R. *Mater. Sci. Eng. R* **2006**, *55*, 1.

- 
14. Musumeci, C.; Zappala, G.; Martsinovich, N.; Orgiu, E.; Schuster, S.; Quici, S.;  
Zharnikov, M.; Troisi, A.; Licciardello, A.; Samori, P. *Adv. Mater.* **2014**, *26*, 1688.
16. Mativetsky, J. M.; Orgiu, E.; Lieberwirth, I.; Pisula, W.; Samorì, P. *Adv. Mater.*  
**2013**, *26*, 430.
17. Gemayel, M. E.; Treier, M.; Musumeci, C.; Li, C.; Müllen, K.; Samorì, P. *J. Am.*  
*Chem. Soc.* **2012**, *134*, 2429.
18. Pei, Q.; Zuccarello, G.; Ahlskogt, M.; Inganas, O. *Polymer* **1994**, *35*, 1347.
19. Nikolou, M.; Malliaras, G. G. *Chem. Rec.* **2008**, *8*, 13.
20. Das, A.; Lei, C. H.; Elliott, M.; Macdonald, J. E.; Turner, M. L. *Org. Electron.*  
**2006**, *7*, 181.
21. Musumeci, C.; Hutchison, J. A.; Samori, P. *Nanoscale* **2013**, *5*, 7756.

---

## Abstract

The field of organic, or plastic, electronics was introduced in the late seventies, when Alan MacDiarmid, Hideki Shirakawa, and Alan Heeger probed electrical conduction in conjugated polymers, also showing the possibility of modulating the conductivity by doping.<sup>1,2</sup> In conjugated polymers the carbon orbitals are in the  $sp^2 p_z$  configuration; the orbitals of successive carbon atoms along the backbone overlap, leading to electron delocalization along the backbone of the polymer. This electronic delocalization provides the path for charge mobility along the backbone of the polymer chain. Similarly, conjugated oligomers and small molecules can also transport charges and show electrical properties.<sup>3</sup>

---

Over the past decades,  $\pi$ -conjugated molecules has been employed for the fabrication of electronic devices such as Organic Thin-Film Transistor (OTFTs),<sup>4,5</sup> Organic Light-Emitting Diodes (OLEDs),<sup>6</sup> Organic Photovoltaics (OPVs),<sup>7,8</sup> Organic Memories,<sup>9</sup> Organic Sensors<sup>10</sup> and Radio Frequency Identification (RF-ID) tags<sup>11</sup> for integration into large-area electronics, towards logic solutions.

In the same years Aviram and Ratner, proposed electrical rectification or diode behavior by a single organic molecule with appropriate electronic asymmetry,<sup>12</sup> giving the birth to molecular electronics. Molecular electronics regards the electrical and electronic processes that involve one or very few molecules.

Bridging the gap between molecular and plastic electronics, i.e. going from the single molecule level to the bulk function of the organic materials, supramolecular electronics aims to construct and investigate the optoelectronic properties of tailored supramolecular nanoarchitectures.<sup>13</sup>

Compared to the traditional lithography-based inorganic electronics, the technologies involving organic molecules, being mainly solution-based and additive, are much simpler. Their low-cost and low-temperature fabrication procedures are compatible with substrates such as plastic, which also allows the integration on flexible

---

supports. However, to get optimal performance from an organic material, the key issue is to get a complete control of its structure and its organization in the solid state. In fact, the optoelectronic properties of the conjugated materials are closely related to their supramolecular organization.<sup>13</sup> In this respect, the aim of this thesis is to get control over the organization of organic molecular systems and correlate their structure with the electrical properties.

The electrical characterizations were carried out both at the microscale, by fabricating two electrodes devices and organic transistors, and at the nanoscale by employing advanced Conductive Atomic Force Microscopy (C-AFM) techniques.

C-AFM is a particularly appropriate tool for the characterization of mesoscopic molecular structures since it gives an immediate correlation between the morphology of the material and its local conductivity at the nanoscale by measuring the current flowing between the tip and the conductive sample. In the simplest setup a feedback loop is used to move the probe along the Z-axis in order to maintain a constant cantilever deflection  $z$ ; considering the cantilever as a perfect spring, a controlled constant force  $F$  is therefore exerted by the tip on the sample surface according to Hooke's law ( $F = k \cdot z$ ), where  $k$  is the spring stiffness. As a result, the tip follows the

---

contour of the sample surface and provides a map of the surface topography. Simultaneously, a voltage is applied between the conductive tip, acting as a movable electrode, and a counter-electrode, and the resulting current is measured.<sup>15</sup>

Different strategies have been employed for engineering molecular architectures on surface. In the first part we discuss a molecular assembly guided by specific metal-ligand interactions in supramolecular coordination compounds,<sup>16</sup> i.e. a control of the assembly achieved by chemical design.

We exploit a coordination chemistry strategy to fabricate Fe(II)-bis(terpyridine) conductive molecular assemblies by means of a layer-by-layer growth on gold substrate, with the aim to get insights into the charge transport mechanisms of these ordered nanowire structures. Structural properties have been investigated using a large variety of technique, such as NEXAFS, XPS, UV-Vis Spectroscopy and AFM. By employing Conductive Atomic Force Microscopy (C-AFM) we effectively built up nanoscale metal-molecule-metal junctions and we studied the dependence of the electrical properties on the molecular length, i.e. the number of coordination steps. All the experimental data provides unambiguous evidence for the existence of a hopping charge transport mechanism, characterized by a very low current attenuation and a

---

regime transition from Ohmic conduction to Space Charge Limited Conduction (SCLC) at higher bias. Theoretical calculations performed on different models of the wire showed that the reorganization energy due to the addition of a hole on the iron center is much larger than the electronic coupling between iron sites, unambiguously indicating that the electron transport process cannot be ruled by resonant tunneling, but rather by hopping between adjacent sites. The remarkable electrical characteristics of these molecular junctions not only make them ideal systems for fundamental studies on long-range charge transport in solid-state metal-organic wires, but also pave the way towards their exploitation in molecular and/or organic electronic applications.

Similar molecular systems where the ligand was based on an anthracene core bearing two ethynyl groups equipped with a pyridine and a terpyridine group at the poles. When the complexation of this ligand is carried by employing Co(II) and Pd(II) ions, polymer structures are formed as a suspension in the solvent of the two reactants. This suspension can be drop cast on solid substrates and studied in the solid phase. The morphological characterization of the polymers having the two different metals showed that the assembly at the nanoscale is governed by the coordination geometry. The octahedric Co-based complex gives in fact globular polycrystalline structures, as seen

---

by Atomic Force Microscopy and X-ray diffraction techniques. On the contrary, the squared planar coordination of the Pd ions produced fibrillar structures where crystalline domains tend to have a specific preferred orientation along the out-of-plane direction. Consistently, the polymer structures with the different morphologies also have different electrical behavior. While no conductivity is detected on a two electrode device when the Co complex is used as active layer, conduction is shown by the Pd complex. Conduction of the fiber-like structures is also probed at the nanoscale by C-AFM. Theoretical calculations are also used here to get insights on the Pd polymer crystalline structure and its conductive properties.

In the second part of the thesis an example of guided assembly is shown, where a monomolecular film of an organic semiconductor is formed through the Langmuir-Blodgett technique, i.e. the control over the assembly is given by an external mechanical force, which is the pressure exerted by two barrier on the molecules spread over a water layer. A LB monolayer film of a perylene based molecule could be obtained at the air water interface and transferred on solid substrates such as gold, silicon oxide and glass. The electrical transport could be tested in a nanoscopic C-AFM vertical junction when the film deposited on gold, showing rectification properties. The

---

horizontal transport was tested in macroscopic OTFT devices and high performances are obtained in thin film transistor of different channel lengths.

On these monomolecular thin films post-deposition processing<sup>17</sup> was also performed, which have been largely employed to modify the microstructure of organic materials.

Thermal annealing favored the reorganization of the LB monolayer film into  $\mu\text{m}$ -long and few nm thin layered crystal-like structures. The layered structure of these thin nanocrystals resembled the structure of micrometric crystals obtained by solvent induced precipitation methods,<sup>18</sup> as proven by AFM and C-AFM analysis and also corroborated by the photophysical characterization. The electrical characterization of these structures was carried out by C-AFM on different crystal thickness giving insights on the vertical charge transport. Also the effect of the light irradiation on the conduction was investigated as comparison with similar microscopic architectures.<sup>19</sup>

Finally we show how organized structures can be also obtained by exploiting external electric field through *in situ* electrochemical processes.

We employed a model polymer system, poly(3,4-ethylenedioxythiophene) (PEDOT), which is largely employed as conducting polymer for the fabrication of organic

---

electronic devices, due to its good electrical conductivity, excellent transparency in the visible range and environmental stability.<sup>20,21</sup> It can be obtained by the polymerization of 3,4-ethylenedioxythiophene both by chemical oxidation and electrochemical methods. Here we exploited an in-situ electropolymerization procedure,<sup>22</sup> in order to investigate the possibility of obtaining a functional polymer directly deposited on a micrometer gap device. We found<sup>23</sup> that the morphology of electrochemically synthetized PEDOT can be finely tuned directly in a device, by carefully guiding the nucleation and growth processes as well as electromigration phenomena. In particular, high electric field intensities favor the formation of aligned wires bridging the gap, as a result of instantaneous nucleation, diffusion-limited growth and electromigration processes. Conversely, lower electric field strengths lead to the formation of thin films via progressive nucleation and 2D growth. Significantly, the electrical function of the electropolymerized material was found being strongly affected by the morphology, as evidenced by the different resistive behavior.

In conclusion, this thesis work shows how engineering organized nanostructured materials is fundamental for tuning the electrical properties of organic  $\pi$ -conjugated materials. The exploited strategies requires simultaneously the tuning of the molecular

---

design, a full control over the interplay of interactions (molecule-molecule, molecule-substrate, molecule solvent), the kinetics of the processes (self-assembly vs. self-organization) and the presence of external forces. In particular, we engineered molecular architectures by molecular design exploiting specific and directional metal-ligand coordination interactions, we guided the assembly of high performing organic semiconductor at the air water interface by Langmuir-Blodgett approaches, modifying the monolayer architecture through post-deposition thermal annealing. Finally, we forced a polymer organization exploiting an electric field.

The presented results showed that the solution-based processes are simple, versatile and effective, enabling the investigation of the materials at the supramolecular level and the creation of efficient devices for applications in nanotechnology, smart materials, organic electronics and biosensors.

## References

1. Shirakawa, H.; Louis, E. J.; MacDiarmid, A. G.; Chiang, C. K.; Heeger, A. J. *J. Chem. Soc., Chem. Commun.* **1977**, 578.
2. Heeger, A. *Angew. Chem. Int. Ed.* **2001**, *40*, 2591
3. Fichou, D.; Horowitz, G.; Nishikitani, Y.; Garnier, F. *Synth. Met.* **1989**, *28*, C723.

- 
4. Zaumseil, J.; Sirringhaus, H. *Chem. Rev.* **2007**, *107*, 1296.
  5. Zhao, Y.; Guo, Y.; Liu, Y. *Adv. Mater.* **2013**, *25*, 5372.
  6. Friend, R. H.; Gymer, R. W.; Holmes, A. B.; Burroughes, J. H.; Marks, R. N.; Taliani, C.; Bradley, D. D. C.; Santos, D. A. D.; Brédas, J. L.; Lögdlund, M.; Salaneck, W. R. *Nature* **1999**, *397*, 121.
  7. Thompson, B. C.; Frechet, J. M. *Angew. Chem. Int. Ed. Engl.* **2008**, *47*, 58.
  8. Mishra, A.; Bauerle, P. *Angew. Chem. Int. Ed.* **2012**, *51*, 2020.
  9. Scott, J. C.; Bozano, L. D. *Adv. Mater.* **2007**, *19*, 1452.
  10. Mabeck, J. T.; Malliaras, G. G. *Anal. Bioanal. Chem.* **2006**, *384*, 343.
  11. Baude, P. F.; Ender, D. A.; Haase, M. A.; Kelley, T. W.; Muyres, D. V.; Theiss, S. D. *Appl. Phys. Lett.* **2003**, *82*, 3964.
  12. Aviram, A.; Ratner, M. A. *Chem. Phys. Lett.* **1974**, *29*, 277.
  13. Lèclerc, P.; Surin, M.; Brocorens, P.; Cavallini, M.; Biscarini, F.; Lazzaroni, R. *Mater. Sci. Eng. R* **2006**, *55*, 1.
  14. Musumeci, C.; Zappala, G.; Martsinovich, N.; Orgiu, E.; Schuster, S.; Quici, S.; Zharnikov, M.; Troisi, A.; Licciardello, A.; Samori, P. *Adv. Mater.* **2014**, *26*, 1688.

- 
16. Mativetsky, J. M.; Orgiu, E.; Lieberwirth, I.; Pisula, W.; Samorì, P. *Adv. Mater.* **2013**, *26*, 430.
  17. Gemayel, M. E.; Treier, M.; Musumeci, C.; Li, C.; Müllen, K.; Samorì, P. *J. Am. Chem. Soc.* **2012**, *134*, 2429.
  18. Pei, Q.; Zuccarello, G.; Ahlskogt, M.; Inganas, O. *Polymer* **1994**, *35*, 1347.
  19. Nikolou, M.; Malliaras, G. G. *Chem. Rec.* **2008**, *8*, 13.
  20. Das, A.; Lei, C. H.; Elliott, M.; Macdonald, J. E.; Turner, M. L. *Org. Electron.* **2006**, *7*, 181.
  21. Musumeci, C.; Hutchison, J. A.; Samori, P. *Nanoscale* **2013**, *5*, 7756.



---

## Abbreviations

AFM	Atomic Force Microscopy
C-AFM	Conductive Atomic Force Microscopy
D-A	Donor-Acceptor
EDOT	3,4-ethylenedioxothiophene
ET	Electron transfer
GIXRD	Grazing Incidence X-ray Diffraction
HOMO	Highest Occupied Molecular Orbital
LB	Langmuir-Blodgett
LUMO	Lowest Unoccupied Molecular Orbital
Mma	Mean molecular area
MB	Benzethiol
MPTP	4-[2,2':6',2"-terpyridin]-4'-yl-benzenethiol
NEXAFS	Near Edge X-ray Absorption Fine Structure Spectroscopy
OFET	Organic Field Effect Transistor
OTFT	Organic Thin Film Transistor
PEDOT	poly(3,4-ethylenedioxothiophene)
PDI	Perylene diimide
PDIF-CN <sub>2</sub>	N,N'-1H,1H-perfluorobutyl dicyanoperylenecarboxydiimide
SAM	Self-assembled monolayer
SC	Spin-coated
SCLC	Space Charge Limited Current
SIP	Solvent Induced Precipitation
SP	Surface Pressure
SPM	Scanning Probe Microscopy
SVA	Solvent Vapor Annealing
TAP	4'-(10-[2-(4-pyridinyl)ethynyl]-9-anthracenyl)-2,2':6',2"-Terpyridine
TPT	4',4''''-(1,4-phenylene)bis(2,2':6',2''-terpyridine)
TR-TUNA AFM	Torsion Resonance Tunneling Current Atomic Force Microscopy
UV-Vis	Ultraviolet-Visible
XPS	X-ray Photoelectron Spectroscopy
XRR	X-Ray reflectivity



# 1. Introduction

## 1.1. Motivation

The field of organic electronics was introduced in the late seventies, when Alan MacDiarmid, Hideki Shirakawa, and Alan Heeger probed electrical conduction in conjugated polymers, also showing the possibility of modulating the conductivity by doping.<sup>1,2</sup> In conjugated polymers the carbon orbitals are in the  $sp^2$ - $p_z$  configuration; the  $\pi$ -orbitals of adjacent carbon atoms along the backbone overlap, leading to electron delocalization along the backbone of the polymer. This electronic delocalization provides the path for charge mobility along the backbone of the polymer chain. Similarly, conjugated oligomers and small molecules can also transport charges and show electrical properties.<sup>3</sup>

Over the past decades,  $\pi$ -conjugated molecules has been employed for the fabrication of electronic devices such as Organic Thin-Film Transistor (OTFTs),<sup>4,5</sup> Organic Light-Emitting Diodes (OLEDs),<sup>6</sup> Organic Photovoltaics (OPVs),<sup>7,8</sup> Organic Memories,<sup>9</sup> Organic Sensors<sup>10</sup> and Radio Frequency Identification (RF-ID) tags<sup>11</sup> for integration into large-area electronics, towards logic solutions. Compared to the traditional lithography-based inorganic electronics, the technologies involving organic molecules, being mainly solution-based and additive, are much simpler. Their low-cost and low-temperature fabrication procedures are compatible with substrates such as plastic, which also allows the integration on flexible supports, from where the definition plastic electronics derives.

In the same years Aviram and Ratner, following the considerations of Richard Feynman envisaging the ultimate integrated circuit to be constructed at the molecular or atomic level (“There is plenty of room at the bottom”),<sup>12</sup> proposed electrical rectification or diode behavior by a single organic

molecule with appropriate electronic asymmetry,<sup>13</sup> giving the birth to molecular electronics. Molecular electronics regards the electrical and electronic processes that involve one or very few molecules; the measurement of these conduction properties then imply to reach and touch individual molecules with electrodes without damaging them and exploiting their chemical structure to control the flow of electrical signal.<sup>14</sup> The great attention received by the field rely on the hope that molecules could become technologically useful devices, pushing to the limit the exponential shrinking of the electronic component in integrated circuits predicted by Moore in 1965 after observing that the number of components in integrated circuits had doubled every year from the invention of the integrated circuit in 1958.<sup>15</sup>

Bridging the gap between molecular and plastic electronics, i.e. going from the single molecule level to the bulk function of the organic materials, supramolecular electronics aims to construct and investigate the optoelectronic properties of tailored supramolecular nanoarchitectures.<sup>16</sup>

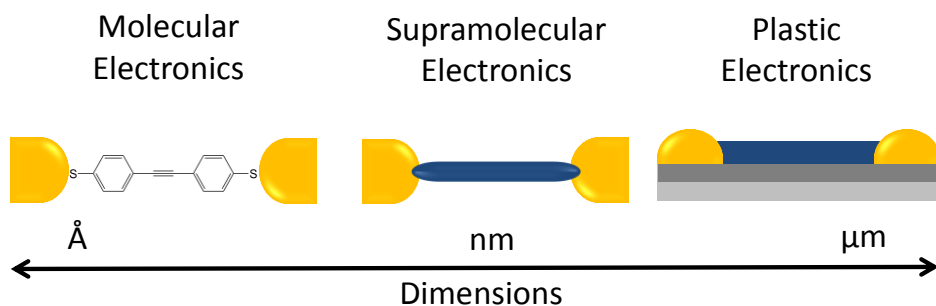


**Figure 1.1:** Schematic representation illustrating the gap, with respect to length scale, between molecular electronics, where single molecules are studied, and plastic (or organic) electronics, which relies on bulk properties of conjugated polymers. [Adapted from<sup>16</sup>].

The optoelectronic properties of the conjugated materials indeed are closely related to their supramolecular organization.<sup>17</sup> Thus, to get optimal performances from an organic material, the key issue is to get a complete control of its structure and its organization in the solid state. In organic (semi)conductive conjugated materials the electron energy states are delocalized within the molecule due to the  $\pi$ -orbital overlap; to maximize this overlap by proper chemical design and material processing is the task to achieve in order to access to high performance of the materials. In this respect, the aim of this thesis is to get control over the organization of organic molecular systems at the supramolecular level and correlate their structure with the resulting electrical properties.

After addressing the main issues regarding charge transport in organic materials and their assembly into controlled architectures in the following paragraphs, I will present in the Chapter 2 the

experimental approaches used in this thesis to investigate both the structural and electrical properties of these nanoarchitectures, with particular attention to Scanning Probe Microscopy techniques, such as Conductive Atomic Force Microscopy (C-AFM) which, giving an immediate correlation between the morphology of the material and its local conductivity at the nanoscale is particularly appropriate for the characterization of molecular nanoarchitectures. Then I will show how to get a control on conductive 1D molecular assemblies by exploiting the specific and directional properties of chemical bonds in coordination compounds (Chapters 3 and 4). An example of molecular assembly controlled by an external mechanical force will be then provided, where the pressure exerted by two barriers on the organic conjugated molecules spread over a water layer favors the formation of functional monomolecular ultrathin films. Post-deposition processes on these films, favoring the intermolecular interaction, will result in self-assembled nanostructures with precise electrical properties (Chapter 5). Finally, a potential approach to guide the formation of organic polymeric 1D structures or thin films by electropolymerization methods *in-situ* will be presented in Chapter 6. Conclusions and perspectives will be outlined in Chapter 7.

## 1.2. Charge transport in organic molecules

The performance of organic conjugated materials depends on the efficiency with which charge carriers, electrons and/or holes, move within the  $\pi$ -conjugated materials. The charge carriers are either injected into the organic molecules from metal electrodes in the case of molecular junctions, field-effect transistors or diodes, or generated within the materials in the case of solar cells via photon-induced charge separation at the interface between electron-donor and electron-acceptor components.<sup>18</sup>

Molecular junctions, where single molecules or few molecules in parallel are sandwiched between two metal electrodes, are extremely important to get insights into the mechanisms of charge transport along single molecules. The total current passing through the junction has three components: (1) the elastic, lossless, current due to tunneling through space, (2) the elastic current due to tunneling through molecular orbitals, and (3) the inelastic current due to electron scattering within the molecule.<sup>19</sup>

Tunneling through space may be the largest contribution, especially when the Fermi energies are not in resonance with a relevant molecular orbital.<sup>20</sup> Direct tunneling dominates for example in alkyl systems, due to their large ( $\sim 8$  eV) highest occupied molecular orbital–lowest unoccupied molecular orbital (HOMO-LUMO) gaps, i.e. to their insulating character.<sup>21</sup> For these systems a transition to hopping or diffusive transport is difficult, because field-induced breakdown occurs prior of reaching the bias necessary to have a change in mechanism. However, also for sufficiently short

conjugated molecules connected to electrodes, electrons can tunnel between the two contacts.<sup>22-24</sup> In this situation, the junction resistance increases exponentially with molecular length and is only weakly temperature dependent. The decreased HOMO-LUMO gap of the conjugated species increases the likelihood of accessing different transport mechanisms, such as resonant tunneling or electron hopping, prior to device breakdown.<sup>25</sup> Resonant tunneling current is expected to occur when the Fermi level of the electrode is in resonance with (i.e., has the same energy as) a molecular orbital; orbital mediated tunneling can be thus defined as a through-molecule current.<sup>26</sup> The low bias junction resistance for tunneling mechanisms is:  $R = R_0 e^{\beta L}$ , where  $R_0$  is the effective contact resistance,  $L$  is the molecular length, and  $\beta = \frac{2\sqrt{2m\varphi}}{\hbar}$  is a structure-dependent tunneling attenuation factor that depends on the effective tunneling barrier height  $\varphi$ , the electron effective mass  $m$ , and the Planck's constant. The tunneling barrier height  $\varphi$  is often approximated as the energy difference between the Fermi level and the closest frontier orbital.<sup>25</sup>

For longer conjugated systems, such as molecular wires,<sup>27</sup> charges can be injected into frontier orbitals and transported by incoherent hopping mechanism.<sup>28</sup> The transport is generally thermally activated and the length dependence of resistance is predicted to be linear. For hopping, the junction resistance follows:  $R = R_0 + \alpha L = R_0 + \alpha_\infty L e^{(E_a/kT)}$ , where again  $R_0$  is the contact resistance,  $\alpha$  is a molecule specific parameter with units resistance per unit length,  $L$  is the molecular length as above, and  $E_a$  is the activation energy associated with hopping. Tunneling in general has much stronger length dependence than hopping (for typical  $\beta$  values  $0.1 - 1 \text{ \AA}^{-1}$ ). Furthermore, as noted already, strong temperature dependence is very characteristic for hopping, while in tunneling the temperature dependence is weak. The Arrhenius-type thermal activation for hopping transport is explained in the Marcus picture of electron transfer.<sup>25</sup>

According to Marcus electron transfer theory,<sup>29</sup> the electron transfer (ET) processes involve vibrational motions driving the reaction coordinates from reactants to products and the rate of electron transfer in weakly coupled donor-acceptor pairs depends: i) on the electronic coupling between the two moieties, which dependence on increasing separation can be approximated by a tunneling formula, and ii) on the so called Franck-Condon factor, which represents the energy  $\lambda$  of reorganization of bond lengths and bond angles required for the donor moiety D to lose its electron (and become a cation  $D^+$  in its own equilibrium geometry) and for the acceptor moiety A to gain the electron (and become an anion  $A^-$  in its own equilibrium geometry).<sup>30</sup>

The reorganization energy is usually expressed as the sum of inner and outer contributions. The inner (intramolecular) reorganization energy arises from the change in equilibrium geometry of the donor (D) and acceptor (A) sites consecutive to the gain or loss of electronic charge upon ET. The

outer reorganization energy is due to the electronic and nuclear polarization/relaxation of the surrounding medium.<sup>18</sup> As an example an increase in the intramolecular reorganization energy of pentacene<sup>18</sup> by about 50% is caused by the introduction of ethynylsilyl substitutions<sup>31</sup> due to the involvement of the side chains in the geometry relaxation process upon ionization. In contrast, with saturated substituents, which do not couple to the geometry relaxations of the conjugated backbone, like in the case of a tetra-methyl derivative, the reorganization energy do not change.<sup>32</sup>

When going from single molecules to bulk materials one has to consider that the charge transport properties critically depend on the molecular packing and the order in the solid state as well as on the density of impurities and structural defects. Overall, the transport mechanism results from a balance between the energy gained by electron delocalization in an electronic band and the energy gained by geometry relaxation of an individual molecular chain around a charge to form a polaron; the latter term is often referred to as the relaxation (binding) energy of the polaron.<sup>18</sup> In other words, in a conjugated molecule, a charge is self-trapped by the deformation it induces in the chain. This mechanism of self-trapping is often described through the creation of localized states in the gap between the valence and the conduction bands.

In highly purified molecular single crystals, transport at low temperature can be described within a band picture, the charge carriers are fully delocalized and their mobilities are a function of the width of the valence or conduction band, i.e., of the extent of electronic coupling between oligomer chains.

When the temperature increases, the mobilities progressively decrease as a result of scattering processes, transport can then be described on the basis of effective bandwidths that are smaller than the bandwidths obtained for a rigid lattice. At an elevated temperature, transport operates via a thermally assisted polaron hopping regime where localized charge carriers jump between adjacent molecules. At the microscopic level, polaron hopping can be viewed as a self-exchange ET reaction where a charge hops from an ionized oligomer to an adjacent neutral oligomer, likewise what occurs on single molecules, in a D-A ET processes. The carrier mobilities are a direct function of the ET rates that, as was described above, are determined by two major parameters: (i) the electronic coupling between adjacent molecules, which needs to be maximized (the electronic coupling is often assimilated to the transfer integral,  $t$ , between adjacent molecules) and (ii) the reorganization energy  $\lambda$ , which needs to be minimized.

### 1.3. Self-assembly

Self-assembly can be defined as the spontaneous association of molecules into stable, structurally well-defined, aggregates through non-covalent interactions (e.g. hydrogen bonding, metal coordination, van der Waals, electrostatic or host-guest interactions).<sup>33</sup> High-selectivity and self-healing character typical of self-assembly interactions in nature can be exploited in order to assemble molecular modules and to build up very definite and complex architectures.<sup>34</sup> Among the various interactions, H-bonding<sup>35</sup> and metal coordination bonds have the advantage of being highly directional and this makes possible to access to vectorial properties (e.g. dipoles) which can be exploited to address specific functions.

In case of molecular structures deposited on solid surfaces, the final architecture is the result of the interplay of intramolecular, intermolecular, and interfacial interactions, and also includes the shear forces applied to the solution during the dewetting process, which are due to surface tension forces.<sup>36</sup> If the molecule-molecule interactions are too strong, the molecules will be poorly soluble in the chosen solvent; if molecule-substrate interactions are dominant, the molecules will be kinetically trapped on the surface instead of interacting with each other and thus undergoing reorganization. Finally, if molecule-solvent interactions are too strong, the molecules will tend to follow the solvent during the dewetting to ultimately give amorphous structures. Thus, if one of the forces dominates over the others, ordered self-assembly is not achieved.

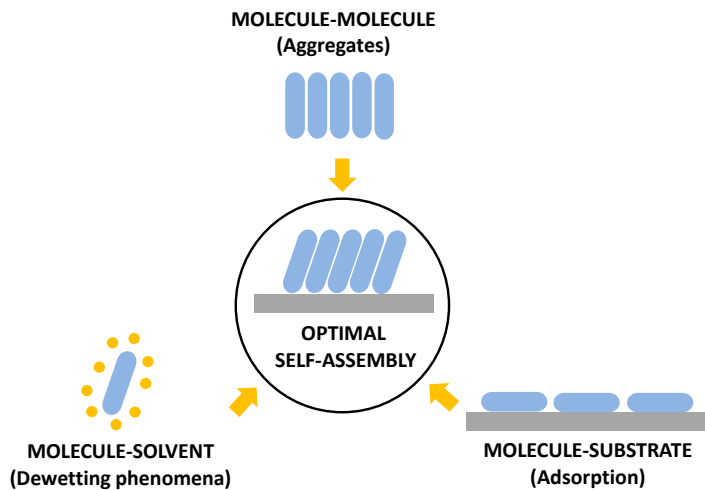


**Figure 1.2:** Schematic drawing showing the main interactions playing a role during solvent-assisted deposition. [Adapted from<sup>36</sup>]

There exist different methods which allow one to act on the equilibrium by favoring one kind of interaction with respect to the others in order to achieve the desired assembly and to fabricate

functional nano-architectures where one dimension, such as fiber diameter or film thickness can be fully controlled. Self-assembling of molecules before the deposition on the solid substrate can be achieved directly in solution, by solvent-induced precipitation (SIP) method, where the molecule-molecule interactions are favored by lowering the effect of the molecule-solvent ones. For example, by making use of this method very long fibers of conjugated discotic molecules can be obtained where, because of the enhanced  $\pi$ - $\pi$  interactions, also electrical properties are addressed.<sup>37,38</sup> The same purposes can also be achieved through post-processing methods,<sup>39</sup> such as solvent vapor annealing (SVA) or thermal annealing.<sup>39,40</sup> Indeed, because of fast solvent evaporation, the deposition of molecular thin film often results in kinetically trapped morphologies.<sup>41</sup> However, by providing mobility to the molecules more thermodynamically favored structures become accessible. In Chapter 5 an example of molecular reorganization will be provided induced by post deposition thermal treatment.

Beyond spontaneous self-assembly processes, external stimuli such as pressure, temperature gradient, electric field, magnetic field, or light can be exploited to guide the organization of molecules in desired morphologies in directed self-assembly procedures.<sup>42,43</sup> We will report on an example where an external pressure is exploited to assemble molecules at the air/water interface through Langmuir-Blodgett techniques in Chapter 5 and an example where an electric field guides the formation of a polymer *in-situ* in a device in Chapter 6.

### **1.3.1. From self-assembled monolayer to layer-by-layer growth**

Self-assembled monolayers (SAMs) are organic assemblies formed by the specific adsorption of molecular constituents from solution or gas phase onto the surface of solids; the adsorbates organize spontaneously into crystalline or semicrystalline structures.<sup>44-46</sup> In many cases the affinity of the molecules for the surface is so strong that it also displaces adsorbed adventitious organic materials from the surface.<sup>44</sup> The most common SAMs consist on thiols adsorbed on noble metal surfaces.<sup>47</sup> The high affinity of these molecular systems makes it possible to generate well-defined organic surfaces with useful and highly variable chemical functionalities displayed at the exposed interface, which eventually can be further exploited to build multilayered structures.

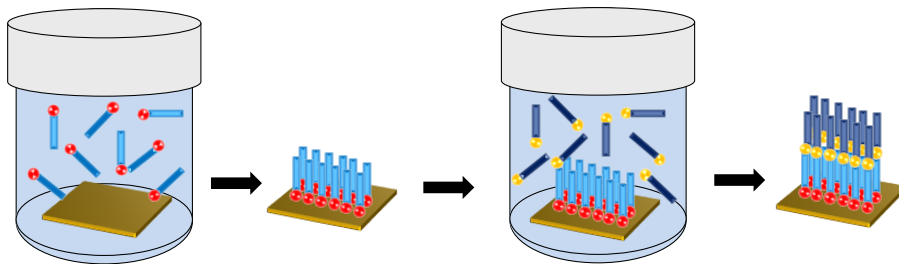


**Figure 1.3:** Scheme of a self-assembled monolayer and multilayer fabrication by molecular adsorption from solution.

The fabrication of multilayered structures having a precise control at the molecular level has a very high importance in wet processes for obtaining definite optical and electrical properties. Beyond physical methods, a control of multilayered structures can be obtained also by approaches involving specific chemical binding events. Netzer and Sagiv<sup>48</sup> were the first demonstrating the possibility of growing a layered siloxane films on surface by a self-assembly procedure. Their strategy was based on a two-step sequence involving a monolayer adsorption followed by chemical activation of the exposed surface, in order to provide suitable adsorption sites for the anchoring of the next monolayer. They employed a terminal ethylenic double bond which provided a convenient path for the activation of the monolayer outer surface via activation to terminal hydroxyls. Many other functional groups were also exploited such as carboxylates<sup>49</sup> and phosphonates<sup>50</sup> for example. Orthogonal approaches, i.e. employing the combination of different interaction motifs, also enable the preparation of hierarchical supramolecular assemblies of soft materials.<sup>51</sup> Coordination chemistry offers a very good versatility on this respect. In Chapter 3 we will show how by exploiting the specific bonds of metal-terpyridine complexes it is possible to grow molecular nanowires grafted on solid substrates by binding, via sequential solution soaking steps, a bis(terpyridine) ligand and a metal ion, i.e. through a layer-by-layer growth similar to the one used for charged polymers, yet with a much greater, i.e. atomic precision, on the assembly process.<sup>52</sup>

### 1.3.2. Assembly by Langmuir-Blodgett technique

Monomolecular thin films can be assembled at the air-water interface through the Langmuir-Blodgett technique. This technique has some advantages over other solution processes for film deposition, which are the precise control of the monolayer thickness at the molecular level and the homogeneous deposition over large areas.<sup>53</sup> It has been largely used to study the assembly of

amphiphilic molecules in monomolecular films mimicking biological systems,<sup>54-56</sup> but also to assemble functional organic conjugated materials showing peculiar optical and electrical properties.<sup>57</sup>

The technique is based on the principle that the air/water interface possesses an excess free energy originating from the difference in environment between the molecules at the surface and those in the bulk. This interfacial free energy is accessible by measurements of the surface tension,  $\gamma$ . Since the surface tension of water (73 mN/m at 20°C) is exceptionally high compared to other liquids, it is a perfect subphase for monolayer studies.

A LB monolayer film is fabricated by employing ultra clean water subphase in a teflon trough. The surface area of the trough can be varied by sweeping movable barriers. When a solution of an amphiphile in a water-insoluble solvent is placed on the water surface, the solution spreads rapidly to cover the available area. As the solvent evaporates, a monolayer is formed. When the available area for the molecules is large their interactions are weak. The monolayer can then be regarded as a two-dimensional gas (*gas phase* in Figure 1.4). Under these conditions the monolayer has little effect on the surface tension of water. If the available surface area of the monolayer is reduced by mechanically compressing the two barriers, the molecules start to exert a repulsive effect on each other. This two-dimensional analogue of a pressure is called surface pressure, SP or  $\Pi$ , and is given by the following relationship:

$$\Pi = \gamma - \gamma_0$$

where  $\gamma$  is the surface tension in absence of a monolayer and  $\gamma_0$  the surface tension when the monolayer is present. At some area/molecule ( $Mma$  = mean molecular area) the pressure will begin a rapid increase as the solid phase is reached while the area per molecule remains approximately constant. If the pressure increases much further the film will be liable of collapse.

In a typical LB experiment the surface pressure vs.  $Mma$  curve is recorded while compressing the barrier, as shown in Figure 1.4 for the docosanoic acid as an example.

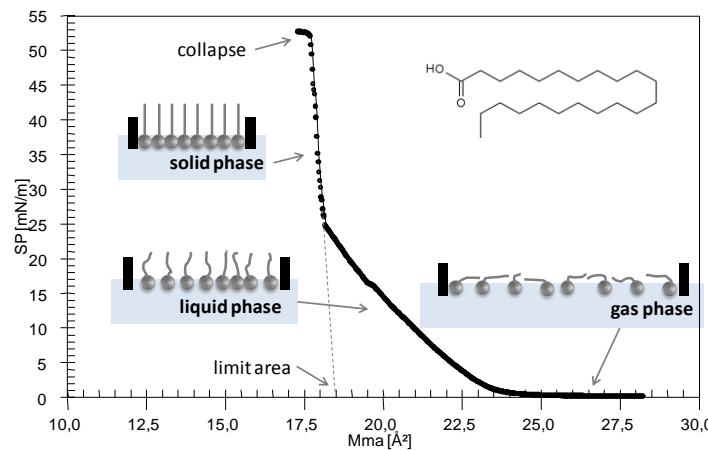


**Figure 1.4:** Surface pressure vs. mean molecular area isotherm curve of docosanoic acid  $C_{22}H_{44}O_2$ .

The surface pressure is measured by the Wilhelmy plate-method, which is based on the measurement of the force due to surface tension on a plate suspended and partially immersed in the subphase (Figure 1.5).

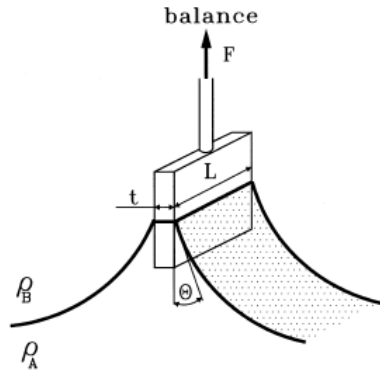


**Figure 1.5:** A Wilhelmy plate partially immersed in a water surface [Reproduced from<sup>58</sup>].

When a vertically suspended plate touches a liquid surface, a force  $F$ , which correlates with the surface tension  $\gamma$  and with the contact angle  $\theta$  according to the following equation,<sup>58</sup> acts on this plate:

$$\gamma = \frac{F}{p \cos \theta} = \frac{F}{2(L + t) \cos \theta}$$

where  $p$  is the perimeter of the three-phase contact line and  $\theta$  is the contact angle measured for the liquid meniscus in contact with the object surface. The force applied to the plate is equal to the weight of the liquid meniscus uplifted over the horizontal surface. This force, measured by the microbalance, is used to calculate the interfacial tension. The surface pressure is then determined by measuring the change in  $F$  for a stationary plate between a clean surface and the same surface with a monolayer present.

The LB deposition is traditionally carried out in the “solid” phase. The surface pressure is then high enough to ensure sufficient cohesion in the monolayer, e.g. the attraction between the molecules in the monolayer is high enough so that the monolayer does not fall apart during transfer to the solid substrate. At the chosen target pressure in the solid phase the film pressure can be held steady. A substrate may now be passed through the air/water interface and as monolayers are picked up the film area will reduce. The pressure is held constant by feedback from a pressure monitor and the reduction of area is monitored to find a transfer ratio = (area of slide covered)/(loss of area from film on trough). Ideally this should be 1 but it may be greater, if for example the molecules are slowly diffusing into the subphase, or smaller in case of incomplete coverage of the substrate.

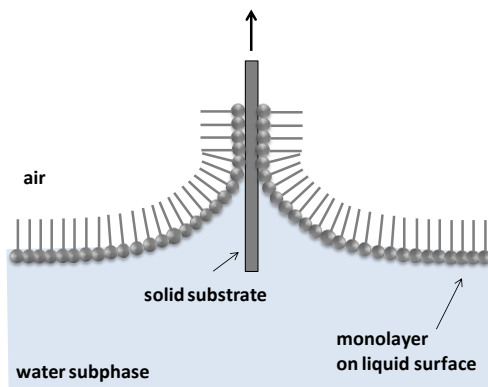


**Figure 1.6:** Example of monolayer transfer by substrate withdrawing from water to air.

Being induced by a mechanical compression, the formation of a monolayer at the air/water interface by Langmuir-Blodgett techniques is an example of self-assembly assisted by an external stimulus. In Chapter 5 we will show an example where the mechanical compression of small conjugated molecules will result in a homogeneous crystalline monomolecular thin film with high long-range order.

### 1.3.3. *Electric-field assisted assembly*

Among various external fields that can be used to direct the self-assembly, the use of an electric field has the advantages of being relatively easy and fast as well as accessible in common laboratories.

Directed self-assembly processes involving electric field gradients have been used to introduce long-range in-plane molecular orientation in organic semiconductor thin films with the possibility of producing ordering of the organic molecules over large areas.<sup>59</sup> The driving force for electric field induced alignment is the orientation-dependent polarization in a material having domains that are anisotropic in shape. The use of electric field-induced ordering and assembly indeed has been already reported by a few research groups for a variety of different structures including nanowires<sup>60</sup> carbon nanotubes<sup>61,62</sup> and  $\pi$ -conjugated supramolecular fibers.<sup>42,63,64</sup> An electric field applied across the source and drain electrodes during the solvent-vapor annealing procedure induced also P3HT polymer films to preferentially crystallize with  $\pi$ -stacking perpendicular and chains parallel to the electrodes.<sup>65</sup>

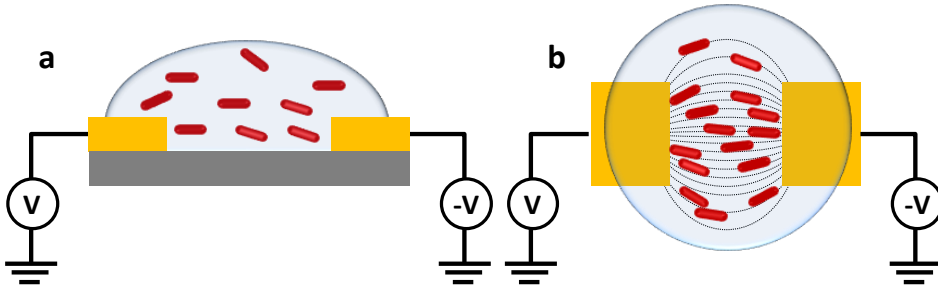


**Figure 1.7:** Cartoons showing the electric field directed assembly of nanostructures, represented by the red rods: a) side view of a droplet containing the rods between two electrodes on which a potential is applied; b) top view highlighting the electric field lines guiding the orientation of the rods.

When an external electric field is applied to polar molecules, the molecules will align so that their dipole moments are generally oriented in the direction of the electric field. However, a molecule does not need to be polar to respond to an electric field. Electric fields can induce a dipole in non-polar molecules through slight distortion of the distribution of charges within the molecules. The strength of the induced dipole is proportional to the electric susceptibility of the molecule, which is rarely isotropic along molecular axes. The anisotropy arises from asymmetry in the molecular structure, which can be exploited to induce preferential in-plane ordering. If the molecule's electrical susceptibility differs along two orthogonal molecular axes, then the molecule will align so that the axis with the largest electrical susceptibility, and therefore largest induced dipole, aligns with the applied electrical field.<sup>59</sup>

Dielectrophoretic forces are responsible of the alignment of molecules and nanostructures under alternating current (AC) electric fields: the induced dipole moment on the polarizable particles interacts with the inhomogeneous electric field giving rise to a translational motion along the electric field gradient.<sup>61</sup> Also DC electric fields have been used to align nanostructures by exploiting electrophoretic forces.<sup>66</sup> In this case, however, polar or charged structures are needed in order to achieve alignment, and the possibility of material modification or degradation has to be considered.

When dealing with electric fields applied on liquids or solutions, one has indeed to take into account the possibility of electrochemical processes to occur. Some cases have been reported regarding the exploitation of electric field applied across micrometric electrodes in order to fabricate metal nanowires from solution of their salts.<sup>67-70</sup> Few cases have also been reported regarding organic materials;<sup>71-73</sup> the latter cases are particularly interesting since the alignment occurred simultaneously to a reaction of polymerization. Since it is known that the morphology of electrochemically synthesized polymers strongly depends on the experimental conditions,<sup>74,75</sup> in Chapter 7 we will exploit DC electric field assisted assembly combined with electropolymerization, aiming to get insights on the

variables affecting the morphology of the electrochemically obtained polymer and to correlate them with the electrical properties.

## 1.4. References

1. Shirakawa, H., Louis, E. J., MacDiarmid, A. G., Chiang, C. K. & Heeger, A. J. Synthesis of electrically conducting organic polymers: halogen derivatives of polyacetylene, (CH)<sub>x</sub>. *J. Chem. Soc., Chem. Commun.*, 578-580, (1977).
2. Heeger, A. Semiconducting and Metallic Polymers: The Fourth Generation of Polymeric Materials (Nobel Lecture). *Angew. Chem. Int. Ed.* **40**, 2591 - 2611, (2001).
3. Fichou, D., Horowitz, G., Nishikitani, Y. & Garnier, F. Semiconducting conjugated oligomers for molecular electronics. *Synth. Met.* **28**, C723-C727, (1989).
4. Zaumseil, J. & Sirringhaus, H. Electron and Ambipolar Transport in Organic Field-Effect Transistors. *Chem. Rev.* **107**, 1296, (2007).
5. Zhao, Y., Guo, Y. & Liu, Y. 25th anniversary article: recent advances in n-type and ambipolar organic field-effect transistors. *Adv. Mater.* **25**, 5372-5391, (2013).
6. Friend, R. H., Gymer, R. W., Holmes, A. B., Burroughes, J. H., Marks, R. N., Taliani, C., Bradley, D. D. C., Santos, D. A. D., Brédas, J. L., Lögdlund, M. & Salaneck, W. R. Electroluminescence in conjugated polymers. *Nature* **397**, 121-128, (1999).
7. Thompson, B. C. & Frechet, J. M. Polymer-fullerene composite solar cells. *Angew. Chem. Int. Ed. Engl.* **47**, 58-77, (2008).
8. Mishra, A. & Bauerle, P. Small molecule organic semiconductors on the move: promises for future solar energy technology. *Angew. Chem. Int. Ed.* **51**, 2020-2067, (2012).
9. Scott, J. C. & Bozano, L. D. Nonvolatile Memory Elements Based on Organic Materials. *Adv. Mater.* **19**, 1452-1463, (2007).
10. Mabeck, J. T. & Malliaras, G. G. Chemical and biological sensors based on organic thin-film transistors. *Anal. Bioanal. Chem.* **384**, 343-353, (2006).
11. Baude, P. F., Ender, D. A., Haase, M. A., Kelley, T. W., Muyres, D. V. & Theiss, S. D. Pentacene-based radio-frequency identification circuitry. *Appl. Phys. Lett.* **82**, 3964, (2003).
12. Feynman, R. P. There's plenty of room at the bottom. *Caltech Engineering and Science* **23**, 22-36, (1960).
13. Aviram, A. & Ratner, M. A. Molecular rectifier. *Chem. Phys. Lett.* **29**, 277, (1974).
14. Metzger, R. M. Six Unimolecular Rectifiers and What Lies Ahead. *Lect. Notes Phys.* **680**, 313-349, (2005).
15. Moore, G. E. Cramming more components onto integrated circuits. *Electronics* **38**, (1965).
16. Schenning, A. P. H. J., Jonkheijm, P., Hoeben, F. J. M., van Herrikhuyzen, J., Meskers, S. C. J., Meijer, E. W., Herz, L. M., Daniel, C., Silva, C., Phillips, R. T., Friend, R. H., Beljonne, D., Miura, A., De Feyter, S., Zdanowska, M., Uji-i, H., De Schryver, F. C., Chen, Z., Würthner, F., Mas-Torrent, M., den Boer, D., Durkut, M. & Hadley, P. Towards supramolecular electronics. *Synth. Met.* **147**, 43-48, (2004).
17. Lèclerc, P., Surin, M., Brocorens, P., Cavallini, M., Biscarini, F. & Lazzaroni, R. Supramolecular assembly of conjugated polymers: From molecular engineering to solid-state properties. *Mater. Sci. Eng. R* **55**, 1, (2006).
18. Brédas, J.-L., Beljonne, D., Coropceanu, V. & Cornil, J. Charge-Transfer and Energy-Transfer Processes in  $\pi$ -Conjugated Oligomers and Polymers: A Molecular Picture. *Chem. Rev.* **104**, 4971-5003, (2004).
19. Honciuc, A., Metzger, R. M., Gong, A. & Spangler, C. W. Elastic and Inelastic Electron Tunneling Spectroscopy of a New Rectifying Monolayer. *J. Am. Chem. Soc.* **129**, 8310-8319, (2007).
20. Simmons, J. G. Generalized Formula for the Electric Tunnel Effect between Similar Electrodes Separated by a Thin Insulating Film. *J. Appl. Phys.* **34**, 1793, (1963).
21. Beebe, J., Kim, B., Gadzuk, J., Daniel Frisbie, C. & Kushmerick, J. Transition from Direct Tunneling to Field Emission in Metal-Molecule-Metal Junctions. *Phys. Rev. Lett.* **97**, (2006).
22. Kim, B., Choi, S. H., Zhu, X. Y. & Frisbie, C. D. Molecular Tunnel Junctions Based on  $\pi$ -Conjugated Oligoacene Thiols and Dithiols between Ag, Au, and Pt Contacts: Effect of Surface Linking Group and Metal Work Function. *J. Am. Chem. Soc.* **133**, 19864-19877, (2011).
23. McCreery, R. L. Molecular Electronic Junctions. *Chem. Mater.* **16**, 4477-4496, (2004).

24. Wold, D. J. & Frisbie, C. D. Fabrication and Characterization of Metal-Molecule- Metal Junctions by Conducting Probe Atomic Force Microscopy. *J. Am. Chem. Soc.* **123**, 5549, (2001).
25. Luo, L., Choi, S. H. & Frisbie, C. D. Probing Hopping Conduction in Conjugated Molecular Wires Connected to Metal Electrodes. *Chem. Mater.* **23**, 631-645, (2011).
26. Mazur, U. & Hipps, K. W. Resonant Tunneling Bands and Electrochemical Reduction Potentials. *J. Phys. Chem.* **99**, 6684-6688, (1995).
27. Siebbeles, L. D. A. & Grozema, F. C. *Charge and Exciton Transport through Molecular Wires*. (WILEY-VCH Verlag GmbH & Co. KGaA, 2011).
28. Nitzan, A. & Ratner, M. A. Electron transport in molecular wire junctions. *Science* **300**, 1384-1389, (2003).
29. Marcus, R. A. Electron Transfer Reactions in Chemistry : Theory and Experiment (Nobel Lecture). *Angew. Chem. Int. Ed. Engl.* **32**, 1111 -1121, (1993).
30. Metzger, R. M. Unimolecular Electrical Rectifiers. *Chem. Rev.* **103**, 3803–3834, (2003).
31. Anthony, J. E., Brooks, J. S., Eaton, D. L. & Parkin, S. R. Functionalized Pentacene: Improved Electronic Properties from Control of Solid-State Order. *J. Am. Chem. Soc.* **123**, 9482-9483, (2001).
32. Meng, H., Bendikov, M., Mitchell, G., Helgeson, R., Wudl, F., Bao, Z., Siegrist, T., Kloc, C. & Chen, C.-H. Tetramethylpentacene: Remarkable Absence of Steric Effect on Field Effect Mobility. *Adv. Mater.* **15**, 1090-1093, (2003).
33. Whitesides, G. M. & Grzybowski, B. Self-Assembly at All Scales. *Science* **295**, 2418, (2002).
34. Lehn, J.-M. Perspectives in Supramolecular Chemistry-From Molecular Recognition towards Molecular Information Processing and Self-organization. *Angew. Chem. Int. Ed. Engl.* **29**, 1304–1319, (1990).
35. Bonini, M., Zalewski, L., Orgiu, E., Breiner, T., Dötz, F., Kastler, M. & Samori, P. H-Bonding Tuned Self-Assembly of Phenylene-Thiophene-Thiophene-Phenylene Derivatives at Surfaces: Structural and Electrical Studies. *J. Phys. Chem. C* **115**, 9753-9759, (2011).
36. Palermo, V. & Samori, P. Molecular self-assembly across multiple length scales. *Angew. Chem. Int. Ed. Engl.* **46**, 4428-4432, (2007).
37. Savage, R. C., Orgiu, E., Mativetsky, J. M., Pisula, W., Schnitzler, T., Eversloh, C. L., Li, C., Mullen, K. & Samori, P. Charge transport in fibre-based perylene-diimide transistors: effect of the alkyl substitution and processing technique. *Nanoscale* **4**, 2387-2393, (2012).
38. Gemayel, M. E., Treier, M., Musumeci, C., Li, C., Müllen, K. & Samori, P. Tuning the Photoresponse in Organic Field-Effect Transistors. *J. Am. Chem. Soc.* **134**, 2429-2433, (2012).
39. De Luca, G., Pisula, W., Credgington, D., Treossi, E., Fenwick, O., Lazzerini, G. M., Dabirian, R., Orgiu, E., Liscio, A., Palermo, V., Müllen, K., Cacialli, F. & Samori, P. Non-conventional Processing and Post-processing Methods for the Nanostructuring of Conjugated Materials for Organic Electronics. *Adv. Funct. Mater.* **21**, 1279-1295, (2011).
40. De Luca, G., Liscio, A., Maccagnani, P., Nolde, F., Palermo, V., Müllen, K. & Samori, P. Nucleation-Governed Reversible Self-Assembly of an Organic Semiconductor at Surfaces: Long-Range Mass Transport Forming Giant Functional Fibers. *Adv. Funct. Mater.* **17**, 3791-3798, (2007).
41. Fabiano, S. & Pignataro, B. Engineering 3D ordered molecular thin films by nanoscale control. *Phys. Chem. Chem. Phys.* **12**, 14848-14860, (2010).
42. Sardone, L., Palermo, V., Devaux, E., Credgington, D., de Loos, M., Marletta, G., Cacialli, F., van Esch, J. & Samori, P. Electric-Field-Assisted Alignment of Supramolecular Fibers. *Adv. Mater.* **18**, 1276, (2006).
43. Kumar, P. Directed Self-Assembly: Expectations and Achievements. *Nanoscale research letters* **5**, 1367-1376, (2010).
44. Love, J. C., Estroff, L. A., Kriebel, J. K., Nuzzo, R. G. & Whitesides, G. M. Self-Assembled Monolayers of Thiolates on Metals as a Form of Nanotechnology. *Chem. Rev.* **105**, 1103-1169, (2005).
45. Claridge, S. A., Liao, W. S., Thomas, J. C., Zhao, Y., Cao, H. H., Cheunkar, S., Serino, A. C., Andrews, A. M. & Weiss, P. S. From the bottom up: dimensional control and characterization in molecular monolayers. *Chem. Soc. Rev.* **42**, 2725-2745, (2013).
46. Ulman, A. Formation and Structure of Self-Assembled Monolayers. *Chem. Rev.* **96**, 1533-1554, (1996).
47. Bain, C. D., Troughton, E. B., Tao, Y. T., Evall, J., Whitesides, G. M. & Nuzzo, R. G. Formation of Monolayer Films by the Spontaneous Assembly of Organic Thiols from Solution onto Gold. *J. Am. Chem. Soc.* **111**, 321-335, (1989).
48. Netzer, L. & Sagiv, J. A New Approach to Construction of Artificial Monolayer Assemblies. *J. Am. Chem. Soc.* **105**, 674-676, (1983).
49. Tillman, N., Ulman, A. & Penner, T. L. Formation of Multilayers by Self-Assembly. *Langmuir* **5**, 101-111, (1989).

50. Cao, G., Hong, H. G. & Mallouk, T. E. Layered Metal Phosphates and Phosphonates: From Crystals to Monolayers. *Acc. Chem. Res.* **25**, 420–427, (1992).
51. Yilmaz, M. D. & Huskens, J. Orthogonal supramolecular interaction motifs for functional monolayer architectures. *Soft Matter* **8**, 11768, (2012).
52. Decher, G. Fuzzy Nanoassemblies: Toward Layered Polymeric Multicomposites. *Science* **277**, 1232, (1997).
53. Kuhn, H. & Moebius, D. Systems of Monomolecular Layers-Assembling and Physico-Chemical Behavior. *Angew. Chem. Int. Ed. Engl.* **10**, 620-637, (1971).
54. Langmuir, I. The Constitution and Fundamental Properties of Solids and Liquids. II. Liquids. I. *J. Am. Chem. Soc.* **39**, 1848-1906, (1917).
55. Blodgett, K. Films Built by Depositing Successive Monomolecular Layers on a Solid Surface. *J. Am. Chem. Soc.* **57**, 1007-1022, (1935).
56. McConnell, H. M. Structures and transitions in lipid monolayers at the air-water interface. *Annu. Rev. Phys. Chem* **42**, 171-195, (1991).
57. Ariga, K., Yamauchi, Y., Mori, T. & Hill, J. P. 25th anniversary article: what can be done with the langmuir-blodgett method? Recent developments and its critical role in materials science. *Adv. Mater.* **25**, 6477-6512, (2013).
58. Drelich, J., Fang, C. & White, C. L. in *Encyclopedia of Surface and Colloid Science* (ed Inc. Marcel Dekker) 3152-3166 (New York 2003).
59. Hiszpanski, A. M. & Loo, Y.-L. Directing the film structure of organic semiconductors via post-deposition processing for transistor and solar cell applications. *Energy Environ. Sci.*, (2014).
60. Duan, X., Huang, Y., Cui, Y., Wang, J. & Lieber, C. M. Indium phosphide nanowires as building blocks for nanoscale electronic and optoelectronic devices. *Nature* **409**, 66, (2001).
61. Krupke, R., Hennrich, F., Lohneysen, H. & Kappes, M. M. Separation of metallic from semiconducting single-walled carbon nanotubes. *Science* **301**, 344-347, (2003).
62. Zhang, Y., Chang, A., Cao, J., Wang, Q., Kim, W., Li, Y., Morris, N., Yenilmez, E., Kong, J. & Dai, H. Electric-field-directed growth of aligned single-walled carbon nanotubes. *Appl. Phys. Lett.* **79**, 3155, (2001).
63. Cristadoro, A., Lieser, G., Rader, H. J. & Mullen, K. Field-force alignment of disc-type pi systems. *Chemphyschem* **8**, 586-591, (2007).
64. Yoshio, M., Shoji, Y., Tochigi, Y., Nishikawa, Y. & Kato, T. Electric Field-Assisted Alignment of Self-Assembled Fibers Composed of Hydrogen-Bonded Molecules Having Laterally Fluorinated Mesogens. *J. Am. Chem. Soc.* **131**, 6763-6767, (2009).
65. Fischer, F. S. U., Tremel, K., Sommer, M., Crossland, E. J. C. & Ludwigs, S. Directed crystallization of poly(3-hexylthiophene) in micrometre channels under confinement and in electric fields. *Nanoscale* **4**, 2138, (2012).
66. Li, L., Beniash, E., Zubarev, E. R., Xiang, W., Rabatic, B. M., Zhang, G. & Stupp, S. I. Assembling a lasing hybrid material with supramolecular polymers and nanocrystals. *Nature Mater.* **2**, 689-694, (2003).
67. Cheng, C., Gonela, R. K., Gu, Q. & Haynie, D. T. Self-assembly of metallic nanowires from aqueous solution. *Nano Lett.* **5**, 175-178, (2005).
68. Kawasaki, J. K. & Arnold, C. B. Synthesis of Platinum Dendrites and Nanowires Via Directed Electrochemical Nanowire Assembly. *Nano Lett.* **11**, 781, (2011).
69. Yin, A. J., Li, J., Jian, W., Bennett, A. J. & Xu, J. M. Fabrication of highly ordered metallic nanowire arrays by electrodeposition. *Appl. Phys. Lett.* **79**, 1039, (2001).
70. Talukdar, I., Ozturk, B., Flanders, B. N. & Mishima, T. D. Directed growth of single-crystal indium wires. *Appl. Phys. Lett.* **88**, 221907, (2006).
71. Thapa, P. S., Ackerson, B. J., Grischkowsky, D. R. & Flanders, B. N. Directional growth of metallic and polymeric nanowires. *Nanotechnology* **20**, 235307, (2009).
72. Thapa, P. S., Yu, D. J., Wicksted, J. P., Hadwiger, J. A., Barisci, J. N., Baughman, R. H. & Flanders, B. N. Directional growth of polypyrrole and polythiophene wires. *Appl. Phys. Lett.* **94**, 033104, (2009).
73. Das, A., Lei, C. H., Elliott, M., Macdonald, J. E. & Turner, M. L. Non-lithographic fabrication of PEDOT nano-wires between fixed Au electrodes. *Org. Electron.* **7**, 181, (2006).
74. Desilvestro, J. & Scheifele, W. Morphology of electrochemically prepared polyaniline. Influence of polymerization parameters. *J. Mater. Chem.* **3**, 263, (1993).
75. Gao, W., Sattayasamitsathit, S., Uygun, A., Pei, A., Ponadal, A. & Wang, J. Polymer-based tubular microbots: role of composition and preparation. *Nanoscale* **4**, 2447, (2012).





## 2. Exploring multiscale structural and electrical properties of materials

### 2.1. Photon-based characterization techniques

Light-matter interactions, such as absorption, emission, scattering, and diffraction can be used to probe different characteristics of the structure of thin films of organic materials at different length scales.

The optical properties of organic thin films, measured by absorption or emission spectra, contain lots of structural information and can provide information about the degree of order in the organic material. In the absorption process, electrons are excited from the bonding into unoccupied antibonding orbitals. Since the occupancy of the orbitals affects the bonding energy and therefore bonding distances, the photoexcitation and the emission processes are accompanied by changes in the molecular geometry. For this reason the spectra are sensitive to the geometry and the environment of the molecules.<sup>1</sup> Typical features are for example the decreased band gaps due to increased conjugation lengths in polymers or oligomers,<sup>2</sup> or the presence of J or H photophysical aggregates,<sup>3</sup> i.e. aggregates which exhibit respectively blue or red shifted absorption bands, useful to get information on the occurring intermolecular interactions. Some studies have been performed for instance on organic dyes such as perylene derivatives: typical H-aggregates, where molecules are perfectly cofacial, showed blue-shifts in the absorbance spectra, while displaced  $\pi$ - $\pi$ -stacking (slip-stacked packing) resulted in red-shifted J- absorption bands; interestingly different behavior is exhibited depending on the peripheral substitutions.<sup>4,5</sup>

However, though valuable examples of quantitative analyses are present in the literature, optical analysis often remains a qualitative evaluation of the structural properties of a conjugated material. Structural characterization by X-ray based techniques instead has been shown successful in revealing a broad range of microstructural and morphological features from sub-Ångstrom molecular scale to device-scale.<sup>6</sup> X-rays are indeed well-suited to study the structural complexities of organic electronic materials because radiation in this region of the electromagnetic spectrum has wavelengths on the order of the physical features being investigated.

In the X-ray regime in the range of around 0.3–10 nm, the photon energies correspond to core–shell transitions of elements used in organic materials, which strongly depend on elements and chemical environment.<sup>7</sup> X-ray photoelectron spectroscopy (XPS) technique concerns with a photoemission, i.e. the ejection of an electron from a core level by an X-ray photon of energy  $h\nu$  (Figure 2.1). The kinetic energy ( $E_K$ ) of the emitted photoelectrons is the experimental quantity measured by the spectrometer, but this is dependent on the photon energy of the X-rays employed. The binding energy of the electron ( $E_B$ ) is the parameter which identifies the electron specifically and it is defined as:  $E_B = h\nu - E_K$ , where  $h\nu$  is the photon energy and  $E_K$  is the kinetic energy of the photoelectron. The photoelectron spectrum will give information about the atomic composition but also, and more importantly on the chemical environment of the single atoms. The keystone of the technique is indeed the XPS chemical shift, i.e. the change in binding energy of a core electron of an element due to a change in the chemical bonding of that element. For example, the C–O bond in an organic material is shifted 1.6 eV relative to the methylene carbon, while C=O and O–C–O are both shifted by 2.9 eV. As a general rule the more bonds with electronegative atoms are in place, the greater is the positive XPS chemical shift.<sup>8</sup>

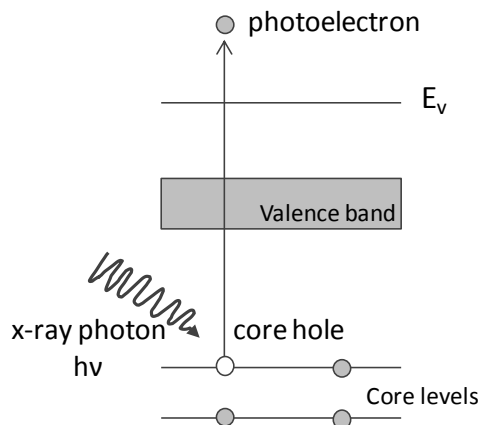


**Figure 2.1:** Schematic diagram of the XPS process, showing photoionization of an atom by the ejection of a 1s electron.

Another X-ray based technique largely employed for structural studies on ultrathin films is the Near Edge X-ray Absorption Fine Structure (NEXAFS) Spectroscopy, which is based on the principle that the absorption of X-rays excites core electrons into empty states near the photoionization threshold which are typically low-lying antibonding orbitals of  $\pi^*$  or  $\sigma^*$  character. The absorption spectra of organic molecules feature pronounced and well-resolved resonances near the ionization edge that correspond to these transitions, which sensitively depend on the local element-specific electronic and bonding structure.

In conjugated materials the  $\pi^*$ -resonance is prominent. The  $\pi^*$ -orbital orientation can be represented by a vector normal to a C=C double bond. The  $C-1s_{(C=C)} \rightarrow \pi^*_{(C=C)}$  transition dipole is therefore the logical choice in the spectral analysis of local molecular conformation. The orientation of a transition dipole can be quantified by fitting the trend of the integrated resonance intensity as a function of the incidence angle. In a well-behaved system, the plot of the intensity versus the squared sine of the incident angle is linear and can be used to determine the dichroic ratio, R, which can vary from 1 for an edge-on conjugated plane to  $-1$  for a flat (face-on) conjugated plane. This value can also be represented as the average angle between the  $C-1s \rightarrow \pi^*$  C=C dipole and the surface normal.<sup>9</sup> In this way, NEXAFS provides very useful information on the composition and orientation of molecules adsorbed on solid surfaces.

Among all the techniques for structural characterization the one based on diffraction phenomena are the most common. The principle is based on the fact that as incident X-ray waves propagate through a film, a fraction of them are diffracted by the periodic planes of atomic or molecular species. Diffraction peaks from a polycrystalline thin film or single crystal only occur at discrete scattering vectors  $q$ , specifically those for which the scattered waves from adjacent lattice planes interfere constructively. The angle at which diffraction occurs is related to the spacing between the planes while the direction of the diffracted beam is related to the orientation of the planes. The magnitude of the scattering vector is

$$q = \left(\frac{4\pi}{\lambda}\right) \sin \theta$$

for a given scattering angle  $2\theta$  and X-ray wavelength  $\lambda$ . The Bragg condition is

$$q = q_B = \left(\frac{2\pi}{d_{hkl}}\right)$$

where  $h$ ,  $k$ ,  $l$  are Miller indices used to designate planes within a crystal and  $q_B$  is orthogonal to the lattice planes, which are spaced apart by a distance  $d_{hkl}$ .

When the scattering vector is normal to the sample plane ( $q_z$ ), the observed intensity pattern describes the periodicity out of the substrate plane. This case is known as the true specular geometry (Figure 2.2a). When the scattering vector points only along the sample plane ( $q_{xy}$ ), the diffracting lattice planes are perpendicular to the sample plane. In this case, a glancing incident angle,  $\alpha$ , and this configuration is called grazing incidence X-ray diffraction, GIXRD (Figure 2.2b).

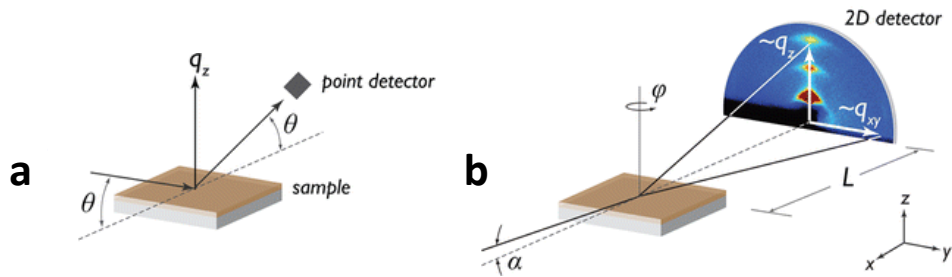


**Figure 2.2:** Wide-angle X-ray scattering geometries on thin films. (A) Specular diffraction (also used in X-ray reflectivity (XRR) and powder diffraction). (B) Grazing incidence wide-angle X-ray diffraction (GIXD),  $\alpha$  is the incidence angle, and  $\varphi$  is an in-plane, azimuthal, rotation. [Adapted from <sup>7</sup>]

Although the real lattice vectors (a, b, c) describe the distance and orientation of unit cells in the crystal, the magnitudes and orientations of the corresponding interplanar spacings  $d_{hkl}$  for a family of lattice planes with Miller indices  $hkl$  form a lattice of their own, called the reciprocal lattice ( $a^*$ ,  $b^*$ ,  $c^*$ ). It is convenient to discuss diffraction within the context of the reciprocal lattice, because  $q$  values that satisfy the Bragg condition ( $q_B$ ) can be constructed from the reciprocal lattice vectors:

$$q_{hkl} = (ha^* + kb^* + lc^*)$$

Because of the relationship between real and reciprocal space lattices, the real space unit cell can be reconstructed from diffraction data. Moreover, the shape and intensity distribution of diffraction peaks can be used to describe the orientation of the diffracting crystallites. A film with no preferred crystallographic orientation (such as in powder diffraction) will result in a ring of uniform intensity in a GIXRD experiment. Differently, for a film that has a preferred out-of-plane orientation but is isotropic in-plane (a textured film), the diffraction pattern will contain spots or arcs of different intensity, depending on the spread of the crystallite orientation distribution.<sup>10</sup>

The specular configuration is very useful to investigate ultrathin films in X-ray reflectivity (XRR) experiments by observing the low scattering angle intensity.<sup>11</sup> The observed decay and intensity oscillations with increasing scattering angle contain in fact information about the electron density

profile perpendicular to the substrate plane, the thickness, and the roughness, and it can be very useful to understand the molecular orientation in monomolecular thin films such as SAMs<sup>12</sup> or Langmuir-Blodgett films.<sup>13</sup>

All the techniques briefly reviewed here above have been demonstrated to be very powerful in discovering chemical and structural properties in the condensed state. However, it has to be reminded that they probe large areas so that the delivered information are mediated signals which are irretrievably affected by inhomogeneities and defects. Thus, if one wants to achieve insights on local properties of the materials Scanning Probe Microscopy (SPM) techniques should be the chosen methods. Below I focus on AFM and C-AFM techniques, which are the ones employed throughout the entire thesis.

## 2.2. Atomic Force Microscopy

The Atomic Force Microscope (AFM) was introduced in 1986 by Binnig, Quate and Gerber<sup>14</sup> after the introduction in the early 80's of the Scanning Tunneling Microscope (STM) by Binnig and Rohrer at the Zurich IBM Research, which earned them the Nobel Prize for Physics in 1986. These techniques have been continuously implemented in terms of mode of operation and applicative tools, giving the possibility to investigate a wide range of materials (metals, ceramics, organic materials, biomolecules) and also accessing to their local properties at the nanoscale, such as mechanical, chemical, electrical and magnetic properties.

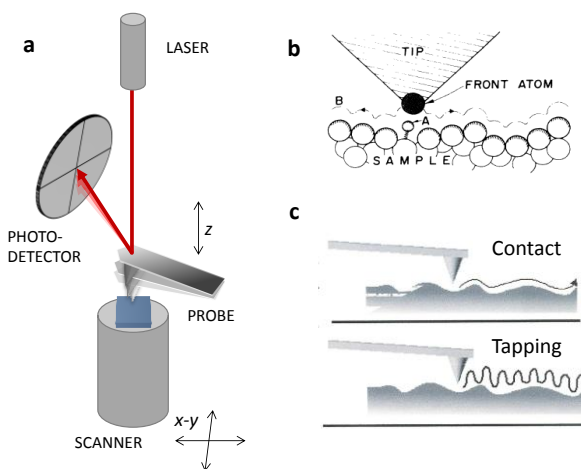


**Figure 2.3:** Working principle of an AFM microscope: a) the tip position is monitored by the position of a reflected laser beam on a photodetector; b) The tip follows contour B to maintain constant force between tip and sample (AFM) [reproduced from<sup>14</sup>]; c) Tip operating in contact and tapping modes.

The principle of operation is based on a nanoscopic sharp probe which is rastered over a surface, represented by a matrix of points in the X-Y plane. The tip follows the contour of the sample surface and provides a 3D map of the surface topography since for each point in the X-Y plane the position of the tip in the Z-axis is registered. The position of the tip is mapped by monitoring a laser beam reflected from the backside of the cantilever into a photodetector, as depicted in Figure 2.3. In order to maintain a constant separation between the tip and the sample a feedback loop is used which moves the probe along the Z-axis. Differently from STM, where the feedback controls the tip-sample separation by keeping constant the flowing tunneling current, in AFM the force exerted between tip and sample is kept constant.

When operated in the most simple imaging mode, contact mode, the AFM tip scans the surface at a constant cantilever deflection  $z$ ; considering the cantilever as a perfect spring, a controlled constant force  $F$  is therefore exerted by the tip on the sample surface according to Hooke's law ( $F = k \cdot z$ ), where  $k$  is the spring stiffness. Although the contact mode works well on hard surfaces, unwanted damage can sometimes occur on more delicate samples such as organic and biological systems. For soft materials, an alternative imaging mode called tapping mode, or intermittent contact mode, is often employed. In this case, the cantilever is driven to oscillate, and the amplitude of the oscillation is monitored. In response to tip-sample interactions, the amplitude decreases when it is brought sufficiently close to the surface. To measure topography, the cantilever oscillation amplitude is maintained at a constant value while the tip is scanned over the sample surface.

### 2.2.1. **Conductive Atomic Force Microscopy (C-AFM): state of the art**

In the Conductive Atomic Force Microscopy (C-AFM) technique a voltage is applied between the conductive metal or metal-coated tip, acting as a movable electrode, and a counter-electrode, thus simultaneously measuring the morphology and the resulting current of the material. In this way a direct correlation between the nanoscale structure and local electric conductivity becomes possible. Normally C-AFM measurements are carried out in contact mode at very low contact forces. In case of studies of very soft and fragile materials a different method can also be employed, named *Torsional Resonance Tunneling Atomic Force Microscopy (TR-TUNA AFM)*. In this operational mode the cantilever is vibrated by a pair of piezoelectric actuators so that, in addition to the fundamental flexural resonance, there is also a torsional resonance mode that can be excited by a specific vibration frequency. Lateral forces that act on the tip can cause a change in the torsional resonant frequency, amplitude, and/or phase of the cantilever when the tip gets close to the sample surface. The decrease in amplitude is used as a feedback signal for the tip sample separation.<sup>15,16</sup> The key advantage of TR-TUNA AFM is that,

like other new dynamic modes,<sup>17</sup> it allows for a reduction of the vertical and lateral tip-sample interaction forces to values comparable to the tapping mode regime<sup>18</sup> but at the same time the tip is continuously kept in the near field, in an adhesion region corresponding to negative flexural deflection,<sup>19</sup> at the boundary between direct contact and the long-range force regime, so that tunneling currents can be measured.<sup>19-21</sup>

In the simplest configuration the organic material is deposited on top of a conductive substrate and the conductive tip is scanned over such a surface (Figure 2.4a) by measuring point by point the current flowing vertically. Conversely, in a horizontal configuration the organic material is deposited on an insulating support and the electrical connection is obtained by laterally patterning a metal electrode (Figure 2.4b). Current can in this way flow through the organic layer, from the biased lateral contact to the movable metal-coated scanning probe tip. Figure 2.4c portrays a configuration named *Photoconductive-AFM* (PC-AFM): it exploits a light source to excite the sample, and the resulting photocurrent is measured by the AFM probe.

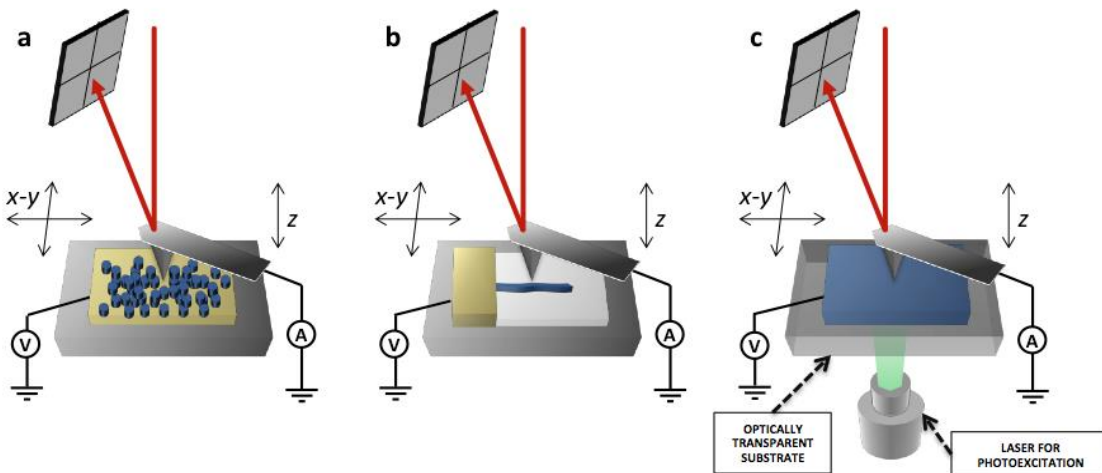


**Figure 2.4:** Cartoons showing the different setups here presented: C-AFM in (a) vertical and (b) horizontal configuration, (c) PC-AFM.

In the following recent C-AFM works are highlighted aiming at getting fundamental information on the nanoscale electrical properties of organic materials effectively employed for real opto-electronic devices, and to correlate them with the behavior at the macroscale.

Following the seminal C-AFM work by Wold and Frisbie exploring the local current-voltage properties on alkanethiol SAMs covalently grown on Au(111),<sup>22</sup> C-AFM became a popular tool to characterize the resistivity of SAMs chemisorbed on conductive substrates. By studying the dependence of the conductivity on the molecular length C-AFM gives valuable information on the

charge transport along a molecular wires. Since the mechanism responsible for charge transport in these cases is tunneling, measuring the current decay factor  $\beta$  is a suitable method to describe and compare the electrical characteristics of different molecular systems. As a result, many alkanethiols, alkanedithiols, and alkylamines molecules have been investigated by C-AFM, most of them revealing  $\beta$  values in the range  $0.7\text{-}1 \text{ \AA}^{-1}$ .<sup>23</sup>

The conductivity of SAMs made with  $\pi$ -conjugated molecules has been the subject of many experimental and theoretical investigations because of the better capability of conjugate systems to transport charges though longer distances. Because of this reason, rigid conjugated molecules have attracted a lot of interest because of their potential technological application as molecular wires. Accordingly, lower tunneling decay factors have been measured with respect to non-conjugated molecules of comparable lengths.<sup>24</sup> Average  $\beta$  values of  $0.42 \pm 0.07 \text{ \AA}^{-1}$  were determined for example for oligophenylene thiolate SAMs, to be compared to the  $\beta = 0.94 \pm 0.06 \text{ \AA}^{-1}$  for alkanethiolate SAMs on the same length.<sup>24</sup> When site-specific disruption of conjugation is introduced via chemical design, higher resistances are measured compared to the equivalent fully conjugated wire.<sup>25,26</sup>

The junction resistance is also strongly affected by the type of head group used to tether the molecule to the electrode surface. For rigid conjugated oligoacenes with a contour length ranging from one to four aromatic rings ( $0.8\text{-}1.5 \text{ nm}$  in length), the  $\beta$  was estimated being  $0.5 \text{ \AA}^{-1}$  for the monothiol- and  $0.2 \text{ \AA}^{-1}$  for the corresponding dithiol-capped. The contact resistance ( $R_0$ ) was 10-100 times lower for dithiol junctions, indicating that chemical contacts reduce both the tunneling barrier height and contact resistance significantly.<sup>27</sup> When different metal substrates are employed it was shown that the  $\beta$  values are independent of their work function, while  $R_0$  exhibited strong work function dependence.<sup>28</sup>

The possibility to employ conjugated molecules as molecular wires to transport the current over long distances has led to the engineering of new molecular systems that can be grown up to tens of nanometers in length in a controlled manner. Oligophenyleneimine (OPI) (Figure 2.5),<sup>25</sup> oligo-naphthalenefluoreneimine (ONI)<sup>26</sup> and donor/acceptor oligo-tetrathiafulvalene-pyromelliticdiimide-imine (OTPI)<sup>29</sup> wires, with lengths ranging from 1 to 7-20 nanometers, have been synthesized and linked on gold surfaces. Local current-voltage J-V characteristics performed by C-AFM in vertical configuration made it possible to observe the theoretically predicted change in charge transport from tunneling to hopping as a function of the wire length.

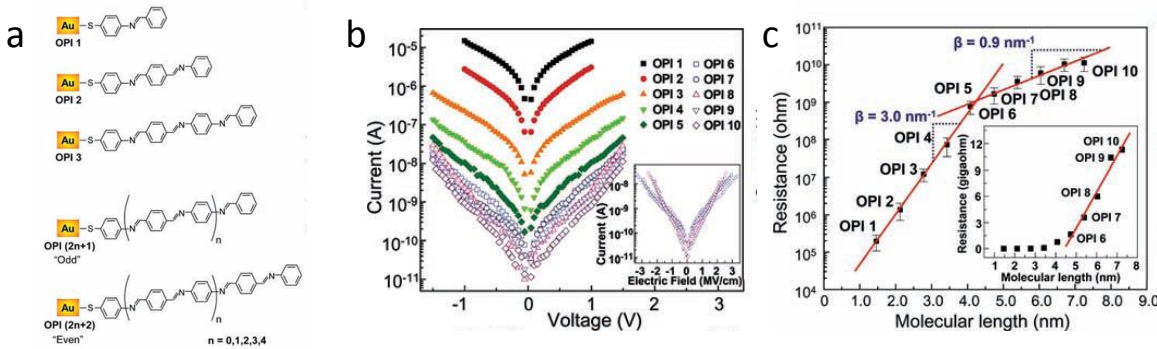


**Figure 2.5:** Length dependent current-voltage C-AFM measurements performed on oligophenyleneimine (OPI) molecular wires. By plotting the resistance as a function of the molecular length different charge transport mechanisms are evidenced. [Reproduced from<sup>25</sup>]

Additionally to the studies of SAMs conductivity in dependence of their molecular lengths, another technique is becoming popular, named Transition Voltage Spectroscopy.<sup>30</sup> It involves the analysis of the current-voltage curves at higher bias. An inflection point on a Fowler-Nordheim plot, i.e. a  $\ln(I/V^2)$  vs.  $(1/V)$  plot, for short wires having  $L < 3\text{-}4 \text{ nm}$ , is consistent with a change in the transport regime from direct tunneling to field emission. The voltage ( $V_{\text{trans}}$ ) at which this transition occurs was found to depend linearly on the energy offset between the metal Fermi level and molecular energy levels.<sup>31</sup> Since the magnitude of  $V_{\text{trans}}$  is independent on the contact area, information on the effective barrier height of a molecule can be garnered without possessing a specific knowledge of the number of molecules in the junction. Moreover, by looking at the dependence of the  $V_{\text{trans}}$  on the work function of the metal it is also possible to discriminate between a HOMO-mediated transport (hole tunneling) or a LUMO-mediated one (electron tunneling) thereby providing information on the dominant charge carrier.<sup>32</sup>

In addition to the metal-molecule energy differences caused by the molecular structure ( $\pi$ - or  $\sigma$ -bond), charge transport through molecules is also greatly influenced by the conformations and configuration that the molecules adopt on the solid support. Monolayers consisting of photochromic molecules undergoing a light-induced isomerization can behave as molecular switches. The direct immobilization of diarylethene having an acetylene moiety onto a hydrogen-terminated Si(111) surfaces using a thermal hydrosilylation reaction gave an approximately 2-fold increase in current when going from the *open* form to the *close* one.<sup>33</sup> Similarly, two different conductance states have been measured in azobenzene-based SAMs have been detected depending on the present isomeric form (*trans* or *cis*). The current in nanoscopic molecular junctions incorporating bis(diphenyl)-azobenzene molecules showed a 30-fold decrease in resistance when going from the *trans* to the *cis* state,<sup>34</sup> as the

result of a decrease in tunneling barrier length associated with the molecular conformational change (Figure 2.6). An even higher photoinduced  $I_{on}/I_{off}$  ratio up to  $7 \times 10^3$  between the *cis* and *trans* configurations was found on azobenzene-bithiophene derivatives linked to gold<sup>35</sup> and attributed to a synergic combination of SAM thickness variation and modification of the energy offset between the lowest unoccupied molecular orbital (LUMO) and the electrode Fermi energy.<sup>35</sup>

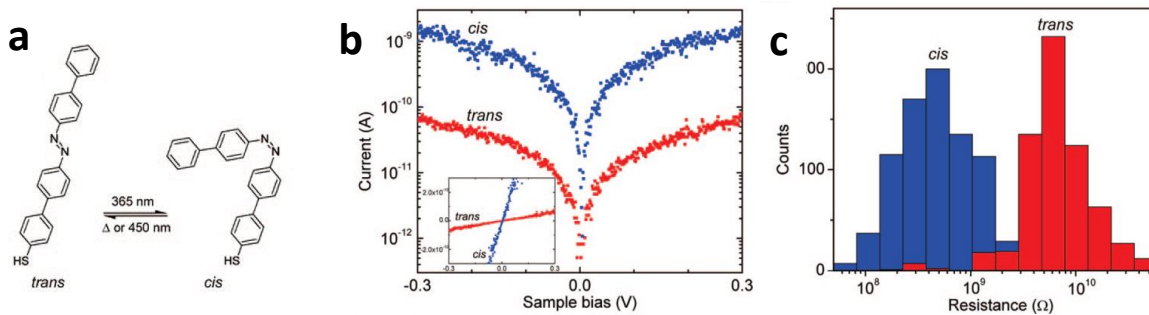


**Figure 2.6:** (a) Molecular switch based on thiolated azobenzene designed to be chemisorbed on Au (111) surfaces. (b-c) Photoinduced conformational change in bis(diphenyl)-azobenzene molecules showed a 30-fold decrease in resistance when going from the *trans* to the *cis* state. [Reproduced from<sup>36</sup>].

The possibility of C-AFM of controlling the load force exerted by the tip on the molecular junction has also allowed studying the effect of an applied force on the electrical properties of a material at the nanoscale. For example it allows to gain insight into the dependence of the electrical transport on the tilt angle of molecules adsorbed on a surface. It was shown that by increasing tilt angle, alkanethiol SAMs exhibit improved intermolecular charge transfer. In fact, as the molecular tilt angle increases with the tip-loading force, the chain-to-chain tunneling becomes significant, in addition to the already existing through-bond tunneling in overall transport.<sup>37</sup> Moreover, the onset for Fowler-Nordheim tunneling ( $V_{trans}$ ), shifts to lower voltages as the tip loading force is augmented, increasing the tilt angle, as a result of an enhancement of field emission due to a barrier thinning and consequently increasing electric field.<sup>38</sup>

It is worth stressing that reliable current-voltage measurements on SAMs require collection of a large set of data to be analyzed using statistical tools. One of the first systematic approach employed molecules of 1,8-octanedithiol which were inserted into an octanethiol monolayer on Au(111) using a replacement reaction. The thiol groups at the top of the film were used to bind gold nanoparticles. This allowed locating individual nanoparticles and to contact them with the AFM tip. Current-voltage curves were then quantized as integer multiples of one fundamental curve to identify single-molecule contacts.<sup>39</sup> Similar approaches have also been reported to evaluate single molecule conductivity by C-

AFM break-junction measurements.<sup>40-43</sup> Recently, a different approach was proposed<sup>44</sup> employing large arrays of sub-10 nm single crystal Au nanodots electrodes on silicon substrate. Each nanodot was covered by the SAM of interest and the C-AFM tip was scanned over the whole array at a fixed voltage. By analyzing the current map images with a thresholding program, the authors were then able to reconstruct conductance histograms referred to thousands of junctions. Another methodology consisted in building up two-dimensional histograms by logarithmically binning the  $dI/dV$  values, determined numerically from thousands of  $I$ - $V$  curves, for each voltage applied. This method made it possible to distinguish general tendencies in the  $dI/dV$  curves from statistical variations in the conductance values, making it possible to recognize destructive quantum interference effects in the transport of cross conjugated molecular wires compared to the corresponding linearly conjugated ones.<sup>45</sup>

A lateral transport governed by the interconnection among individual fullerene molecules was recently measured by Bassani and co-workers by growing a fullerene terminate SAM covalently linked to  $\text{SiO}_2$ . The resistance between the C-AFM tip contacting the SAM and a patterned counter electrode was determined. The charge transport, which was detected up to 1.5  $\mu\text{m}$  away from the electrode, appears to be intrinsically space-charge limited, and governed by the connectivity of the fullerene clusters.<sup>46</sup> Lateral transport was also probed in oligothiophene Langmuir-Blodgett monolayer islands deposited on native oxide-covered Si-p<sup>+</sup> bottom electrode. Because of the larger resistance associated with the oxide layer with respect to that between the molecules, the current was found to depend linearly on the island diameter as a result of an increased contact area. Moreover, the transport in a single grain was found to occur preferentially in one direction, corresponding to the direction where  $\pi$ -orbitals of the thiophene units overlap more.<sup>47</sup> Already in the late '90s, Frisbie et al. had assessed the horizontal electrical transport of single sexithiophene (6T) grains both in two and three terminal devices at the nanoscale, also estimating the resistance at one single grain boundary (Figure 2.7).<sup>48-51</sup> The interconnection among crystalline domains was shown to drastically affect charge transport also in polycrystalline organic semiconducting thin films,<sup>52,53</sup> so that understanding the nature of these boundaries and how they influence charge transport is critical to the field of organic electronics. Spherulites, i.e. structures arising from a single nucleation point and including a distribution of orientations around the radial axis, are frequently observed in polycrystalline solution-processed organic semiconductor thin films, such as triethylsilylethynyl anthradithiophene (TES ADT). The boundaries between neighboring spherulites exhibit varying angles of molecular orientation mismatch along their lengths. C-AFM revealed that current flow is unaffected when the mismatch of molecular

orientation along a boundary is low (low-angle interspherulite boundaries), while charge transport is limited by the presence of high-angle interspherulite boundaries.<sup>54</sup> As a result, guiding crystallization in order to eliminate the presence of high-angle interspherulite boundaries was demonstrated to be a promising route towards the improvement of the overall organic thin-film transistor (OTFT) device performance (Figure 2.7).<sup>54</sup>

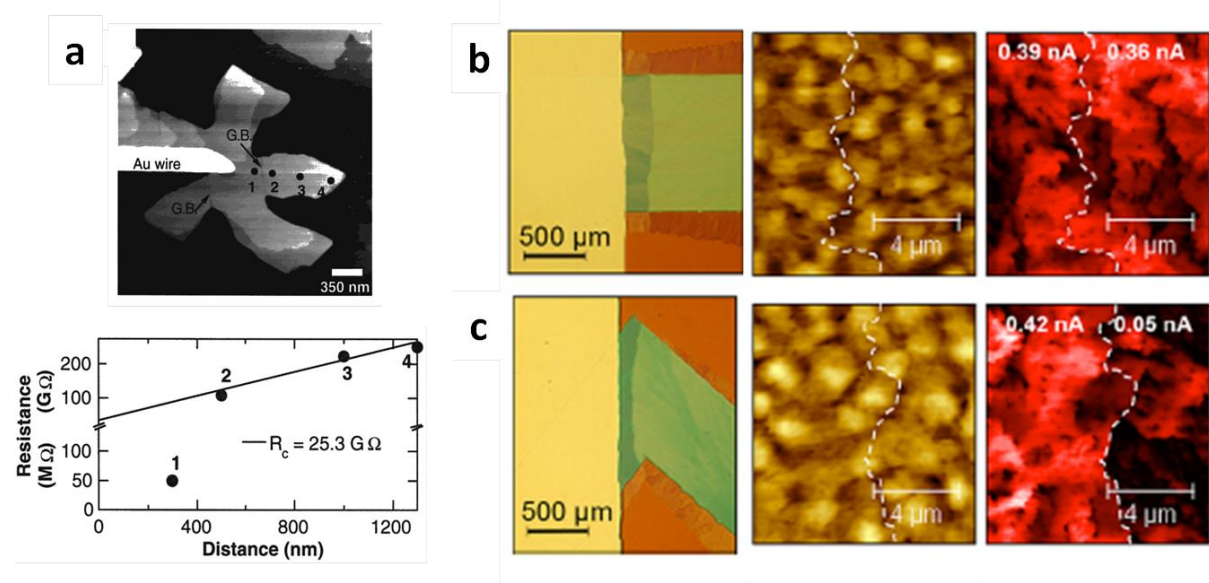


**Figure 2.7:** (a) Topography of a 6T crystal connected to a microfabricated Au wire on SiO<sub>2</sub>, and plot reporting the resistance versus probe-wire separation distance, measured from local I-V on point marked as 1-4. The linear fit through points 2, 3, and 4 has been used to estimate the grain boundary resistance. [Reproduced from<sup>52</sup>]. (b-c) Optical images, AFM topography images (Z-scale=25 nm) and current maps (0-1.4 nA current scale) of (b) low-angle, and (c) wide-angle interspherulite boundaries in TES ADT polycrystalline films. [Reproduced from<sup>54</sup>].

The study of the electrical properties of individual nanostructures such as single fibers and wires has also represented a big challenge in the field of organic electronics, although it can be seen as just the first step towards the exploration of ensembles of nanostructures which communicate among each other with the ultimate goal of producing high performing device. The intrinsic electron mobility of individual N,N'-1H,1H-perfluorobutyl-dicyanoperylene-carboxydiimide PDIF-CN<sub>2</sub> supramolecular fibers was determined by three-terminal C-AFM to be  $(1.5 \pm 0.8) \times 10^{-2} \text{ cm}^2 \text{ V}^{-1} \text{ s}^{-1}$  under ambient conditions, being nearly three orders of magnitude higher than that of fiber ensembles.<sup>55</sup> Conversely, the longitudinal mobility  $\mu_L$  on a single poly(3-alkylthiophene) nanofiber was estimated  $0.07 \pm 0.03 \text{ cm}^2 \text{ V}^{-1} \text{ s}^{-1}$ , differently from its transversal mobility  $\mu_T$  of  $10^{-5}$ – $10^{-6} \text{ cm}^2 \text{ V}^{-1} \text{ s}^{-1}$ . For one single nanofiber  $\mu_T$  was found to decrease with increasing alkyl side chain length while  $\mu_L$  was alkyl chain length independent.<sup>56</sup> Interestingly, the hole mobility of one fiber resulted to be similar to the mobility

of a web of nanofibers; this finding was explained by the fact that the bridging of two or more individual nanofibers can be neglected with respect to the intrinsic resistance of the single nanofiber.<sup>57</sup> In 1996 for the first time the resistance of a single multiwall carbon nanotube of 14 nm diameter, physisorbed on an insulating SiO<sub>2</sub> substrate and contacted with a gold electrode, was measured by C-AFM;<sup>58</sup> by employing NbN coated tips as counter electrodes the estimated resistance amounted to 0.06 MΩ/μm. Later, the resistance of single wall carbon nanotubes (SWNT) was studied in detail in correlation to the presence of defects; it revealed that just a 0.03% of di-vacancies produces an increase of three orders of magnitude in the resistance of a SWNT of 400 nm length.<sup>59</sup> Beside organic polymer wires also metal-organic wires have been studied on the nanoscale.<sup>60,61</sup> The length dependent resistance measurements on metal-organic [Pt<sub>2</sub>(dta)<sub>4</sub>I]<sub>n</sub> (dta=dithioacetate) nanoribbons allowed the estimation of the distance between defects, finding that the inter-fibre transport is the limiting process in the crystals while transport along the single chains dominated in the nanoribbons.<sup>62</sup>

In summary, C-AFM exhibit the unique capability of correlating structural and electronic properties in nanoscale architectures being important issues for both technological and scientific studies, since in electronic devices the performance is strongly dependent on the order at the supramolecular level.

### 2.3. Organic Thin Film Transistors (OTFTs)

The main parameter which is normally used to describe the electrical performance of an organic material is the charge carrier mobility. In absence of an external electric field the charges move around an average position by diffusion. If the transport of the charges is instead caused by an external field, the resulting current is due to drift. The mobility is a measurement of the rate of transport by drift, and it is measured in cm<sup>2</sup>·V<sup>-1</sup>·s<sup>-1</sup>, being the ratio of the charge velocity with respect to the external field.

Organic thin film transistors OTFTs offer a straightforward method to investigate the charge transport properties of organic semiconductors. An OTFT is a three-terminal device, containing a source, a drain and a gate electrode. In dependence of the relative position of the various layers an OTFT can be assembled in different configurations or geometries, as shown in Figure 2.8. It operates like a capacitor where one plate is a conducting channel between two electrodes (source and drain) and the second plate is a third electrode called gate which modulates the charge density in the channel.

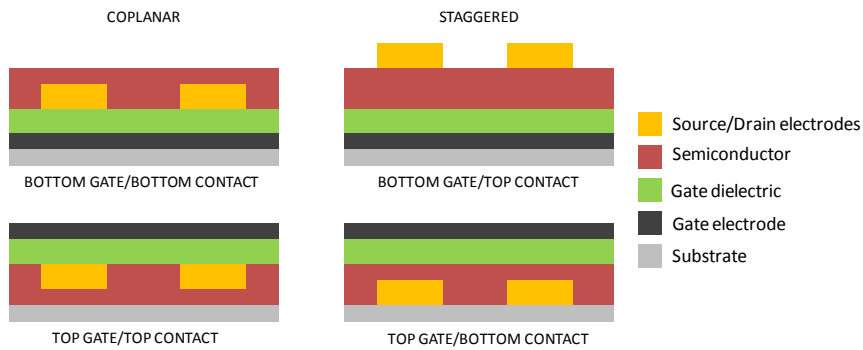


**Figure 2.8:** Different configurations for OTFTs.

Organic electronic materials have been classified as hole or electron transporting materials even though this is not an intrinsic property of the material itself but it relies on the ease of injection of carriers from the source and drain electrodes, i.e. the matching of the work function of the metal with the HOMO or the LUMO of the material favors the injection of electron (n-type operation) or holes (p-type operation), respectively. The “field effect” is clarified in the simplified electronic energy level diagrams shown in Figure 2.9.

Figure 2.9 shows the positions of the HOMO and LUMO orbitals of the organic semiconductor relative to the Fermi levels of the source and drain contacts. At zero gate bias, if small source-drain bias were applied, there would be no conduction because there are no mobile charges in the semiconductor, i.e. the device is in the off state.<sup>63</sup>

For an *n*-type operation, a positive gate voltage produces a large electric field at the organic/dielectric interface, which causes the HOMO and LUMO levels in the semiconductor to shift down with respect to the Fermi levels of the metal contacts. If the gate field is large enough, the LUMO becomes resonant with the Fermi levels of the contacts, and electrons can then flow from the contacts into the LUMO, i.e. there are mobile electrons at the semiconductor/dielectric interface, which upon application of a drain voltage produce an electric current between the source and drain.

Similarly, for a *p*-type operation a negative gate bias causes the HOMO and LUMO levels to shift up such that the HOMO becomes resonant with the contact Fermi levels and electrons spill out of the semiconductor and into the contacts, leaving positively charged holes. These holes are now the mobile charges that move in response to an applied drain voltage.

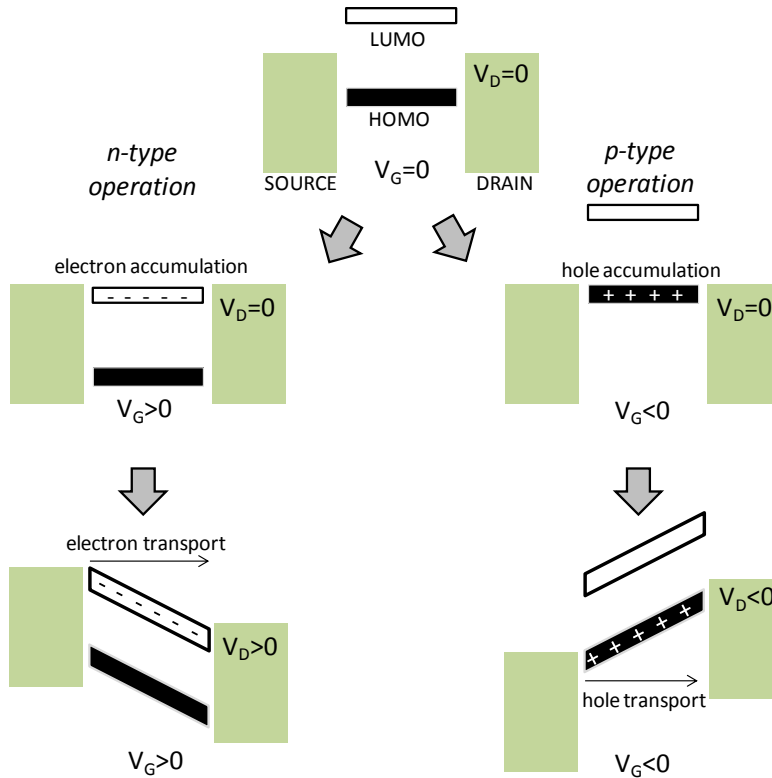


**Figure 2.9:** (a) Idealized energy level diagram demonstrating the principle of field effect transistor operation for the case of n-type and p-type operation.

In real devices the point at which mobile charge carriers are first introduced into the organic film does not correspond to  $V_G = 0$ . For an *n*-channel semiconductor, a mismatch between the Fermi level of the metal and the organic LUMO results in charge transfer between the metal and organic, causing a dipole and band bending in the organic. This necessitates the application of a nonzero  $V_G$  (often referred to as  $V_{FB}$  in the literature) just to achieve the flat-band condition. Moreover, if there are large numbers of deep electron traps present in the film (rendering the electrons effectively immobile), these will have to be filled before the channel can conduct. Conversely, if the channel is inadvertently doped with negative carriers, due for example to impurities, it will be conductive at  $V_G = 0$ .

To handle these various situations, it is convenient to define a threshold gate voltage,  $V_T$ , necessary to induce mobile charges. Typical I-V characteristics of a TFT are shown in Figure 2.10, for an n-type operation.

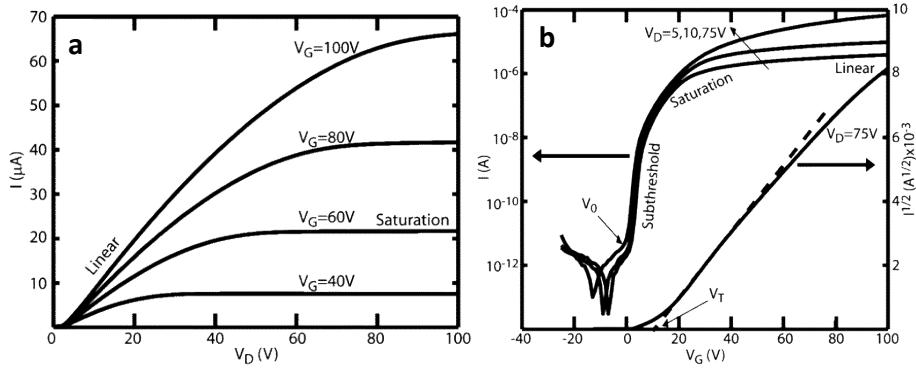


**Figure 2.10:** Output and transfer curves for an n-type semiconductor TFT. The linear and saturation regime are highlighted in the pictures. [Reproduced from<sup>63</sup>].

The output characteristics are  $I_d$ - $V_d$  curves at various  $V_g$ . The transfer characteristics show the variation of  $I_d$  as a function of  $V_g$  at fixed  $V_d$ . When the bias on the drain  $V_d$  is much smaller than the bias on the gate  $V_g$ , i.e.  $|V_d| \ll |V_g - V_T|$ , the transistor is operate in linear regime and the current is described by the following:

$$I_d = -\mu_{lin} \frac{C_i W}{L} (V_g - V_T) V_d$$

where  $W$  and  $L$  are the width and the length of the channel,  $C_i$  is the dielectric capacitance,  $\mu_{lin}$  the mobility of the charge carriers and  $V_T$  the threshold voltage.

From the transfer characteristics in the linear regime the mobility can then be extracted as:

$$\mu_{lin} = \left( \frac{\partial I_d}{\partial V_g} \right) \frac{L}{V_d C_i W}$$

When the drain bias is much larger than the gate bias, i.e.  $|V_d| \geq |V_g - V_T|$ , the transistor is driven in saturation and the current is:

$$I_d = -\mu_{sat} \frac{C_i W}{2L} (V_g - V_T)^2$$

Thus, the value of the field effect mobility in saturation can be obtained from plot of the square root of the  $I_d$  as a function of  $V_g$ :

$$\mu_{sat} = \left( \frac{\partial \sqrt{I_d}}{\partial V_g} \right)^2 \frac{2L}{C_i W}$$

Other parameters which are extracted from the transfer characteristics are the threshold voltage  $V_T$ , which can be calculated from the intercept of a the linear region of the  $\sqrt{I_d}$  vs.  $V_g$  plot as shown in Figure 2.10b, and the  $I_{on}/I_{off}$  which is the ratio of the drain current in the on-state to that in the off-state.

## 2.4. References

1. Salleo, A., Kline, R. J., DeLongchamp, D. M. & Chabinyc, M. L. Microstructural characterization and charge transport in thin films of conjugated polymers. *Adv. Mater.* **22**, 3812-3838, (2010).
2. Cornil, J., Beljonne, D., Heller, C. M., Campbell, I. H., Laurich, B. K., Smith, D. L., Bradley, D. D. C., Muellen, K. & Bredas, J. L. Photoluminescence spectra of oligo-paraphenylenevinylenes: a joint theoretical and experimental characterization. *Chem. Phys. Lett.* **278**, 139-145, (1997).
3. Spano, F. C. The Spectral Signatures of Frenkel Polarons in H- and J-Aggregates. *Acc. Chem. Res.* **43**, 429-439, (2010).
4. Wurthner, F., Kaiser, T. E. & Saha-Moller, C. R. J-aggregates: from serendipitous discovery to supramolecular engineering of functional dye materials. *Angew Chem Int Ed Engl* **50**, 3376-3410, (2011).
5. Glaz, M. S., Biberdorf, J. D., Nguyen, M. T., Travis, J. J., Holliday, B. J. & Vanden Bout, D. A. Perylene diimide functionalized polynorbornene: a macromolecular scaffold for supramolecular self-assembly. *J. Mater. Chem. C* **1**, 8060, (2013).
6. Henke, B. L., Gullikson, E. M. & Davis, J. C. X-ray interactions: photoabsorption, scattering, transmission, and reflection at  $E=50\text{-}30000\text{ eV}$ ,  $Z=1\text{-}92$ . *At. Data. Nucl. Data Tables* **54**, 181-342, (1993).
7. Rivnay, J., Mannsfeld, S. C., Miller, C. E., Salleo, A. & Toney, M. F. Quantitative determination of organic semiconductor microstructure from the molecular to device scale. *Chem Rev* **112**, 5488-5519, (2012).
8. Watts, J. F. & Wolstenholme, J. *An introduction to surface analysis by XPS and AES*. (Wiley, 2003).
9. Ade, H. & Hitchcock, A. P. NEXAFS microscopy and resonant scattering: Composition and orientation probed in real and reciprocal space. *Polymer* **49**, 643-675, (2008).
10. Chabinyc, M. L. X-ray Scattering from Films of Semiconducting Polymers. *Polym. Rev.* **48**, 463-492, (2008).
11. Chason, E. & Mayer, T. M. Thin film and surface characterization by specular X-ray reflectivity. *Critical Reviews in Solid State and Materials Sciences* **22**, 1-67, (1997).
12. Smits, E. C. P., Mathijssen, S. G. J., van Hal, P. A., Setayesh, S., Geuns, T. C. T., Mutsaers, K. A. H. A., Cantatore, E., Wondergem, H. J., Werzer, O., Resel, R., Kemerink, M., Kirchmeyer, S., Muzafarov, A. M., Ponomarenko, S. A., de Boer, B., Blom, P. W. M. & de Leeuw, D. M. Bottom-up organic integrated circuits. *Nature* **455**, 956-959, (2008).
13. Kurth, D. G., Lehmann, P., Volkmer, D., Müller, A. & Schwahn, D. Biologically inspired polyoxometalate-surfactant composite materials. Investigations on the structures of discrete, surfactant-encapsulated clusters, monolayers, and Langmuir-Blodgett films of  $(\text{DODA})_{40}(\text{NH}_4)_2[(\text{H}_2\text{O})_n \subset \text{Mo}_{132}\text{O}_{372}(\text{CH}_3\text{CO}_2)_{30}(\text{H}_2\text{O})_{72}]$ . *J. Chem. Soc., Dalton Trans.*, 3989-3998, (2000).
14. Binnig, G., Quate, C. F. & Gerber, C. Atomic Force Microscope. *Phys. Rev. Lett.* **56**, 930-933, (1986).
15. Huang, L. & Su, C. A torsional resonance mode AFM for in-plane tip surface interactions. *Ultramicroscopy* **100**, 277-285, (2004).
16. Reinstädler, M., Kasai, T., Rabe, U., Bhushan, B. & Arnold, W. Imaging and measurement of elasticity and friction using the TRmode. *J. Phys. D: Appl. Phys.* **38**, R269, (2005).
17. Desbiez, S., Hergué, N., Douhéret, O., Surin, M., Dubois, P., Geerts, Y., Lazzaroni, R. & Leclère, P. Nanoscale investigation of the electrical properties in semiconductor polymer-carbon nanotube hybrid materials. *Nanoscale* **4**, 2705, (2012).
18. Su, C., Huang, L., Prater, C. B. & Bhushan, B. in *Applied Scanning Probe Methods V - Scanning Probe Microscopy Techniques* (eds Bharat Bhushan, Satoshi Kawata, & Harald Fuchs) 113-148 (Springer Berlin Heidelberg, 2007).
19. Weber, S. A. L. & Berger, R. d. Electrical tip-sample contact in scanning conductive torsion mode. *Appl. Phys. Lett.* **102**, 163105, (2013).

20. Weber, S. A. L., Haberkorn, N., Theato, P. & Berger, R. d. Mapping of Local Conductivity Variations on Fragile Nanopillar Arrays by Scanning Conductive Torsion Mode Microscopy. *Nano Lett.* **10**, 1194, (2010).
21. Musumeci, C., Rosnes, M. H., Giannazzo, F., Symes, M. D., Cronin, L. & Pignataro, B. Smart High- $\kappa$  Nanodielectrics Using Solid Supported Polyoxometalate-Rich Nanostructures. *ACS Nano* **5**, 9992, (2011).
22. Wold, D. J. & Frisbie, C. D. Formation of Metal-Molecule-Metal Tunnel Junctions: Microcontacts to Alkanethiol monolayers with a Conducting AFM Tip. *J. Am. Chem. Soc.* **122**, 2970, (2000).
23. Mativetsky, J. M., Palma, M. & Samorì, P. Exploring electronic transport in molecular junctions by conducting atomic force microscopy. *Top. Curr. Chem.* **285**, 157-202, (2008).
24. Wold, D. J., Haag, R., Rampi, M. A. & Frisbie, C. D. Distance Dependence of Electron Tunneling through Self-Assembled Monolayers Measured by Conducting Probe Atomic Force Microscopy: Unsaturated versus Saturated Molecular Junctions. *J. Phys. Chem. B* **106**, 2813, (2002).
25. Ho Choi, S., Kim, B. & Frisbie, C. D. Electrical resistance of long conjugated molecular wires. *Science* **320**, 1482-1486, (2008).
26. Ho Choi, S., Risko, C., Delgado, M. C. R., Kim, B., Bredas, J.-L. & Frisbie, C. D. Transition from Tunneling to Hopping Transport in Long, Conjugated Oligo-imine Wires Connected to Metals. *J. Am. Chem. Soc.* **132**, 4358, (2010).
27. Kim, B., Choi, S. H., Zhu, X. Y. & Frisbie, C. D. Molecular Tunnel Junctions Based on  $\pi$ -Conjugated Oligoacene Thiols and Dithiols between Ag, Au, and Pt Contacts: Effect of Surface Linking Group and Metal Work Function. *J. Am. Chem. Soc.* **133**, 19864-19877, (2011).
28. Engelkes, V. B., Beebe, J. M. & Frisbie, C. D. Length-Dependent Transport in Molecular Junctions Based on SAMs of Alkanethiols and Alkanedithiols: Effect of Metal Work Function and Applied Bias on Tunneling Efficiency and Contact Resistance. *J. Am. Chem. Soc.* **126**, 14287, (2004).
29. Ho Choi, S. & Frisbie, C. D. Enhanced Hopping Conductivity in Low Band Gap Donor-Acceptor Molecular Wires Up to 20 nm in Length. *J. Am. Chem. Soc.* **132**, 16191, (2010).
30. Ricœur, G., Lenfant, S., Guérin, D. & Vuillaume, D. Molecule/Electrode Interface Energetics in Molecular Junction: A “Transition Voltage Spectroscopy” Study. *J. Phys. Chem. C* **116**, 20722-20730, (2012).
31. Beebe, J., Kim, B., Gadzuk, J., Daniel Frisbie, C. & Kushmerick, J. Transition from Direct Tunneling to Field Emission in Metal-Molecule-Metal Junctions. *Phys. Rev. Lett.* **97**, (2006).
32. Beebe, J. M., Kim, B., Frisbie, C. D. & Kushmerick, J. G. Measuring Relative Barrier Heights in Molecular Electronic Junctions with Transition Voltage Spectroscopy. *ACS Nano* **2**, 827, (2008).
33. Uchida, K., Yamanoi, Y., Yonezawa, T. & Nishihara, H. Reversible on/off conductance switching of single diarylethene immobilized on a silicon surface. *J. Am. Chem. Soc.* **133**, 9239-9241, (2011).
34. Mativetsky, J. M., Pace, G., Elbing, M., Rampi, M. A., Mayor, M. & Samorì, P. Azobenzenes as Light-Controlled Molecular Electronic Switches in Nanoscale Metal-Molecule-Metal Junctions. *J. Am. Chem. Soc.* **130**, 9192, (2008).
35. Smaali, K., Lenfant, S., Karpe, S., Oçafrain, M., Blanchard, P., Deresmes, D., Godey, S., Rochefort, A., Roncali, J. & Vuillaume, D. High On • Off Conductance Switching Ratio in Optically-Driven Self-Assembled Conjugated Molecular Systems. *ACS Nano* **4**, 2411, (2010).
36. Mativetsky, J. M., Pace, G., Elbing, M., Rampi, M. A., Mayor, M. & Samorì, P. Azobenzenes as Light-Controlled Molecular Electronic Switches in Nanoscale Metal-Molecule-Metal Junctions. *J. Am. Chem. Soc.* **130**, 9192, (2008).
37. Song, H., Lee, H. & Lee, T. Intermolecular Chain-to-Chain Tunneling in Metal-Alkanethiol-Metal Junctions. *J. Am. Chem. Soc.* **129**, 3806-3807, (2007).
38. Wang, G., Kim, T.-W., Jo, G. & Lee, T. Enhancement of Field Emission Transport by Molecular Tilt Configuration in Metal-Molecule-Metal Junctions. *J. Am. Chem. Soc.* **131**, 5980-5985, (2009).
39. Cui, X. D., Primak, A., Zarate, X., Tomfohr, J., Sankey, O. F., Moore, A. L., Moore, T. A., Gust, D., Harris, G. & Lindsay, S. M. Reproducible measurement of single-molecule conductivity. *Science* **294**, 571-574, (2001).
40. Aradhya, S. V., Frei, M., Hybertsen, M. S. & Venkataraman, L. Van derWaals interactions at metal/organic interfaces at the single-molecule level. *Nat. Mater.* **11**, 872, (2012).
41. Frei, M., Aradhya, S. V., Koentopp, M., Hybertsen, M. S. & Venkataraman, L. Mechanics and Chemistry: Single Molecule Bond Rupture Forces Correlate with Molecular Backbone Structure. *Nano Letters* **11**, 1518-1523, (2011).
42. Kamenetska, M., Quek, S. Y., Whalley, A. C., Steigerwald, M. L., Choi, H. J., Louie, S. G., Nuckolls, C., Hybertsen, M. S., Neaton, O. J. B. & Venkataraman, L. Conductance and Geometry of Pyridine-Linked Single-Molecule Junctions. *J. Am. Chem. Soc.* **132**, 6817-6821, (2010).

43. Xu, B., Xiao, X. & Tao, N. J. Measurements of Single-Molecule Electromechanical Properties. *J. Am. Chem. Soc.* **125**, 16164-16165, (2003).
44. Smaali, K., Clémén, N., Patriarche, G. & Vuillaume, D. Conductance Statistics from a Large Array of Sub-10 nm Molecular Junctions. *ACS Nano* **6**, 4639, (2012).
45. Guédon, C. M., Valkenier, H., Markussen, T., Thygesen, K. S., Hummelen, J. C. & van der Molen, S. J. Observation of quantum interference in molecular charge transport. *Nat. Nanotech.* **7**, 305-309, (2012).
46. Dubacheva, G. V., Devynck, M., Raffy, G., Hirsch, L., Del Guerzo, A. & Bassani, D. M. Probing Lateral Charge Transport in Single Molecule Layers: How Charge is Transported Over Long Distances in Fullerene Self-Assembled Monolayers. *Small* **10**, 454-461, (2014).
47. Hendriksen, B. L., Martin, F., Qi, Y., Mauldin, C., Vukmirovic, N., Ren, J., Wormeester, H., Katan, A. J., Altoe, V., Aloni, S., Fréchet, J. M., Wang, L. W. & Salmeron, M. Electrical transport properties of oligothiophene-based molecular films studied by current sensing atomic force microscopy. *Nano Letters* **11**, 4107-4112, (2011).
48. Loiacono, M. J., Granstrom, E. L. & Frisbie, C. D. Investigation of Charge Transport in Thin, Doped Sexithiophene Crystals by Conducting Probe Atomic Force Microscopy. *J. Phys. Chem. B* **102**, 1679, (1998).
49. Granstrom, E. L. & Frisbie, C. D. Field Effect Conductance Measurements on Thin Crystals of Sexithiophene. *J. Phys. Chem. B* **103**, 8842, (1999).
50. Kelley, T. W. & Frisbie, C. D. Point contact current-voltage measurements on individual organic semiconductor grains by conducting probe atomic force microscopy. *J. Vac. Sci. Technol. B* **18**, 632, (2000).
51. Kelley, T. W. & Frisbie, C. D. Gate Voltage Dependent Resistance of a Single Organic Semiconductor Grain Boundary. *J. Phys. Chem. B* **105**, 4538-4540, (2001).
52. Kelley, T. W., Granstrom, E. L. & Frisbie, C. D. Conducting probe atomic force microscopy:a characterization tool for molecular electronics. *Adv. Mater.* **11**, 261, (1999).
53. Chwang, A. B. & Frisbie, C. D. Temperature and gate voltage dependent transport across a single organic semiconductor grain boundary. *J. Appl. Phys.* **90**, 1342, (2001).
54. Lee, S. S., Mativetsky, J. M., Loth, M. A., Anthon, J. E. & Loo, Y.-L. Quantifying Resistances across Nanoscale Low- and High-Angle Interspherulite Boundaries in Solution-Processed Organic Semiconductor Thin Films. *ACS Nano* **6**, 9879, (2012).
55. Mativetsky, J. M., Orgiu, E., Lieberwirth, I., Pisula, W. & Samorì, P. Charge Transport Over Multiple Length Scales in Supramolecular Fiber Transistors: Single Fiber Versus Ensemble Performance. *Adv. Mater.* **26**, 430-435, (2014).
56. Bolsée, J.-C., Oosterbaan, W. D., Lutsen, L., Vanderzande, D. & Manca, J. CAFM on conjugated polymer nanofibers: Capable of assessing one fiber mobility. *Org. Electron.* **12**, 2084-2089, (2011).
57. Bolsée, J.-C., Oosterbaan, W. D., Lutsen, L., Vanderzande, D. & Manca, J. The Importance of Bridging Points for Charge Transport in Webs of Conjugated Polymer Nanofibers. *Adv. Funct. Mater.* **23**, 862-869, (2013).
58. Dai, H., Wong, E. W. & Liebert, C. M. Probing Electrical Transport in Nanomaterials: Conductivity of Individual Carbon Nanotubes. *Science* **272**, 523-526, (1996).
59. Gomez-Navarro, C., de Pablo, P. J., Gomez-Herrero, J., Biel, B., Garcia-Vidal, F. J., Rubio, A. & Flores, F. Tuning the conductance of single-walled carbon nanotubes by ion irradiation in the Anderson localization regime. *Nat. Mater.* **4**, 534-539, (2005).
60. Welte, L., Calzolari, A., Felice, R. D., Zamora, F. & Gómez-Herrero, J. Highly conductive self-assembled nanoribbons of coordination polymers. *Nat. Nanotech.* **5**, 111-115, (2010).
61. Gómez-Herrero, J. & Zamora, F. Coordination Polymers for Nanoelectronics. *Adv. Mater.* **23**, 5311-5317, (2011).
62. Hermosa, C., Álvarez, J. V., Azani, M.-R., Gómez-García, C. J., Fritz, M., Soler, J. M., Gómez-Herrero, J., Gómez-Navarro, C. & Zamora, F. Intrinsic electrical conductivity of nanostructured metal-organic polymer chains. *Nat. Comm.* **4**, 1709, (2013).
63. Newman, C. R., Frisbie, C. D., Filho, D. A. d. S., Bredas, J.-L., Ewbank, P. C. & Mann, K. R. Introduction to Organic Thin Film Transistors and Design of n-Channel Organic Semiconductors. *Chem. Mater.* **16**, 4436-4451, (2004).



### **3. Nanoscale electrical investigation of layer-by-layer grown molecular wires**

#### **3.1. Introduction**

Because of their tunable composition, metallo-ligand complexes are multifunctional nanoscale architectures. Among them, chelate complexes based on N-heteroatomic ligands, like 2,2':6'2"-terpyridine derivatives, are considered an ever-expanding synthetic and structural frontier because of their unique electrochemical, photophysical, catalytic and magnetic properties.<sup>1</sup>

Hitherto, a great effort has been devoted to the understanding of the photophysical properties of these compounds by looking at the photoinduced electron transfer reactivity,<sup>2-4</sup> which in turn has led to their use in optoelectronic devices, e.g. as dye sensitizers.<sup>5</sup> Conversely, their application in electronics has been hampered by a relative lack of knowledge on their charge transport behavior in the solid state. Some electrochemical studies aimed at exploring the redox conduction properties of polymers bearing terpyridine complexes in the side chains; for these systems the measured fast charge transport dynamics suggested sequential electron hopping between discrete localized valence states as the most probable charge transport mechanism.<sup>6,7</sup> Since the structural versatility of the coordination compounds allows for the fabrication of well-defined architectures, such as quasi-1D structures, they are also being considered possible building blocks for the fabrication of conductive molecular wires.<sup>8,9</sup> Stepwise coordination reactions involving terpyridine functions have been successfully exploited to connect the molecular wires to solid surfaces such as gold,<sup>10,11</sup> silicon,<sup>12</sup> carbon<sup>13</sup> and oxides,<sup>14,15</sup> and to lengthen the wires up to tens of nanometers.<sup>16-19</sup> By taking advantage of the redox-active properties of these compounds, Nishihara et al. analyzed how the redox currents for the metal-bis(terpyridine)

moieties flow through the complex wires, postulating an intrawire redox conduction in which the electrons hop sequentially between the neighboring metal-bis(terpyridine) sites.<sup>20</sup>

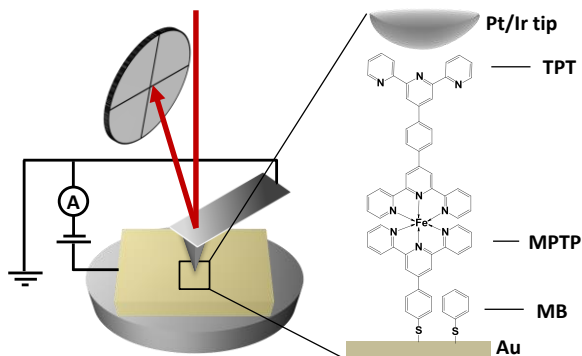


**Figure 3.1:** Cartoon of the C-AFM experimental setup. The molecular structure shows the 1FeTPT layer, i.e. an iron-bis(terpyridine) unit grafted on gold through a mixed MB/MPTP self-assembled monolayer.

Herein we focus on a Fe(II)-bis(terpyridine) molecular system based on 4',4''''-(1,4-phenylene)bis(2,2':6',2''-terpyridine) (TPT) ligand attached to planar gold substrates through a 4-[2,2':6',2''-terpyridin]-4'-yl-benzenethiol (MPTP) self-assembled monolayer (Figure 3.1). This system has been proved to self-assemble via a layer-by-layer growth along the direction perpendicular to the basal plane of Au planar electrodes, up to about 40 nm in length;<sup>16</sup> in these assemblies charge hopping through the metal centers was suggested as the most likely charge transport mechanism, in light of the low attenuation factor calculated from electrical measurements by using macroscopic Hg drop junctions. In this chapter we characterize electrically the system on the nanoscale by Conductive Atomic Force Microscopy (C-AFM), corroborated by theoretical calculations, synchrotron-based X-ray photoelectron spectroscopy (XPS) and angle-resolved Near Edge X-ray Absorption Fine Structure spectroscopy (NEXAFS) to gain deeper insight into its charge transport mechanism, composition and structural order within the assembly.

### 3.2. Experimental details

Benzethiol ( $\geq 99\%$ , MB), iron(II) sulfate heptahydrate ( $\geq 99\%$ ,  $\text{FeSO}_4 \cdot 7\text{H}_2\text{O}$ ), and 4',4''''-(1,4-Phenylene)bis(2,2':6',2''-terpyridine) (TPT), chloroform ( $\text{CHCl}_3$ ) and ethanol ( $\text{EtOH}$ ) were purchased from Sigma Aldrich and used without further purification. 4-[2,2':6',2''-terpyridin]-4'-yl-benzenethiol (MPTP) was synthesized as previously reported.<sup>21</sup> Ultrapure milliQ water with resistivity of 18  $\text{M}\Omega \cdot \text{cm}$  was used when required.

For C-AFM measurements the nanowires were grown on ultraflat gold substrates on mica prepared by thermal evaporation of 100 nm Au at 0.01 nm/s and 450°C. For NEXAFS and XPS

analysis gold was thermally evaporated (100 nm) on silicon oxide employing 5 nm of Cr adhesion layer. For UV-Vis characterization semitransparent ultrathin gold substrates were prepared by thermal evaporation of 10 nm of gold on Fused Silica Plates (UQG Optics Ltd, Cambridge). The gold substrates were cleaned by 5 min UV-Ozone treatment immediately prior to the incubation in a 0.5 mM mixed solution of MB and MPTP in EtOH in a 1:1 ratio. After 24 hours incubation the MB/MPTP samples were washed with EtOH and dried in a stream of nitrogen.

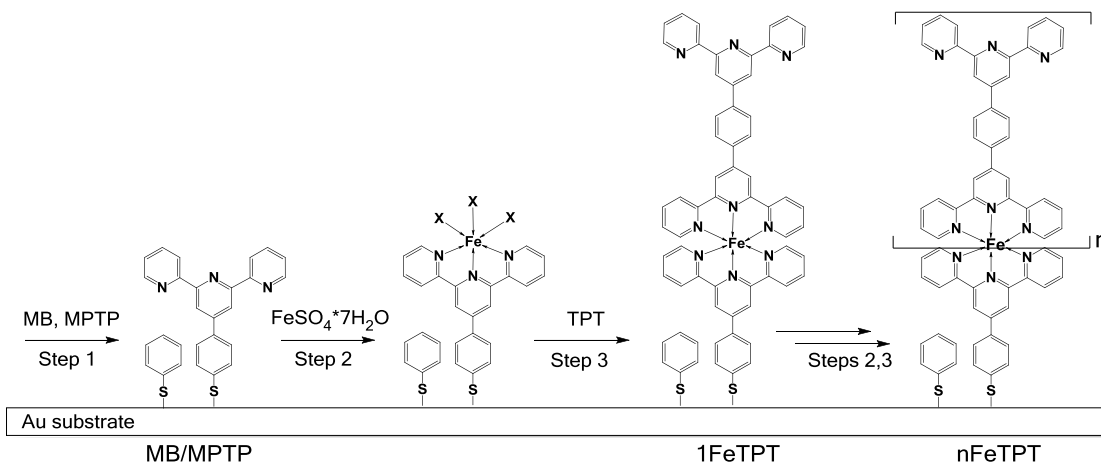


**Figure 3.2:** Scheme of the multilayer preparation procedure. MB: benzenethiol; MPTP: 4-[2,2':6',2"-terpyridine]-4'-yl-benzenethiol; TPT: 4',4'''-(1,4-Phenylene)bis(2,2':6',2"-terpyridine).

The molecular self-assembled platform was prepared by incubating for 24 hours the Au substrates in a mixed solution of benzenethiol (MB) and MPTP in ethanol in a 1:1 ratio, the presence of the MB allowing for a better assembly of the MPTP on the surface.<sup>21,22</sup> To fabricate the layers, previously washed Au-MB/MPTP samples (hereafter MB/MPTP) samples were immersed for 90 sec in a saturated solution of the iron(II) sulfate in water/ethanol (1:1) and rinsed with water, ethanol and chloroform (i), then immersed for 15 min in a 0.5 mM solution of TPT in chloroform and rinsed with warm chloroform, ethanol and water (ii). Stages (i) and (ii) were repeated iteratively, to reach the desired molecular length, each iteration representing a coordination step, adding one metal (Fe) - ligand (TPT) unit to the molecular nanowire.<sup>16</sup>

XPS and NEXAFS measurements were carried out at the HE-SGM beamline (bending magnet) of the synchrotron storage ring BESSY II in Berlin, Germany, using a custom designed experimental station.<sup>23</sup> All experiments were performed at room temperature and UHV conditions at a base pressure lower than  $1 \times 10^{-9}$  mbar. The spectrum acquisition time was selected in such a way that no noticeable damage by the primary X-rays occurred during the experiments. The XP spectra were measured using a Scienta R3000 spectrometer. The X-ray energy was set to either 350 or 580 eV. The spectrum

acquisition was carried out in normal emission geometry with an energy resolution of ~0.3-0.4 eV, depending on the photon energy. The energy scale of the XP spectra was referenced to the Au 4f<sub>7/2</sub> peak at a binding energy (BE) of 84.0 eV.<sup>24</sup>

The acquisition of the NEXAFS spectra was performed at the C and N K-edges in the partial electron yield (PEY) mode with a retarding voltage of -150 and -300 V, respectively. Linear polarized synchrotron light with a polarization factor of ~0.91 was used. The energy resolution of the whole setup was estimated to be on the order of 0.3-0.4 eV, getting lower with the increasing photon energy. The photon energy scale was referenced to the pronounced  $\pi^*$  resonance of highly oriented pyrolytic graphite at 285.38 eV.<sup>25</sup> Raw NEXAFS spectra were normalized to the incident photon flux by dividing a spectrum of a clean, freshly sputtered gold sample, and were reduced to the standard form by subtracting linear pre-edge background and normalizing to the unity edge jump (determined by a nearly horizontal plateau 40–50 eV above the respective absorption edges). To monitor the orientational order in the films, the incidence angle of the synchrotron light was varied from 90° (normal incidence; E-vector in the surface plane) to 20° (grazing incidence; E-vector near the surface normal) in steps of 10-20°.<sup>26</sup>

UV-Vis measurements were performed on a Jasco V-650 UV-VIS spectrophotometer in absorbance mode.

AFM and C-AFM measurements were carried out in air in a Dimension 3100 microscope with a NanoScope IV controller (Digital Instrument). Commercial silicon cantilevers with a nominal spring constant of 40 N/m were used for morphological characterization in tapping mode while Pt/Ir coated silicon probes with a nominal spring constant of 0.2 N/m were used to perform the current-voltage measurement in contact mode by applying a constant load force of 5 nN. For each sample about 100 current-voltage characteristics in the range -1 to 1V were measured on different points of the surface.

Density-functional theory calculations were performed using Gaussian 03 software,<sup>27</sup> with the B3LYP functional for exchange and correlation and 6-31G\* basis set. The systems studied were: Fe(II)-bis(terpyridine) ion, the corresponding dimer containing two Fe(II)-bis(terpyridine) species connected by a phenylene unit, and Fe(II)-bis(terpyridine) ion with HSO<sub>4</sub><sup>-</sup> counterion. The reorganization energy was computed as in ref.<sup>28</sup>

### 3.3. Structural characterization

#### 3.3.1. XPS analysis

The X-ray photoelectron spectra of the different layers are reported in Figure 3.3. The Au 4f<sub>7/2</sub> spectra of the MB/MPTP and nFeTPT films showed that the intensity of the substrate signal decreases

consequently upon the successive addition of the TPT units due to the increasing attenuation of the photoelectron signal by the growing overlayer. The intensity decrease is especially pronounced upon the attachment of the first TPT unit to the MB/MPTP template. The C 1s spectra of the nFeTPT films exhibit only one emission at a BE of 285.0-285.1 eV related to the carbon atoms in the TPT units. The spectrum of the MB/MPTP template differs to some extent from the spectra of the nFeTPT films due to the contribution of the MB molecules and effect of the substrate. The N 1s spectra of the nFeTPT films exhibit only one emission at a BE of ~399.7 eV related to the nitrogen atoms in the terpyridine moieties.<sup>29,30</sup> The analogous emission in the spectrum of the MB/MPTP template is shifted to lower BE (~398.9 eV) due to the effect of the substrate. The Fe 3p spectra of the nFeTPT films exhibit pronounced Fe 3p<sub>3/2,1/2</sub> doublet at a BE of ~56.0 eV assigned to the bridging Fe atoms in the nFeTPT chains. The spectrum of the MB/MPTP template exhibits a Au 5p<sub>1/2</sub> emission at ~57.4 eV.<sup>24</sup> Except for the Au 4f<sub>7/2</sub> spectra, no intensity differences were detected between the spectra because of the signal saturation.

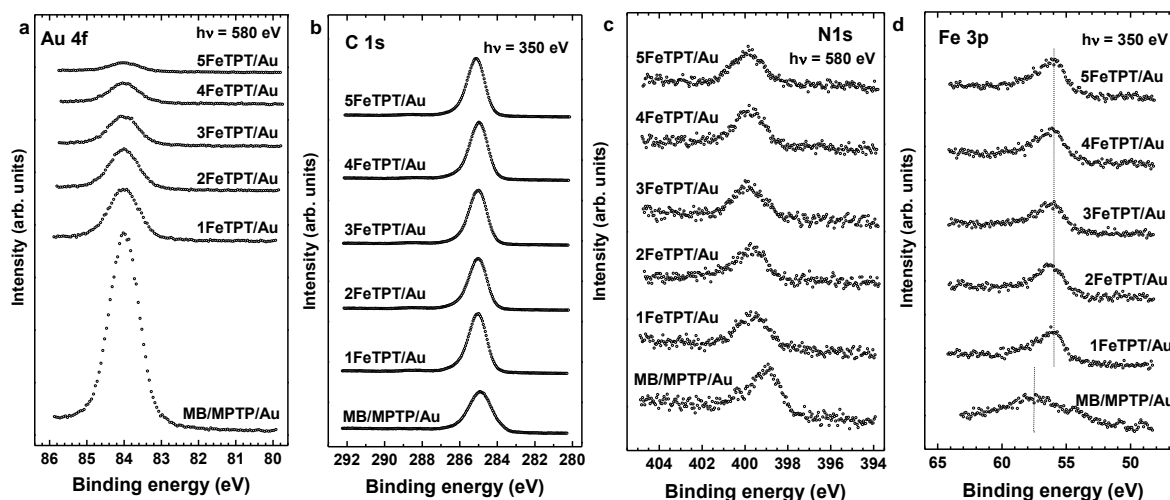


**Figure 3.3:** Au 4f<sub>7/2</sub> (a), C 1s (b), N 1s (c) and Fe 3p (d) XP spectra of the MB/MPTP and nFeTPT films. The acquisition of the spectra in b was carried out at photon energy of 350 eV, the others at 580 eV. The vertical dashed lines are guides for the eyes.

XPS spectroscopy suggests then that both MB/MPTP and nFeTPT films are well defined and contamination-free. The spectra exhibit the characteristic features of terpyridine and bridging iron, in accordance with the molecular composition of the nFeTPT moieties. The intensity of the substrate signal decreases consequently upon the successive addition of the TPT units supporting the proposed architecture of the nFeTPT moieties.

### 3.3.2. NEXAFS analysis

The C K-edge and N K-edge NEXAFS spectra are shown in Figure 3.4. The C K-edge NEXAFS spectra of the nFeTPT films exhibit the characteristic double peak comprised of the two merged,  $\pi^*$ -like resonances of terpyridine at 285.0 eV (1) and 285.5 eV (2),<sup>30</sup> observed also for pyridine-substituted self-assembled monolayers.<sup>29</sup> These resonances are marked by numbers. The weight of the resonance 1 is larger in the spectrum of the MB/MPTP template since it overlaps with the  $\pi_1^*$  resonance from the MB moieties. The difference between the C K-edge spectra of the MB/MPTP and nFeTPT films collected at normal ( $90^\circ$ ) and grazing ( $20^\circ$ ) angles of X-ray incidence for the above samples is representative of the linear dichroism in X-ray absorption. The positive peaks at the positions of the resonances 1 and 2 suggest predominant upright orientation of the MPTP and MB moieties in the case of the MB/MPTP template and nFeTPT chains in the case of the nFeTPT films. The difference peaks are especially strong in the spectrum of the MB/MPTP template due to the contribution of the MB moieties which seem to have pronounced upright orientation.

The N K-edge NEXAFS spectra of the nFeTPT films exhibit the characteristic  $\pi^*$ -like resonances of terpyridine at 398.70 eV,<sup>30</sup> observed also for pyridine-substituted self-assembled monolayers.<sup>29</sup> The positive peaks at the positions of the absorption resonance at 398.70 eV in the difference between the spectra collected at normal ( $90^\circ$ ) and grazing ( $20^\circ$ ) angles suggest predominant upright orientation of the MPTP moieties and the nFeTPT chains. The difference between the individual spectra is presumably statistical one.

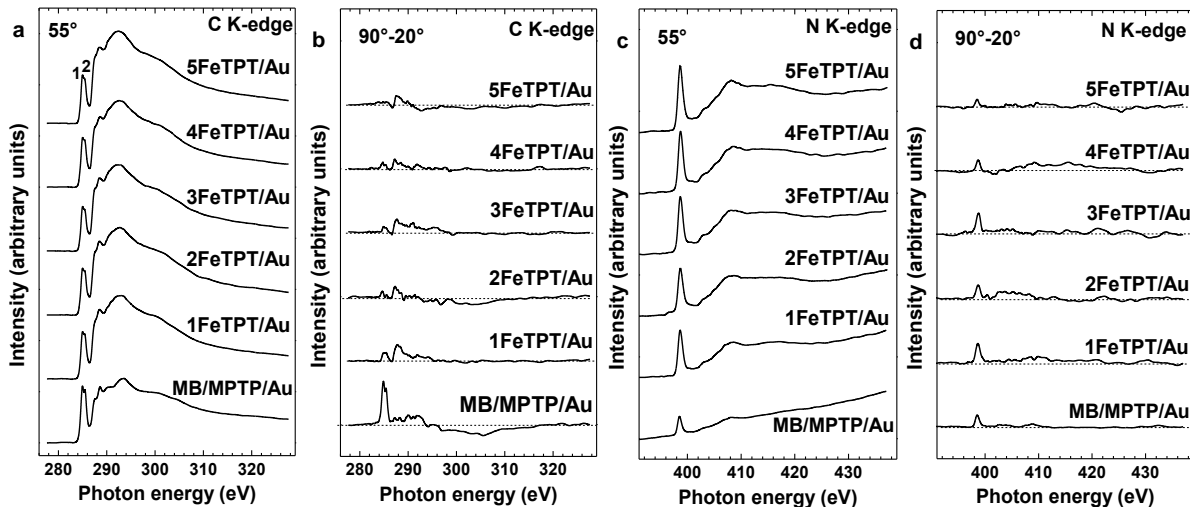


**Figure 3.4:** C K-edge (a) and N K-edge (c) NEXAFS spectra of the MB/MPTP and nFeTPT films acquired at an X-ray incidence angle of  $55^\circ$ . Difference between the C K-edge spectra (b) and N K-edge spectra (d) of the MB/MPTP and nFeTPT films collected at normal ( $90^\circ$ ) and grazing ( $20^\circ$ ) angles of X-ray incidence for the above samples. The horizontal dashed lines correspond to zero.

Along with the qualitative statements regarding the predominant upright orientation of the MPTP moieties, a quantitative evaluation of the NEXAFS data was performed. In the case of the MB/MPTP template, both C K-edge and N K-edge data were used; in the case of the nFeTPT films, the N K-edge data only were utilized. We relied on the most pronounced  $\pi^*$ -like resonances in the C and N K-edge spectra and used the standard formalism for the evaluation of the NEXAFS data in the case of a vector type molecular orbital.<sup>26</sup> The average tilt angle of the pyridine moieties in the MB/MPTP template was estimated at  $\sim 28^\circ$ . It was essentially the same in the case of the 1FeTPT film ( $\sim 28^\circ$ ) and then increased continuously to  $\sim 34^\circ$  with increasing n. Note, however, that the above average tilt angles can only be considered as fingerprint parameters in the given case, since the terpyridine moieties in the target films have complex conformation, with all three pyridine rings being tilted and twisted differently. It can then only be said that the MPTP moieties in the MB/MPTP template and nFeTPT chains in the respective films have predominant upright orientation, with slightly increasing orientational disorder with increasing n.

### 3.3.3. UV-Vis characterization

The UV-visible spectra of Au island films exhibit a characteristic absorption band attributed to excitation of localized surface plasmon (SP) polaritons. The SP band is strongly sensitive to the thickness of adsorbed molecular film. Consequently, the growth of multilayers can be followed by monitoring the surface plasmon band in the UV-Vis spectral region.<sup>31,32</sup> The shift of the surface plasmon maximum of the gold substrate as a function of the number of coordination steps is shown in Figure 3.5.

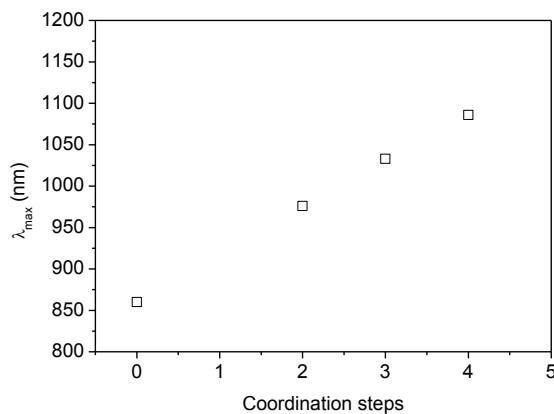


**Figure 3.5:** Absorbance maxima vs. number of coordination steps.

### 3.3.4. AFM morphological characterization

As measured by AFM images in tapping mode, the gold substrates obtained by thermal evaporation on mica at high temperature exhibit smooth grains of 200 - 500 nm in diameter, the roughness  $R_{RMS}$  being of 0.1 - 0.3 nm on  $300 \times 300 \text{ nm}^2$  areas (see Figure 3.6a and Table 3.1), allowing for a relatively high yield of good junctions to be obtained by the conductive tip in the C-AFM measurements. The immobilization of the MB/MPTP SAM results into a highly uniform layer on the gold grains, accompanied by the  $R_{RMS}$  increase to 0.6 – 0.7 nm, as shown in Figure 3.6b. The surface roughness increases further upon the growth of the nFeTPT film (Figures c and d), remaining, however, below 1 nm within  $300 \times 300 \text{ nm}^2$  areas (Table 3.1).

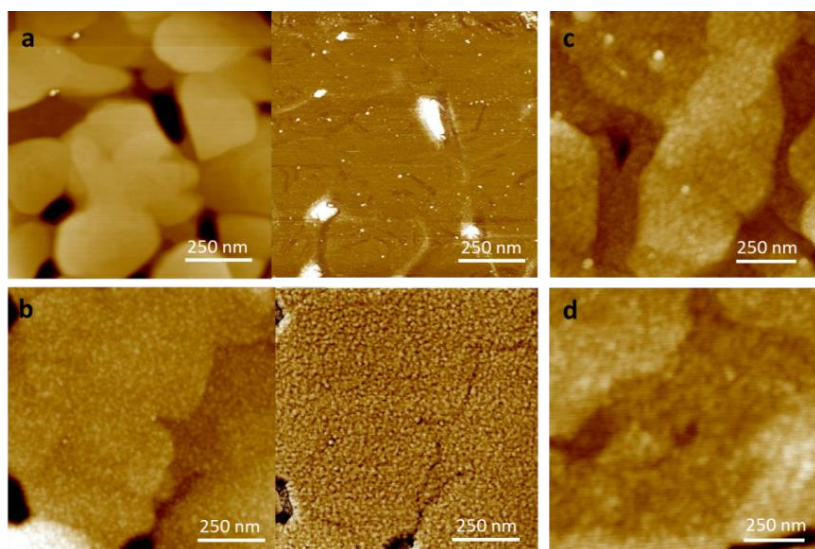


**Figure 3.6:** Morphology studied films: bare gold substrate (a), MB/MPTP platform (b), 1FeTPT (c) and 4FeTPT (d). Along with the topographic images, phase images are shown on the right side of (a) and (b) further highlighting the modification of the surface after the grafting of the MB/MPTP monolayer on the ultraflat gold terraces.

**Table 3.1:** Roughness of the studied films

Layer	$R_{RMS}$ ( $0.3 \times 0.3 \mu\text{m}^2$ ) <sup>b</sup>
Au <sup>a</sup>	0.1 – 0.3 nm
MB/MPTP <sup>a</sup>	0.6 – 0.7 nm
1FeTPT <sup>a</sup>	0.5 – 0.7 nm
2FeTPT	0.6 – 0.9 nm
3FeTPT	0.8 – 0.9 nm
4FeTPT <sup>a</sup>	0.7 – 0.9 nm

<sup>a</sup>see Figure 3.6; <sup>b</sup>the ranges are obtained by measurements on different grains and different samples.

### 3.4. Electrical nanojunction by C-AFM

Around one hundred junctions were established on each molecular layer by the conductive probe. The load force was carefully chosen in order to ensure no damage or undesired modification to the molecular layers as well as a firm electrical contact. The current-voltage (I-V) current-voltage data were treated as follow: as a first step, both the zero-current plots and the saturated ones were discarded, being originated from false contacts or direct contact of the C-AFM tip with the gold substrate, respectively. Then the average curve was calculated for each layer. The plot in Figure 3.7a shows the average I-V curves measured for all the samples going from the MB/MPTP platform to the layer obtained by four subsequent coordination steps (4FeTPT), showing a clear scaling of the current with the number of layers, i.e. with the film thickness L. The current at low bias (Figure 3.7b) as well as the low voltage resistance measured as the inverse of the slope of the linear fit (see inset), are plotted for the different curves as a function of L, which was measured previously.<sup>16</sup>

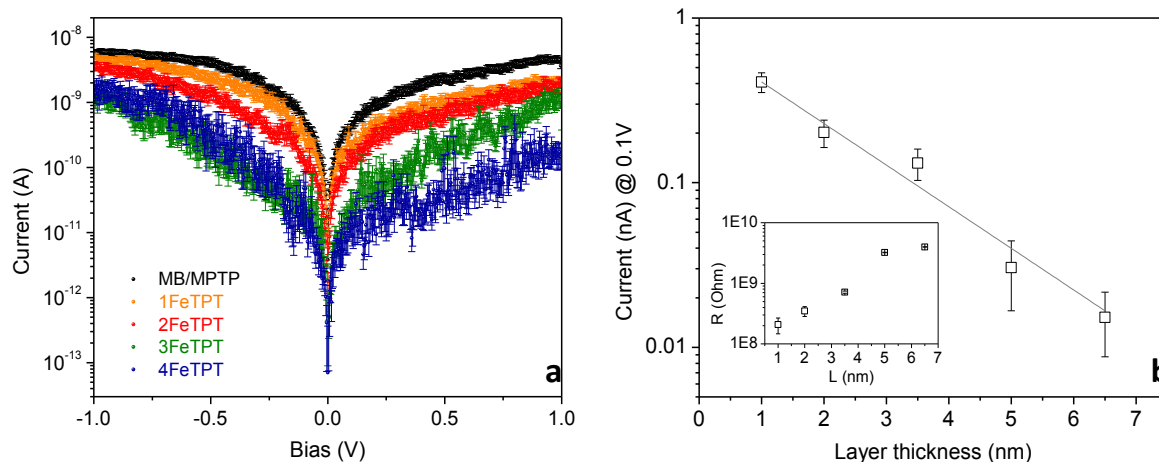


**Figure 3.7:** (a) Current-voltage characteristics of five different molecular layers grown on gold, from the self-assembled MB/MPTP platform to four coordinated layers 4FeTPT. The curves are averages and the error bars represent the standard error based on a number of measurements detailed in Table 3.2. (b) Dependence of current and resistance on the layer thickness (error bars of the inset plot represent the standard error relative to the linear fit for the slope calculation).

A suitable parameter to describe transport properties of molecular systems is the tunneling decay factor  $\beta$  which has been widely used to give a correlation between low bias current and the length of a molecular wire.<sup>33-35</sup> In our case  $\beta$  was estimated from both the current values at a fixed voltage ( $I=I_0 e^{(-\beta L)}$ ) and the low bias resistances ( $R=R_0 e^{\beta L}$ ). A  $\beta$  value of  $0.058 \pm 0.006 \text{ \AA}^{-1}$  is obtained by a linear fitting of the plots of Figure 3.7b, being the same order of magnitude as the one measured

with the Hg drop technique ( $0.028 \text{ \AA}^{-1}$ ).<sup>16</sup> The small discrepancy between the two values may be due to inherent differences in the measurement methods: the Hg drop experiment is a measurement where a macroscopic (in the order of  $\text{mm}^2$ ) area is probed, while with the AFM tip only tens of wires are contacted in a single junction event (in the order of  $\text{nm}^2$ ); this in turn may lead to different extent of molecular layer deformation (which could be possible in Hg drop experiments, while it is avoided by a precise control of the exerted force in the AFM ones) as well as differences in sensitivity to defects at domain boundaries.

**Table 3.2:** Statistical evaluation of the current-voltage measurements by C-AFM

Layer	n. of junctions <sup>a)</sup>	n. of good junctions <sup>b)</sup>	% of working junctions
MB/MPTP	111	48	43%
1FeTPT	139	65	47%
2FeTPT	100	53	53%
3FeTPT	210	56	27%
4FeTPT	91	30	33%

<sup>a)</sup> Established tip-sample contacts on different points of the surface; <sup>b)</sup> Junctions showing non-zero current and non-shorting contacts curves.

Significantly, consistent decay coefficients were also estimated on analogous bis(terpyridine)-based wires by measuring thermodynamic parameters of electron transfer through electrochemical methods.<sup>20,36</sup> Similar ultralow  $\beta$  factors based on electrochemical studies have also been reported in the case of redox-active metal complex layers, containing other chelate ligands.<sup>14,37</sup>

Weak dependences of conductivity on the wire lengths are typically considered being a signature of a hopping mechanism, i.e. a series of electron transmission events between redox units, even though some cases of long-range tunneling have been reported.<sup>38</sup>

In the case of conjugated molecular wires it was shown that a transition of mechanism from direct tunneling ( $\beta > \sim 0.1 \text{ \AA}^{-1}$ ) to hopping ( $\beta < \sim 0.1 \text{ \AA}^{-1}$ ) occurs when going from small (less than 3-4 nm) to longer wires.<sup>35</sup> In our case no transition seems to be present, and the data fit with a single straight line, which gives only one low attenuation coefficient even at the smallest lengths. Accordingly, the current vs. electric field traces of the short wires collapse on top of one another similarly to what was reported for long conjugated molecular wires<sup>39</sup> (see Figure 3.8). This behavior indicates that the transport is field driven rather than voltage driven, as expected for a hopping mechanism where the charges are pushed along the molecules by electric field.<sup>39</sup>

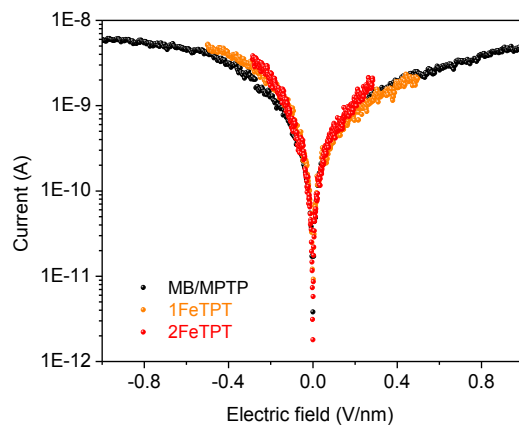


**Figure 3.8:** Current vs. electric field dependence for the MB/MPTP template and successive short nFeTPT wires.

We also found a linear dependence of the current on the inverse of the wire length, as shown in Figure 3.9a. This is again consistent with a hopping mechanism, since it was demonstrated that, in steady state measurements in case of hopping through long wires, the current is proportional to  $1/N$ , with  $N$  being the number of redox centres (that is, the distance  $L$ ).<sup>40,41</sup>

The intramolecular through-bond charge transport in similar molecular systems based on iron-bis(terpyridine) has also been probed by potential-step chronoamperometry electrochemical experiments, which demonstrated that the redox conduction in the oligomer films does not occur in a random-walk process (diffusion) but by successive electron hopping between neighboring redox sites within a molecular wire.<sup>42</sup>

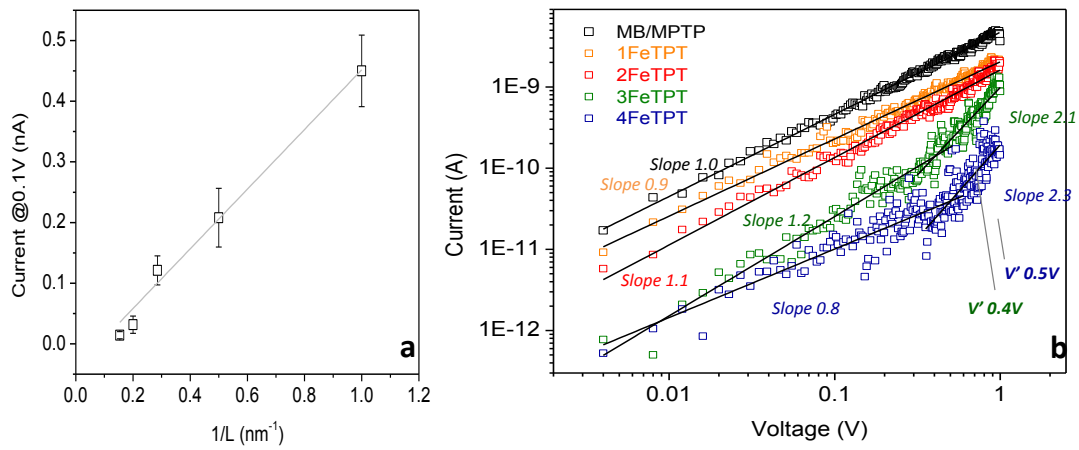


**Figure 3.9:** (a) Dependence of the current on the inverse of the length. (b) logI – logV plots of successive layers, from MB/MPTP to 4FeTPT. The black straight lines are linear fits whose slope values are marked beside.

The log-log plot of the I-V characteristics portrayed in Figure 3.9b makes it possible to discern different transport regimes as a function of the voltage. For the shorter wires, from MB/MPTP to 2FeTPT (3.5 nm) the plots are linear within the examined bias range with a slope of about 1, indicating Ohmic conduction. Longer 3FeTPT and 4FeTPT wires instead exhibit a second regime at voltages higher than 0.4 V and 0.5 V, respectively, with the current roughly following a quadratic dependence on the bias, as predicted by a Space Charge Limited Current (SCLC) theory. Consistently an inflection region can be observed for these longer wires in  $\ln(I/V^2)$  vs.  $1/V$  plots which have already been ascribed to the transitional regime (SCLC) between Ohmic hopping and field emission (Figure 3.10).

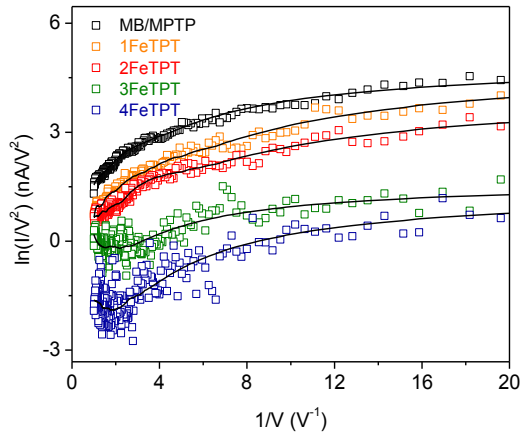


**Figure 3.10:** Fowler-Nordheim plot for the successive coordination layers. The black curves are obtained by applying a smoothing filter to the plots to better visualize the trends. The field emission regime can be revealed by Fowler-Nordheim plots of  $\ln(I/V^2)$  vs.  $I/V$ , when the current scales linearly with  $1/V$  with a negative slope, above a transition voltage.

No negatively sloped line is visible in these graphs but an inflection point can be observed for the longer wires 3FeTPT and 4FeTPT, likely corresponding to the transition (SCLC) between Ohmic hopping and field emission regimes. SCLC predicts that the current density ( $J$ ) at a given electric field ( $E$ ) decreases with increasing layer thickness ( $L$ ) according to a power law:  $J(E) \propto L^{-l}$ , where  $l = 1$  in the trap-free space charge transport regime. In our case a slope  $l > 1$  is found when plotting the current at fixed electric field for different thickness, consistent with the appearance of more defects/trapping with increasing the number of coordination sites.<sup>43-45</sup> (Figure 3.11).

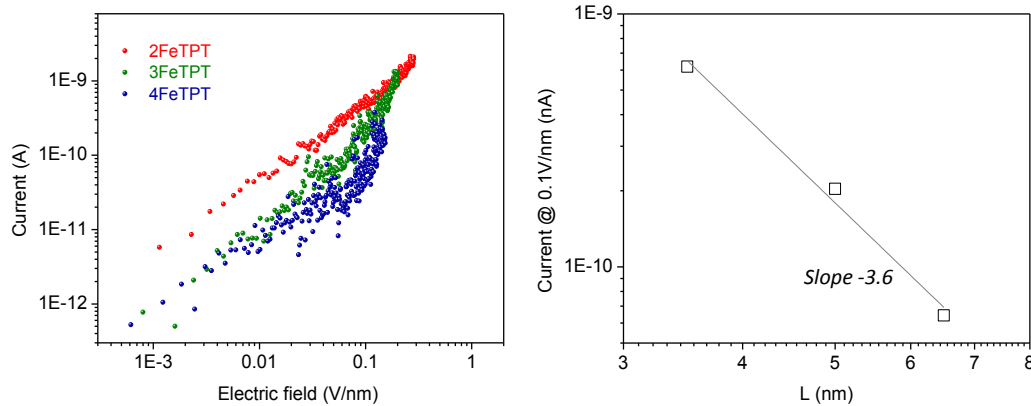


**Figure 3.11:** In the framework of SCLC transport regime the current density ( $J$ ) at a given electric field ( $E$ ) decreases with increasing layer thickness ( $L$ ) according to a power law:  $J(E) \propto L^{-l}$ , where  $l = 1$  in the trap-free space charge transport regime and  $l > 1$  in the case of trapping. In our case a slope  $l > 1$  is found when plotting the current at fixed electric field for different thickness.

### 3.5. Theoretical calculation

We characterized the parameters influencing the transport mechanism by performing electronic structure calculations on different models of the wire (monomer and dimer with and without counterions). As in all Fe(II) compounds, the hopping mechanism is possible via oxidation of one of the iron centers to Fe(III), i.e. via hole hopping. The important parameters for charge transport are therefore the electronic coupling between the iron centers and the reorganization energy, i.e. the nuclear relaxation around the iron centre when an additional hole is placed on it. The degeneracy of the three highest occupied orbitals of Fe(II) complex (often indicated as t<sub>2g</sub> assuming a perfectly octahedral ligand field) is lifted by the presence of the neighboring iron complex. The highest occupied orbital, the one that would be occupied by a hole, has a very strong d<sub>xy</sub> character (assuming that z is the direction connecting the iron centres). The coupling between the d<sub>xy</sub> orbitals of neighboring Fe atoms is extremely small (less than 0.15 meV, the resolution of the electronic structure calculation). Figure 3.12 shows the highest occupied Fe d-orbitals and their energies for [Fe(terpy)<sub>2</sub>]<sup>2+</sup> and its dimer and

illustrates negligible coupling between the highest occupied  $d_{xy}$  orbitals and larger coupling between lower-lying  $d_{xz}$  and  $d_{yz}$  orbitals of the dimer.

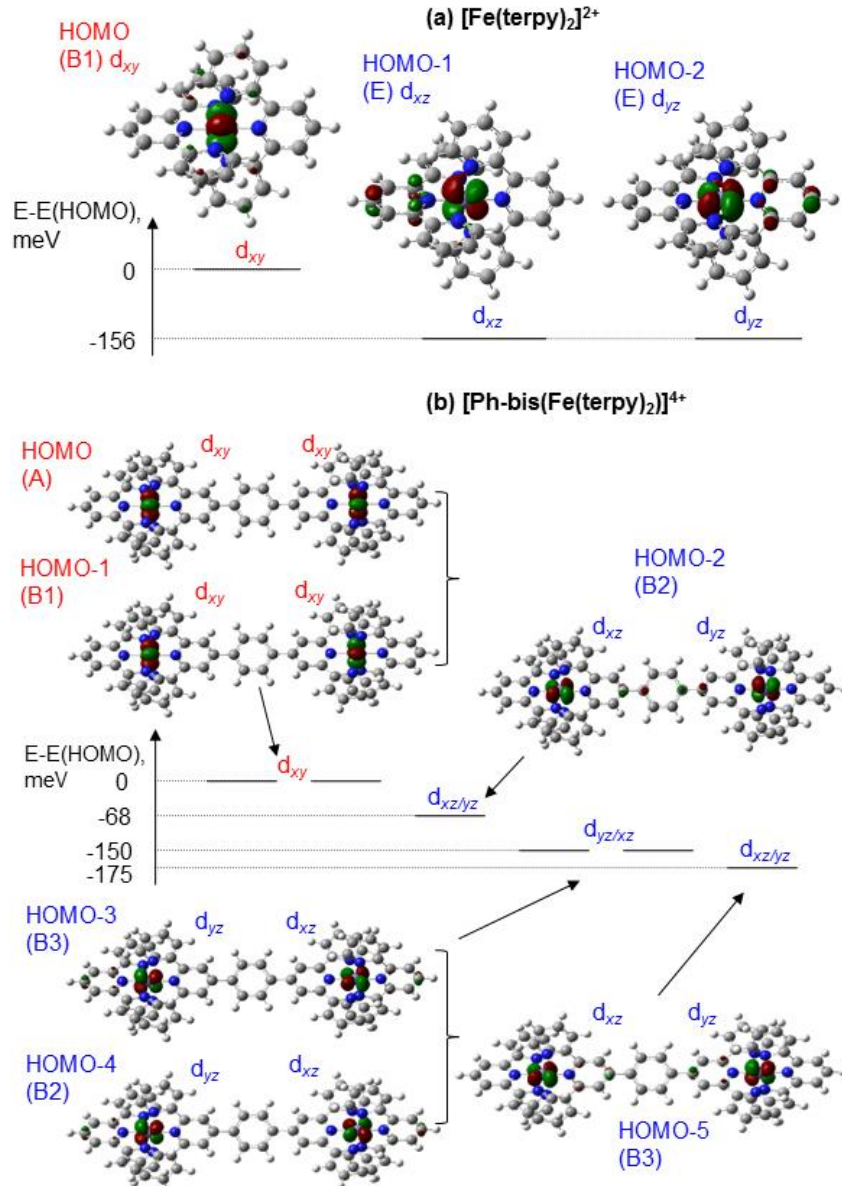


**Figure 3.12:** Highest occupied d-orbitals of (a)  $[\text{Fe}(\text{terpy})_2]^{2+}$  and (b) dimer  $[(\text{Ph})\text{-bis}(\text{Fe}(\text{terpy})_2)]^{4+}$ . Irreducible symmetry representations of the molecular orbitals are in parentheses. The main atomic d orbitals contributing to these MO are also indicated.

The computed reorganization energy for the hole hopping reaction is slightly affected by the choice of the model (with or without counterion as described in the Annex A) and it is evaluated between 60-200 meV (without counterion) and 170-1140 meV (with  $\text{HSO}_4^-$  counterion, possibly more

accurately representing the experimental system). Under the condition of reorganization energy much larger than electronic coupling, resonant tunneling is essentially impossible and the only viable mechanism is hopping between sites. Further, the calculation illustrates (i) that it is not possible to neglect vibronic coupling in these type of complexes,<sup>14</sup> and (ii) that the coupling between iron sites is so weak that resonant tunnelling is also very difficult. In fact, any tiny alternation of the orbital levels (e.g. due to the counterions) will completely destroy the resonance between the metal sites. A modified hopping mechanism may involve the promotion of the hole on the Fe complex from the  $d_{xy}$  orbital to next energetically available d-orbital on the same centre, which is, on average, only 122 meV away and more strongly coupled with its neighbour (HOMO-2 and HOMO-5 orbitals in Figure 3.12; the coupling between these orbitals derived from the energy splitting is 54 meV). A full orbital analysis and the various hopping pathways available in these molecular wires are described in more detail in the Annex A.

### 3.6. Conclusions

In conclusion, we have demonstrated nanoscopic metal-molecule-metal junctions consisting of Fe-bis(terpyridine) based ordered nanostructures grown in layer-by-layer fashion on solid support. Structural and charge transport properties have been investigated using a large variety of technique, such as NEXAFS, XPS, UV-Vis Spectroscopy, AFM and C-AFM. All the experimental data provides unambiguous evidence for the existence of a hopping charge transport mechanism, characterized by a very low current attenuation ( $\beta = 0.058 \pm 0.006 \text{ \AA}^{-1}$ ) and a regime transition from Ohmic conduction to SCLC at higher bias. Theoretical calculations performed on different models of the wire showed that the reorganization energy due to the addition of a hole on the iron center is much larger than the electronic coupling between iron sites, unambiguously indicating that the electron transport process cannot be ruled by resonant tunneling, but rather by hopping between adjacent sites. The remarkable electrical characteristics of these molecular junctions not only make them ideal systems for fundamental studies on long-range charge transport in solid-state metal-organic wires, but also pave the way towards their exploitation in molecular and/or organic electronic applications.

### 3.7. References

1. Schubert, U. S., Winter, A. & Newkome, G. R. *Terpyridine-based materials: For Catalytic, Optoelectronic and Life Science Applications.* (Wiley-VCH Verlag GmbH & Co. KGaA, 2011).
2. De Cola, L. & Belser, P. Photoinduced energy and electron transfer processes in rigidly bridged dinuclear Ru/Os complexes. *Coord. Chem. Rev.* **177**, 301, (1998).

3. Balzani, V. & Juris, A. Photochemistry and photophysics of Ru(II)-polypyridine complexes in the Bologna group. From early studies to recent developments. *Coord. Chem. Rev.* **211**, 97, (2001).
4. Wild, A., Winter, A., Schlüter, F. & Schubert, U. S. Advances in the field of  $\pi$ -conjugated 2,2':6',2"-terpyridines. *Chemical Society Reviews* **40**, 1459, (2011).
5. Nazeeruddin, M. K., Pechy, P., Renouard, T., Zakeeruddin, S. M., Humphry-Baker, R., Comte, P., Liska, P., Cevey, L., Costa, E., Shklover, V., Spiccia, L., Deacon, G. B., Bignozzi, C. A. & Gratzel, M. Engineering of Efficient Panchromatic Sensitizers for Nanocrystalline TiO<sub>2</sub>-Based Solar Cells. *J. Am. Chem. Soc.* **123**, 1613, (2001).
6. Hurrell, H. C. & Abruiia, H. D. Redox Conduction in Electropolymerized Films of Transition-Metal Complexes of Os, Ru, Fe, and Co. *Inorg. Chem.* **29**, 736-741, (1990).
7. Hjelm, J., Handel, R. W., Hagfeldt, A., Constable, E. C., Housecroft, C. E. & Forster, R. J. Electropolymerisation dynamics of a highly conducting metallopolymer: poly-[Os(4'-(5-(2,2'-bithienyl))-2,2':6',2"-terpyridine)2]2+. *Electrochem. Comm.* **6**, 193-200, (2004).
8. Nishihara, H., Kanaizuka, K., Nishimori, Y. & Yamanoi, Y. Construction of redox- and photo-functional molecular systems on electrode surface for application to molecular devices. *Coord. Chem. Rev.* **251**, 2674-2687, (2007).
9. Sedghi, G., Esdaile, L. J., Anderson, H. L., Martin, S., Bethell, D., Higgins, S. J. & Nichols, R. J. Comparison of the Conductance of Three Types of Porphyrin-Based Molecular Wires:  $\beta$ ,meso, $\beta$ -Fused Tapes, meso-Butadiyne-Linked and Twisted meso-meso Linked Oligomers. *Adv. Mater.* **24**, 653-657, (2012).
10. Kurita, T., Nishimori, Y., Toshimitsu, F., Muratsugu, S., Kume, S. & Nishihara, H. Surface Junction Effects on the Electron Conduction of Molecular Wires. *J. Am. Chem. Soc.* **132**, 4524-4525, (2010).
11. Kosbar, L., Srinivasan, C., Afzali, A., Graham, T., Copel, M. & Krusin-Elbaum, L. Self-Assembled Multilayers of Transition-Metal-Terpyridinyl Complexes; Formation, and Characterization. *Langmuir* **22**, 7631-7638, (2006).
12. Maeda, H., Sakamoto, R., Nishimori, Y., Sendo, J., Toshimitsu, F., Yamanoi, Y. & Nishihara, H. Bottom-up fabrication of redox-active metal complex oligomer wires on an H-terminated Si(111) surface. *Chem. Comm.* **47**, 8644, (2011).
13. Kubo, W., Nagao, M., Otsuka, Y., Homma, T. & Miyata, H. Formation of Multinuclear Metal-Terpyridyl Complexes Covalently Bound to Carbon Substrates. *Langmuir* **25**, 13340-13343, (2009).
14. Terada, K.-i., Nakamura, H., Kanaizuka, K., Haga, M.-a., Asai, Y. & Ishida, T. Long-Range Electron Transport of Ruthenium-Centered Multilayer Films via a Stepping-Stone Mechanism. *ACS Nano* **6**, 1988-1999, (2012).
15. Spampinato, V., Tuccitto, N., Quici, S., Calabrese, V., Marletta, G., Torrisi, A. & Licciardello, A. Functionalization of oxide surfaces by terpyridine phosphonate ligands: surface reactions and anchoring geometry. *Langmuir* **26**, 8400-8406, (2010).
16. Tuccitto, N., Ferri, V., Cavazzini, M., Quici, S., Zhavnerko, G., Licciardello, A. & Rampi, M. A. Highly conductive about 40-nm-long molecular wires assembled by stepwise incorporation of metal centres. *Nat. Mater.* **8**, 41, (2009).
17. Tuccitto, N., Delfanti, I., Torrisi, V., Scandola, F., Chiorboli, C., Stepanenko, V., Würthner, F. & Licciardello, A. Supramolecular self-assembled multilayers of terpyridine-functionalized perylene bisimide metal complexes. *Phys. Chem. Chem. Phys.* **11**, 4033, (2009).
18. Mondal, P. C., Yekkoni Lakshmanan, J., Hamoudi, H., Zharnikov, M. & Gupta, T. Bottom-Up Assembly of Multicomponent Coordination-Based Oligomers. *J. Phys. Chem. C* **115**, 16398-16404, (2011).
19. Gupta, T., Mondal, P. C., Kumar, A., Jeyachandran, Y. L. & Zharnikov, M. Surface-Confining Heterometallic Molecular Dyads: Merging the Optical and Electronic Properties of Fe, Ru, and Os Terpyridyl Complexes. *Adv. Funct. Mater.* **23**, 4227, (2013).
20. Sakamoto, R., Katagiri, S., Maeda, H. & Nishihara, H. Bis(terpyridine) metal complex wires: Excellent long-range electron transfer ability and controllable intrawire redox conduction on silicon electrode. *Coord. Chem. Rev.* **257**, 1493-1506, (2013).
21. Auditore, A., Tuccitto, N., Marzanni, G., Quici, S., Punzoriero, F., Campagna, S. & Licciardello, A. Organized assemblies of thiol-terpyridine and thiophenol on gold surfaces: preferential composition of mixed species evidenced. *Chem. Comm.*, 2494, (2003).
22. Auditore, A., Tuccitto, N., Quici, S., Marzanni, G., Punzoriero, F., Campagna, S. & Licciardello, A. ToF-SIMS investigation of functional mixed aromatic thiol monolayers on gold. *App. Surf. Sci.* **231-232**, 314-317, (2004).

23. Nefedov, A. & Wöll, C. in *Springer Series in Surface Science* Vol. 51 (eds G. Bracco & B. Holst) 277-306 (Springer-Verlag, 2013).
24. Moulder, J. F., Stickle, W. E., Sobol, P. E. & Bomben, K. D. *Handbook of X-ray Photoelectron Spectroscopy*. (Perkin-Elmer Corp.: Eden Prairie, 1992).
25. Batson, P. E. Carbon 1s Near-Edge-Absorption Fine Structure in Graphite. *Phys. Rev. B* **48**, 2608-2610, (1993).
26. Stöhr, J. *NEXAFS Spectroscopy*. (Springer-Verlag, 1992).
27. Frisch, M. J., Trucks, G. W., Schlegel, H. B., Scuseria, G. E., Robb, M. A., Cheeseman, J. R., Jr., J. A. M., Vreven, T., Kudin, K. N., Burant, J. C., Millam, J. M., Iyengar, S. S., Tomasi, J., Barone, V., Mennucci, B., Cossi, M., Scalmani, G., Rega, N., Petersson, G. A., Nakatsuji, H., Hada, M., Ehara, M., Toyota, K., Fukuda, R., Hasegawa, J., Ishida, M., Nakajima, T., Honda, Y., Kitao, O., Nakai, H., Klene, M., Li, X., Knox, J. E., Hratchian, H. P., Cross, J. B., Bakken, V., Adamo, C., Jaramillo, J., Gomperts, R., Stratmann, R. E., Yazyev, O., Austin, A. J., Cammi, R., Pomelli, C., Ochterski, J. W., Ayala, P. Y., Morokuma, K., Voth, G. A., Salvador, P., Dannenberg, J. J., Zakrzewski, V. G., Dapprich, S., Daniels, A. D., Strain, M. C., Farkas, O., Malick, D. K., Rabuck, A. D., Raghavachari, K., Foresman, J. B., Ortiz, J. V., Cui, Q., Baboul, A. G., Clifford, S., Cioslowski, J., Stefanov, B. B., Liu, G., Liashenko, A., Piskorz, P., Komaromi, I., Martin, R. L., Fox, D. J., Keith, T., Al-Laham, M. A., Peng, C. Y., Nanayakkara, A., Challacombe, M., Gill, P. M. W., Johnson, B., Chen, W., Wong, M. W., Gonzalez, C. & Pople, J. A. (Gaussian, Inc. , Wallingford, CT, USA 2004).
28. Maggio, E., Martsinovich, N. & Troisi, A. Evaluating Charge Recombination Rate in Dye-Sensitized Solar Cells from Electronic Structure Calculations. *J. Phys. Chem. C* **116**, 7638-7649, (2012).
29. Hamoudi, H., Döring, K., Chesneau, F., Lang, H. & Zharnikov, M. Self-assembly of pyridine-substituted alkanethiols on gold: the electronic structure puzzle in the ortho- and para-attachment of pyridine to the molecular chain. *J. Phys. Chem. C* **116**, 861-870, (2012).
30. Darlatt, E., Traulsen, C. H.-H., Poppenberg, J. s., Richter, S., Kühn, J., Schalley, C. A. & Unger, W. E. S. Evidence of click and coordination reactions on a self-assembled monolayer by synchrotron radiation based XPS and NEXAFS. *J. Electron Spectrosc. Relat. Phenom.* **185**, 85- 89, (2012).
31. Doron-Mor, I., Cohen, H., Barkay, Z., Shanzer, A., Vaskevich, A. & Rubinstein, I. Sensitivity of transmission surface plasmon resonance (T-SPR) spectroscopy: self-assembled multilayers on evaporated gold island films. *Chem. Eur. J.* **11**, 5555-5562, (2005).
32. Kalyuzhny, G., Vaskevich, A., Schneeweiss, M. A. & Rubinstein, I. Transmission Surface-Plasmon Resonance (T-SPR) Measurements for Monitoring Adsorption on Ultrathin Gold Island Films. *Chem. Eur. J.* **8**, 3850, (2002).
33. Wold, D. J., Haag, R., Rampi, M. A. & Frisbie, C. D. Distance Dependence of Electron Tunneling through Self-Assembled Monolayers Measured by Conducting Probe Atomic Force Microscopy: Unsaturated versus Saturated Molecular Junctions. *J. Phys. Chem. B* **106**, 2813, (2002).
34. Ho Choi, S., Kim, B. & Frisbie, C. D. Electrical resistance of long conjugated molecular wires. *Science* **320**, 1482-1486, (2008).
35. Choi, S. H. & Frisbie, C. D. Enhanced Hopping Conductivity in Low Band Gap Donor-Acceptor Molecular Wires Up to 20 nm in Length. *J. Am. Chem. Soc.* **132**, 16191, (2010).
36. Nishimori, Y., Kanaizuka, K., Kurita, T., Nagatsu, T., Segawa, Y., Toshimitsu, F., Muratsugu, S., Utsuno, M., Kume, S., Murata, M. & Nishihara, H. Superior Electron-Transport Ability of  $\pi$ -Conjugated Redox Molecular Wires Prepared by the Stepwise Coordination Method on a Surface. *Chem. Asian J.* **4**, 1361-1367, (2009).
37. Motiei, L., Lahav, M., Gulino, A., Iron, M. A. & Boom, M. E. v. d. Electrochemical Characteristics of a Self-Propagating Molecular-Based Assembly. *J. Phys. Chem. B* **114**, 14283-14286, (2010).
38. Sedghi, G., Garcia-Suarez, V. M., Esdaile, L. J., Anderson, H. L., Lambert, C. J., Martin, S., Bethell, D., Higgins, S. J., Elliott, M., Bennett, N., Macdonald, J. E. & Nichols, R. J. Long-range electron tunnelling in oligo-porphyrin molecular wires. *Nat. Nanotech.* **6**, 517, (2011).
39. Choi, S. H., Risko, C., Delgado, M. C. R., Kim, B., Bredas, J.-L. & Frisbie, C. D. Transition from Tunneling to Hopping Transport in Long, Conjugated Oligo-imine Wires Connected to Metals. *J. Am. Chem. Soc.* **132**, 4358, (2010).
40. Segal, D., Nitzan, A., Davis, W. B., Wasielewski, M. R. & Ratner, M. A. Electron Transfer Rates in Bridged Molecular Systems 2. A Steady-State Analysis of Coherent Tunneling and Thermal Transitions. *J. Phys. Chem. B* **104**, 3817-3829, (2000).

41. Nitzan, A. Electron transmission through molecules and molecular interfaces. *Annu. Rev. Phys. Chem.* **52**, 681–750, (2001).
42. Nishimori, Y., Kanaizuka, K., Murata, M. & Nishihara, H. Synthesis of Molecular Wires of Linear and Branched Bis(terpyridine)-Complex Oligomers and Electrochemical Observation of Through-Bond Redox Conduction. *Chem. Asian J.* **2**, 367-376, (2007).
43. Steyrleuthner, R., Schubert, M., Jaiser, F., Blakesley, J. C., Chen, Z., Facchetti, A. & Neher, D. Bulk electron transport and charge injection in a high mobility n-type semiconducting polymer. *Adv. Mater.* **22**, 2799-2803, (2010).
44. Joung, D., Chunder, A., Zhai, L. & Khondaker, S. I. Space charge limited conduction with exponential trap distribution in reduced graphene oxide sheets. *Appl. Phys. Lett.* **97**, 093105, (2010).
45. Steyrleuthner, R., Bange, S. & Neher, D. Reliable electron-only devices and electron transport in n-type polymers. *J. Appl. Phys.* **105**, 064509, (2009).

## **4. Tailoring the conductive properties of metal-organic supramolecular polymers by chemical design**

### **4.1. Introduction**

Among the huge number of metal–organic coordination networks, conductive or semiconductive systems remain relatively rare.<sup>1-4</sup> The most recognized conductive coordination polymers consist of macrocyclic metal complexes, such as phthalocyanine-based systems, like alkyne-linked conjugated porphyrins, or edge-fused structures.<sup>5</sup> The conductivity of these 1D coordination polymers depends on the interaction of the metal d-orbitals with the  $\pi^*$  level of the bridging ligand.<sup>3</sup> Another class of phthalocyanine showing conductive properties includes complex of Ni, Pd and Pt, which often stack in layers. In these compounds, it is not the  $\pi^*$ -d orbitals overlapping that is responsible for conductivity, but instead a  $\pi-\pi$  orbital overlap present between the different layers.<sup>6-9</sup>

As already mentioned in the previous Chapter, the application of terpyridine based systems in electronics is not fully established, although long-range transport abilities have been shown.<sup>10</sup> During the past few years, numerous one-, two-, and three-dimensional coordination polymers have been generated from transition metal templates with rigid and flexible pyridyl containing bidentate or multidentate organic spacers. Self-assembly processes involving carefully designed multidentate ligands and metal ions provide indeed an effective means for the construction of different novel polymers with different motifs.<sup>11</sup>

These systems are highly versatile in terms of tailoring the energetics (excited-state energies, redox potentials) by appropriate choice of metals and ligands. A suitable choice of the components such as metal ions, peripheral ligands, and modular bridging ligands leads to the possibility of

controlling the overall structure in terms of geometry, electronic interaction and distance between the metal centers and allows the occurrence of interesting photoinduced processes such as vectorial transport of energy or electronic charge, charge separation, multiredox processes.<sup>12</sup>

An example of organic ligand bearing a monodentate and a tridentate units at the poles is the (4'-(4'''-pyridyl)-2,2':6'2''-terpyridine).<sup>13</sup> This ligand contains the 2,2':6',2''-terpyridine (terpy) coordinative site and another pyridyl (py) site at the 4'-position; these two sites are able to bind with different metal ions, thus leading to the coordination polymers with various frameworks.<sup>14</sup> Most of its metalated complexes are in the form of  $[M(\text{pyterpy})_2]^{n+}$  with two terpy sites connected to the metal ions and remaining two pyridyl sites uncoordinated, the structural features of which are very similar to the well-known 4,4'-bipyridyl ligand.<sup>13,15</sup> Because of such unique structural features, the  $[M(\text{pyterpy})_2]^{n+}$  complexes can act as a “ligand-like” coordinative unit for the assembly of large amounts of bimetallic coordination polymers.<sup>16</sup> For example the  $\text{Ru}(\text{pyterpy})_2^{2+}$  complex, behaving like an expanded 4,4'-bipyridine, was used as a bidendate ligand to construct coordination polymer.<sup>17</sup> Other geometries can be however obtained, such as squared oligomers<sup>18</sup> and grids<sup>19</sup> or channels.<sup>20</sup> Interestingly, even linear polymers have been obtained where the metal center was coordinated by a terpyridine and a pyridine unit, and chlorine atoms completed the octahedral coordination sphere by occupying the apical positions.<sup>21</sup>

Aiming at the construction of 1D polymer structures, one may envisage the use of either octahedral dicationic metals associated with two coordinating anions occupying the apical positions<sup>22,23</sup> or square-planar metal centers.<sup>24</sup> High directionality was inferred to the supramolecular structures with the introduction for example of an anthracene core bearing two ethynyl groups to connect the terpyridil and the pyridil units, 4'-[10-[2-(4-pyridinyl)ethynyl]-9-anthracenyl]- 2,2':6',2''-Terpyridine (TAP) leading to an inline disposition of the two coordinating poles.<sup>25</sup>

The physisorption of a solution containing the neutral complex formed by the TAP ligand and  $\text{CoCl}_2$  on graphite led to straight nanostructures up to 400 nm long.<sup>25</sup> These 1D nanostructures appeared in STM images as made of aligned and regularly spaced circular spots which corresponded to the Co ions. These spots were not laterally correlated, but grew either as single anisotropic nano-objects or as tightly packed parallel wires separated by a variable distance. The use instead of the Pd(II) cation, by design, yields a polycationic 1D network. Indeed, because of the dicationic nature of palladium, its binding by the neutral ligand generates a charged square-planar assembling node formed by the palladium center and one terpyridine and one pyridine unit belonging to consecutive tectons.<sup>25,26</sup> STM images showed in this case that the straight, parallel 1D wires obtained on graphite were laterally correlated, because of the lateral intercalation with the counteranion forming overall a 2D neutral supramolecular array.<sup>25</sup>

Here we aimed to compare the structure of the CoTAP and PdTAP polymers (Figure 4.1) as possible functional materials, and to correlate it with the electrical properties.

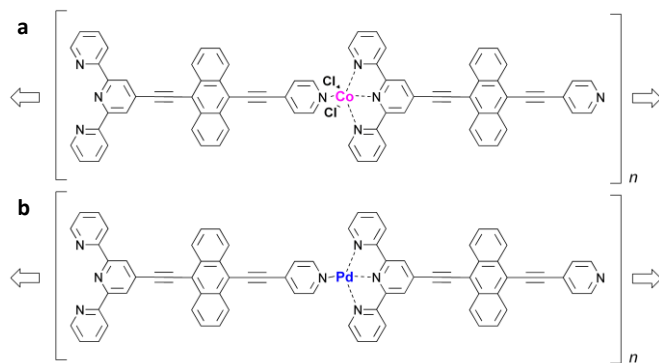


**Figure 4.1:** Molecular structures of the terpyridine-antracene-pyridine (TAP) complexes: (a) CoTAP, (b) PdTAP.

## 4.2. Experimental details:

Cobalt chloride hexahydrate ( $\text{CoCl}_2 \cdot 6\text{H}_2\text{O}$ ), Palladium acetate  $\text{Pd}(\text{CH}_3\text{COO})_2 \cdot 4\text{H}_2\text{O}$  and chloroform  $\text{CHCl}_3$  were purchased by Sigma Aldrich. The terpyridine-antracene-pyridine TAP ligand was synthesized as described elsewhere<sup>25</sup>. The polymer preparation was carried out by mixing 1 mM solution in  $\text{CHCl}_3$  of the ligand and the metal. A dispersion in chloroform was obtained which was then drop cast on the silicon oxide support.

Grazing Incidence X-ray Diffraction (GIXRD) measurements were performed at XRD1 beamline of ELETTRA Synchrotron facility in Trieste (Italy) using a monochromatic beam of energy  $E = 12.4$  keV, (corresponding to a wavelength,  $\lambda$ , of 1 Å) and size  $200 \times 200 \mu\text{m}^2$ . The incident angle of the X-ray beam,  $\alpha_i$ , was chosen close to the critical angle for total reflection of the organic film (i.e. 0.1°). The diffraction pattern were collected by a 2D camera (Pilatus detector) placed normal to the incident beam direction at a distance of 250 mm from the sample. All the results are expressed in terms of scattering vector  $\mathbf{q}$  defined as  $q = \frac{4\pi}{\lambda} \sin(\theta)$ , where  $\theta$  is half of the scattering angle.

Atomic Force Microscopy (AFM) morphological characterization was performed in tapping mode in a Dimension 3100 microscope equipped with a Nanoscope IV controller (Digital Instruments). Commercial silicon cantilevers with a nominal spring constant of 40 N/m were used for morphological characterization in tapping mode.

Torsion-resonance tunneling current (TR-TUNA AFM) images were obtained in a Multimode V (Veeco) microscope equipped with a Nanoscope V controller using Pt/Ir-coated Si tips with 225 μm long cantilever and spring constant in the range 0.5 – 9.5 N/m. The torsion amplitude was used as the

feedback signal to measure surface morphology. The current maps were obtained by biasing a bottom gold electrode and mapping the current of the material on top of the gold.

Gold electrodes on silicon dioxide (Fraunhofer Institute) substrates were cleaned by subsequent ultrasonication bath in acetone and isopropanol prior to use. A Keithley 2636A source meter was used for the two probe current-voltage characteristics measurements under controlled atmosphere. Two terminal bottom contacts devices were prepared by drop casting the complex solution onto patterned substrates.

The packing of the system has been simulated with the Material Studio v6.0 program, with the Forcite module to optimize the structure at the molecular mechanics (MM) level with pcff ForceField. Following, Molecular Dynamic (MD) calculations have been performed at two temperatures and time scales; the first MD run at 600K for 3ns has been followed by a shorter (1 ns) run at room temperature (RT). This procedure has been repeated until stable at RT crystal structures have been obtained. The GIWAXS (synchrotron wavelength of 1 Å) patterns of these stable structures have then been compared with the experimental data.

The interchain charge transport has been estimated by calculating charge transfer integrals (DFT/B3LYP with the DZ basis set) for  $\pi$ -stacked dimers of monomers extracted from the crystal systems using the ADF software.

### 4.3. Morphological and structural characterization

The morphological analysis of the CoTAP and the PdTAP polymers was carried out by AFM on samples prepared by drop casting around 50  $\mu\text{L}$  of the dispersion in  $\text{CHCl}_3$  on silicon oxide substrates. For comparison also the TAP ligand was deposited on silicon oxide by drop casting a solution 1 mM in chloroform and imaged by AFM.

The TAP ligand organized in an anisotropic fashion on the surface, forming fibers which aggregate in the peculiar way as shown in Figure 4.2. The fibers organize in “sheaf-like” spherulite structures around a central point from where they seem to expand.<sup>27</sup> The bundles have lengths of around 3-5  $\mu\text{m}$  and the smallest fibers measured at the periphery of the spherulites have thickness of about 6-8 nm and width of 20-30 nm.

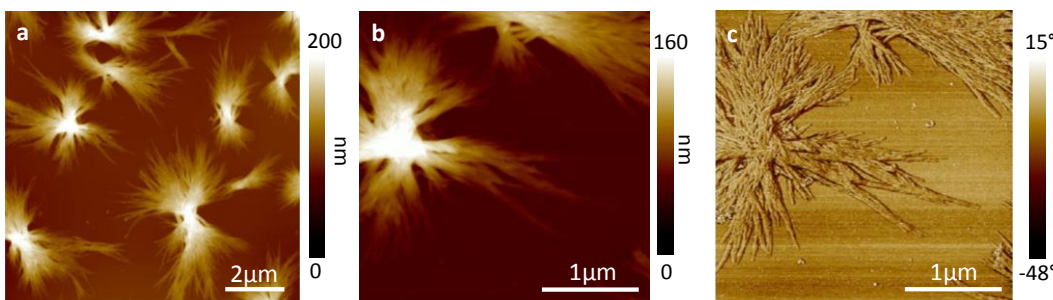


**Figure 4.2:** Tapping mode AFM images of the ligand TAP deposited on silicon dioxide by drop-casting from a solution 1 mM in chloroform. a) large scan image; b, c) topography and phase small scale images.

The morphology of the complexes, after coordination with the metal ions is very different. The CoTAP film appears as formed by small globular aggregates of around 50 nm in diameter randomly spread over the substrate. (Figure 4.3 a, b). On the contrary, the morphology of the PdTAP film shows fibrillar structures which are interconnected in networks (Figure 4.3 c, d). We hypothesized that the different morphology of the two complexes could be explained by considering the coordination geometry of the metal centers. In particular, in the CoTAP, the metal site is octahedrally coordinated with three coordination sites bound to a terpyridine, one bound to a pyridine of the consecutive ligand and two positions being occupied by two Cl anions. The octahedrally coordinated center hampers then a intermolecular packing which can be instead be favored by a planar architecture such as the one of PdTAP, where being the  $\text{Pd}^{2+}$  tetracoordinate and planar, favor the formation of more packed structures (see supramolecular motifs in Figure 4.1).

Indeed the  $\pi-\pi$  interactions can play an important role in controlling the packing or assembly also of metal coordination compounds. In many structural descriptions of metal-ligand complexes  $\pi-\pi$  stacking is invoked as a motif, where the most common  $\pi$  interaction is an offset or slipped stacking, i.e. the rings are parallel displaced.<sup>28</sup> In our case the planarity of the Pd-based polymer is expected to favor the intermolecular interactions through  $\pi-\pi$  non-covalent bonds.

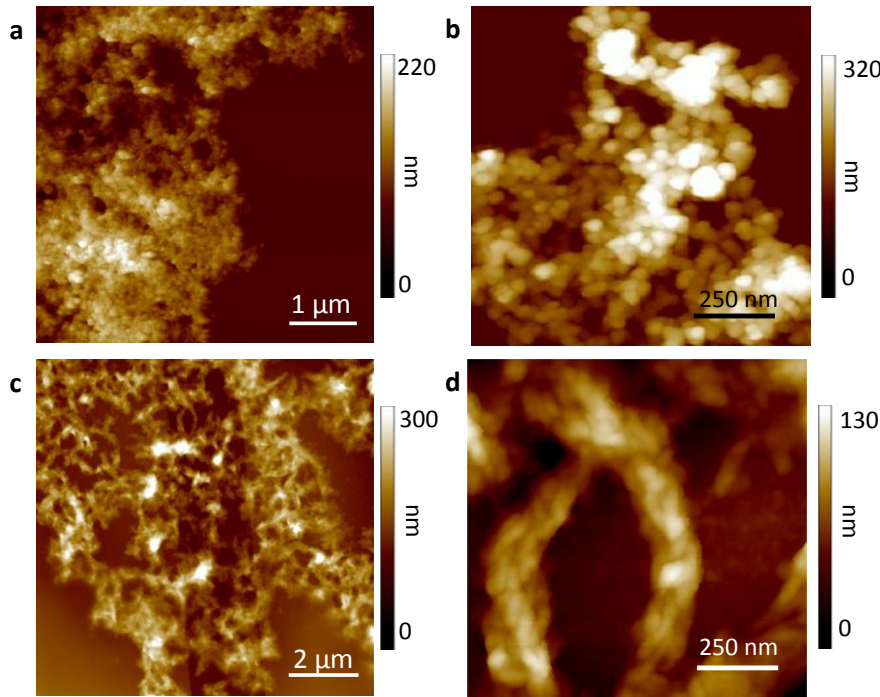


**Figure 4.3:** AFM topography images of the CoTAP complex. (a, b) and of the PdTAP complex. (c, d) drop cast on solid substrates.

To confirm our observations, we performed Grazing Incidence X-ray Diffraction (GIXRD) analysis on the film of CoTAP and PdTAP deposited on silicon oxide substrates. The diffraction patterns are shown in Figure 4.4.

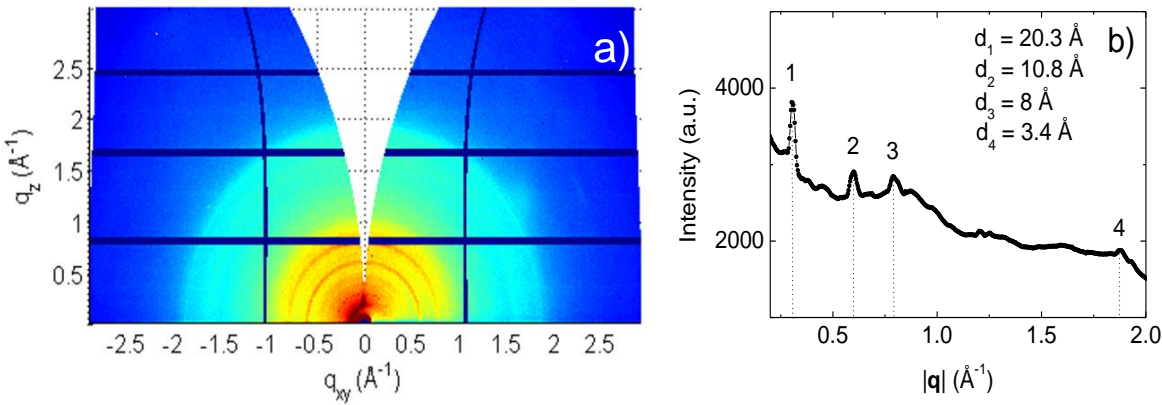


**Figure 4.4:** (a) 2D-GIXRD images of the CoTAT film. (b) Radial integration of the 2D-GIXRD image.

The 2D-GIXRD image collected for CoTAP film, reported Figure 4.4a, show uniform rings, indicating the polycrystallinity of the film which is formed by crystalline domains randomly oriented.

From the radial integration of the diffraction pattern, four main periodicities (d-spacings) are detected: 20.3 Å, 10.8 Å, 8 Å and 3.4 Å. The former one could be related to the repetition of the monomer length, whereas the latter one could be ascribed to the  $\pi$ - $\pi$  interaction between single monomers. From the full width at half maximum (FWHM) of the peaks ( $\Delta q$ ), the average size of the crystalline domains (D) along the three crystallographic directions is estimated by using the Sherrer equation ( $D = 2\pi K / \Delta q$ , where K is a form factor with value close to 0.9) and the results are shown in Table 4.1.

**Table 4.1:** Average crystalline domains size calculated from the main periodicities in Figure 4.4b.

Peak	$\Delta q$ (Å <sup>-1</sup> )	D (Å)
1	0.027	209
2	0.021	269
3	0.040	141
4	0.060	94

Differently from CoTAP, the diffraction pattern of PdTAP film (see Figure 4.5) contains arc shaped Bragg spots with cylindrical symmetry, which are characteristic of a film with a preferred out-of-plane orientation but isotropic in-plane (a textured film). Figure 4.5c reports the scattering profile along the specular direction ( $q_{xy} \sim 0$ ), where the most intense Bragg spot corresponds to a periodicity of 12 Å between lattice planes parallel to the surface and could be associated to the lamellae stacking. From the lamellae peak width ( $\Delta q_z^{-1} = 0.11$  Å<sup>-1</sup>) the crystallite thickness is estimated to be ~5.1 nm. The distribution of crystallite orientations produces arcs of diffracted intensity. The average degree of this misorientation was estimated to be ~50° from the FWHM of the scattering profile determined along the arc slice of the most intense spot (shown in Figure 4.5b).

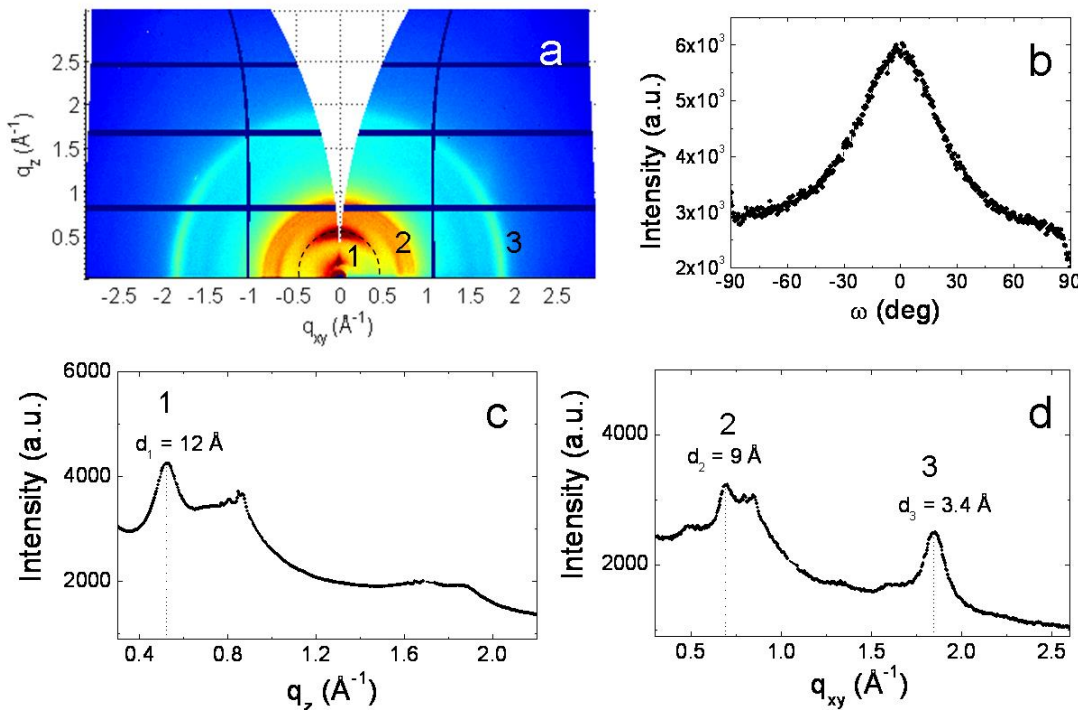


**Figure 4.5:** (a) 2D-GIXRD images of the PdTAT film. (b) Scattering profile along the arc slice of peak 1. Scattering intensity integrated along the specular ( $q_{xy} \sim 0$ ) (c) and in-plane (d) directions. The most relevant peaks are highlighted and the corresponding  $d$ -spacing are indicated.

Along the in-plane direction (Figure 4.5d) two periodicities of  $3.4 \text{ \AA}$  and  $9 \text{ \AA}$  are clearly detected. In the first case the average size of the contributing crystalline domains along this specific direction is estimated to be  $\sim 3.8 \text{ nm}$  and the reflection is ascribed to the  $\pi-\pi$  interaction between the antracene moieties, whereas in the second case the domains are bigger ( $\sim 5.6 \text{ nm}$ ) and the peak could be related to the repetition of half of the chain backbone.

All these findings suggest that the majority of PdTAP crystallites adopt an edge-on configuration. To confirm the orientation and find out the molecular packing of PdTAP films, we performed simulations of the diffraction pattern.

The monomer shown in Figure 4.6a has been used as repeating unit to perform the calculations. The unit cell created to found the packing consists in four monomers and eight acetate counterions (to balance the positive charge of each Pd(II) metal center) packed in an opposite manner to balance the dipole moment of each chain, as shown in Figure 4.6b. The ‘head-to-tail’ orientation of stacked pyridyls is indeed energetically more favorable than the ‘head-to-head’ one.<sup>29</sup>

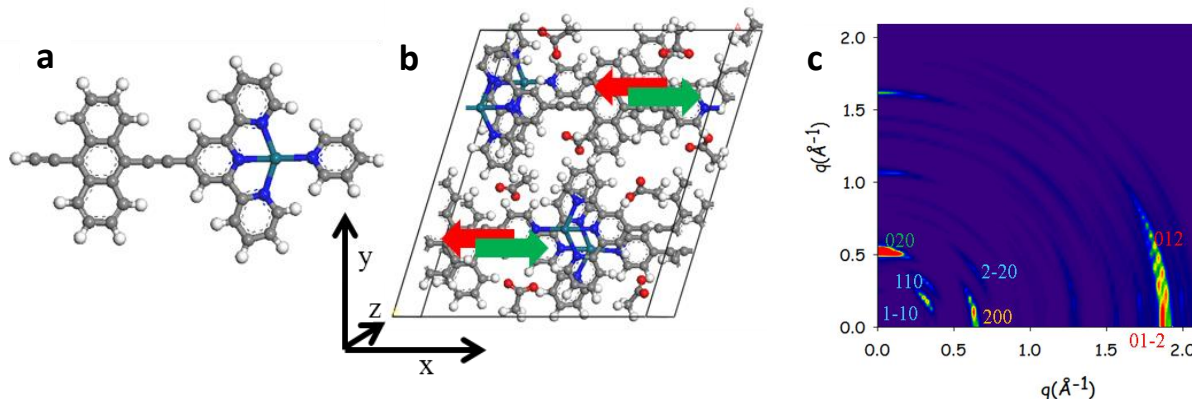


**Figure 4.6:** a) Structure of the monomer used for the packing. b) Unit cell adopted for the simulations with acetate counterions; the two monomer dimers point in different directions to neutralize the dipole moment, as indicated by green and red arrows. Green balls refer to Pd, blue to N, red to O, grey to C and white to H atoms. c) Simulated diffraction spectra of the PdTAT film, corresponding to the packing in b).

Three possible orientations of the polymer on the surface were simulated (see Annex B) and the only diffraction pattern matching with the experimental one corresponded to a packing with the molecular width perpendicular to the surface (x-z plane in Figure 4.6b). In the cell the monomers are shifted by 2 Å with respect to each other along the lamellae direction (y-axis) and by 4 Å along the amol direction (x-axis). The simulated diffraction pattern is reported in Figure 4.6c.

The numbers in Figure 4.6c correspond to the Miller index planes; the peak associate to the 020 index is along the lamellae direction (y-axis; the shortest distance in between two polymer chain is about 2.6 Å); the peak associate to the 200 index is along the molecule (x-axis, corresponding to half of the monomer length); the peaks associated to the 012 and 01-2 indexes are in the  $\pi$ -stacking direction (z-axis); the peaks associated to the 110/1-10/2-20 indexes are mainly due to the counterions.

The calculated lamellae direction is of 11.49 Å, the direction along the molecular length of 9.74 Å and the  $\pi$ -stacking direction of 3.36 Å, in good agreement with the values extrapolated by the experimental spectra of 12, 9 and 3.40 Å (see Figure 4.5) for the lamellae, molecular length and  $\pi$ -stacking directions, respectively. The above diffraction pattern is not very sensitive to little changes in geometry of the system; in fact, when shifting the two polymer chains towards a perfect cofacial packing, no significant change have been detected.

The characterizations presented above clearly show markedly different supramolecular organizations of the two compounds, with a distinct  $\pi$ - $\pi$  aggregation of the planar PdTAP polymer. The different intermolecular aggregation was found to affect also the electrical properties of the two materials.

#### 4.4. Electrical behavior in two terminal devices and at the nanoscale

Two probe current voltage measurements were performed on films fabricated by drop-casting few  $\mu\text{L}$  of the suspension containing the CoTAP or the PdTAP polymers on silicon oxide substrates where gold electrodes were pre-patterned. Being the polymers insoluble at this concentration they are not easy to process. As a result the films are extremely inhomogeneous, as one can see from the optical images in Figure 4.7b -c. Current-voltage measurements showed conductivity in the PdTAP films, whereas current below the detection limit was obtained for the CoTAP film (Figure 4.7). In the case shown in Figure 4.7 the electrode separation ( $L$ ) was 10  $\mu\text{m}$  and for the Pd polymer currents of the order of  $\mu\text{A}$  were measured in the bias range of  $\pm 10$  V. Because of the inhomogeneity of the films in terms of coverage of the electrodes, the measurements showed currents spanning several orders of magnitude from one device to another; and no trend could be observed on devices with different  $L$ , as shown in Figure 4.8. The electrical behavior of the PdTAP polymer was also probed on three electrodes devices (field-effect transistor) in bottom-gate configuration, but no gate modulation was observed.

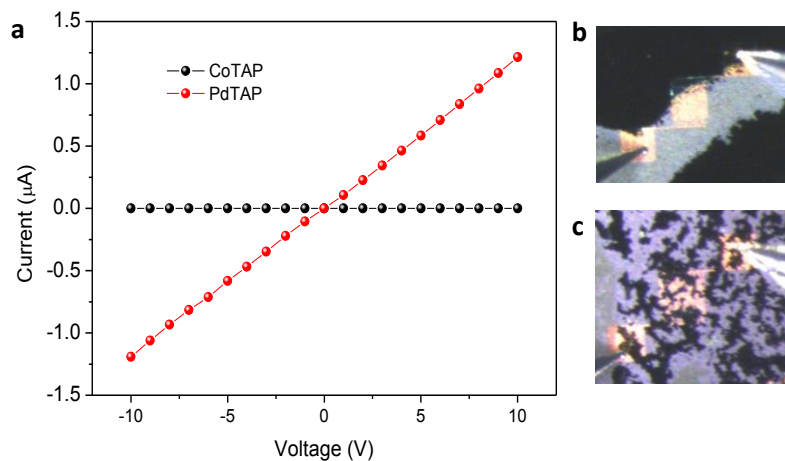


**Figure 4.7:** (a) Current-voltage behavior of the CoTAP and PdTAP polymers deposited on prepatterned silicon oxide substrates with prepatterned interdigitated gold electrodes ( $L=10 \mu\text{m}$ ,  $W=10 \text{ mm}$ ). Optical microscopy images of the CoTAP film (b, the material correspond to the brighter area) and PdTAP film (c, the material corresponds to the darker areas).

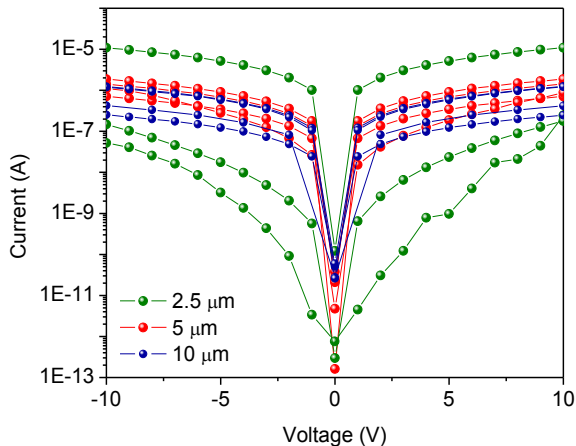


**Figure 4.8:** Current-voltage characteristics of PdTAP measured on different devices having different electrode separation  $L$  of 2.5, 5 and 10  $\mu\text{m}$ . The width  $W$  is 10 mm for all the devices.

Conductivity measurements of the PdTAP complex at the nanoscale were performed by C-AFM in a vertical configuration on gold substrate. The conductive tip was scanned over the surface of the film and the voltage was varied during the same scan, as marked in the current maps of Figure 4.9. From the comparison of the topography and current maps it is possible to see the response in terms of current modulation with the bias applied between the gold electrode and the C-AFM tip. The average currents detected in the bias range of  $\pm 10\text{ V}$  are in the order of a few pA (see the average currents marked in Figure 4.9d), the average currents at  $+5\text{ V}$  and  $-5\text{ V}$  are 0.40 and 0.42 pA (see the current map in Figure 4.9a), respectively, which indicate that there is not preferential charge injection from one electrode (C-AFM tip) with respect to the other (gold substrate). Such low current values are very common in TR-TUNA AFM experiments;<sup>30,31</sup> as an example vertical nanorods of semiconductive triarylamine polymers around 160 nm high, showed currents of about 400 fA at a bias of 12 V. However, it has to be remarked that the films are hundreds of nm thick; the fibers marked with the arrows in Figure 4.9, for example, which show very definite current profiles, are more than 100 nm far away from the biased substrate, as an indication of the existence of efficient pathways for charges along the thick film. By comparing the current maps at a fixed bias with the topography images, one can also see that there is not a clear scaling of the current with the thickness of the film, which may be an indication contact limited junction. However, as it can also be observed by the comparison of the height section with the current profile in Figure 4.9c, when the tip, during the lateral scan, meets a topographical protrusion a sudden increase in the current signal is recorded. This can be ascribed to a variation of the actual contact area and/or to a slow response of the feedback loop.

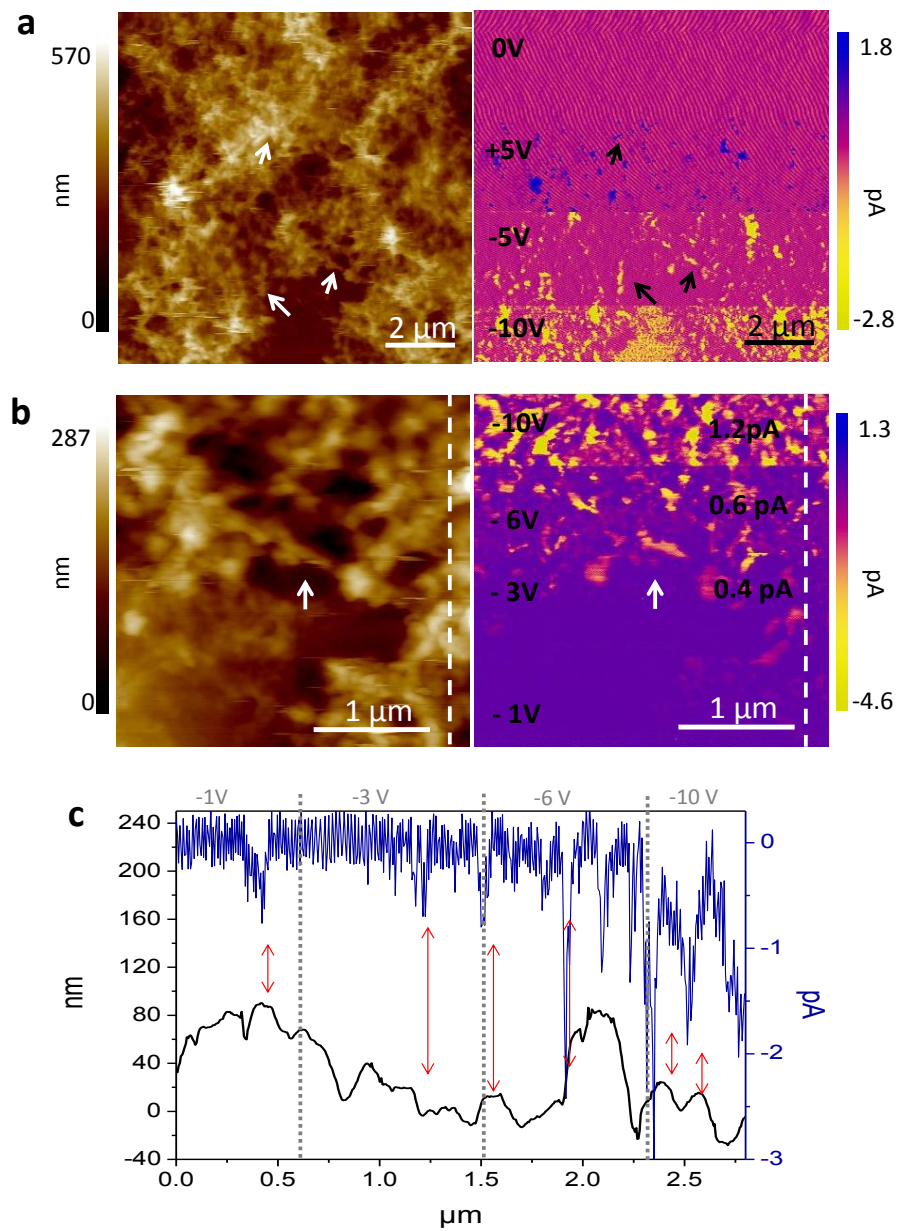


**Figure 4.9:** C-AFM topography and current map images of a network of molecular wires of PdTAP on a gold electrode. In the current map in (a) four different areas are visible corresponding to 0, +5, -5 and -10V applied on the gold bottom electrode. In (b) the current map image shows the increasing of the average current with the increasing bias. The arrows highlight fiber structures in the film. c) Height (black) and current (blue) profiles along the white dashed lines marked in b).

Both the macroscopic and the C-AFM electrical measurements showed promising charge transport properties for the PdTAP polymer. However, the difficulty of processing such a material, did not allow at the present conditions the extraction of more quantitative information. On this respect

more effort should be done to improve the film deposition procedures or to fabricate mesoscopic more defined structures of the supramolecular polymer.

As mentioned above, electron transfer processes taking place between adjacent molecules via two possible pathways i.e. metal- $\pi$  and/or  $\pi$ - $\pi$  interactions have been reported for other transition-metal coordinated systems in literature.<sup>32</sup> The presence of strong aromatic interactions favoring the assembly of coordination polymers into  $\pi$ - $\pi$  interacted supramolecular structures was demonstrated in many cases to be a supplementary requirement for the conductivity of this type of compounds.<sup>33,34</sup> In our case, it is likely that the presence of the  $\pi$ - $\pi$  interchains interactions have an important role in this respect. Further investigations on the intrachain transport are ongoing. Below we report instead some theoretical findings on the interchain transport of the PdTAP polymer.

## 4.5. Theoretical insights on charge transport

We considered a perfect cofacial packing for the calculation of the interchain charge transport, considering as dominant the charge transport along the  $\pi$ -stacking direction. Details on the calculated transfer integrals along the lamellae direction and for different degrees of shift can be found in the Annex B.

To analyze the shape of the frontier orbitals, we consider Pd (II) and two negative (-1e) point charges instead of counterions, at a distance of 3.5 Å from the metal center as reported in experimental work with similar ligand.<sup>35</sup> The frontier orbitals obtained for the monomer are reported in Figure B3 in the Annex. Although the addition of point charges lead to not negligible differences on the relative energies of the MOs, a weak influence on their shapes is found, namely a slightly increased localization of the HOMO and LUMO orbitals. In fact, with and without point charges, the frontier orbitals localize in the same way: the HOMO is mainly localized in the antracene group forming the ligand, while the LUMO is mainly localized on the metal center and partly on the terpyridine and pyridine groups. Interestingly, a similar localization of the frontier orbitals is found when the pyridine is twisted by up to 90° with respect to the molecular plane.

Two different dimers have been used for the transfer integral calculations. In the first, only the Pd-Pd metal centers overlap, while in the second only the antracene groups of the ligand overlap, as depicted in Figure 4.10.

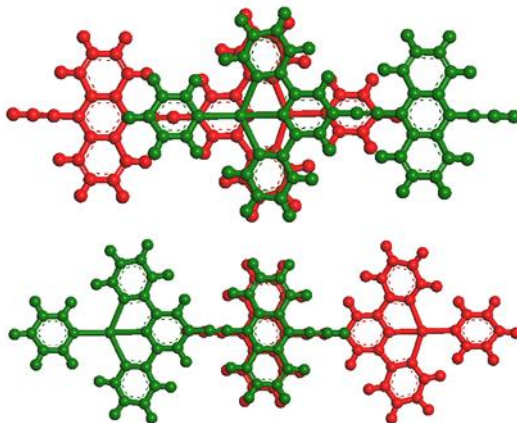


**Figure 4.10:** Representation of the two different monomers' overlap considered for the TI calculations, with overlap of the metal centers (*top*) and of the antracene groups of the ligand (*bottom*). Green structures are in front, red structures at the back.

The charge transport abilities (the electronic coupling/charge transfer integral) along the  $\pi$ -stacking hopping direction are relatively high for both holes and electrons, reaching up to  $\sim 2.5 \cdot 10^{-1}$  eV and  $\sim 6 \cdot 10^{-2}$  eV respectively, when the antracene groups are overlapping. The values are smaller when the metal centers overlap, and reaching up to  $\sim 10^{-3}$  eV for holes and  $\sim 5.5 \cdot 10^{-3}$  eV for electrons. On the other hand, along the lamellae direction, the TI calculated for both holes and electrons are lower than the  $\pi$ -stacking pathway by up two orders of magnitude, for both overlaps (see figure B5 in the Annex).

Hence, the overall interchain transfer integral is strongly influenced by the relative position of the two chains within the cell, and a strong interaction of the antracene groups lead to very high values of transfer integral for holes, up to  $\sim 2.5 \cdot 10^{-1}$  eV, suggesting that the polymer structure is much likely to behave as a holes transporting material.

## 4.1. Conclusions

In conclusion, the organization of metal-coordination polymers where the ligand was based on an anthracene core bearing two ethynyl groups equipped with a pyridine and a terpyridine group at the poles was investigated. The morphological and structural characterization of the polymers showed that the supramolecular assembly was governed by the coordination geometry of the metal centers. In particular, the planarity of squared Pd(II) based polymers allowed for the formation of  $\pi$ - $\pi$  stacked fibrillar structures where crystalline domains had specific preferred orientations. The improved order of these molecular systems, with respect to the corresponding octahedral Co(II) polymer, where the  $\pi$ - $\pi$

stacking is less favored, resulted in completely different electrical behavior. Conduction of the Pd(II) based fiber-like structures was probed both at the microscale and at the nanoscale and theoretical calculations showed high charge transport abilities, in terms of electronic coupling, for both holes and electrons due to the overlapping of the antracene moieties.

We believe that the presented results open new perspectives on the engineering of conductive metal coordination polymers, towards the application in functional devices.

## 4.2. References

1. Givaja, G., Amo-Ochoa, P., Gómez-García, C. J. & Zamora, F. Electrical conductive coordination polymers. *Chem. Soc. Rev.* **41**, 115, (2012).
2. Xu, Z. A selective review on the making of coordination networks with potential semiconductive properties. *Coord. Chem. Rev.* **250**, 2745-2757, (2006).
3. Janiak, C. Engineering coordination polymers towards applications. *Dalton Trans.*, 2781-2804, (2003).
4. Gómez-Herrero, J. & Zamora, F. Coordination Polymers for Nanoelectronics. *Adv. Mater.* **23**, 5311-5317, (2011).
5. Anderson, H. L. Building molecular wires from the colours of life: conjugated porphyrin oligomers. *Chem. Commun.*, 2323-2330, (1999).
6. Hendon, C. H., Tiana, D. & Walsh, A. Conductive metal-organic frameworks and networks: fact or fantasy? *Phys. Chem. Chem. Phys.* **14**, 13120-13132, (2012).
7. Bao, Z., Lovinger, A. J. & Brown, J. New Air-Stable n-Channel Organic Thin Film Transistors. *J. Am. Chem. Soc.* **120**, 207-208, (1998).
8. Yoon, S. M., Lou, S. J., Loser, S., Smith, J., Chen, L. X., Facchetti, A. & Marks, T. Fluorinated Copper Phthalocyanine Nanowires for Enhancing Interfacial Electron Transport in Organic Solar Cells. *Nano Letters* **12**, 6315-6321, (2012).
9. Zhang, W., Ochi, K., Fujiki, M., Naito, M., Ishikawa, M., Kaneto, K.-i., Takashima, W., Saeki, A. & Seki, S. Programmed High-Hole-Mobility Supramolecular Polymers from Disk-Shaped Molecules. *Adv. Funct. Mater.* **20**, 3941-3947, (2010).
10. Sakamoto, R., Katagiri, S., Maeda, H. & Nishihara, H. Bis(terpyridine) metal complex wires: Excellent long-range electron transfer ability and controllable intrawire redox conduction on silicon electrode. *Coord. Chem. Rev.* **257**, 1493-1506, (2013).
11. Yan, Y. & Huang, J. Hierarchical assemblies of coordination supramolecules. *Coord. Chem. Rev.* **254**, 1072-1080, (2010).
12. De Cola, L. & Belser, P. Photoinduced energy and electron transfer processes in rigidly bridged dinuclear Ru/Os complexes. *Coord. Chem. Rev.* **177**, 301, (1998).
13. Constable, E. C. & Thompson, A. M. W. C. Ligand Reactivity in Iron(ii) Complexes of 4'-(4'''-Pyridyl)-2,2':6',2''-terpyridine. *J. Chem. Soc., Dalton Trans.*, 2947, (1992).
14. Robin, A. Y. & Fromm, K. M. Coordination polymer networks with O- and N-donors: What they are, why and how they are made. *Coord. Chem. Rev.* **250**, 2127-2157, (2006).
15. Kaes, C., Katz, A. & Hosseini, M. W. Bipyridine: The Most Widely Used Ligand. A Review of Molecules Comprising at Least Two 2,2'-Bipyridine Units. *Chem. Rev.* **100**, 3553-3590, (2000).
16. Zhang, C.-F., Huang, H.-X., Liu, B., Chen, M. & Qian, D.-J. Spectroscopic study on the 4'-(4-pyridyl)-2,2':6',2''-terpyridine and its metal complexes. *Journal of Luminescence* **128**, 469-475, (2008).
17. Beves, J. E., Constable, E. C., Housecroft, C. E., Kepert, C. J. & Price, D. J. The first example of a coordination polymer from the expanded 4,4'-bipyridine ligand [Ru(pytpy)<sub>2</sub>]<sup>2+</sup>(pytpy = 4'-(4-pyridyl)-2,2':6',2''-terpyridine). *CrystEngComm* **9**, 456, (2007).

18. Sun, S.-S. & Lees, A. J. Self-Assembly Organometallic Squares with Terpyridyl Metal Complexes as Bridging Ligands. *Inorg. Chem.* **40**, 3154-3160, (2001).
19. Hou, L., Li, D., Shi, W.-J., Yin, Y.-G. & Ng, S. W. Ligand-Controlled Mixed-Valence Copper Rectangular Grid-Type Coordination Polymers Based on Pyridylterpyridine. *Inorg. Chem.* **44**, 7825-7832, (2005).
20. Pitarch López, J., Kraus, W., Reck, G., Thünemann, A. & Kurth, D. G. Alternating perpendicular 1-D channels in the supramolecular structure of the copper(II) complex  $[\text{Cu}(\text{pyterpy})_2](\text{PF}_6)_2 \cdot \text{CH}_3\text{OH} \cdot 0.5 \text{CH}_2\text{Cl}_2$  (pyterpy=4'-(4'''-pyridyl)-2,2':6',2''-terpyridine). *Inorganic Chemistry Communications* **8**, 281-284, (2005).
21. Hayami, S., Hashiguchi, K., Juhász, G., Ohba, M., Ohkawa, H., Maeda, Y., Kato, K., Osaka, K., Takata, M. & Inoue, K. 1-D Cobalt(II) Spin Transition Compound with Strong Interchain Interaction:  $[\text{Co}(\text{pyterpy})\text{Cl}_2]_x$ . *Inorg. Chem.* **43**, 4124-4126, (2004).
22. Jouaiti, A., Hosseini, M. W. & Kyritsakas, N. Non-centrosymmetric packing of 1-D coordination networks based on chirality. *Chem. Comm.*, 1898–1899, (2002).
23. Jouaiti, A., Jullien, V., Hosseini, M. W., Planeix, J.-M. & De Cian, A. Controlling the formation of discrete complexes or a 1-D directional coordination network by the binding ability of anions. *Chem. Commun.*, 1114-1115, (2001).
24. Eryazici, I., Moorefield, C. N. & Newkome, G. R. Square-Planar Pd(II), Pt(II), and Au(III) Terpyridine Complexes: Their Syntheses, Physical Properties, Supramolecular Constructs, and Biomedical Activities. *Chem. Rev.* **108**, 1834-1895, (2008).
25. Surin, M., Samorì, P., Jouaiti, A., Kyritsakas, N. & Hosseini, M. W. Molecular Tectonics on Surfaces: Bottom-Up Fabrication of 1D Coordination Networks That Form 1D and 2D Arrays on Graphite. *Angew. Chem.* **119**, 249-253, (2007).
26. Beves, J. E., Constable, E. C., Housecroft, C. E., Neuburger, M. & Schaffner, S. A palladium(II) complex of 4'-(4-pyridyl)-2,2':6',2''-terpyridine: Lattice control through an interplay of stacking and hydrogen bonding effects. *Inorg. Chem. Commun.* **10**, 1185-1188, (2007).
27. Hutter, J. L. & Bechhoefer, J. Banded spherulitic growth in a liquid crystal. *J. Cryst. Growth* **217**, 332–343, (2000).
28. Janiak, C. A critical account on  $\pi$ - $\pi$  stacking in metal complexes with aromatic nitrogen-containing ligands. *J. Chem. Soc., Dalton Trans.*, 3885-3896, (2000).
29. Khlobystov, A. N., Blake, A. J., Champness, N. R., Lemenovskii, D. A., Majouga, A. G., Zyk, N. V. & Schroeder, M. Supramolecular design of one-dimensional coordination polymers based on silver(I) complexes of aromatic nitrogen-donor ligands. *Coord. Chem. Rev.* **222**, 155-192, (2001).
30. Weber, S. A. L. & Berger, R. d. Electrical tip-sample contact in scanning conductive torsion mode. *Appl. Phys. Lett.* **102**, 163105, (2013).
31. Weber, S. A. L., Haberkorn, N., Theato, P. & Berger, R. d. Mapping of Local Conductivity Variations on Fragile Nanopillar Arrays by Scanning Conductive Torsion Mode Microscopy. *Nano Lett.* **10**, 1194, (2010).
32. Zheng, S.-L., Zhang, J.-P., Wong, W.-T. & Chen, X.-M. A Novel, Highly Electrical Conducting, Single-Component Molecular Material:  $[\text{Ag}_2(\text{o phen})_2]$  (Hophen = 1H-[1,10]phenanthrolin-2-one). *J. Am. Chem. Soc.* **125**, 6882-6883, (2003).
33. Munakata, M., Wu, L. P., Kuroda-Sowa, T., Maekawa, M., Suenaga, Y., Ning, G. L. & Kojima, T. Supramolecular Silver(I) Complexes with Highly Strained Polycyclic Aromatic Compounds. *J. Am. Chem. Soc.* **120**, 8610-8618, (1998).
34. Munakata, M., Ning, G. L., Suenaga, Y., Kuroda-Sowa, T., Maekawa, M. & Ohta, T. A One-Dimensional Metallocyclophane with Columnar Aromatic Stacking: The Silver(I)  $\eta^2$ -Coordination Complex of 1,2-Benztriphenylene. *Angew. Chem. Int. Ed.* **39**, 4555–4557, (2000).
35. Bugarčić, Ž. D., Petrović, B. & Zangrando, E. Kinetics and mechanism of the complex formation of  $[\text{Pd}(\text{NNN})\text{Cl}]^+$  with pyridines in methanol: synthesis and crystal structure of  $[\text{Pd}(\text{terpy})(\text{py})](\text{ClO}_4)_2$ . *Inorg. Chim. Acta* **357**, 2650-2656, (2004).

## 5. On the electrical properties of perylenecarboxydiimide-based nanoarchitectures

### 5.1. Introduction

Several efforts have recently been made towards the downscaling of organic thin film transistors in terms of thickness of the semiconductor layer,<sup>1-4</sup> the dielectric<sup>5</sup> and the lateral dimension (source – drain distance).<sup>6,7</sup> Shrinking the dimension of the single components in fact may lead to the improvement of the device performance, such as larger carrier mobilities, increased device speed, lower power dissipation, and enhanced  $I_{on}/I_{off}$  ratios.<sup>8</sup> For applications such as sensing for example, where changes in the OFET electrical characteristics are expected due to physical/chemical interactions between the semiconductor and the analyte, a few nanometers thick active layer with high mobility, in a bottom contact/bottom gate configuration is desired.<sup>9</sup> Langmuir techniques are very useful to obtain ordered monomolecular-thin films and had allowed both organic functional polymers<sup>10</sup> and small molecules<sup>11</sup> to be assembled both for technological applications<sup>12</sup> and as model systems for fundamental studies of charge transport.<sup>13,14</sup>

Among conjugated organic small molecules, perylene diimide derivatives have been largely employed in organic electronics as n-type semiconductor in organic thin film transistors<sup>15</sup> and as acceptors in organic solar cells<sup>16</sup> because they exhibit relatively high electron affinities, high electron mobilities, and excellent chemical, thermal, and photochemical stabilities.<sup>17</sup> In particular, N,N'-1H,1H-perfluorobutyl dicyanoperylenecarboxydiimide (PDIF-CN<sub>2</sub>) has been largely investigated because of its excellent stability in air and high electron transport properties.<sup>18</sup> In fact the addition of highly

electron-withdrawing core substituents, lowers the energies of the LUMO below that of most atmospheric trapping levels.<sup>15</sup> Single crystals of PDIF-CN<sub>2</sub> grown by sublimation had revealed a crystal structure composed by a slightly twisted polycyclic core (torsion angle of about 58°) with slip-stacked face-to-face molecular packing and an interplanar spacing of 3.40 Å.<sup>18</sup> This motif, allowing considerable intermolecular π–π overlap, is considered responsible for the excellent charge-transport properties. The highest mobilities reported for single crystals are indeed of 1·6 cm<sup>2</sup>·V<sup>-1</sup>·s<sup>-1</sup>.<sup>19-21</sup> PDIF-CN<sub>2</sub>-based OFETs where the semiconductor was thermally evaporated in polycrystalline films reached mobilities of 0.5 cm<sup>2</sup>·V<sup>-1</sup>·s<sup>-1</sup>,<sup>22</sup> while 0.15 cm<sup>2</sup>·V<sup>-1</sup>·s<sup>-1</sup> was the mobility measured in vacuum in a bottom-gate/bottom-contact transistor, after thermal treatment of the spin-coated films.<sup>23</sup> Electron mobilities of ~0.08 cm<sup>2</sup>·V<sup>-1</sup>·s<sup>-1</sup> were anyway still measured after 20 days of continuous exposure to air.<sup>23</sup> The edge-on orientation of the PDIF-CN<sub>2</sub> molecules with respect to the substrate was demonstrated to be the reason of the enhanced FETs performance after the annealing treatment.<sup>23,24</sup>

Herein we report on monomolecular thin layers of PDIF-CN<sub>2</sub> fabricated by the Langmuir-Blodgett technique and on nanoscopic ultrathin 1D structures obtained by its post-deposition thermal treatment. The investigation of the electrical properties of these nanoarchitectures is carried out at the nanoscale and at the microscale in field-effect transistor (FET) devices.

## 5.2. Experimental details

N,N'-1H,1H-perfluorobutyl dicyanoperylenecarboxydiimide PDIF-CN<sub>2</sub> (N1100 Polyera ActivInk®) was solubilized in chloroform (Sigma Aldrich, 99.9%) at a concentration of 1 mg/mL. For optical characterization in solution a concentration 1·10<sup>-5</sup> M was used.

Langmuir-Blodgett experiments were carried out in a KSV minitrough apparatus by employing ultra-pure MilliQ water with a resistivity of 18 MΩ·cm as a subphase. Drops of the PDIF-CN<sub>2</sub> solution were randomly spread over the aqueous subphase. After few minutes to evaporate the solvent, the floating films were linearly compressed by the two mobile barriers at a rate of 5 mm/min. Surface-pressure versus molecular-area isotherms were recorded by film balance measurement (Wilhelmy plate method). The ultrathin film transfers were performed onto the different substrates by an upstroke operation at speed of 5 mm/min.

Spin coated (SC) films were fabricated at speed of 1500 rpm from a solution 2 mg/mL in chloroform.

Micrometric fibers were obtained by SIP method, by dropping 50 µL of solution 2 mg/mL in chloroform in 950 µL of methanol, as reported in<sup>25</sup>.

The films were dried in vacuum oven at 30°C and stored in nitrogen atmosphere before characterization. Post-deposition treatments were performed by thermal annealing at 110°C in ambient atmosphere.

For optical measurements, absorption and fluorescence spectra, the films were transferred on glass substrates, which were washed in acetone and isopropanol prior to use. For C-AFM nanojunction fabrication the ultrathin films were transferred on epitaxial gold (111) substrates (Georg Albert PVD, Germany).

Bottom-gate/bottom-contact small channels (2.5 to 20  $\mu\text{m}$ , *short-L*) transistor devices were fabricated by transferring the films on  $\text{Si}^{n++}/\text{SiO}_2$  substrates with patterned interdigitated gold electrodes (Fraunhofer Institute). Bottom gate/bottom contact long channels (60 to 120  $\mu\text{m}$ , *long-L*) transistors were fabricated on  $\text{Si}^{n++}/\text{SiO}_2$  substrates (Fraunhofer Institute) on which 30 nm thick interdigitated gold electrodes were thermally evaporated through a shadow mask. All the substrates used for transistors fabrications were cleaned by subsequent ultrasonication bath in acetone and isopropanol prior to use.

GIXRD and XRR measurements were performed at the ESRF in Grenoble. The LB film for these characterizations were prepared on  $\text{Si}^{n++}/\text{SiO}_2$  substrates (Fraunhofer Institute).

Absorption spectra of films were recorded on a JASCO spectrophotometer - V670. For the fluorescence spectra a spectrofluorimeter Fluorolog 3 by Jobin-Yvon in a front-face configuration was used to minimize the self-absorption (inner filter effect).

AFM and C-AFM characterizations were carried out in a Multimode V (Veeco) microscope equipped with a Nanoscope V controller. Commercial silicon cantilevers with a nominal spring constant of 40 N/m were used for morphological characterization in tapping mode while Pt/Ir coated silicon probes with a nominal spring constant of 0.2 N/m were used to perform imaging in contact mode and local current-voltage measurements by applying a constant load force of 2 nN. All the measurements were performed under nitrogen atmosphere, with a humidity level below 5%.

A Keithley 2636A source meter was employed for the OTFTs characterization in controlled atmosphere ( $\text{O}_2$  and  $\text{H}_2\text{O}$  content below 10 ppm and 2 ppm, respectively).

### 5.3. Assembly and structural characterization

The Figure 5.1b shows the surface pressure (SP) vs. mean molecular area (Mma) curve obtained by compressing by the two mobile barriers the PDIF-CN<sub>2</sub> molecules spread on the water

subphase by a solution in chloroform. The curve shows a clear transition from an expanded phase to a condensed one.<sup>26</sup>

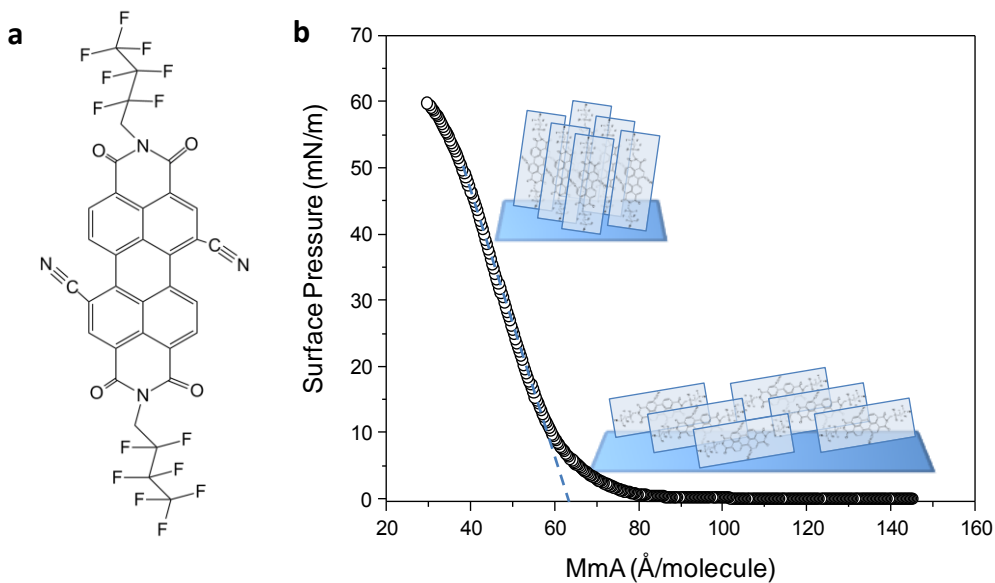


**Figure 5.1:** Molecular structure of the PDIF-CN<sub>2</sub> molecule employed in this study (a) and surface pressure vs. mean molecular area curve relative to the film formation at the air-water interface (b). The scheme in the inset shows the possible molecular arrangement at the limit area and at high surface pressure.

By considering a molecular length of 22.8 Å<sup>18</sup> and a width of around 10 Å (as estimated by ChemDraw), a face on conformation of the molecules in the condensed phase can be easily ruled out. An edge on conformation would have instead a MmA of 31 Å<sup>2</sup> and 78 Å<sup>2</sup> if the molecular long axis is respectively perpendicular or parallel to the surface, if considering a π-π spacing of 3.4 Å<sup>18</sup>. Interestingly, the limiting area at zero pressure (63 Å<sup>2</sup>) would correspond to a conformation where the molecules in the π-π stack direction are not perfectly facing one to another but slightly tilted, similarly to what happens in single crystals where the length of the unit cell in the *c* direction is 18.8 Å (18.8 Å × 3.4 = 64 Å<sup>2</sup>).<sup>18</sup> It seems then more likely that the molecules pack in a tilted manner. Moreover, the SP vs. Mma curves are not steep but they rise gradually suggesting that the molecules are further tilting on compression.<sup>26,27</sup>

The transfer of the monolayer on solid substrates was performed at 20 and 45 mN/m by an upstroke operation. The area per molecule at the transfer pressure was 56 Å<sup>2</sup> and 43 Å<sup>2</sup>, respectively, again indicating tilting of the molecules on the surface plane upon compression. It is noteworthy that the area at which the film starts to collapse is slightly less than 40 Å<sup>2</sup>, which resembles the area of the

single crystal unit cell in the *ab* plane ( $a=5.2 \times b=7.6$ ),<sup>18</sup> indicating that the molecule before collapsing are standing on the water with their long axis almost perpendicular to the surface.

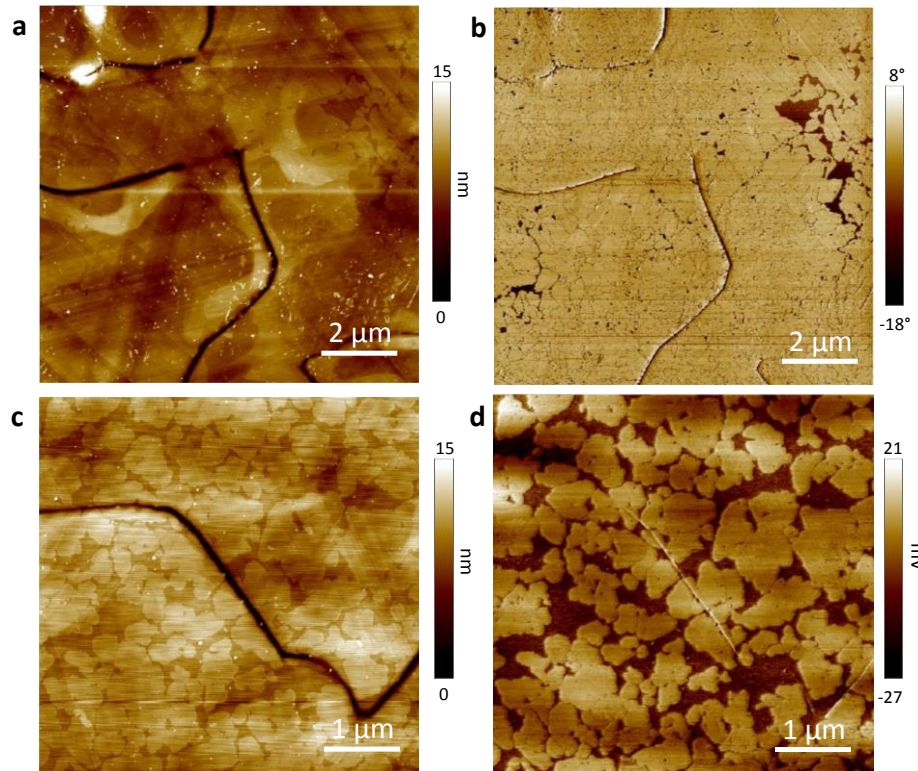


**Figure 5.2:** AFM images of the PDIF-CN<sub>2</sub> film deposited on gold at 20 mN/m. On the area showed in (a) (topography) and (b) (phase) an 86% coverage was estimated. On the area showed in (c) (topography) and (d) (friction) the coverage was estimated 77%.

The morphology of the film deposited on gold substrates is shown in Figure 5.2. From the height pictures (a) and (c) the morphology of the gold appears very clear as formed by large grains with terraces; the monolayer instead is barely visible, especially when the coverage is very high as in the case of figures (a, b). In such cases, phase images (b) (in tapping mode operation) or friction images (d) (in contact mode operation) are extremely important to properly visualize the ultrathin films. These images allowed for the estimation of the surface coverage through a thresholding method. The coverage was estimated to be higher than 80%. The film morphology resembles that of a typical LB monolayer film formed by islands aggregated upon compression at the air-water interface. The thickness of the film estimated by AFM was around 1.5 nm for the film transferred at 20 mN/m and around 2 nm for the film transferred at 45 mN/m.

We characterized the monolayer deposited at 45 mN/m by X-ray reflectivity and GIXRD. The results are reported in Figure 5.3

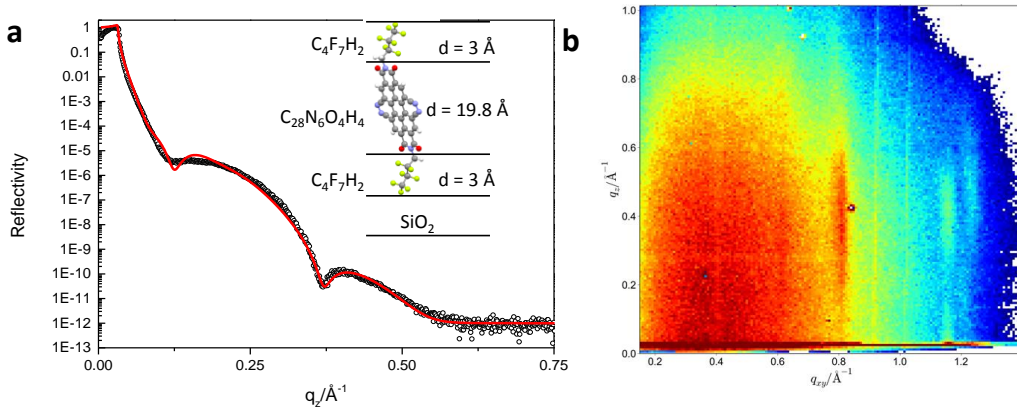


**Figure 5.3:** a) X-ray reflectivity (XRR) of the monolayer deposited on silicon dioxide. The solid red line is the fit to the experimental data. The inset shows the chemical structure of the molecule and the thicknesses obtained from the fit. b) GIXRD pattern showing Bragg rods.

X-ray reflectivity data were fitted with a three-layers model of three different electron densities, similarly to what was reported for self-assembled monolayer film.<sup>1</sup> From the fitted curve a layer thickness of 25.8 Å is deduced, which is consistent with the length of a single molecule augmented by about a 3 Å length referred to van der Waals radii of fluorine atoms. From this result a fully upright standing monolayer geometry is deduced which is consistent with the mean molecular area value at the transfer pressure.

The GIXRD showed the occurrence of Bragg rods in the diffraction pattern, as an evidence of a crystalline structure. The Bragg rods are normally due to the absence of periodicity perpendicular to the ordered layer, thus indicating that the LB film is a homogeneous, smooth monolayer film.

From GIXRD it is also possible to deduce the tilt of the molecular backbone with respect to the sample normal. The rods have enhanced intensity at about  $q_z = 0.4 \text{ \AA}^{-1}$ , which points towards an inclination of the molecular backbone, as expected for this kind of molecule. From its coordinates of maximum intensity,  $q_z = 0.4 \text{ \AA}^{-1}$  and  $q_{xy} = 0.8 \text{ \AA}^{-1}$ , we can estimate for the rods a tilt angle of 63°, which is in the range of what we would expect for the molecule if upright standing. Since the angle between the backbone and the end-to-end axis of the molecule is around 25°, the total tilt angle is estimated to be around 90°.

The morphology of the LB monolayer transferred on gold at 45 mN/m is totally modified after post-deposition thermal annealing. The thermal treatment indeed allows the molecules in the film to

rearrange and move on the surface, resulting in the formation of ultrathin nanocrystals exhibiting 1D well definite layered structures, as shown in Figure 5.4.

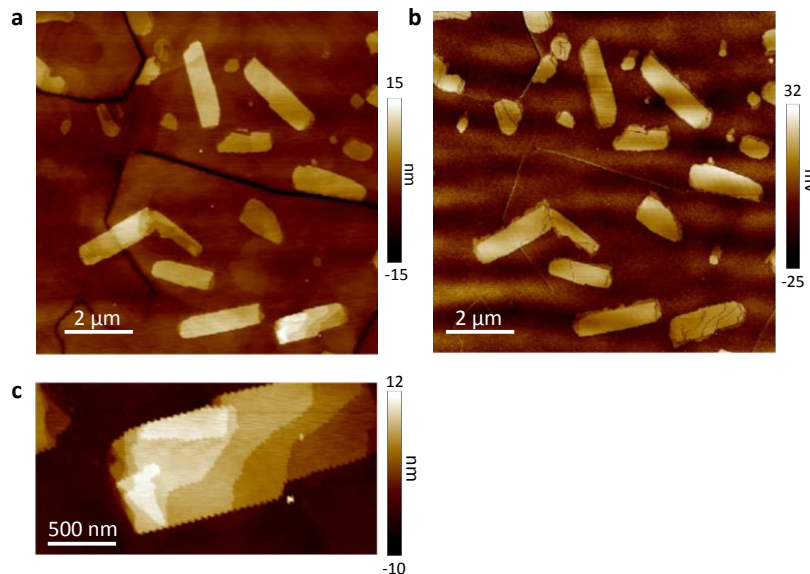


**Figure 5.4:** AFM images showing the morphology of the LB film transferred at 45 mN/m on gold substrates and annealed at 110°C for 2h. (a) and (c) are topography images performed in contact mode, (b) is a friction image.

From statistical analysis on large area images we evaluated an average width of  $0.93 \pm 0.33$  μm, an average length of  $3.01 \pm 1.98$  μm and an average thickness  $6.8 \pm 3.1$  nm.

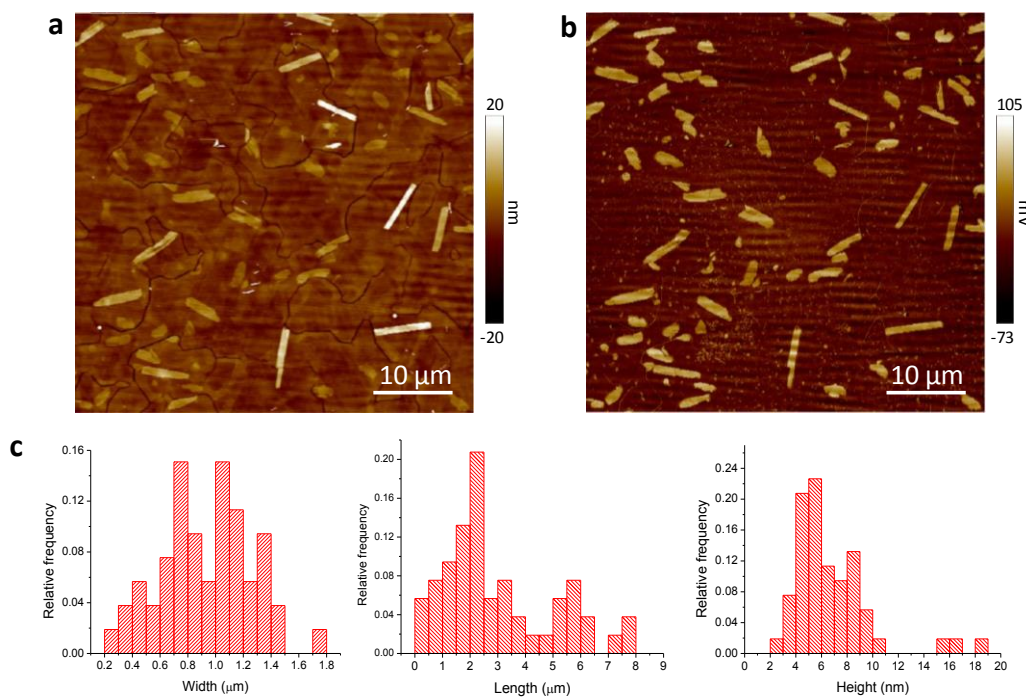


**Figure 5.5:** Statistical analysis of the size of the ultrathin crystals. The AFM images are performed in contact mode and show the topography (a) and the friction image (b) on a large (50x50 μm) area.

To get insights into the molecular packing we carried out compared spectroscopic and morphological analysis on the LB films as deposited and thermally annealed and we compared them with thin films prepared by spin-coating (SC) and films of microscopic fibers obtained by solvent induced precipitation (SIP) and drop cast on glass substrates, for which structural characterizations have already been reported in literature.<sup>23-25,28</sup> Figure 5.6 a and b show the normalized absorption (a) and emission (b) spectra of the different films on glass compared also to the isolated molecule in  $\text{CHCl}_3$  solution. All the films show a red-shift in the absorbance and photoluminescence (PL) emission maxima. These data indicated not only strong solid-state intermolecular interactions but also the presence of J-aggregates among the PDIF-CN<sub>2</sub> molecules.

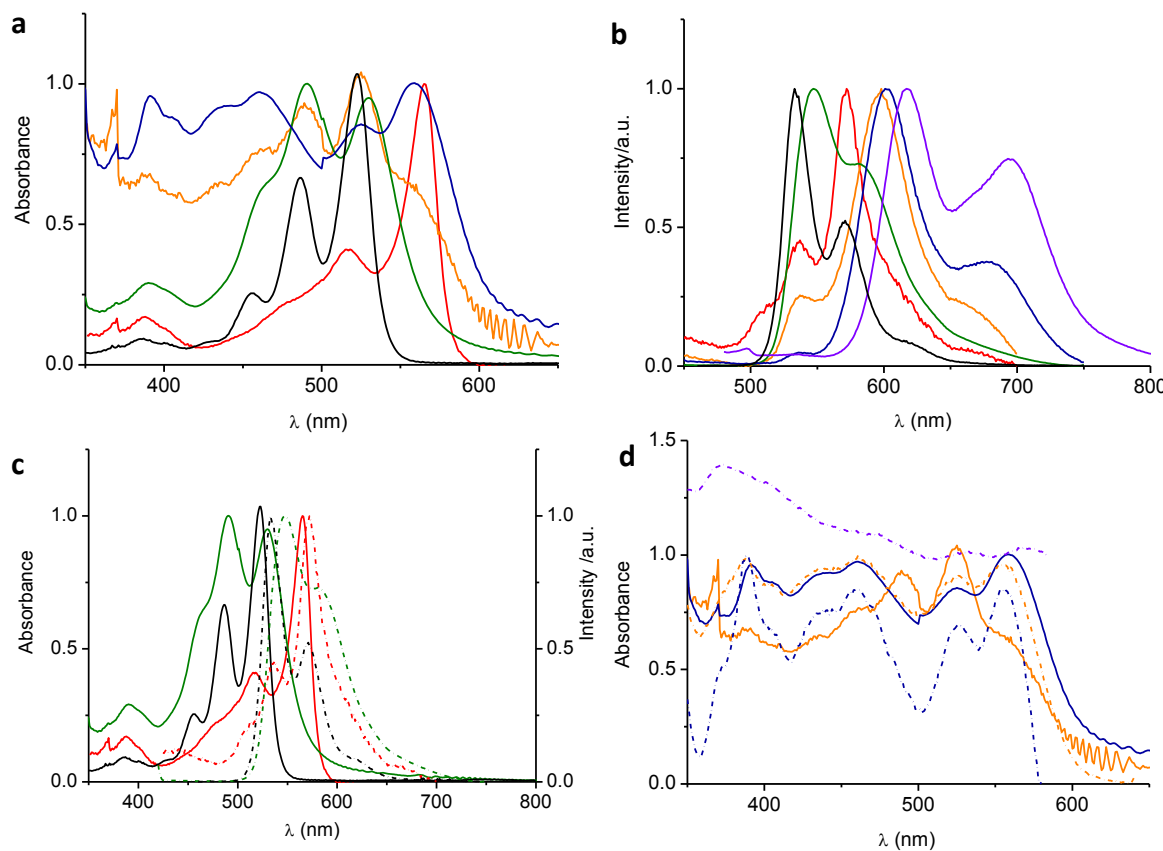


**Figure 5.6:** Normalized absorption (a) and PL at  $\lambda_{\text{exc}} = 395 \text{ nm}$  (b) spectra of LB film as deposited (red) and after annealing (blue), SC film as deposited (green) and after annealing (orange) and SIP fibers (violet), as well as the PDIF-CN<sub>2</sub> spectra in  $1 \times 10^{-5} \text{ M}$  chloroform solution (black). In (c) the absorbance (line) and PL  $\lambda_{\text{exc}} = 395 \text{ nm}$  (dashed line) of the LB (red) and SC (green) films are compared. In (d) the absorbance (line) and excitation (dashed line) spectra of the LB film after annealing (orange,  $\lambda_{\text{em}} = 650 \text{ nm}$ ), SC film after annealing (blue,  $\lambda_{\text{em}} = 650 \text{ nm}$ ) and SIP fibers (violet,  $\lambda_{\text{em}} = 700 \text{ nm}$ ).

In particular, the predominant narrow red-shifted 0-0 line absorption spectra (at 565 nm vs. 520 nm of the solution) and a quite null Stokes shift in the LB film (see Figure 5.6c) confirm the high degree of structural order in J-type aggregates of this sample.<sup>29</sup>

This structural order is lost in the film fabricated by spin-coating (SC); this latter one, in fact, shows a smaller red shift and a broader absorbance and emission band than the LB one (see Figure 5.6c). The photophysical properties of the SC film look pretty similar to the molecules in solution. It is known in fact that in spin coated films the molecules adopt random orientations because the fast evaporation reduces the ability of the molecule to self-organize on the substrate.<sup>30</sup> This is also confirmed by the AFM images (Figure 5.7a) showing a morphology consisting of small grains, with no evidence of a definite structural order.

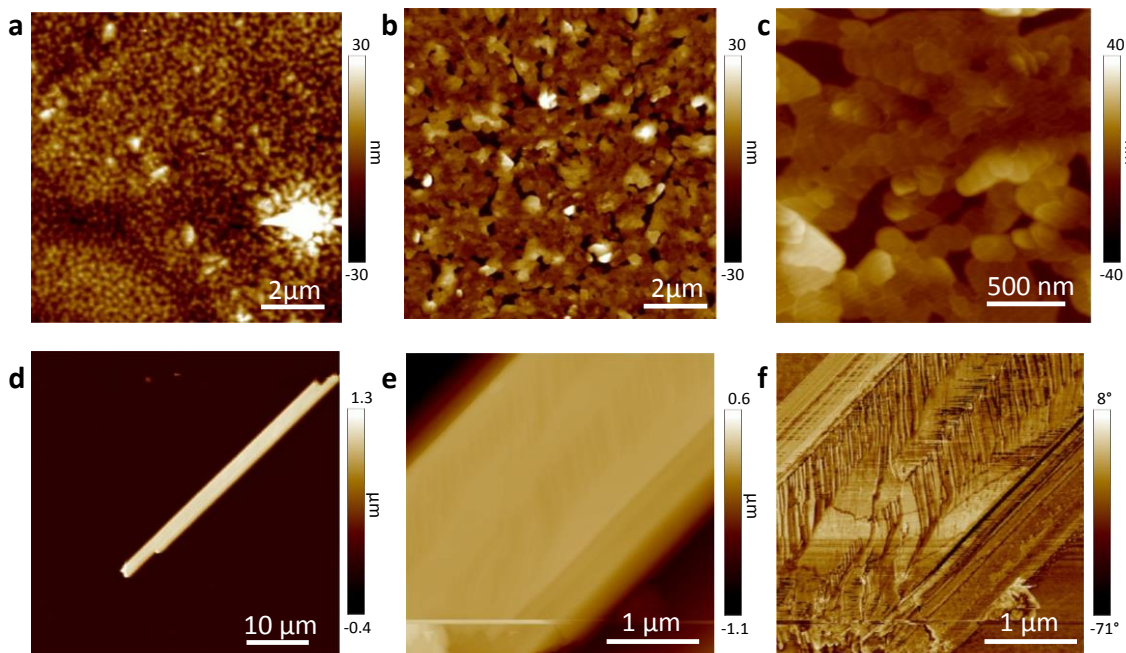


**Figure 5.7:** AFM topography images of the SC film before (a) and after (b, c) thermal annealing and of a crystal obtained by SIP (d, e). The figure in (e) is a zoom in on the surface of the crystal whose phase image highlighting the presence of a layered structure is reported in (f).

Interestingly, both the LB film and the SC one reach the same kind of supra-molecular order after thermal annealing, testified by the very good matching of their absorption, excitation (Figure 5.6d) and PL spectra. Moreover, we observe higher Stokes shifts with respect to the films as deposited, and the presence of the excimer emissions (at 680 nm) which indicate a higher degree of cofacial arrangement of the molecules in the film. The excimer states indeed are characterized by broad and featureless emission and are determined by excited state delocalized over two or more molecules arranged cofacially.

The greater red-shift and the stronger excimer emission is showed in the SIP fibers spectra (AFM images are shown in Figure 5.7d-f), whose structures has been demonstrated to be of single crystalline nature.<sup>25</sup> Noteworthy, the photophysical features of the LB and SC annealed films are very similar to the SIP ones and these data are in agreement with the increased  $\pi$ - $\pi$  overlap after thermal annealing.

Thermal annealing has been in fact demonstrated to produce an efficient structural reorganization of spin-coated films of PDIF-CN<sub>2</sub> inducing the molecules to orient in an tilted upright configuration so that layered films having steps of about 2 nm were observed.<sup>24</sup> We indeed observed the same behavior as shown also by the AFM images (Figure 5.7b, c) where a clear morphology change can be seen caused by the annealing process, and the occurring of layered structures is well visible (see the small scale image in Figure 5.7c). The effect of thermal annealing on the LB films is similar: once the films are annealed, molecules organize in almost upright orientation, as corroborated also by the height of about 2 nm of the planes steps (see Figure 5.4). In this configuration the  $\pi$ - $\pi$  overlap is maximized and the spectroscopical properties are similar to those of the single crystal.

## 5.4. Vertical charge transport in the LB monolayer

The electrical characterizations performed by C-AFM of the monolayer deposited on gold at SP of 20 and 45 mN/m are reported in Figure 5.8 (a-c) and (d-f), respectively. The pictures in (a) shows the current map corresponding to the film deposited at 20 mN/m (see the morphology in Figure 5.2c) and obtained by biasing the gold electrode at 100 mV. The white areas correspond to saturated current signal on the gold substrate, the bright brown areas correspond to current attenuated by the monolayer film and the darker brown regions to areas where no current is detected. The image in (d) shows the topography of the monolayer deposited at 45 mN/m. The curves correspond to the average current-voltage characteristics obtained from around 170 local measurements on different points of the films, after discarding both the zero-current and the saturated plots, originated respectively from false contacts or direct contact of the C-AFM tip with the gold substrate. The ratios of good junctions with respect to the total ones were about 60% and 80% for the two samples, respectively. The histograms show the distribution of the resistance values calculated from the slopes of each I-V curve in the low bias region (-100 mV to 100 mV). The average resistances were estimated  $17.6 \pm 0.3$  G $\Omega$  and  $33.0 \pm 0.6$  G $\Omega$  for the films prepared at SP of 20 mN/m and 45 mN/m, respectively. These values are one order of magnitude higher than the ones typically measured on molecular monolayer chemically linked to metal substrates.<sup>31,32</sup> The slightly higher resistance obtained for the film deposited at higher surface

pressure further corroborate our hypothesis of increased tilting angle induced by the barrier compression at the air-water interface.

Another feature of the experimental I-V curves is a clear asymmetry, which shows a favored electron injection from the AFM tip (positively biased Au substrate). The rectification ratio, defined as (current at 0.4 V)/(current at -0.4 V) is about 4.

Molecular rectification has been observed in junctions based on single-molecules or few molecules in parallel, chemisorbed or physisorbed to metal substrates, which has been ascribed to different mechanisms.<sup>33</sup> Some of these mechanisms can be easily excluded in our case. The Aviram-Ratner unimolecular diode mechanism, for example, requires the molecule to be composed by a donor and an acceptor unit separated by a sigma bridge.<sup>34,35</sup> Rectification is also expected if the part of the molecule whose molecular orbital must be accessed during conduction is placed asymmetrically within a metal/molecule/metal sandwich, for example because of the presence of one long alkyl tail.<sup>36,37</sup> In our case the molecule is symmetric and we expect both the HOMO and LUMO levels to be spread over the whole perylene core.<sup>38</sup> We neither expect the molecule of being closer to one electrode with respect to the other, as found in some STM nanojunctions.<sup>39</sup>

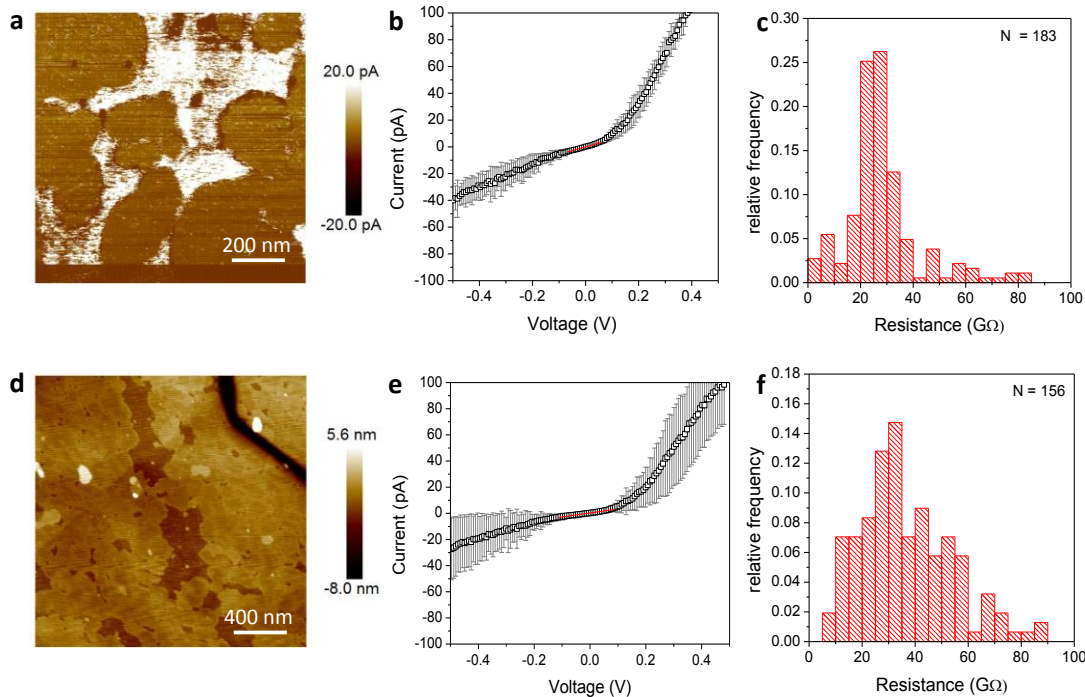
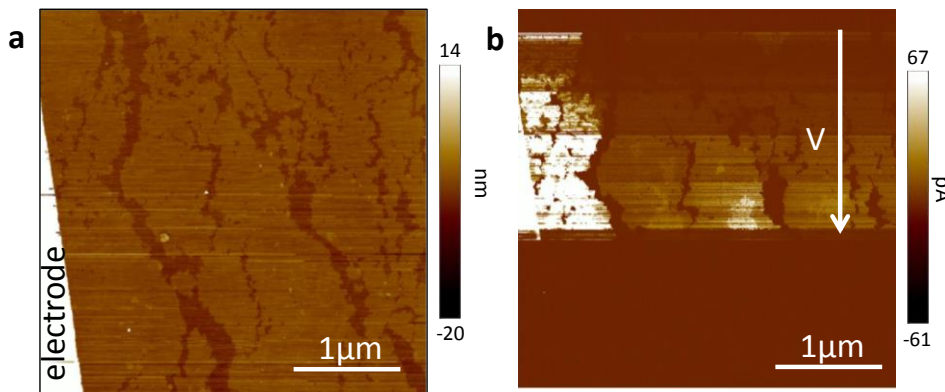


**Figure 5.8:** Electrical characterization performed by C-AFM of the monolayer deposited on gold at SP of 20mN/m (a-c) and 45 mN/m (d-f): (a) Current map at 100 mV bias. (d) Topography image. (b, e) Average I-V curves based on 183 and 156 working nanojunctions, respectively; the grey areas represent the standard error of the average. (c, f) Histograms of the resistance values measured from the slope of the single I-V curves in the low bias range (marked in red in Figs. b, e).

Asymmetric behavior due to Shottky barriers at the electrodes interfaces was also reported, depending on the mismatch between the molecular HOMO or LUMO and the substrate Fermi level.<sup>33,40-42</sup> PDIF-CN<sub>2</sub> is an n-type semiconductor whose LUMO level (~4.5 eV)<sup>15</sup> is close to the work function of both the Au (~4.8 - 5 eV) and Pt/Ir (~5 - 5.2 eV)<sup>43</sup> electrodes, therefore we do not expect the asymmetry to be due to a simple mismatch. The energy barrier is known to be sensitive to the detailed structure and chemical nature of the metal/organic interface and to interfacial dipole formation.<sup>44</sup> Similarly to what was observed<sup>45</sup> on a monolayer of a pentathiophene derivative on a SiO<sub>2</sub>/Si<sup>+</sup> substrate probed by Pt C-AFM tip, we could expect then the asymmetry to be attributed to pinning of the molecular orbitals to the Fermi level of the bottom gold electrode, as it may be also corroborated by observations on similar PDI molecules on macroscopic junctions.<sup>46</sup> However, an enhanced carrier injection from the AFM probe was also explained as possibly due to the high field associated with the probe point contact, resulting from geometrical effects.<sup>47</sup>

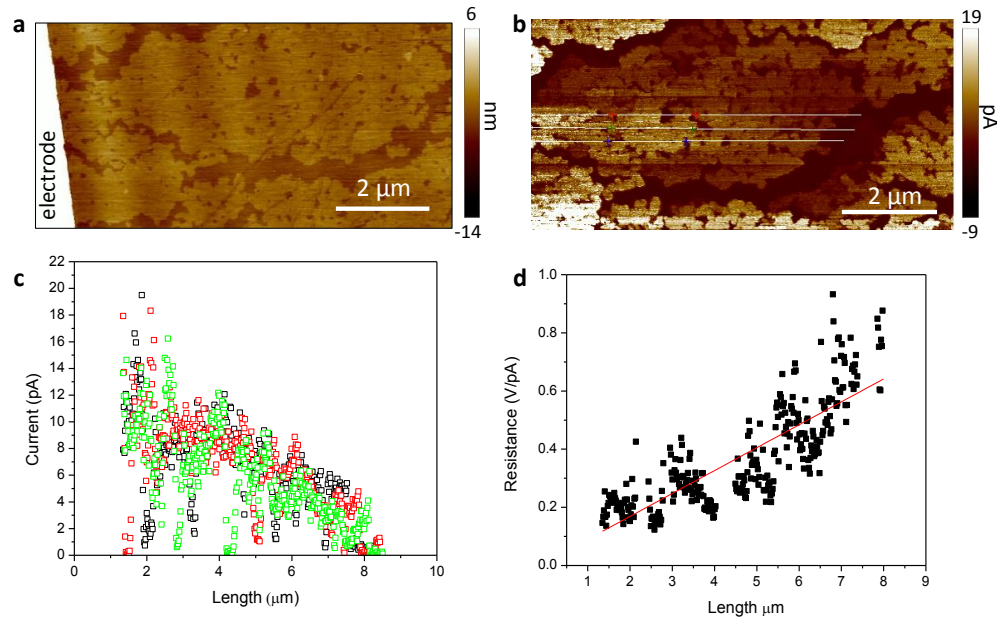
## 5.5. Horizontal charge transport in the LB monolayer

Figure 5.9 shows the morphology of the monolayer deposited at 45 mN/m on a Si<sup>n++</sup>/SiO<sub>2</sub> substrate with pre-patterned gold electrodes. The film is characterized by directional fractures probably due to instabilities occurring in the transfer process. The corresponding C-AFM current map obtained by varying the bias on the gold electrode of few Volts is shown in Figure 5.9b. The current signal is close to saturation in the regions which are directly in contact with the electrode, and it drops immediately at the right of the first fracture/boundary. However, current is detected up to several μm away from the electrode and it is increasing as bias is increased, indicating that efficient percolation paths for charges are present throughout the whole film in the channel.



**Figure 5.9:** Topography (a) image of a monolayer film deposited on a silicon oxide substrate having gold electrodes and corresponding current map (b) obtained by biasing the electrode on the left of the scan with an increasing bias as marked by the white arrow.

To deeper visualize the lateral charge transport in the film we focused on a grain of the film directly connected to the gold electrode, as the one we show in Figure 5.10. We registered an image of the morphology at no bias, and then we zoomed in an area sufficiently far away ( $\sim 1 \mu\text{m}$ ) from the electrode to avoid instabilities and spikes due to the high current values when applying a bias. From the current map we could observe a scaling of the current with the distance from the electrode. It was shown that C-AFM can also be used to evaluate the contact resistance of molecular structures connected to one electrode.<sup>48</sup> To apply this method to our case we calculated the total resistance by the current profiles on different lines as marked in Figure 5.10b and we plotted it as a function of the distance from the gold. From a linear fitting of this curves we extrapolated resistances at zero length of 10 - 100 G $\Omega$ , relative to the contact resistance of the gold/monolayer and monolayer/AFM probe junctions.



**Figure 5.10:** AFM morphology of a region of the monolayer where a grain almost insulated is present due to the surrounding fracture/defects of the film. b) Current map at 2 V applied to the gold electrode, which is visible on the image in a). c) Current profiles along the marked lines in (b). d) Calculated total resistance as a function of L.

To measure the in-plane charge carrier mobility of the monolayer we fabricated TFT devices in bottom-gate/bottom-contact configurations and with different channel lengths. In Figure 5.11 the output and transfer characteristics of two representative devices are reported. Figure (a) and (b) refers to a device with a 5 μm long channel. Although the performances of this device are not bad, for the case of a monolayer transistor, a clear deviation from linearity is visible in the output curves at low

bias. The same non-linear output curves were obtained for short-channel transistors (2.5 to 20  $\mu\text{m}$ , *short-L*). This feature was not present instead in the long channel transistors (60 to 120  $\mu\text{m}$ , *long-L*) which displayed Ohmic behavior at low bias, as shown for a channel of 60  $\mu\text{m}$  in Figure (c) and (d).

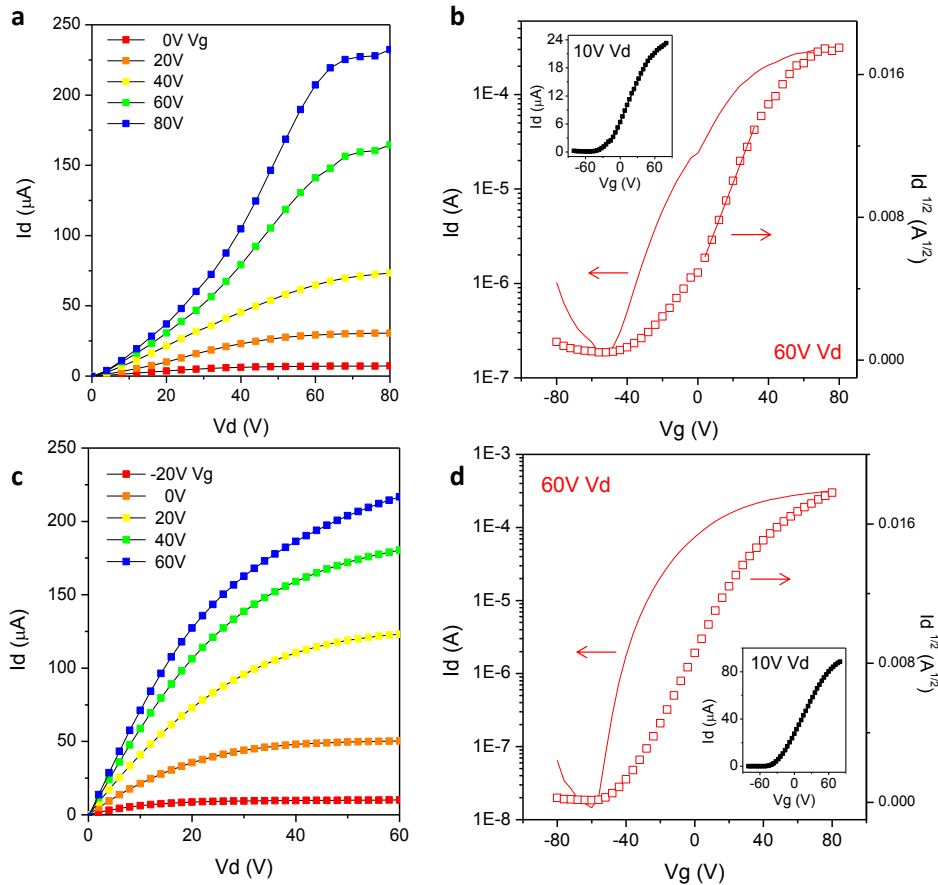


**Figure 5.11:** Output (a, c) and transfer (b, d) characteristics of representative device having 5  $\mu\text{m}$  (a, b) and 60  $\mu\text{m}$  (c, d) channel lengths.

The highest contribution of the contact resistance in devices with short channel lengths is a known issue in organic electronics. Below determinate lengths the contacts can no more supply for the charge demand of the channel and the device become contact limited.<sup>49</sup> Contact limited devices can be recognized by the non-linear S-shaped output curves at low drain bias and mobilities extracted in the linear regime much lower than the ones extracted in the saturation regime. For the devices of Figure 5.11 for example the linear mobilities for the 5  $\mu\text{m}$  and 60  $\mu\text{m}$  channel devices are respectively  $9.7 \cdot 10^{-4}$   $\text{cm}^2 \cdot \text{V}^{-1} \cdot \text{s}^{-1}$  and  $3.8 \cdot 10^{-2}$   $\text{cm}^2 \cdot \text{V}^{-1} \cdot \text{s}^{-1}$ , while the saturation mobilities are  $4.5 \cdot 10^{-3}$   $\text{cm}^2 \cdot \text{V}^{-1} \cdot \text{s}^{-1}$ , and  $3.1 \cdot 10^{-2}$

$\text{cm}^2 \cdot \text{V}^{-1} \cdot \text{s}^{-1}$ , respectively. The average parameters extracted by *short-* and *long-L* devices are summarized in Figure 5.12.

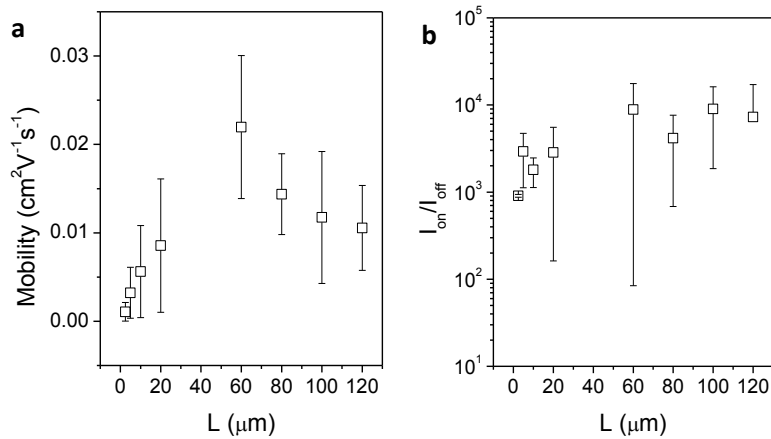


**Figure 5.12:** Average mobilities (a) and  $I_{\text{on}}/I_{\text{off}}$  ratio (c) for transistors with different channel lengths.

In the *short-L* devices the field-effect mobility lowers with the decreasing channel lenght spanning around one order of magnitude, as again one would expect in contact limited devices.<sup>49</sup> A dependence of the performances on the transfer direction of the film with respect to the electrode orientation has also been remarked, as shown in Figure 5.13 for a single chip with 16 devices of different channel lengths. In particular, since the defects of the films are more pronounced in one direction with respect to the other, because they come from instabilities during the film transfer from the air/water interface, we expect the percolation paths for charges between source and drain to be affected by the orientation of these defects within the channel. Indeed, by comparing two by two the devices with the same channel length and with the same height position during the transfer, in most of the cases the highest performance, in terms of mobility are obtained when the source and drain electrodes are parallel to the transfer direction, as depicted in Figure 5.13b.

In *long-L* devices the films were transferred with the electrodes perpendicular to the transfer direction. The average mobility in these devices was  $(1.5 \pm 0.7) \cdot 10^{-2} \text{ cm}^2 \cdot \text{V}^{-1} \cdot \text{s}^{-1}$ . The best performing device was a  $60 \mu\text{m}$  long channel device showing saturated mobility of  $3.1 \cdot 10^{-2} \text{ cm}^2 \cdot \text{V}^{-1} \cdot \text{s}^{-1}$ , a threshold voltage  $V_t$  of  $-43 \text{ V}$  and an  $I_{\text{on}}/I_{\text{off}}$  ratio of  $10^4$ . The large threshold voltages may be due to doping and/or to dipoles at the interface between bare  $\text{SiO}_2$  and the semiconductor,<sup>50</sup> as found also in other monolayer transistors.<sup>12</sup>

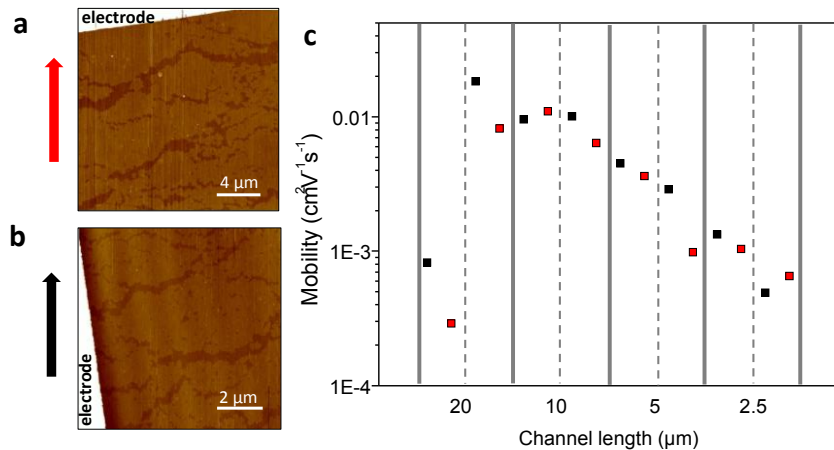


**Figure 5.13:** AFM images showing the morphology of the monolayer film when the electrode is perpendicular (a) or parallel (b) with respect to the transfer direction, marked by the arrows. In (c) the mobilities relative to 16 devices of one representative chip are plotted, the red points representing the situation in (a) and the black ones the situation in (b).

The mobilities obtained on our monolayer devices are actually remarkable. A thermal evaporated pentacene monolayer TFT, showed very low saturated current, with a mobility amounted of only  $10^{-5} \text{ cm}^2 \cdot \text{V}^{-1} \cdot \text{s}^{-1}$ .<sup>9</sup> Mobilities of the order of  $10^{-5} \text{ cm}^2 \cdot \text{V}^{-1} \cdot \text{s}^{-1}$  were also obtained on PDI self-assembled monolayer field-effect transistors (SAMFETs).<sup>51</sup> Although mobilities of the order of  $10^{-2} \text{ cm}^2 \cdot \text{V}^{-1} \cdot \text{s}^{-1}$  were obtained for three layers n-type poly((N,N'-bis(2-octyldodecyl)-naphthalene-1,4,5,8-bis(dicarboximide)-2,6-diyl)-alt-5,5'-(2,2'-bithiophene)) (P(NDI2OD-T2) in a top-gate FET architecture, the monolayer of the same polymer showed saturated mobility one order of magnitude lower.<sup>13,14</sup> To the best of our knowledge, comparable values were found only for monomolecular thin layers *p*-channel devices of quinque thiophene (5T) SAMFETs<sup>1</sup> and of 2-octyldodecyl-disubstituted septithiophene monolayers obtained by spin-coating procedures and measured in vacuum.<sup>52</sup> It noteworthy that the authors remarked that in the case of not fully covered SAMFETs, long channel transistors  $>7.5 \mu\text{m}$  did not show any drain current, because of the absence of percolating path connecting the monolayer islands in the channel.<sup>4</sup> Our *long-L* devices instead have excellent performances up to  $120 \mu\text{m}$  channels. Moreover, in the *long-L* devices, where the contact resistances can be neglected, the mobility seems to be almost independent on the channel length. The slight decrease observed going from the  $60 \mu\text{m}$  to the  $120 \mu\text{m}$  long channels can be attributed to the fact that in long channels the effect of the film defects becomes more important in affecting the charge transport,<sup>24</sup> similarly to what happen to incomplete SAMFET,<sup>1,4</sup> where the major contribution to the current was found to come from paths connected perpendicularly between the source and drain electrodes, and the effective percolating paths to decrease with increasing L.

## 5.6. Vertical charge transport in the ultrathin nanocrystals

As already shown in Figure 5.4, after thermal annealing the LB monolayer rearrange forming nanostructures consisting of layers about 1.8 - 2 nm in height. These structures have been demonstrated to have photophysical, thus structural, properties comparable to the ones of thermally annealed spin-coated films and micrometric crystals obtained by SIP. In the following paragraphs the vertical charge transport is investigated at the nanoscale by C-AFM by employing nanojunctions on gold substrates.

Figure 5.14 shows a comparison between the average current-voltage characteristics of the LB monolayer as deposited (a) and one-layer thick planes (1L) of the thin nanocrystals obtained after annealing. The resistance in the low bias range calculated  $33.0 \pm 0.6$  G $\Omega$  for the untreated LB film transferred at 45 mN/m (already shown in Figure 5.8e), becomes  $22.6 \pm 0.4$  G $\Omega$  for an annealed 1L layer. This could be the result of an increased tilting of the molecule after annealing induced by the cofacial  $\pi$ - $\pi$  interaction of the perylene cores.

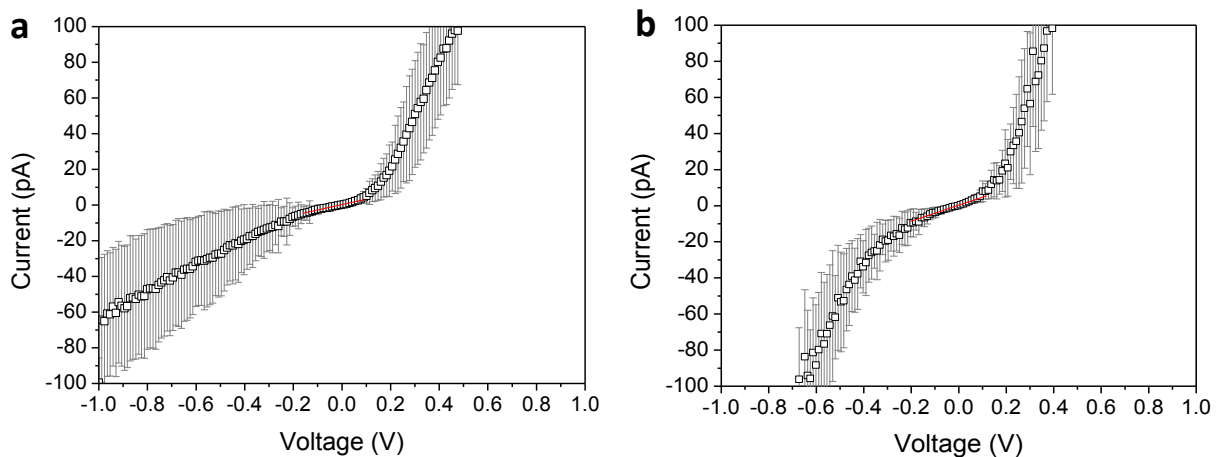


**Figure 5.14:** Average current-voltage characteristics measured on the LB monolayer as deposited (a) and on one-layer thick planes of the thin nanocrystals (b).

An interesting feature of the I-V curve is that in the annealed monomolecular thin layer, though a favored injection from the tip is still visible, this seems less pronounced with respect to the non-annealed film, so that the curves are less asymmetric. We speculate that this could be due to an improved interface after the thermal induced molecular reorganization which in turn results in improved charge injection from the gold electrode.

We also performed local I-V measurements on the different layers of the nanocrystals to investigate the charge transport in the vertical direction. Measurements performed on a representative nanostructure are shown in Figure 5.15 a-d. From the AFM image, steps of about 1.9, 3.6, 5.2 nm are measured which are consistent with 1, 2 and 3 layers (Figure 5.15 a, b).

The average I-V curves measured from 5 to 10 junctions on each layer are reported in Figure 5.15 c and d in a linear and log-lin scale, showing a clear scaling of the current with the number of layers when going from the 1L to the 3L. Moreover, it can be noted that the current is strongly suppressed for negative substrate bias, already in the second layer, and even more for the third. In the low bias regime for the 1L layer it is likely that the transport occurs by tunneling mechanism, and then it changes to an orbital-mediated mechanism at higher bias. In the thicker layers, instead, no current is detected at low bias and it is necessary to overwhelm a barrier to allow charges to be injected from the electrodes; once again the injection from the AFM tip is favored, i.e. a lower voltage is necessary to overcome the barrier than in the case of the gold electrode.

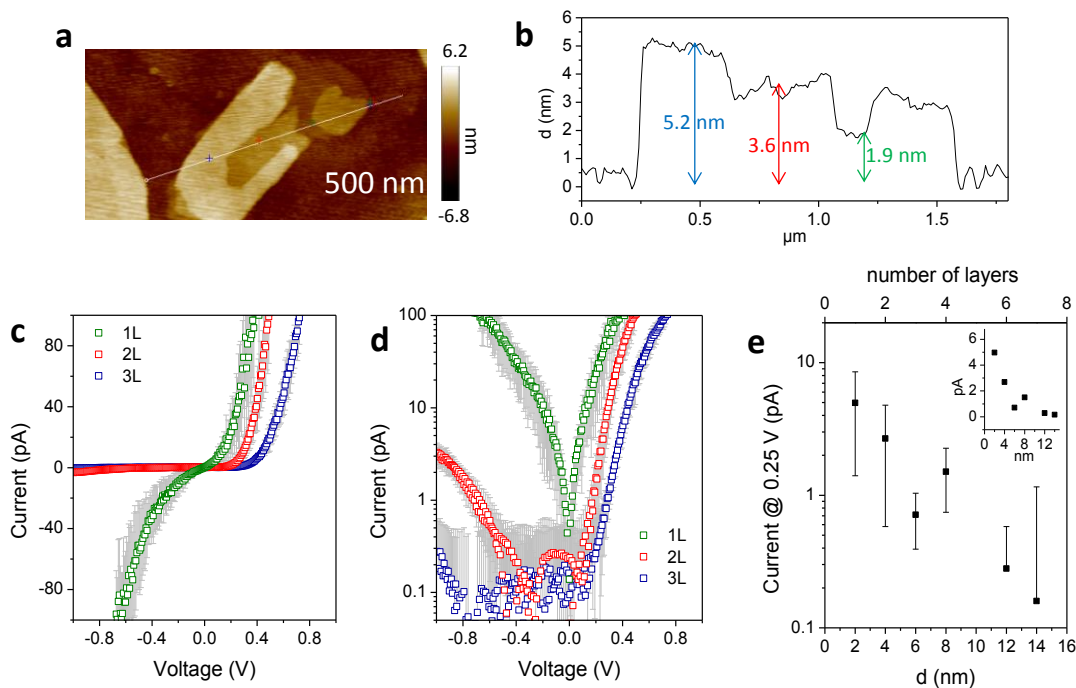


**Figure 5.15:** a) AFM image of a single nanostructure consisting of three layers; b) height profile along the white line marked in a); c) linear plot of the average I-V measurements; d) log-lin plot of the average I-V curves; e) average currents measured at 0.25 V for different layers and crystals as a function of the height distance  $d$  (in the inset the same plot is shown in linear scale).

In Figure 5.15e the average currents measured at a fixed bias (0.25 V) for different layers and different nanocrystals are plotted as a function of the thickness, showing a clear, likely exponential, decay up the 6L structures (12 nm).

To get more insights on the vertical transport on these nanostructures, we focused on a nanocrystal where planes thicker than 1L were present, like the one in Figure 5.16, where it was possible to perform I-V measurements on the layers 2L, 5L and 6L.

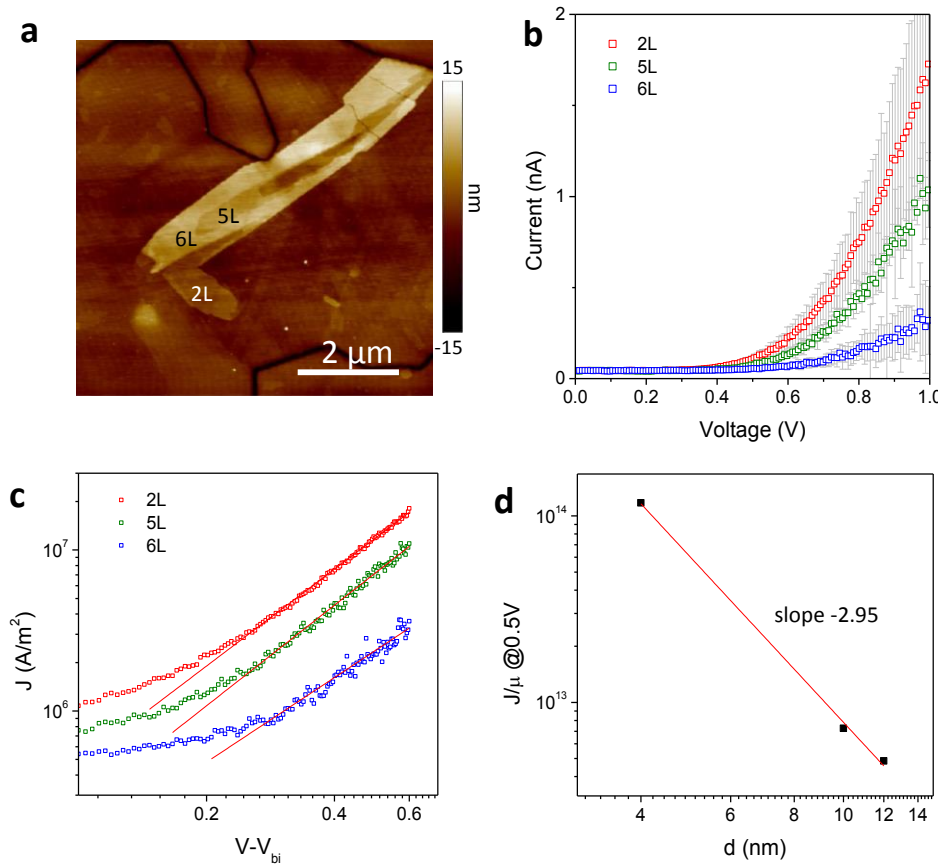


**Figure 5.16:** a) AFM image showing a layered structure where different layers are visible; current-voltage measurements performed on the layers marked as 2L, 5L and 6L are shown in b); c) Fitting to SCLC model); d) Plot showing the dependence on the thickness  $d$ .

Charge mobilities can be extracted in devices built by sandwiching the organic layer between two electrodes in the framework of the space charge limited current (SCLC) model. C-AFM have been also employed to extract local mobilities in organic materials.<sup>53-57</sup> Such behavior corresponds to the current obtained when the number of injected charges reaches a maximum because their electrostatic potential prevents the injection of additional charges.<sup>58,59</sup>

The current density  $J$  scales quadratically with the applied bias  $V$  and it is governed by the Mott-Gurney law:

$$J = \frac{9}{8} \varepsilon_0 \varepsilon_r \mu \frac{V^2}{d^3}$$

where  $\varepsilon_0$  is the permittivity in vacuum and  $\varepsilon_r$  is the dielectric constant of the material,  $\mu$  is the mobility,  $V$  is the voltage drop across the device and  $d$  is the thickness. The I-V curves were then fitted to this law and the details on the fitting are reported in Table 5.1.

**Table 5.1:** Parameters extracted from by fitting of the curves in Figure 5.16c

	$a^\ddagger$	$\mu$ (cm <sup>2</sup> ·V <sup>-1</sup> ·s <sup>-1</sup> )	R <sup>2</sup>
2L	2.00 ± 0.01	1.020 e-3 ± 9 e-6	0.997
5L	2.08 ± 0.03	1.02e-2 ± 2 e-4	0.987
6L	1.75 ± 0.05	4.62e-3 ± 1.7 e-4	0.944

<sup>†</sup> The fitting equation is written as:  $= \frac{9}{8} \varepsilon_0 \varepsilon_r \mu \frac{V^2}{d^3}$ , with  $\varepsilon_r = 3$ .<sup>53,58</sup> R<sup>2</sup> is the coefficient of determination. The contact area is estimated as 10 nm<sup>2</sup> because of the employed load force of 2nN.<sup>32</sup> Voltages were corrected for a built-in potential of 0.4 V estimated from the difference in work function between gold (~4.8 eV) and Pt/Ir (~5.2 eV).<sup>60,61</sup>

The curves showed a quadratic dependence on the voltage and the average charge mobility could be then calculated as  $5.2 \pm 0.1 \cdot 10^{-3}$  cm<sup>2</sup> · V<sup>-1</sup> · s<sup>-1</sup>. The dependence on the thickness was evaluated by plotting the current density relative to the mobility as a function of the thickness, and a dependence of  $J \propto d^{-3}$  was found. This seems to be in contradiction with what was found by Reid et al.<sup>53</sup> who showed a deviation from the  $d^{-3}$  to a  $d^{-1}$  dependence in SCLC measurements performed by C-AFM, caused by geometrical factors. Similar findings were discussed by Woellner et al.<sup>62</sup> who modeled the current-voltage relation in the SCLC regime with geometrical effects included through an enhancement factor dependent on the ratio  $\lambda = \text{tip radius}/\text{sample thickness}$ , for  $\lambda \leq 1$ . However, the thickness of our nanostructures is smaller than the AFM tip radius (20 nm),<sup>32</sup> so that our case approaches the Mott-Gurney law for planar electrodes.

## 5.7. Conclusions

In conclusion, we reported a detailed study on the electrical properties of nanostructures on PDIF-CN<sub>2</sub> obtained by the Langmuir-Blodgett technique and a post-deposition treatment. A monomolecular thin layer could be obtained at the air water interface and transferred onto different solid substrates. At high transfer pressures the molecules adopted a fully upright standing configuration within the film, featuring the photophysical characteristics of J-aggregates with pronounced red-shift in the absorption and photoluminescence maxima, and a quite null Stokes shift. The vertical charge transport probed by C-AFM nanojunctions revealed higher resistance values compared to covalently linked self-assembled monolayers and a clear rectification. A slight dependence on the transfer pressure, hence the molecular tilt angle, was also observed. The in-plane charge transport was probed both by C-AFM in horizontal configuration and by macroscopic field effect transistors, showing electron mobilities as high as  $3.1 \cdot 10^{-2} \text{ cm}^2 \cdot \text{V}^{-1} \cdot \text{s}^{-1}$ , comparable to the ones of the best performing reported *p*-type monolayer transistors.

Post deposition thermal annealing on the LB monolayer favored a reorganization of the molecule on the surface, forming ultrathin layered architectures, having morphological and photophysical properties comparable to thermally annealed films deposited by spin coating and microscopic crystals obtained by solvent induced precipitation, where structural analyses had revealed an upright tilted molecular configuration similar to the one of single crystals, where the cofacial arrangement of the perylene cores are maximized. The out-of-plane charge transport on these nanostructures was also probed by C-AFM and described in the framework of a space charge limited current regime, finding an average mobility of  $5.2 \pm 0.1 \cdot 10^{-3} \text{ cm}^2 \cdot \text{V}^{-1} \cdot \text{s}^{-1}$ .

The remarkable electrical characteristics of these nanoarchitectures make them ideal systems for fundamental studies on charge transport at the nanoscale, but also pave the way towards their exploitation in downscaled organic electronic devices.

## 5.8. References

1. Smits, E. C. P., Mathijssen, S. G. J., van Hal, P. A., Setayesh, S., Geuns, T. C. T., Mutsaers, K. A. H. A., Cantatore, E., Wondergem, H. J., Werzer, O., Resel, R., Kemerink, M., Kirchmeyer, S., Muzafarov, A. M., Ponomarenko, S. A., de Boer, B., Blom, P. W. M. & de Leeuw, D. M. Bottom-up organic integrated circuits. *Nature* **455**, 956-959, (2008).
2. Li, L., Gao, P., Schuermann, K. C., Ostendorp, S., Wang, W., Du, C., Lei, Y., Fuchs, H., Cola, L. D., Mullen, K. & Chi, L. Controllable Growth and Field-Effect Property of Monolayer to Multilayer Microstripes of an Organic Semiconductor. *J. Am. Chem. Soc.* **132**, 8807-8809, (2010).

3. Wang, S., Kiersnowski, A., Pisula, W. & Mullen, K. Microstructure evolution and device performance in solution-processed polymeric field-effect transistors: the key role of the first monolayer. *J. Am. Chem. Soc.* **134**, 4015-4018, (2012).
4. Mathijssen, S. G. J., C.P.Smits, E., Hal, P. A. v., J.Wondergem, H., Ponomarenko, S. A., Moser, A., Resel, R., Bobbert, P. A., Kemerink, M., Janssen, R. A. J. & Leeuw, D. M. d. Monolayer coverage and channel length set the mobility in self-assembled monolayer field-effect transistors. *Nat. Nanotech.* **4**, 674, (2009).
5. Facchetti, A., Yoon, M.-H. & Marks, T. J. Gate Dielectrics for Organic Field-Effect Transistors: New Opportunities for Organic Electronics. *Adv. Mater.* **17**, 1705-1725, (2005).
6. Tulevski, G. S., Miao, Q., Fukuto, M., Abram, R., Ocko, B., Pindak, R., Steigerwald, M. L., Kagan, C. R. & Nuckolls, C. Attaching Organic Semiconductors to Gate Oxides: In Situ Assembly of Monolayer Field Effect Transistors. *J. Am. Chem. Soc.* **126**, 15048-15050, (2004).
7. Cao, Y., Steigerwald, M. L., Nuckolls, C. & Guo, X. Current trends in shrinking the channel length of organic transistors down to the nanoscale. *Adv. Mater.* **22**, 20-32, (2010).
8. Noh, Y. Y., Zhao, N., Caironi, M. & Sirringhaus, H. Downscaling of self-aligned, all-printed polymer thin-film transistors. *Nat. Nanotechnol.* **2**, 784-789, (2007).
9. Asadi, K., Wu, Y., Gholamrezaie, F., Rudolf, P. & Blom, P. W. M. Single-Layer Pentacene Field-Effect Transistors Using Electrodes Modified With Self-assembled Monolayers. *Adv. Mater.* **21**, 4109-4114, (2009).
10. Xu, G., Bao, Z. & Groves, J. T. Langmuir-Blodgett Films of Regioregular Poly(3-hexylthiophene) as Field-Effect Transistors. *Langmuir* **16**, 1834-1841, (2000).
11. Sizov, A. S., Agina, E. V., Gholamrezaie, F., Bruevich, V. V., Borshchev, O. V., Paraschuk, D. Y., de Leeuw, D. M. & Ponomarenko, S. A. Oligothiophene-based monolayer field-effect transistors prepared by Langmuir-Blodgett technique. *Appl. Phys. Lett.* **103**, 043310, (2013).
12. Cao, Y., Wei, Z., Liu, S., Gan, L., Guo, X., Xu, W., Steigerwald, M. L., Liu, Z. & Zhu, D. High-performance Langmuir-Blodgett monolayer transistors with high responsivity. *Angew. Chem. Int. Ed.* **49**, 6319-6323, (2010).
13. Fabiano, S., Musumeci, C., Chen, Z., Scandurra, A., Wang, H., Loo, Y.-L., Facchetti, A. & Pignataro, B. From Monolayer to Multilayer N-Channel Polymeric Field-Effect Transistors with Precise Conformational Order. *Adv. Mater.* **24**, 951-956, (2012).
14. Fabiano, S., Yoshida, H., Chen, Z., Facchetti, A. & Loi, M. A. Orientation-dependent electronic structures and charge transport mechanisms in ultrathin polymeric n-channel field-effect transistors. *ACS Appl. Mater. Interfaces* **5**, 4417-4422, (2013).
15. Jones, B. A., Facchetti, A., Wasielewski, M. R. & Marks, T. J. Tuning Orbital Energetics in Arylene Diimide Semiconductors. Materials Design for Ambient Stability of n-Type Charge Transport. *J. Am. Chem. Soc.* **129**, 15259-15278, (2007).
16. Li, C. & Wonneberger, H. Perylene imides for organic photovoltaics: yesterday, today, and tomorrow. *Adv. Mater.* **24**, 613-636, (2012).
17. Zhan, X., Facchetti, A., Barlow, S., Marks, T. J., Ratner, M. A., Wasielewski, M. R. & Marder, S. R. Rylene and related diimides for organic electronics. *Adv. Mater.* **23**, 268-284, (2011).
18. Jones, B. A., Ahrens, M. J., Yoon, M. H., Facchetti, A., Marks, T. J. & Wasielewski, M. R. High-mobility air-stable n-type semiconductors with processing versatility: dicyanoperylene-3,4:9,10-bis(dicarboximides). *Angew. Chem. Int. Ed. Engl.* **43**, 6363-6366, (2004).
19. Molinari, A. S., Alves, H., Chen, Z., Facchetti, A. & Morpurgo, A. F. High Electron Mobility in Vacuum and Ambient for PDIF-CN2 Single-Crystal Transistors. *J. Am. Chem. Soc.* **131**, 2462-2463, (2009).
20. Ono, S., Minder, N., Chen, Z., Facchetti, A. & Morpurgo, A. F. High-performance n-type organic field-effect transistors with ionic liquid gates. *Appl. Phys. Lett.* **97**, 143307, (2010).
21. Willa, K., Häusermann, R., Mathis, T., Facchetti, A., Chen, Z. & Batlogg, B. From organic single crystals to solution processed thin-films: Charge transport and trapping with varying degree of order. *J. Appl. Phys.* **113**, 133707, (2013).
22. Jones, B. A., Facchetti, A., Wasielewski, M. R. & Marks, T. J. Effects of Arylene Diimide Thin Film Growth Conditions on n-Channel OFET Performance. *Adv. Funct. Mater.* **18**, 1329-1339, (2008).
23. Piliego, C., Jarzab, D., Gigli, G., Chen, Z., Facchetti, A. & Loi, M. A. High Electron Mobility and Ambient Stability in Solution-Processed Perylene-Based Organic Field-Effect Transistors. *Adv. Mater.* **21**, 1573-1576, (2009).

24. Fabiano, S., Wang, H., Piliego, C., Jaye, C., Fischer, D. A., Chen, Z., Pignataro, B., Facchetti, A., Loo, Y.-L. & Loi, M. A. Supramolecular Order of Solution-Processed Perylenediimide Thin Films: High-Performance Small-Channel n-Type Organic Transistors. *Adv. Funct. Mater.* **21**, 4479-4486, (2011).
25. Mativetsky, J. M., Orgiu, E., Lieberwirth, I., Pisula, W. & Samori, P. Charge Transport Over Multiple Length Scales in Supramolecular Fiber Transistors: Single Fiber Versus Ensemble Performance. *Adv. Mater.* **26**, 430–435, (2014).
26. Kaganer, V. M., Möhwald, H. & Dutta, P. Structure and phase transitions in Langmuir monolayers. *Reviews of Modern Physics* **71**, 779, (1999).
27. Ashwell, G. J. Photocromic and non-linear optical properties of C16H33-P3CNQ and C16H33-Q3CNQ Langmuir-Blodgett films. *Thin Solid Films* **186** 155-165, (1990).
28. Piliego, C., Cordella, F., Jarzab, D., Lu, S., Chen, Z., Facchetti, A. & Loi, M. A. Functionalized perylenes: origin of the enhanced electrical performances. *Applied Physics A* **95**, 303-308, (2008).
29. Como, E. D., Loi, M. A., Murgia, M., Zamboni, R. & Muccini, M. J-Aggregation in r-Sexithiophene Submonolayer Films on Silicon Dioxide. *J. Am. Chem. Soc.* **128**, 4277-4281, (2006).
30. Yan, H., Zheng, Y., Blache, R., Newman, C., Lu, S., Woerle, J. & Facchetti, A. Solution Processed Top-Gate n-Channel Transistors and Complementary Circuits on Plastics Operating in Ambient Conditions. *Advanced Materials* **20**, 3393-3398, (2008).
31. Choi, S. H. & Frisbie, C. D. Enhanced Hopping Conductivity in Low Band Gap Donor-Acceptor Molecular Wires Up to 20 nm in Length. *J. Am. Chem. Soc.* **132**, 16191, (2010).
32. Mativetsky, J. M., Pace, G., Elbing, M., Rampi, M. A., Mayor, M. & Samori, P. Azobenzenes as Light-Controlled Molecular Electronic Switches in Nanoscale Metal-Molecule-Metal Junctions. *J. Am. Chem. Soc.* **130**, 9192, (2008).
33. Metzger, R. M. Unimolecular Electrical Rectifiers. *Chem. Rev.* **103**, 3803–3834, (2003).
34. Aviram & Ratner, M. A. Molecular rectifier. *Chem. Phys. Lett.* **29**, 277, (1974).
35. Metzger, R. M., Chen, B., Hopfner, U., Lakshmikantham, M. V., Vuillaume, D., Kawai, T., Wu, X., Tachibana, H., Hughes, T. V., Sakurai, H., Baldwin, J. W., Hosch, C., Cava, M. P., Brehmer, L. & Ashwell, G. J. Unimolecular Electrical Rectification in Hexadecylquinolinium Tricyanoquinodimethane. *J. Am. Chem. Soc.* **119**, 10455-10466, (1997).
36. Kornilovitch, P. E., Bratkovsky, A. M. & Stanley Williams, R. Current rectification by molecules with asymmetric tunneling barriers. *Phys. Rev. B* **66**, (2002).
37. Krzeminski, C., Delerue, C., Allan, G., Vuillaume, D. & Metzger, R. Theory of electrical rectification in a molecular monolayer. *Phys. Rev. B* **64**, (2001).
38. Delgado, M. C. R., Kim, E.-G., Filho, D. t. A. d. S. & Bredas, J.-L. Tuning the Charge-Transport Parameters of Perylene Diimide Single Crystals via End and/or Core Functionalization: A Density Functional Theory Investigation. *J. Am. Chem. Soc.* **132**, 3375–3387, (2010).
39. Stabel, A., Herwig, P., Miilen, K. & Rabe, J. P. Diodelike Current - Voltage Curves for a Single Molecule-Tunneling Spectroscopy with Submolecular Resolution of an Alkylated, peri-Condensed Hexabenzocoronene. *Angew. Chem. Int. Ed.* **34**, 1609-1611, (1995).
40. Liu, Y., Xu, Y. & Zhu, D. Schottky diodes fabricated with Langmuir-Blodgett films of C60-doped poly (3-alkylthiophene) s. *Synth. Met.* **90**, 143-146, (1997).
41. Geddes, N. J., Sambles, J. R., Jarvis, D. J., Parker, W. G. & Sandman, D. J. The electrical properties of metal-sandwiched Langmuir-Blodgett multilayers and monolayers of a redox-active organic molecular compound. *J. Appl. Phys.* **71**, 756, (1992).
42. Geddes, N. J., Sambles, J. R., Jarvis, D. J., Parker, W. G. & Sandman, D. J. Fabrication and investigation of asymmetric current-voltage characteristics of a metal/Langmuir-Blodgett monolayer/metal structure. *Appl. Phys. Lett.* **56**, 1916, (1990).
43. Gaillard, N., Gros-Jean, M., Mariolle, D., Bertin, F. o. & Bsiesy, A. Method to assess the grain crystallographic orientation with a submicronic spatial resolution using Kelvin probe force microscope. *Appl. Phys. Lett.* **89**, 154101, (2006).
44. Emmanouil, K., Gawrys, P., Zagorska, M. & Kennou, S. Electronic properties of a perylene bisimide interfaced with gold or aluminum: The influence of the substrate. *Microelectron. Eng.* **112**, 170-173, (2013).
45. Hendriksen, B. L., Martin, F., Qi, Y., Mauldin, C., Vukmirovic, N., Ren, J., Wormeester, H., Katan, A. J., Altoe, V., Aloni, S., Fréchet, J. M., Wang, L. W. & Salmeron, M. Electrical transport properties of oligothiophene-based molecular films studied by current sensing atomic force microscopy. *Nano Lett.* **11**, 4107-4112, (2011).

46. Agrawal, R. & Ghosh, S. Electrical characterization of Fermi level pinning in metal/3,4,9,10 perylenetetracarboxylic dianhydride interfaces. *Appl. Phys. Lett.* **89**, 222114, (2006).
47. Kelley, T. W. & Frisbie, C. D. Point contact current–voltage measurements on individual organic semiconductor grains by conducting probe atomic force microscopy. *J. Vac. Sci. Technol. B* **18**, 632, (2000).
48. Kelley, T. W., Granstrom, E. L. & Frisbie, C. D. Conducting probe atomic force microscopy:a characterization tool for molecular electronics. *Adv. Mater.* **11**, 261, (1999).
49. Natali, D. & Caironi, M. Charge Injection in Solution-Processed Organic Field-Effect Transistors: Physics, Models and Characterization Methods. *Adv. Mater.* **24**, 1357, (2012).
50. Salinas, M., Jager, C. M., Amin, A. Y., Dral, P. O., Meyer-Friedrichsen, T., Hirsch, A., Clark, T. & Halik, M. The relationship between threshold voltage and dipolar character of self-assembled monolayers in organic thin-film transistors. *J. Am. Chem. Soc.* **134**, 12648-12652, (2012).
51. Ringk, A., Christian Roelofs, W. S., Smits, E. C. P., van der Marel, C., Salzmann, I., Neuhold, A., Gelinck, G. H., Resel, R., de Leeuw, D. M. & Strohriegl, P. n-Type self-assembled monolayer field-effect transistors for flexible organic electronics. *Organic Electronics* **14**, 1297-1304, (2013).
52. Defaux, M., Gholamrezaie, F., Wang, J., Kreyes, A., Ziener, U., Anokhin, D. V., Ivanov, D. A., Moser, A., Neuhold, A., Salzmann, I., Resel, R., de Leeuw, D. M., Meskers, S. C. J., Moeller, M. & Mourran, A. Solution-Processable Septithiophene Monolayer Transistor. *Adv. Mater.* **24**, 973-978, (2012).
53. Reid, O. G., Munechika, K. & Ginger, D. S. Space Charge Limited Current Measurements on Conjugated Polymer Films using Conductive Atomic Force Microscopy. *Nano Lett.* **8**, 1602, (2008).
54. Yang, R., Garcia, A., Korystov, D., Mikhailovsky, A., Bazan, G. C. & Nguyen, T.-Q. Control of Interchain Contacts, Solid-State Fluorescence Quantum Yield, and Charge Transport of Cationic Conjugated Polyelectrolytes by Choice of Anion. *J. Am. Chem. Soc.* **128**, 16532-16539, (2006).
55. Lin, H.-N., Lin, H.-L., Wang, S.-S., Yu, L.-S., Perng, G.-Y., Chen, S.-A. & Chen, S.-H. Nanoscale charge transport in an electroluminescent polymer investigated by conducting atomic force microscopy. *Appl. Phys. Lett.* **81**, 2572, (2002).
56. Ionescu-Zanetti, C., Mechler, A., Carter, S. A. & Lal, R. Semiconductive polymer blends: correlating structure with transport properties at the nanoscale. *Adv. Mater.* **16**, 385–389, (2004).
57. Douhéret, O., Lutsen, L., Swinnen, A., Breselge, M., Vandewal, K., Goris, L. & Manca, J. Nanoscale electrical characterization of organic photovoltaic blends by conductive atomic force microscopy. *Appl. Phys. Lett.* **89**, 032107, (2006).
58. Blom, P. W. M., de Jong, M. J. M. & Vleggaar, J. J. M. Electron and hole transport in poly(p-phenylene vinylene) devices. *Appl. Phys. Lett.* **68**, 3308, (1996).
59. Coropceanu, V., Cornil, J., Filho, D. A. d. S., Olivier, Y., Silbey, R. & Brédas, J.-L. Charge Transport in Organic Semiconductors. *Chem. Rev.* **107**, 926-952, (2007).
60. Malliaras, G. G., Salem, J. R., Brock, P. J. & Scott, C. Electrical characteristics and efficiency of single-layer organic light-emitting diodes. *Phys. Rev. B* **58**, R13 411, (1998).
61. de Bruyn, P., van Rest, A. H. P., Wetzelraer, G. A. H., de Leeuw, D. M. & Blom, P. W. M. Diffusion-Limited Current in Organic Metal-Insulator-Metal Diodes. *Physical Review Letters* **111**, (2013).
62. Woellner, C. F., Freire, J. A., Guide, M. & Nguyen, T. Q. The theoretical current-voltage dependence of a non-degenerate disordered organic material obtained with conductive atomic force microscopy. *J. Chem. Phys.* **135**, 084108, (2011).

## 6. Controlling the morphology of conductive PEDOT by *in situ* electropolymerization

### 6.1. Introduction

A given material capable of undergoing different self-assembly pathways depending on the experimental conditions, to form different morphologies and supramolecular organization, can be suitable for different applications.<sup>1</sup> A well-known example is the case of poly(3,4-ethylenedioxythiophene) (PEDOT), which is largely employed as conducting polymer for the fabrication of organic electronic devices, due to its good electrical conductivity, excellent transparency in the visible range and environmental stability.<sup>2-7</sup> While thin and relatively flat films are suitable for example as injection layer in solar cell devices,<sup>8-10</sup> one dimensional arrangements like fibers are preferred for the fabrication of sensors which exploit their increased surface area.<sup>11-14</sup>

The polymerization of 3,4-ethylenedioxythiophene (EDOT) can be accomplished both by chemical oxidation and electrochemical methods.<sup>15,16</sup> Because of its scarce solubility, PEDOT is normally blended with poly(styrenesulphonate) (PSS) to improve its processability; PEDOT:PSS blends are in fact commercially available as dispersions in water.<sup>17-19</sup> In this respect, an *in-situ* polymerization procedure may be preferable to avoid the presence of basically insulating additives or to facilitate the processing steps.

It is well known that the morphology of electrochemically synthesized polymers strongly depends on the experimental conditions.<sup>20,21</sup> It has also been demonstrated that when the electro-polymerization is performed in a microgap between two metal electrodes, fiber-like structures bridging the gap can be obtained. Although “*directed electrochemical nanowire assembly*” procedures have been already

proposed to fabricate both metal and organic nanowires,<sup>22-24</sup> the full understanding of such “on-site” growth phenomena is still lacking.

This chapter reports on methodologies to obtain control over the PEDOT electropolymerization process in a micrometer gap, in order to finely tune its final morphology and thus the electrical properties of the device.

## 6.2. Experimental details

3,4-Ethylenedioxythiophene, 97% (EDOT), acetonitrile anhydrous, 99.8% (MeCN) and anhydrous propylene carbonate, 99.7% (PC) were purchased from Sigma-Aldrich, and used without further purification. Gold electrodes on silicon dioxide (Fraunhofer Institute) substrates were cleaned by subsequent ultrasonication bath in acetone and isopropanol prior to use.

A Keithley 2636A source meter was employed for the polymerization *in-situ* and for the two probe current-voltage characteristics measurements. All the experiments were performed in ambient conditions.

Atomic force microscopy (AFM) topographic images were obtained in tapping mode on a Dimension 3100 (Digital Instruments) microscope with a NanoScope IV controller, by employing commercial 125  $\mu\text{m}$  long silicon cantilevers with a spring constant of 40 N/m. Torsion-resonance tunneling current (TR-TUNA AFM) images were obtained in a Multimode V (Veeco) microscope equipped with a Nanoscope V controller and Pt/Ir-coated Si tips with 225  $\mu\text{m}$  long cantilever and spring constant in the range 0.5 – 9.5 N/m were used. The torsion amplitude was used as the feedback signal to measure surface morphology.

Fluorescence images were acquired with a Nikon Eclipse Ti scanning confocal fluorescence microscope, using continuous wave excitation at 405 nm, a 60x magnification 0.95 numerical aperture plan apo air objective, a 30 micron diameter confocal pinhole, and a 515 nm +/- 15 nm band pass filter before the detector. Spectra were taken at points of interest in the image via a fiber-coupled CCD/spectrograph combination (Princeton LN EEV/Acton SpectraPro 300i).

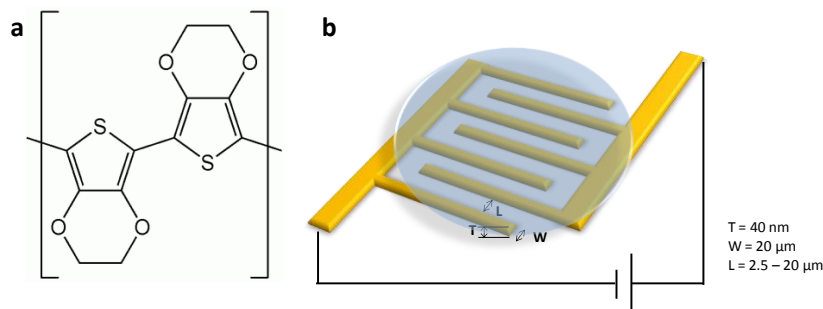


**Figure 6.1:** a) molecular structure of PEDOT; b) scheme of the experimental setup.

2  $\mu\text{L}$  of EDOT 0.1M solution in MeCN or PC were dropped on top of interdigitated 20  $\mu\text{m}$  wide (W) and 40 nm thick gold electrodes patterned on a  $\text{SiO}_2$  substrate, as depicted in the scheme of Figure 6.1, a DC constant bias was applied for 5 sec and the current flowing as a function of time between the two electrodes during the polymerization process was registered as a function of time. After the polymerization, the devices were washed with acetonitrile to remove residual monomers and dried in a stream of  $\text{N}_2$ , prior to two probe resistive characterization. Different inter-electrode gaps ( $L$ ) have been employed ranging from 2.5 to 20  $\mu\text{m}$ .

### 6.3. Electropolymerization at different electric fields

In essence, the system here described operates like an electrochemical cell based on ultramicroelectrodes, i.e. electrodes with at least one dimension equal or smaller than 20  $\mu\text{m}$ .<sup>25</sup> Electrochemical cells employing ultramicroelectrodes exhibit properties which are unavailable in conventional macroscopic systems. In conventional cells resistive solutions cause substantial ohmic drops between the applied and working electrode potentials, whereas ultramicroelectrodes are much less sensitive to large solution resistances, therefore ohmic drops become negligible. For this reason, it is possible to avoid the use of the third electrode and to work in absence of supporting electrolytes, increasing the available electrochemical potential windows.<sup>26</sup> Hence, other technological reasons aside, the *in-situ* electropolymerization across micro-spaced ultramicroelectrodes also allows for a large broadening of possible experimental conditions, opening new perspectives both for scientific and technological applications.

Figure 6.2 shows an atomic force microscopy (AFM) image of PEDOT fibers obtained by electropolymerization across a 10  $\mu\text{m}$  microgap. For this polymerization a fixed voltage of 10 V was applied to a 0.1 M EDOT solution in acetonitrile (MeCN), for 5 s. From the survey topography image the PEDOT fibers appear to be aligned with the direction of the applied electric field. All the fibers are connected to one electrode but not all of them are connected to both, depicting a scenario where the polymerization of EDOT starts at the anode and expands towards the cathode.

The picture in Figure 6.2b reports a current map obtained by Torsional Resonance Tunneling Atomic Force Microscopy (TR-TUNA AFM) on a single fiber. A bias of -8V was applied to the gold electrode and the tunneling current flowing between the substrate and the grounded tip was revealed. This mode was chosen in order to be non-invasive on the soft fiber and to avoid scratching during imaging. As a result, we were able to measure the conductivity on very thin fibers: for example the fiber in Figure 6.2b has a thickness ranging from 5 nm to 350 nm, as shown in the height profile of Figure 6.2c. Figure 6.2c also shows a comparison of the height profiles with the relative current

profiles along two different cross-sections *I* and *II* (marked in Figure 6.2b). No current, but just electrical noise is detectable on the area corresponding to the bare SiO<sub>2</sub> substrate. Instead, tunneling currents in the range of 1 - 5 pA can be measured along the fiber.

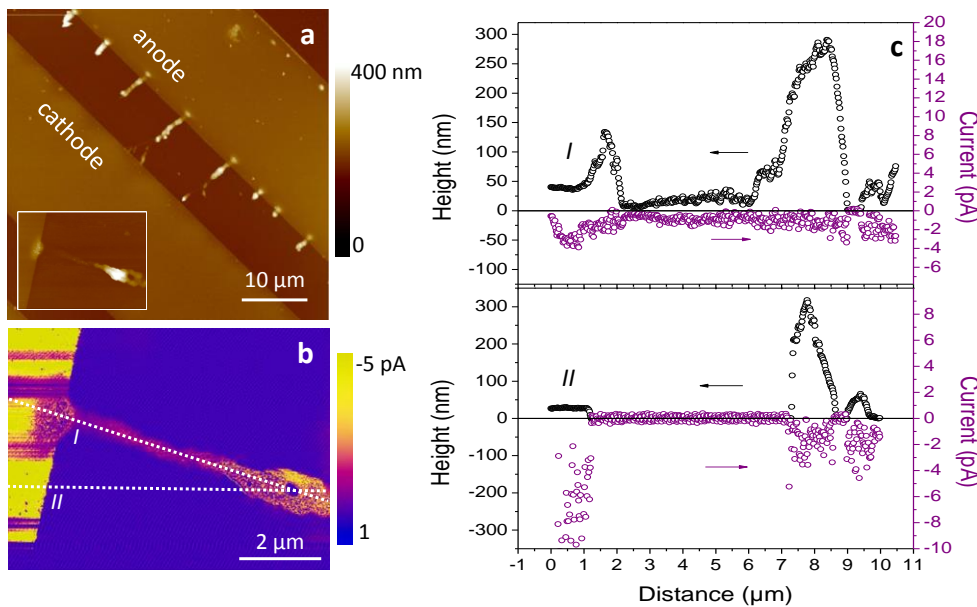


**Figure 6.2:** PEDOT fibers obtained by electropolymerization of EDOT, solution 0.1 M in MeCN at 10 V, 5 s crossing a 10 μm wide gap. a) AFM topographical image showing aligned fibers growing from the anode and bridging the gap. In the inset a single fiber connected to an electrode is shown, which current map obtained by TR-TUNA AFM is reported in b. c) Height and current profiles along the marked lines (I, II) in b: I refers to the fiber connected to the electrode, II considers also the bare SiO<sub>2</sub> substrate.

The experimental electropolymerization conditions here employed were similar in terms of electric field intensity to those reported by Das et al.,<sup>27</sup> in which 5 V were applied across a 5 μm gap (leading to an electric field of 1 MV/m). We observed that when instead a voltage of 5 V is applied for the same time to a 0.1 M EDOT solution in MeCN between two electrodes separated by a 10 μm gap, the polymerization proceeds with the formation of a homogeneous ultrathin film covering the device. The root mean square roughness ( $R_{\text{RMS}}$ ) of this film supported on SiO<sub>2</sub> ranges between 0.9 and 1.3 nm as determined on 1\*1 μm<sup>2</sup> areas (AFM images shown in Figure 6.3).

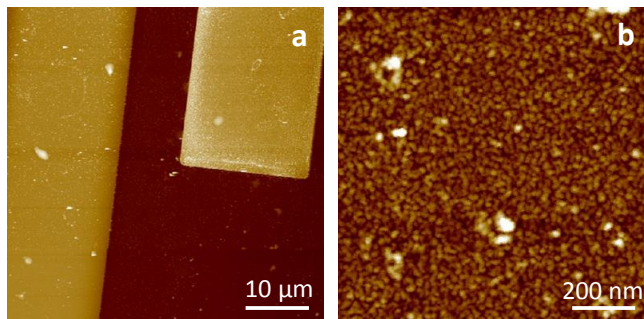


**Figure 6.3:** AFM topography images of thin film obtained by electropolymerization of EDOT, solution 0.1 M in MeCN at 5 V, 5 s, on a 10  $\mu\text{m}$  wide gap. In the survey image (a) no particular feature is visible in-between the electrodes, but the presence of a film in the gap is evident in the zoom-in in b. Z-scale: 140 nm (a); 10 nm (b).

Significantly, both these morphologies exhibit charge transport properties, as revealed also by the current-voltage characteristics described below, but it can be anticipated that while a typical S-shaped  $I$ - $V$  curve is detected for the fibers, a more linear, metallic-like behavior is obtained for the films in the bias range considered, indicative of an improved interface morphology lowering resistance effects at the contacts.<sup>28</sup> Unfortunately, the very small amount of material adsorbed on the surface renders the characterization of the architectures with a chemically sensitive technique non-trivial. We employed laser confocal microscopy to measure photoluminescence images and spectra of both fibers and film finding that the emission spectra of both the morphologies show an emission peak around 535-540 nm, which is typical for PEDOT micro- and nano-structures.<sup>29,30</sup>

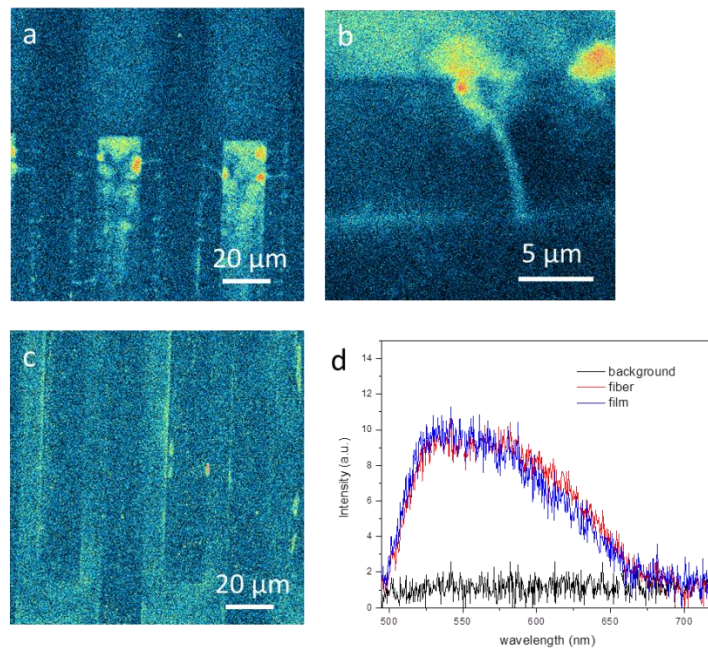


**Figure 6.4:** Confocal fluorescence microscopy images of fibers (a, b) and film (c) based devices, (excitation at 405 nm, emission 500 to 530 nm). The brightest (red/yellow) areas correspond to higher emission. (d) Emission spectra recorded on a single PEDOT fiber, a PEDOT film, and on the bare substrate.

## 6.4. Insights on the electropolymerization mechanisms: nucleation and growth, electromigration

To gain insight into the polymerization mechanism, two different gap widths were chosen and different electric field intensities were explored. Figure 6.5 compares the resistive characteristics and the optical images obtained on the devices with 10 and 20  $\mu\text{m}$  gaps prepared by applying 0.5, 1, and 2 MV/m field intensities during the polymerization. In most of the cases, *i.e.* for 1 and 2 MV/m, fiber-like structures bridging the electrodes are formed. The fibers have widths in the range of 300 – 1000 nm and thickness up to 500 - 600 nanometers with no remarkable difference in size in dependence of the electric field and show S-shaped resistive characteristics (b, c, e, f). Conversely, for 0.5 MV/m applied field (a, d), no features are visible in the optical images, but the presence of ultrathin films covering the electrodes and the gap is confirmed both by their conductivity and the AFM and fluorescence characterizations.

It is well established that during potentiostatic electropolymerization the formation of new phases at the solid–liquid interface generally occurs *via* nucleation and growth mechanisms. Therefore by looking carefully at the relative current-time transients, valuable information about the kinetics of electrodeposition can be obtained.<sup>31-33</sup> As a general trend the transient curves are characterized by the presence of a current peak, whose time position changes depending on the applied potential. The current peaks correspond to the polymer nucleation and growth processes taking place during the electropolymerization.<sup>34</sup> Instantaneous or progressive nucleation processes are possible. Progressive nucleation, where many polymeric nuclei are formed in different active sites of the whole area, leads to the formation of smoother surfaces, while an instantaneous nucleation involves the rapid formation of nuclei followed then only by growth, *i.e.* no further nucleation occurs. Consequently, the resulting surfaces are rough and inhomogeneous.<sup>34</sup> The growth mechanisms, instead, can be either 2D or 3D. For 2D growth the nuclei grow more quickly in the direction parallel to the substrate, so that layered structures are expected. Conversely, in the 3D mechanism the nuclei grow both parallel and perpendicular to the basal plane of the substrate, therefore nodular or peaked structures are more likely to be obtained, leading to a greater surface roughness.<sup>34</sup>

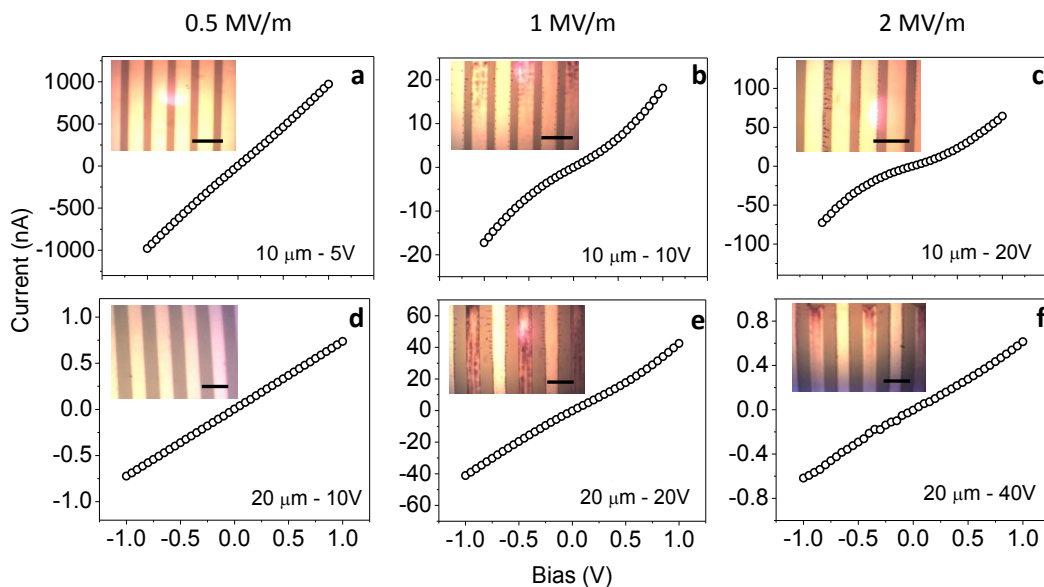


**Figure 6.5:** Current vs. voltage characteristics of PEDOT obtained by electropolymerization at electric field intensities of 0.5 MV/m (a, d); 1 MV/m (b, e); and 2 MV/m (c, f). In the insets optical images (scale bar 40  $\mu\text{m}$ ) show the presence of fiber-like structures for the highest electric field conditions (b, c, e, f) while samples prepared by using lower electric fields (a, d) reveal a homogeneous morphology in the channel.

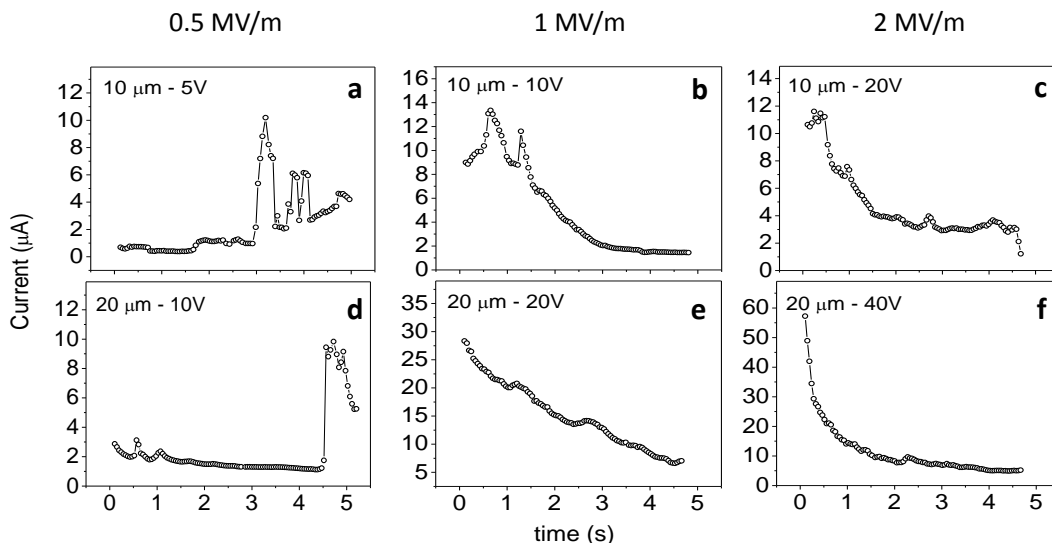


**Figure 6.6:** Current vs. time curves registered during the polymerization processes of EDOT in MeCN solution at electric field intensities of 0.5 MV/m (a, d); 1 MV/m (b, e); and 2 MV/m (c, f).

It has been observed<sup>35</sup> that the maximum of the peak current occurs a short time after higher potentials are applied, indicating that the polymer chains need to reach a considerable length to start nucleation and growth on the electrode, and this can be accomplished either by higher potentials at shorter times or lower potentials at longer times.

The current vs. time curves relative to the polymerization processes resulting in the devices of Figure 6.5, are reported in Figure 6.6. For the highest applied electric fields (1 and 2 MV/m), producing the fiber structures (Figure 6.5 and Figure 6.6 b, c, e, f), the transient starts with a current peak which successively decreases with time. The current spike is due to the immediate oxidation of the EDOT molecules adjacent to the electrode surface, the formation of oligomers and their adsorption on the electrode surface, leading to the nucleation followed by growth phenomena. Once the monomers at the surface have been oxidized, the rate of polymerization becomes controlled by the rate at which the other monomers reach the electrode from the bulk solution, which in turn is determined by the rate of diffusion in solution. The decrease of the current then reflects the formation of a depleted region close to the electrode. Such behavior is indicative of an instantaneous nucleation process which is accompanied by a diffusion-limited growth. As the diffusion flux towards a point is greater than towards a plane, the growth of a protrusion, generally resulting in dendrites, is favorable in a diffusion-limited transport regime.<sup>36</sup> In our case an electromigration transport, which has already been exploited to align particles and polymers,<sup>37-41</sup> has also to be taken into account. The geometry of the electric field therefore becomes a significant factor in the morphological development of the diffusion-limited aggregates. Since the electric field is intensified at a tip protruding from an electrode, the electromigration term will also be enhanced at a tip, stabilizing a single wire against branching.<sup>36</sup>

Conversely, in the case of low electric field intensity (0.5 MV/m), the current vs. time characteristics do not show an initial instantaneous spike of current, but the peaks are shifted toward longer time scales (Figs. 4 a, d) This behavior is consistent with a progressive nucleation process: with time the current increases because of the increased number of nuclei and the growing surface of each nucleus. Since the final morphology of the polymer is an ultrathin film, it is likely that the growth mechanism is a 2D process, where the layers are formed by the incorporation of new material to the growing nuclei periphery.<sup>42</sup> Moreover, the slower growth process in this case allows parts of the oligomers to diffuse away from the electrode and to form an oligomer cloud also on the insulating gap area. Similar behavior has been observed when EDOT is polymerized by standard electrochemical methods on HOPG surface, where it is possible to switch from a progressive 2D mechanism to a 3D diffusive one by increasing the polymerization potential.<sup>43</sup> Significantly, all these measurements have been performed by employing very little volume of solution and using electrode geometries very different to that of standard electrochemical processes. Though the absolute values of current intensity can be affected by slight variability, the general trend is strictly dependent on the electric field, and this makes the procedure appealing for implementation in micropatterning processes such as electrochemical lithography<sup>44</sup>

## 6.5. Electropolymerization of EDOT in propylene carbonate solution

We extended our study to the use of propylene carbonate (PC) as a solvent instead of acetonitrile in order to exploit its lower volatility with the aim of gaining a better control over the polymerization and growth process. Upon application of low electric field intensities (0.5 MV/m) optical microscopy images do not reveal the presence of additional features whereas electrical studies evidenced the absence of detectable current in the final devices. These results suggest that polymerization does not take place in these conditions. Conversely, by applying an electric field of 1 or 2 MV/m, conductive films are obtained on the electrodes and across the microgaps, as showed by the optical and the AFM images in Figure 6.7 and Figure 6.8.

The 3D growth is indeed confirmed by the fact that thick films are formed on the electrodes, as evidenced by optical microscopy (Figure 6.7). We can speculate that in this case the higher viscosity of PC with respect to MeCN causes a slower flux of the monomers toward the electrode hindering an instantaneous nucleation mechanism.

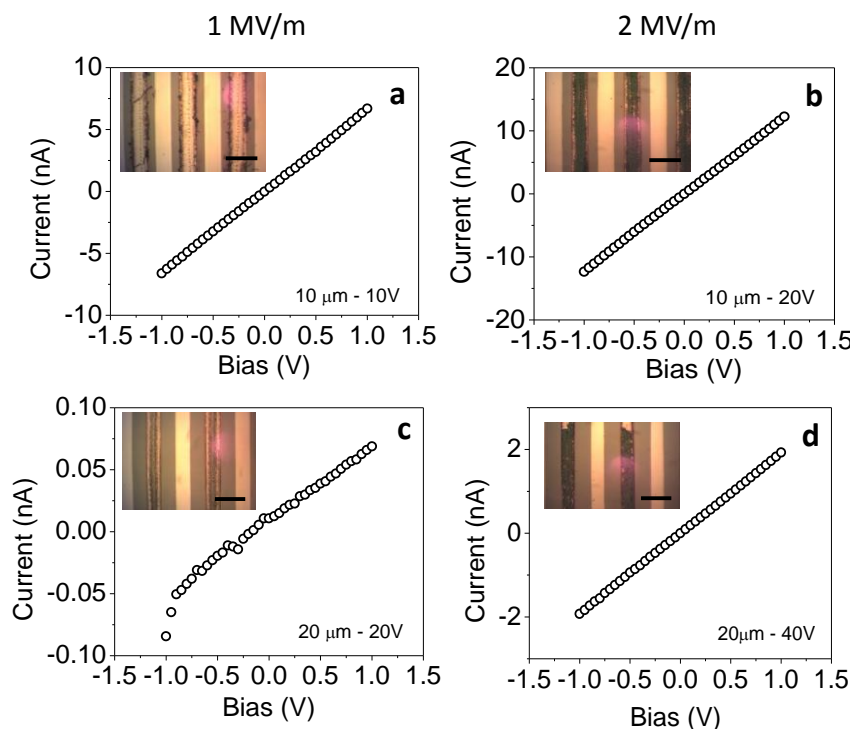


**Figure 6.7:** Current *vs.* voltage characteristics of PEDOT obtained by electropolymerization in propylene carbonate at electric field intensities of 1 MV/m (a, c); and 2 MV/m(b, d). In the insets optical images show the presence of thick films growing in 3D fashion over the electrodes (scale bar 40  $\mu$ m). The films over the electrodes are thicker whereas higher electric fields are used.

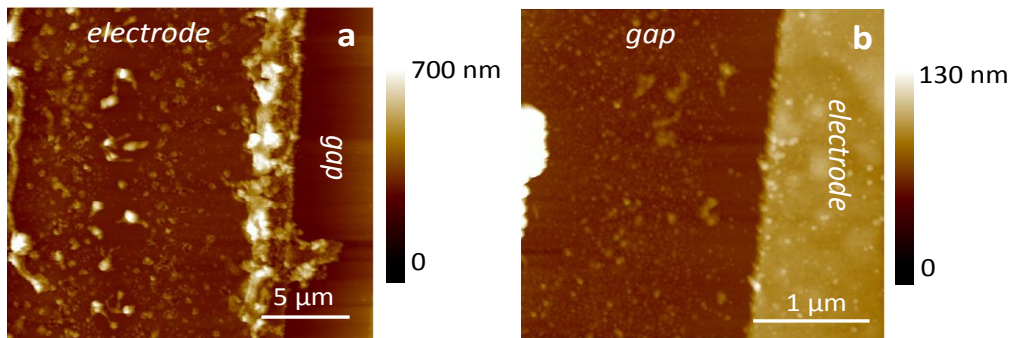


**Figure 6.8:** AFM images showing the morphology of the 10  $\mu\text{m}$  gap devices polymerized at 10V (Figure 6.8a). Nodular structures are present on the electrode which was positively biased (a) and a film is also visible inside the channel (b). With the propylene carbonate solution no fiber-like structures were observed after the polymerization process, seeming to produce only films mostly growing on the positively biased electrode but also covering the channels. So in this case a 3D growth type mechanism seems to be the prominent one under the employed conditions.

Again, these films show a quite linear conductive behavior in the bias range investigated. The current *vs.* time trends during the polymerization revealed an initial increase in current indicating the presence of a progressive nucleation processes which reaches a plateau, the latter being the finger print of a 3D growth mechanism under charge transfer control (Figure 6.9).<sup>31,32</sup>

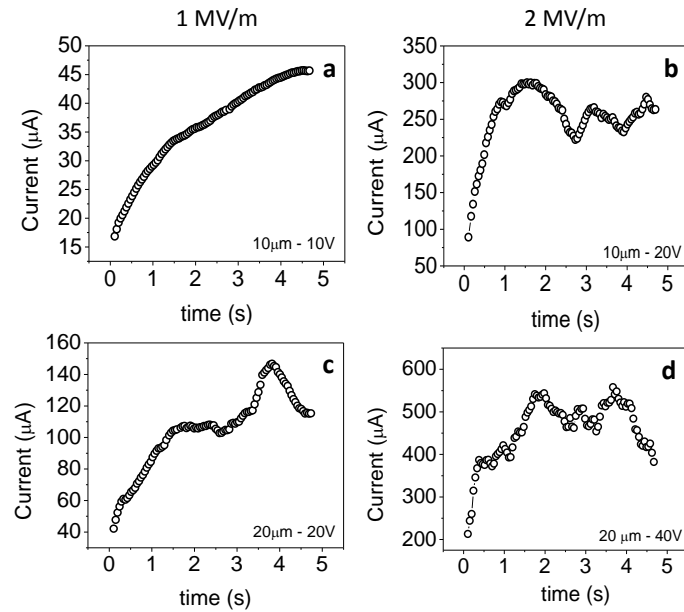


**Figure 6.9:** Current *vs.* time curves registered during the polymerization processes of EDOT in PC solution at electric field intensities of 1 MV/m (a, c) and 2 MV/m (b, d).

## 6.6. Conclusions

In summary, the morphology of electrochemically synthesized PEDOT can be finely tuned *in situ* on a device, by carefully guiding the nucleation and growth processes, as well as electromigration phenomena. In particular, high electric field intensities together with low viscosities favor the formation of aligned wires bridging the gap, as a result of instantaneous nucleation, diffusion-limited growth and electromigration processes. Conversely, lower electric field strengths lead to the formation of thin films via progressive nucleation and 2D growth. Significantly, the electrical function of the electropolymerized material was found being strongly affected by the morphology, as evidenced by the different resistive behavior. Noteworthy, our approach is compatible for implementation in electrochemically tuned lithographic processes.<sup>44</sup> This result opens new avenues of exploration towards the processing of electroactive materials with tunable properties.

## 6.7. References

1. Wang, Y., Tran, H. D., Liao, L., Duan, X. & Kaner, R. B. Nanoscale Morphology, Dimensional Control, and Electrical Properties of Oligoanilines. *J. Amer. Chem. Soc.* **132**, 10365, (2010).
2. Kirchmeyer, S. & Reuter, K. Scientific importance, properties and growing applications of poly(3,4-ethylenedioxythiophene). *J. Mater. Chem.* **15**, 2077, (2005).
3. Pei, Q., Zuccarello, G., Ahlskogt, M. & Inganas, O. Electrochromic and highly stable poly(3,4-ethylenedioxythiophene) switches between opaque blue-black and transparent sky blue. *Polymer* **35**, 1347, (1994).
4. Nikolou, M. & Malliaras, G. G. Applications of poly(3,4-ethylenedioxythiophene) doped with poly(styrene sulfonic acid) transistors in chemical and biological sensors. *Chem. Rec.* **8**, 13, (2008).
5. Groenendaal, L. B., Jonas, F., Freitag, D., Pielartzik, H. & Reynolds, J. R. Poly(3,4-ethylenedioxythiophene) and Its Derivatives: Past, Present, and Future. *Adv. Mater.* **12**, 481, (2000).
6. Rost, H., Ficker, J., Alonso, J. S., Leenders, L. & McCulloch, I. Air-stable all-polymer field-effect transistors with organic electrodes. *Synth. Met.* **145**, 83, (2004).
7. Luzio, A., Musumeci, C., Newman, C. R., Facchetti, A., Marks, T. J. & Pignataro, B. Enhanced Thin-Film Transistor Performance by Combining 13,6-N-Sulfinylacetamidopentacene with Printed PEDOT:PSS Electrodes. *Chem. Mater.* **23**, 1061, (2011).
8. Xia, Y., Sun, K. & Ouyang, J. Solution-Processed Metallic Conducting Polymer Films as Transparent Electrode of Optoelectronic Devices. *Adv. Mater.* **24**, 2436, (2012).
9. Kim, J. S., Granström, M., Friend, R. H., Johansson, N., Salaneck, W. R., Daik, R., Feast, W. J. & Cacialli, F. Indium–tin oxide treatments for single- and double-layer polymeric light-emitting diodes: The relation between the anode physical, chemical, and morphological properties and the device performance. *J. Appl. Phys.* **84**, 6859, (1998).
10. Brown, T. M., Kim, J. S., Friend, R. H., Cacialli, F., Daik, R. & Feast, W. J. Built-in field electroabsorption spectroscopy of polymer light-emitting diodes incorporating a doped poly(3,4-ethylene dioxythiophene) hole injection layer. *Appl. Phys. Lett.* **75**, 1679, (1999).
11. Daoud, W. A., Xin, J. H. & Szeto, Y. S. Polyethylenedioxythiophene coatings for humidity, temperature and strain sensing polyamide fibers. *Sens. Actuators, B* **109**, 329, (2005).
12. Xie, H., Luo, S.-C. & Yu, H.-h. Electric-Field-Assisted Growth of Functionalized Poly(3,4-ethylenedioxythiophene) Nanowires for Label-Free Protein Detection. *Small* **5**, 2611, (2009).

13. Kannan, B., Williams, D. E., Laslau, C. & Travas-Sejdic, J. A highly sensitive, label-free gene sensor based on a single conducting polymer nanowire. *Biosens. Bioelectron.* **35**, 258, (2012).
14. Abidian, M. R., Kim, D. H. & Martin, D. C. Conducting-Polymer Nanotubes for Controlled Drug Release. *Adv. Mater.* **18**, 405, (2006).
15. Groenendaal, L., Zotti, G., Aubert, P.-H., Waybright, S. M. & Reynolds, J. R. Electrochemistry of Poly(3,4-alkylenedioxythiophene) Derivatives. *Adv. Mater.* **15**, 855, (2003).
16. Zhou, C., Liu, Z., Yan, Y., Du, X., Mai, Y. W. & Ringer, S. Electro-synthesis of novel nanostructured PEDOT films and their application as catalyst support. *Nanoscale Res. Lett.* **6**, 364, (2011).
17. Lefebvre, M., Qi, Z., Rana, D. & Pickup, P. G. Chemical Synthesis, Characterization, and Electrochemical Studies of Poly(3,4-ethylenedioxythiophene)/Poly(styrene-4-sulfonate) Composites. *Chem. Mater.* **11**, 262-268, (1999).
18. Crispin, X., Jakobsson, F. L. E., Crispin, A., Grim, P. C. M., Andersson, P., Volodin, A., Haesendonck, C. v., Auweraer, M. V. d., Salaneck, W. R. & Berggren, M. The Origin of the High Conductivity of Poly(3,4-ethylenedioxythiophene)-Poly(styrenesulfonate) (PEDOT-PSS) Plastic Electrodes. *Chem. Mater.* **18**, 4354, (2006).
19. Jönsson, S. K. M., Birgerson, J., Crispin, X., Greczynski, G., Osikowicz, W., Denier van der Gon, A. W., Salaneck, W. R. & Fahlman, M. The effects of solvents on the morphology and sheet resistance in poly(3,4-ethylenedioxythiophene)-polystyrenesulfonic acid (PEDOT-PSS) films. *Synth. Met.* **139**, 1, (2003).
20. Desilvestro, J. & Scheifele, W. Morphology of electrochemically prepared polyaniline. Influence of polymerization parameters. *J. Mater. Chem.* **3**, 263, (1993).
21. Gao, W., Sattayasamitsathit, S., Uygun, A., Pei, A., Ponedal, A. & Wang, J. Polymer-based tubular microbots: role of composition and preparation. *Nanoscale* **4**, 2447, (2012).
22. Thapa, P. S., Ackerson, B. J., Grischkowsky, D. R. & Flanders, B. N. Directional growth of metallic and polymeric nanowires. *Nanotechnology* **20**, 235307, (2009).
23. Thapa, P. S., Yu, D. J., Wicksted, J. P., Hadwiger, J. A., Barisci, J. N., Baughman, R. H. & Flanders, B. N. Directional growth of polypyrrole and polythiophene wires. *Appl. Phys. Lett.* **94**, 033104, (2009).
24. Kawasaki, J. K. & Arnold, C. B. Synthesis of Platinum Dendrites and Nanowires Via Directed Electrochemical Nanowire Assembly. *Nano Lett.* **11**, 781, (2011).
25. Heinze, J. Ultramicroelectrodes in Electrochemistry. *Angew. Chem. Int. Ed. Engl.* **32**, 1268, (1993).
26. Wang, J. in *Analytical Electrochemistry* (Wiley, New York, 2000).
27. Das, A., Lei, C. H., Elliott, M., Macdonald, J. E. & Turner, M. L. Non-lithographic fabrication of PEDOT nano-wires between fixed Au electrodes. *Org. Electron.* **7**, 181, (2006).
28. Natali, D. & Caironi, M. Charge Injection in Solution-Processed Organic Field-Effect Transistors: Physics, Models and Characterization Methods. *Adv. Mater.* **24**, 1357, (2012).
29. Park, D. H., Kim, H. S., Lee, Y. B., Ko, J. M., Lee, J.-Y., Kim, H.-J., Kim, D.-C., Kim, J. & Joo, J. Light emission of a single strand of poly(3,4-ethylenedioxythiophene) (PEDOT) nanowire. *Synth. Met.* **158**, 90, (2008).
30. Feng, W., Li, Y., Wu, J., Noda, H., Fujii, A., Ozaki, M. & Yoshino, K. Improved electrical and optical properties of Poly(3,4-ethylenedioxythiophene) via ordered microstructure. *J. Phys. Condens. Matter* **19**, 186220, (2007).
31. Tamburri, E., Orlanducci, S., Toschi, F., Terranova, M. L. & Passeri, D. Growth mechanisms, morphology, and electroactivity of PEDOT layers produced by electrochemical routes in aqueous medium. *Synth. Met.* **159**, 406, (2009).
32. Randriamahazaka, H., Sini, G. & Van, F. T. Electrodeposition Mechanisms and Electrochemical Behavior of Poly(3,4-ethylenedithiophene). *J. Phys. Chem. C* **111**, 4553, (2007).
33. Heerman, L. & Tarallo, A. Electrochemical nucleation with diffusion-limited growth. Properties and analysis of transients. *Electrochim. Commun.* **2**, 85, (2000).
34. Kalyoncu, E. & Alanyalıoğlu, M. Chronoamperometric and morphological investigation of nucleation and growth mechanism of poly(azure A) thin films. *J. Electroanal. Chem.* **660**, 133, (2011).
35. Kaplan, İ. H., Dağcı, K. & Alanyalıoğlu, M. Nucleation and Growth Mechanism of Electropolymerization of Methylene Blue: The Effect of Preparation Potential on Poly(methylene blue) Structure. *Electroanal.* **22**, 2694-2701, (2010).

36. Kannan, B., Williams, D. E., Khoshmanesh, K., Bowmaker, G. A. & Travas-Sejdic, J. The electrochemical growth of conducting polymer “nanowires”. *J. Electroanal. Chem.* **669**, 82, (2012).
37. Sardone, L., Palermo, V., Devaux, E., Credgington, D., de Loos, M., Marletta, G., Cacialli, F., van Esch, J. & Samorì, P. Electric-Field-Assisted Alignment of Supramolecular Fibers. *Adv. Mater.* **18**, 1276, (2006).
38. Tang, J., Gao, B., Geng, H., Velev, O. D., Qin, L.-C. & Zhou, O. Assembly of 1D Nanostructures into Sub-micrometer Diameter Fibrils with Controlled and Variable Length by Dielectrophoresis. *Adv. Mater.* **15**, 1352, (2003).
39. Annamalai, R., West, J. D., Luscher, A. & Subramaniam, V. V. Electrophoretic drawing of continuous fibers of single-walled carbon nanotubes. *J. Appl. Phys.* **98**, 114307, (2005).
40. Fischer, F. S. U., Tremel, K., Sommer, M., Crossland, E. J. C. & Ludwigs, S. Directed crystallization of poly(3-hexylthiophene) in micrometre channels under confinement and in electric fields. *Nanoscale* **4**, 2138, (2012).
41. Smith, P. A., Nordquist, C. D., Jackson, T. N., Mayera, T. S., Martin, B. R., Mbindyo, J. & Mallouk, T. E. Electric-field assisted assembly and alignment of metallic nanowires. *Appl. Phys. Lett.* **77**, 1399, (2000).
42. Bewick, A., Fleischmann, M. & Thirsk, H. R. Kinetics of the electrocrystallization of thin films of calomel. *Trans. Faraday Soc.* **58**, 2200, (1962).
43. Ventosa, E., Palacios, J. L. & Unwin, P. R. Nucleation and growth of poly(3,4-ethylenedioxythiophene) thin films on highly oriented pyrolytic graphite (HOPG) electrodes. *Electrochem. Commun.* **10**, 1752, (2008).
44. Simeone, F. C., Albonetti, C. & Cavallini, M. Progress in Micro- and Nanopatterning via Electrochemical Lithography. *J. Phys. Chem. C* **113**, 18987, (2009).



## 7. Conclusions and perspectives

In this thesis we investigated several approaches to get control on the molecular organization of functional materials in the condensed phase. By employing both spontaneous and directed assembly processes, we featured the formation of structurally well-definite architectures which allowed studying their electrical properties on a supramolecular scale.

In the spontaneous processes the control over the molecular architectures formation was obtained via *ad-hoc* chemical design, by taking advantage of non-covalent interactions. In particular, by taking advantage of the high control over the geometry of the non-covalent bond, highly directional metal-coordination 1D wires were fabricate, while the  $\pi$ - $\pi$  interactions were exploited to guide the formation of crystalline 2D/3D superstructures.

Fe-bis(terpyridine)-based metal-organic molecular wires featuring controlled length were grown by a layer-by-layer technique and grafted on conductive substrates. Their vertical configuration on the solid supports allowed for the fabrication of nanoscopic metal-molecule-metal junctions of different thickness in dependence of the number of coordination steps. Length-dependent current-voltage measurements provided unambiguous evidence for the existence of a hopping charge transport mechanism, characterized by a very low current attenuation ( $\beta = 0.058 \pm 0.006 \text{ \AA}^{-1}$ ). Theoretical calculations confirmed the occurrence of a charge transport ruled by hopping between adjacent sites rather than by resonant tunneling, since the electronic coupling between iron sites was much smaller than the reorganization energy due to the oxidation of the iron centers.

The organization of metal-coordination polymers in supramolecular materials was explored by using a similar system where the ligand was based on an anthracene core bearing two ethynyl groups equipped with a pyridine and a terpyridine group at the poles. The morphological and structural characterization of the polymers showed that the supramolecular assembly was governed by the coordination geometry of the metal centers. In particular, the planarity of squared Pd(II) based polymers allowed for the formation of  $\pi$ - $\pi$  stacked fibrillar structures where crystalline domains had specific preferred orientations. The improved order of these molecular systems, with respect to the corresponding octahedral Co(II) polymer, where the  $\pi$ - $\pi$  stacking is less favored, resulted in completely different electrical behavior. Conduction of the Pd(II) based fiber-like structures was probed both at the microscale and at the nanoscale and theoretical calculations showed high charge transport abilities, in terms of electronic coupling, for both holes and electrons due to the overlapping of the antracene moieties.

The remarkable electrical characteristics of these metal-terpyridine based molecular systems not only make them ideal systems for fundamental studies on long-range charge transport in solid-state metal-organic wires, but also pave the way towards their exploitation in supramolecular electronic applications.

An example of mechanical pressure- directed assembly was the fabrication of a monomolecular thin layer of the fluorinated perylene dicarboxidiimide molecule, PDIF-CN<sub>2</sub>, through the Langmuir-Blodgett technique. The molecules in the monolayer, assembled at the air/water interface at high transfer pressure, and transferred onto different solid substrates, adopted a fully upright standing configuration and featured the photophysical characteristics of J-aggregates. The vertical charge transport probed by C-AFM nanojunctions revealed higher resistance values compared to covalently-linked self-assembled monolayers and a clear rectification, as well as a slight dependence on the molecular tilt angle. The in-plane charge transport was probed both by C-AFM in horizontal configuration and by fabricating and characterizing macroscopic field-effect transistors, showing outstanding electron mobilities of the order of  $10^{-2} \text{ cm}^2 \cdot \text{V}^{-1} \cdot \text{s}^{-1}$ .

The reorganization of the molecule on the surface by post-deposition thermal annealing on the LB monolayer allowed the formation of ultrathin layered architectures, having a molecular configuration similar to the one of single crystals, where the cofacial arrangement of the perylene cores are maximized. The out-of-plane charge transport on these nanostructures probed by C-AFM and described in the framework of the space charge limited current regime, revealed mobilities of the order of  $5 \cdot 10^{-3} \text{ cm}^2 \cdot \text{V}^{-1} \cdot \text{s}^{-1}$ .

We believe that the reproducible bottom-up fabrication of these nanoarchitectures made out of highly performing conjugated semiconductor molecules open new perspectives for fundamental studies on charge transport on crystal-like structures at the nanoscale, also opening the possibility of their application in downscaled organic electronic devices.

In the last part of the thesis we showed an electric field-directed assembly, combined with an *in-situ* electropolymerization procedure, aimed at getting insights into the variables affecting the morphology of the electrochemically obtained polymer and to correlate them with the electrical properties. The morphology of the electrochemically synthesized poly(3,4-ethylenedioxythiophene) (PEDOT) was finely tuned directly in a device, by carefully guiding the nucleation and growth processes as well as electromigration phenomena. In particular, high electric field intensities favored the formation of aligned wires bridging the gap, as a result of instantaneous nucleation, diffusion-limited growth and electromigration processes. Conversely, lower electric field strengths led to the formation of thin films via progressive nucleation and 2D growth. Significantly, the electrical function of the electropolymerized material was found being affected by the morphology, as evidenced by the different resistive behavior.

We can envisage this procedure to be applied for the fabrication of other materials undergoing electrically/electrochemically triggered polymerization reactions, in order to control their deposition *in-situ* in actual devices.

In summary, this thesis work showed how the engineering of organized nanostructured materials is a viable strategy for tuning the electrical properties of (metal-) organic materials. The exploited strategies require a focused molecular design, the balancing of intermolecular and interfacial interactions, a control on the kinetics of the processes and possibly the exploitation of external forces. The presented results showed that the solution-based assembly processes are simple, versatile and effective, as well as inexpensive and environmentally friendly, enabling the investigation of the materials at the supramolecular level and the creation of efficient devices for applications in nanotechnology, smart materials, organic electronics and biosensors. We believe that the perspectives which this work opens, together with the growing number of papers and publications on this field, are manifold.

As a first point, the employment of metal coordination complexes in the field of organic electronics is not yet fully established. The present work envisages the possibility of their use in real devices. The employment of molecular wires growing in very definite directions should permit the fabrication of conductive interconnections in electronic devices, allowing also for the fabrication of

ramifications by exploiting different metal coordination geometries in more complex systems. The incorporation of diverse metals with different redox properties could also favor the construction of novel multistate devices with unexplored functionalities, towards logic solutions.

The coupling of the electroactive supramolecular architectures to physical stimuli, may permit to access to externally addressable multi-functional devices. As a response to an external stimulus, i.e. an energy input, the supramolecular materials can adapt their state by adjusting their non-covalent interactions. The adaptivity provides a concrete basis for the construction of smart functional materials: for example, chemical sensors, drug-delivery vehicles and mechanical transducers.

The combination and interplay between various components in one material can lead to fascinating physical and chemical properties. The exploitation of different non-covalent bonds and intermolecular and interfacial interactions can boost the development of supramolecular composite materials having a high potential for providing specifically tailored functions. One could also envisage the combined employment of different assembly approaches in orthogonal procedures, for the processing of one material or diverse ones, in order to obtain further enhanced multiple functions.

Bio-inspired assembly procedures could favor the bottom-up construction of functional architectures mimicking biological systems to be fully integrated *in vivo* by the exploitation of specific binding sites. On the longest term, one could think about fully bottom-up approaches to mimic life, as the highest ordered entity operated by a series of programmable non-covalent interactions, which should be instructive for the further development of functional supramolecular materials.

One challenging task is then how to control and manipulate the supramolecular materials at a larger scale. To become technologically marketable it is required for supramolecular electronics to scale up. Though the criteria to get control on the molecular organization on a nano- and micro- scale are recognized, to get control onto the long-range supramolecular ordering, it is really a fundamental task to achieve.

Another fundamental goal is to investigate the stability and long-term use of these functional supramolecular complex systems. The reversibility of the non-covalent interactions could allow for the construction, destruction and reconstruction of the supramolecular materials without requiring too much energy. This could result in recyclable supramolecular materials and materials which are capable of self-repair after mechanical damage. By lowering the costs of fabrication and disposal, one can then envisage the possibility of achieve fully environmental friendly materials.

On shorter term views, we believe that this thesis also give a valuable contribution in the field of the Scanning Probe Microscopies, and particularly Conductive Atomic Force Microscopy (C-AFM). We confirmed indeed their unrivalled possibilities for the investigation of nanostructured supramolecular materials.

Nonetheless, there are still a number of variables to strongly affect C-AFM measurements, such as substrate roughness, tip chemistry, presence of solvent, extensive tip usage, applied load and tip radius. The issue of stability and reproducibility has certainly a huge importance when absolute values are needed in order to estimate the intrinsic electric properties of a single molecular layer. The problem has so far been tackled by exploring a large numbers of junctions in order to get reliable statistics. However, since C-AFM is a pretty slow technique, a sound statistical analysis is extremely time-demanding. In light of this future effort should be devoted to devise rigorous but at the same time simplified procedures that can offer a statistical treatment of huge amount of data, in order to make the technique more easily accessible.

Another major question to be addressed in C-AFM measurements of organic thin films and nanostructures is the maximum spatial resolution that can be achieved. Such a question is strictly related to the size of the contact, i.e., how many molecules are wired and thus explored on the same time during a data collection? A method allowing the control of the effective contact area could highly improve the interpretation of the data, especially when multicomponent blends, phase-segregated films or nanostructures are imaged.

We believe that understanding the local properties of a material on a nanoscale basis is a huge fundamental challenge to bring solutions to both scientific and technological issues, since we also demonstrated that in electronic devices the performances are strongly dependent on the order at the supramolecular level. Because of this reason it is most likely that C-AFM studies combined with appropriate materials assembly procedures, can boost the optimization of the performance of organic electronic devices ultimately providing an important contribution to molecular, supramolecular and organic electronics.



## Acknowledgements

This work would have never been done without the valuable help of many people, who deserve my gratitude.

Firstly I would like to express my deep gratitude to my advisor Prof. Paolo Samorì for giving me the opportunity to work in his group, in such stimulating atmosphere. Thanks to believe in me when assigning me such highly challenging projects and also to give me the possibility and the freedom to follow my curiosity. I am also extremely grateful for having the opportunity to collaborate with several valuable scientists of different research groups in an interdisciplinary work. From everybody I learnt a lot. Thank you, Paolo.

I express my gratitude to Prof. Antonino Licciardello for giving me the opportunity to work on the Fe bis(terpyridine) project and for hosting me in its laboratory at the University of Catania. I really appreciated the time he spent with me in the lab and the stimulating scientific discussions. I particularly thank Dr. Gabriella Zappalà (congratulations for your PhD!) for the good time we had while working together to the project. I thank Prof. Michael Zharnikov and Swen Schuster, from the University of Heidelberg for the XPS and NEXAFS measurements, and Prof. Alessandro Troisi and Dr. Natalia Martsinovich from the University of Warwick for the theoretical calculations and the useful explanations.

I wish to acknowledge Prof. Mir Wais Hosseini and Dr. Abdelaziz Jouaiti from University of Strasbourg for providing me with the terpyridine-antracene-pyridine ligand molecules and Prof. David Beljonne, Silvio Osella and Dorota Niedzialek from the University of Mons for performing the theoretical calculations.

I acknowledge Prof. Norbert Koch and Dr. Ingo Salzmann from the Humboldt-University of Berlin, for the GIXRD and XRR measurements on the perylene monolayer.

My colleagues fully deserve recognition and thanks for all their help, the advices they gave me in many occasions, and the very good time we had all over the last three years. I really enjoyed the time spent together. I wish to thank Dr. Emanuele Orgiu, Dr. Artur Ciesielski, Dr. Oliver Fenwick, Dr. Jörn-Oliver Vogel, Dr. Núria Crivillers, Dr. Markus Döbbelin, Dr. Alexander Klekachev, Dr. Lei

## *Acknowledgements*

---

Zhang, Dr. Karl Börjesson, Dr. Marco Gobbi, Dr. Appan Merari Masillamani, Mirella El Gemayel, Thomas Mosciatti, Wassima Rekab, Dr. Corinna Raimondo, Dr. Andrea Cadeddu, Dr. Mohamed El Garah Sébastien Haar, Marco Squillaci, Dr. Fanny Richard, Dr. Anna Llanes Pallas, and Dr. Nicolas Weibel. Special credits go to Dr. Sara Bonacchi for the stimulating discussions (in and outside the lab!) and for the photophysical measurements, to Dr. James Hutchison for the confocal microscopy, to Laura Ferlauto for the GIXRD measurements on the terpyridine polymers. I am also grateful to Dr. Andrea Liscio for the useful discussions about Scanning Probe Microscopy. Tim Leydecker is kindly acknowledged for the precious help in revising my French résumé. A special mention goes to Maria del Rosso, we arrived to Strasbourg together and we discover France together! I really enjoyed all the time spent chatting, laughing and also doing silly things! You are a great person and I wish you all the best for the future, you deserve it. I cannot forget to mention Marie-Claude Jouati, Axel Duthey, Corinne Ledger, Fabienne Penner and Thierry Muller for their precious assistance in many circumstances. I am going to miss you all!

The most important acknowledgements go to my family. Thanks for being always present and always supporting my choices. I have missed you every moment of life spent apart but I have never felt alone. You are always with me wherever I am.

Finally, I wish to express my final incommensurate thanks to Simone. You are the only one who really believed in my crazy choice three years ago and I will never end being grateful for the constant support you have been giving me since that time. I would have never been able to do this without you by my side. You are a great scientist and a wonderful person. I am really proud of what we are together and I am really looking forward to what the future will be. Thank you.

## Publications

- C. Musumeci, G. Zappalà, N. Martsinovich, E. Orgiu, S. Schuster, S. Quici, M. Zharnikov, A. Troisi, A. Licciardello, and P. Samorì, *Nanoscale electrical investigation of layer-by-layer grown molecular wires*, **Adv. Mater.**, doi: 10.1002/adma.201304848, **COVER page**.
- C. Musumeci, J. A. Hutchison and P. Samorì, *Controlling the morphology of conductive PEDOT by in situ electropolymerization: from thin films to nanowires with variable electrical properties*, **Nanoscale**, 5 (17), 2013, 7756-7761. **Highlighted as a HOT article**, at the Nanoscale blog.
- M. E. Gemayel, M. Treier, C. Musumeci, C. Li, K. Müllen, P. Samorì, *Tuning the Photoresponse in Organic Field-Effect Transistors*. **J. Am. Chem. Soc.**, 134 (4), 2012, 2429-2433.

Publications in preparation:

- C. Musumeci, A. Liscio, V. Palermo, P. Samorì, *Electronic characterization of supramolecular materials at the nanoscale by Conductive Atomic Force and Kelvin Probe Force Microscopies*, submitted for publication.
- C. Musumeci, S. Osella, L. Ferlauto, D. Niedzialek, S. Bonacchi, A. Ciesielski, A. Jouaiti, M.W. Hosseini, D. Beljonne, P. Samorì, *Tailoring the conductive properties of metal-organic supramolecular polymers by chemical design*.
- C. Musumeci, I. Salzmann, S. Bonacchi, N. Koch, P. Samorì *On the electrical properties of perylenecarboxydiimide-based nanoarchitectures*

Previous publications:

- M. H. Rosnes,\* C. Musumeci,\* C. Yvon, A. Macdonell, C. P Pradeep, C. Sartorio, D.-L. Long, B. Pignataro, L. Cronin, *Exploring the Interplay Between Ligand Derivatisation and Cation Type in the Assembly of Hybrid Polyoxometalate Mn-Andersons*, **Small**, 9, 2013, 2316–2324 (\*equal contribution).

- P. Russo, G. Compagnini, C. Musumeci, B. Pignataro, *Raman Monitoring of Strain Induced Effects in Mechanically Deposited Single Layer Graphene*, **J. Nanosci. Nanotech.** 12 (11) **2012**, 8755–8758.
- S. Fabiano, C. Musumeci, Z. Chen, A. Scandurra, H. Wang, Y.-L. Loo, A. Facchetti, B. Pignataro, *From Monolayer to Multilayer N-Channel Polymeric Field-Effect Transistors with Precise Conformational Order*, **Adv. Mater.**, 24, **2012**, 951–956.
- C. Musumeci, M. H. Rosnes, F. Giannazzo, M. D. Symes, L. Cronin, B. Pignataro, *Smart high- $\kappa$  nanodielectrics by polyoxometalate-rich nanocrystals*, **ACS Nano** 5 (12), **2011**, 9992–9999.
- C. Musumeci, A. Luzio, M.H. Rosnes, C. P. Pradeep, H.N. Miras, L. Cronin, B. Pignataro, *Programmable surface-architectures derived from hybrid polyoxometalate-based clusters*, **J. Phys. Chem. C** 115, **2011**, 4446–4455. **COVER page**.
- Luzio, C. Musumeci, C.R. Newman, A. Facchetti, T.J. Marks, B. Pignataro, *Enhanced Thin-Film Transistor Performance by Combining 13,6-N-Sulfinylacetamidopentacene with Printed PEDOT:PSS Electrodes*, **Chem. Mater.** 23(4), **2011**, 1061–1069.
- M.H. Rosnes, C. Musumeci, C. Pradeep, J. Mathieson, D.L. Long, Y. Song, B. Pignataro, R. Cogdell, L. Cronin, *Assembly of Modular Asymmetric Organic-Inorganic Polyoxometalate Hybrids into Anisotropic Nanostructures*, **J. Am. Chem. Soc.**, 132(44), **2010**, 15490–15492.
- G. Arrabito, C. Musumeci, V. Aiello, S. Libertino, G. Compagnini, B. Pignataro, *On the relationship between jetted inks and printed bio-patterns: molecular-thin functional micro-arrays of glucose oxidase*, **Langmuir** 25(11), **2009**, 6312–6318.
- Musumeci, C. Cascio, A. Scandurra, G. F. Indelli, C. Bongiorno, S. Ravesi, B. Pignataro, *Surface effects on the growth of solution processed pentacene thin films*, **Surf. Sci.** 602, **2008**, 993–1005.

## Annex A

### Further computational method on Fe(II)-bis(terpyridine) molecular system based on 4',4''''-(1,4-phenylene)bis(2,2':6',2''-terpyridine) (TPT) ligand

Theoretical calculations were performed on (a)  $[\text{Fe}(\text{terpy})_2]^{2+}$  ion (terpy=2,2':6',2''-terpyridine), (b)  $[\text{Fe}(\text{terpy})(\text{Ph-terpy})]^{2+}$  ion (Ph-terpy=4'-phenyl-2,2':6',2''-terpyridine), (c) dimer of two monomers of (a) connected by a phenylene unit, and (d) cations (a) and (b) with  $\text{HSO}_4^-$  counter-anion. Species (a), (b), (c) are shown in Figure A1.

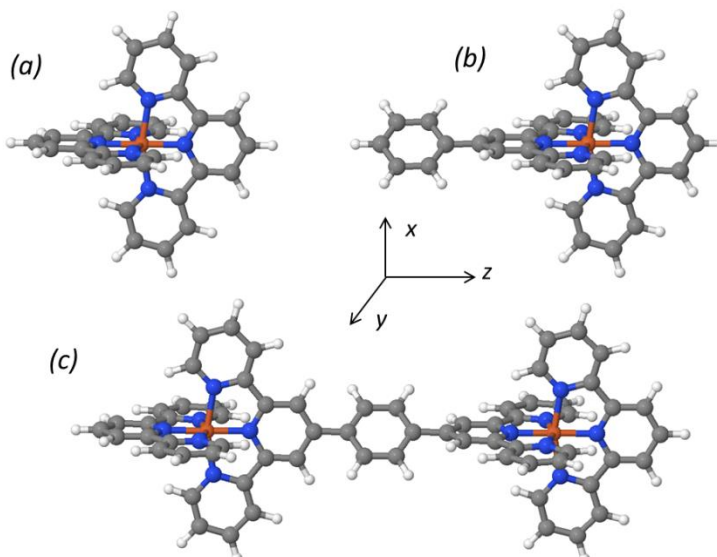


**Figure A1.** (a)  $[\text{Fe}(\text{II})\text{-bis}(2,2':6',2''\text{-terpyridine})]^{2+}$  ( $[\text{Fe}(\text{terpy})_2]^{2+}$ ) ion, (b)  $[\text{Fe}(\text{II})\text{-}(2,2':6',2''\text{-terpyridine})\text{-}(4'\text{-phenyl-}2,2':6',2''\text{-terpyridine})]^{2+}$  ( $[\text{Fe}(\text{terpy})(\text{Ph-terpy})]^{2+}$ ) ion, (c) dimer of two monomers of (a) connected by a phenylene unit. The direction along the molecular wire (shown by arrow) is chosen as the  $z$  axis.

Density-functional theory (DFT) calculations were done with Gaussian 03 software<sup>[6]</sup> using B3LYP hybrid functional and two sizes of basis set: (i) small: 3-21G basis for all atoms except Fe and S in  $(\text{HSO}_4^-)$  for which 6-31G(d) basis was used; (ii) large: 6-31G(d) basis for all atoms.

Geometries and energies obtained using the two basis sets were very similar to each other, confirming that accurate treatment only of the Fe atom is essential. The molecular orbital (MO) energies, couplings and reorganization energies presented in the main text were all obtained using the large basis set.

### Test of accuracy: Fe(II) and Fe(III) spin states

It is known that DFT is not always reliable in description of transition metal complexes with small energy differences between different metal spin states: for example, DFT-LDA (local density approximation) and GGA (generalized gradient approximation) calculations often favour low-spin states; on the other hand, calculations based on Hartree-Fock (HF) theory favour high-spin states; DFT with hybrid functionals performs better than either HF or DFT-LDA and DFT-GGA, but also tends to favour high-spin states.<sup>1</sup>

Therefore, we compare the energies of different spin states of the  $[\text{Fe}(\text{terpy})_2]^{2+}$  and  $[\text{Fe}(\text{terpy})(\text{Ph-terpy})]^{2+}$  complexes obtained in our DFT-B3LYP calculations with high-level quantum chemistry calculations.<sup>3</sup> Table S3 shows that the ordering and the relative energies of singlet, triplet and quintet states of this complex are in reasonable qualitative agreement with higher-level (CASPT2) values<sup>3</sup> and with the estimated experimental range.<sup>2c</sup> The low-spin singlet state of Fe(II) is the lowest-energy one. Similarly, for the Fe(III) complex  $[\text{Fe}(\text{terpy})_2]^{3+}$ , the low-spin doublet state is the lowest-energy one, in agreement with experimental reports.<sup>4</sup> In all the following calculations, we consider the lowest-energy singlet state of the Fe(II) complexes.

**Table A1.** Energies of triplet and quintet states relative to the singlet state, obtained in this work and reported in the literature, for  $[\text{Fe}(\text{terpy})_2]^{2+}$ ,  $[\text{Fe}(\text{terpy})(\text{Ph-terpy})]^{2+}$  and related  $[\text{Fe}(\text{bpy})_3]^{2+}$  (bpy = 2,2'-bipyridine) (<sup>a</sup> CASPT2 calculations, <sup>b</sup> experimental estimate of the electronic contribution to the singlet-quintet energy difference, i.e. excluding vibrational contribution).

Spin state	E-E(singlet), eV					
	$[\text{Fe}(\text{terpy})(\text{Ph-terpy})]^{2+}$		$[\text{Fe}(\text{terpy})_2]^{2+}$	$[\text{Fe}(\text{terpy})_2]^{2+}$	$[\text{Fe}(\text{bpy})_3]^{2+}$	$[\text{Fe}(\text{bpy})_3]^{2+}$
	Small basis	Large basis	Large basis	Literature (theory) <sup>a</sup>	Literature (theory) <sup>a</sup>	Literature (experiment) <sup>b</sup>
Singlet	0.0	0.0	0.0	0.0	0.0	0.0
Triplet	0.56	0.53	0.54	~1.0 <sup>[3c]</sup>	~1.2 <sup>[3b]</sup>	N/A
Quintet	0.25	0.23	0.26	0.73 <sup>[3c]</sup>	0.57 <sup>[3a]</sup> , 0.72 <sup>[3b]</sup>	0.43-0.74 <sup>[2c]</sup>

### Electronic structure

Our calculations took advantage of the symmetry of the molecule, to ensure that MOs related by symmetry are identified. For example, the highest symmetry group for  $[\text{Fe}(\text{terpy})_2]^{2+}$  is  $D_{2d}$ , lowered to  $C_2$  for  $[\text{Fe}(\text{terpy})(\text{Ph-terpy})]^{2+}$  and for the dimer  $[\text{phenylene-bis}(\text{Fe}(\text{terpy})_2)]^{4+}$ .

Recall that in the octahedral ligand field, d-orbitals of the transition metal split into two groups: three lower-energy orbitals with  $t_{2g}$  symmetry (labelled  $d_{xy}$ ,  $d_{xz}$ ,  $d_{yz}$ ) and two higher-energy orbitals with  $e_g$  symmetry (labelled  $d_{x^2-y^2}$ ,  $d_{z^2}$ ). Fe(II) has 6 d-electrons, therefore, all  $t_{2g}$  orbitals are occupied.

The iron complexes in this study have a “special” direction along the wire axis (which we label  $z$ , see Figure A1). Therefore, the three  $t_{2g}$  orbitals are not equivalent to each other:  $d_{xy}$  orbital which has the  $z$  axis as the symmetry axis is clearly different from  $d_{xz}$  and  $d_{yz}$  in symmetry and energy; the latter two orbitals are equivalent to each other in the  $[\text{Fe}(\text{terpy})_2]^{2+}$  monomer, but this equivalence is lost in the dimer and in  $[\text{Fe}(\text{terpy})(\text{Ph-terpy})]^{2+}$  because the symmetry is lowered by addition of the non-coplanar phenyl or phenylene group (see Figure 3.12 in the main text for the relevant orbitals and their energies).

In the dimer, HOMO and HOMO-1 are the symmetric and antisymmetric linear combinations of  $d_{xy}$  orbitals on the two Fe atoms; HOMO-2 to HOMO-5 are linear combinations of  $d_{xz}$  and  $d_{yz}$  orbitals. The two orbitals with the  $d_{xy}$  character have identical energies, i.e. they have negligible splitting. It is clear that  $d_{xy}$  orbitals are higher in energy than  $d_{xz}$  and  $d_{yz}$ , thus  $d_{xy}$  is the orbital where the hole will be located in Fe(III) complexes (this is confirmed by our calculations of the oxidized monomer  $[\text{Fe}(\text{terpy})_2]^{3+}$  and partly oxidized dimer  $[(\text{Ph})\text{-bis}(\text{Fe}(\text{terpy})_2)]^{5+}$  containing Fe(II) and Fe(III), not shown).

The results show that the  $d_{xz}$  and  $d_{yz}$  orbitals on the two Fe centres form two pairs of linear combinations, one of which is strongly coupled to the same combination on the neighbouring atoms (HOMO-2 and HOMO-5) and the other with negligible coupling to the neighbouring atoms (HOMO-3 and HOMO-4). The coupling between the more strongly coupled orbitals is estimated as 54 meV, half of the energy separation between the adiabatic orbital energies. The hopping rate between  $d_{xy}$  orbitals is vanishing because of the vanishing coupling between these orbitals. However, the hopping between neighbouring atoms is possible via thermal activation to one of the d orbitals with larger inter-orbital coupling.

### **Reorganization energy**

Reorganization energy  $\lambda$  for the process of charge (hole) transfer from Fe(II) to Fe(III) was calculated according to the equation:<sup>5</sup>

$$\lambda = E_{\text{II}}^{\text{III}} - E_{\text{II}}^{\text{II}} + E_{\text{III}}^{\text{II}} - E_{\text{III}}^{\text{III}}, \quad (1)$$

where  $E_n^m$  is the energy, the subscript describes the charge state of the Fe complex (Fe(II) or Fe(III)) and the superscript describes the geometry. Thus,  $E_{\text{II}}^{\text{II}}$  and  $E_{\text{III}}^{\text{III}}$  are the energies of optimised  $[\text{Fe}(\text{II})(\text{terpy})_2]^{2+}$  and  $[\text{Fe}(\text{III})(\text{terpy})_2]^{3+}$  complexes,  $E_{\text{II}}^{\text{III}}$  is the energy of the  $[\text{Fe}(\text{II})(\text{terpy})_2]^{2+}$  complex

in the geometry of the  $[\text{Fe(III)}(\text{terpy})_2]^{3+}$  complex, and  $E_{\text{III}}^H$  is the energy of the  $[\text{Fe(III)}(\text{terpy})_2]^{3+}$  complex in the geometry of the  $[\text{Fe(II)}(\text{terpy})_2]^{2+}$  complex.

Only the internal reorganization energy (due to the change in the molecules' geometries) is taken into account; external reorganization energy (due to solvent rearrangement) is ignored in our gas-phase calculations.

Table A2 shows reorganization energies calculated for  $[\text{Fe(II/III)}(\text{terpy})_2]^{2+}$ ,  $[\text{Fe(II/III)}(\text{terpy})(\text{Ph-terpy})]^{2+}$  and these cations with a  $\text{HSO}_4^-$  counterion.

**Table A2.** Reorganization energies

System	Reorganization energy, meV	
	Small basis	Large basis
$[\text{Fe(II/III)}(\text{terpy})_2]^{2+}$	58	66
$[\text{Fe(II/III)}(\text{terpy})(\text{Ph-terpy})]^{2+}$	202	166
$[\text{Fe(II/III)}(\text{terpy})_2]^{2+} + \text{HSO}_4^-$	170	190
$[\text{Fe(II/III)}(\text{terpy})(\text{Ph-terpy})]^{2+} + \text{HSO}_4^-$	386	900-1136

## References

1. R. D. Gaussian 03, Frisch, M. J.; Trucks, G. W.; Schlegel, H. B.; Scuseria, G. E.; Robb, M. A.; Cheeseman, J. R.; Montgomery, Jr., J. A.; Vreven, T.; Kudin, K. N.; Burant, J. C.; Millam, J. M.; Iyengar, S. S.; Tomasi, J.; Barone, V.; Mennucci, B.; Cossi, M.; Scalmani, G.; Rega, N.; Petersson, G. A.; Nakatsuji, H.; Hada, M.; Ehara, M.; Toyota, K.; Fukuda, R.; Hasegawa, J.; Ishida, M.; Nakajima, T.; Honda, Y.; Kitao, O.; Nakai, H.; Klene, M.; Li, X.; Knox, J. E.; Hratchian, H. P.; Cross, J. B.; Bakken, V.; Adamo, C.; Jaramillo, J.; Gomperts, R.; Stratmann, R. E.; Yazyev, O.; Austin, A. J.; Cammi, R.; Pomelli, C.; Ochterski, J. W.; Ayala, P. Y.; Morokuma, K.; Voth, G. A.; Salvador, P.; Dannenberg, J. J.; Zakrzewski, V. G.; Dapprich, S.; Daniels, A. D.; Strain, M. C.; Farkas, O.; Malick, D. K.; Rabuck, A. D.; Raghavachari, K.; Foresman, J. B.; Ortiz, J. V.; Cui, Q.; Baboul, A. G.; Clifford, S.; Cioslowski, J.; Stefanov, B. B.; Liu, G.; Liashenko, A.; Piskorz, P.; Komaromi, I.; Martin, R. L.; Fox, D. J.; Keith, T.; Al-Laham, M. A.; Peng, C. Y.; Nanayakkara, A.; Challacombe, M.; Gill, P. M. W.; Johnson, B.; Chen, W.; Wong, M. W.; Gonzalez, C.; and Pople, J. A.; Gaussian, Inc., Wallingford CT, 2004.
2. a) J. N. Harvey, *Structure and Bonding* **2004**, *112*, 151; b) R. J. Deeth, N. Fey, *J. Comput. Chem.* **2004**, *25*, 1840; c) L. M. L. Daku, A. Vargas, A. Hauser, A. Fouqueau, M. E. Casida, *ChemPhysChem* **2005**, *9*, 1393.
3. a) K. Pierloot, S. Vancoillie, *J. Chem. Phys.* **2006**, *125*, 124303; b) C. D. Graaf, C. Sousa, *Chem Eur. J.* **2010**, *16*, 4550; c) M. Pápai, G. Vankó, C. d. Graaf, T. Rozgonyi, *J. Chem. Theory Comput.* **2013**, *9*, 509.
4. W. M. Reiff, W. A. B. Jr., N. E. Erickson, *J. Am. Chem. Soc.* **1968**, *90*, 4794.
5. M. Misra, D. Andrienko, B. Baumeier, J.-L. Faulon, O. A. v. Lilienfeld, *J. Chem. Theory Comput.* **2011**, *7*, 2549.

## Annex B

### Further computational methods on Pd(II)-(terpyridine-antracene-pyridine) (TAP) polymer

#### *GIXRD simulations*

To investigate on the molecular packing on the surface GIXRD simulations were performed. Three possible orientations of the polymer on the surface were simulated: molecular length perpendicular to the surface, face-on and molecular width perpendicular to the surface (see Figure B1). The respective GIWAXS simulated diffraction patterns are reported in figure B2. The only diffraction pattern matching with the experimental one corresponded to a packing with the molecular width perpendicular to the surface

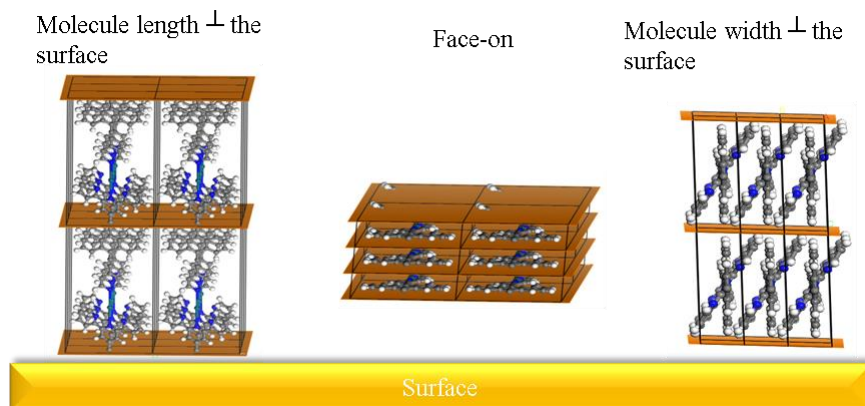


**Figure B1.** Possible orientations of the polymer on the surface, used in the simulation. The orange planes refer to the Miller planes

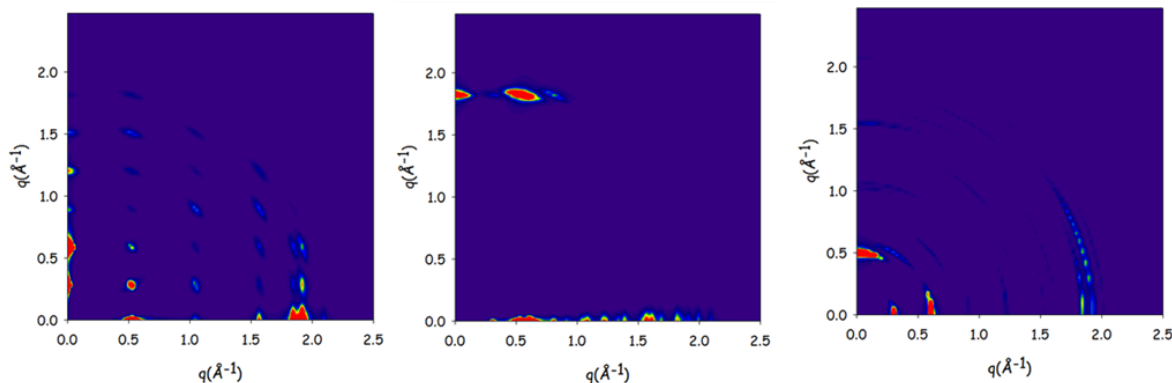


**Figure B2.** GIWAXS patterns simulated for the three possible orientations depicted in Figure B1.

### ***Frontier orbitals obtained for the monomer***

To analyze the shape of the frontier orbitals, we consider Pd (II) and two negative (-1e) point charges instead of counterions, at a distance of 3.5 Å from the metal center. The frontier orbitals obtained for the monomer are reported in Figure B3

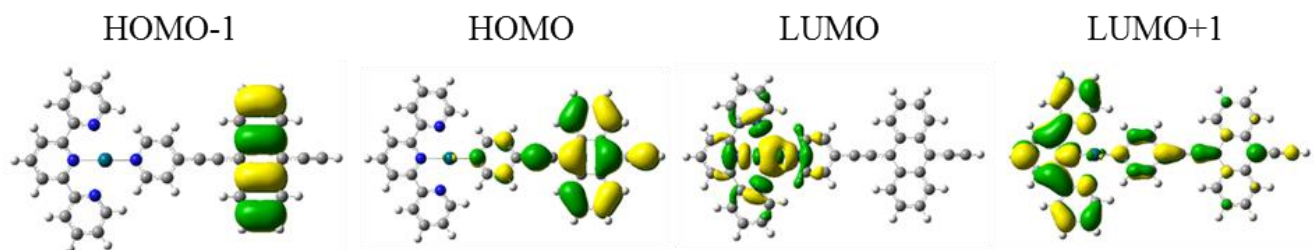


**Figure B3.** Frontier molecular orbital shapes for the monomer with the application of two point charges perpendicular to the square planar coordination plane and at a distance of 3.5 Å from the metal center.

The HOMO is mainly localized in the antracene group forming the ligand, while the LUMO is mainly localized on the metal center and partly on the terpyridine and pyridine group

### Transfer Integral analysis with shift of polymer chains

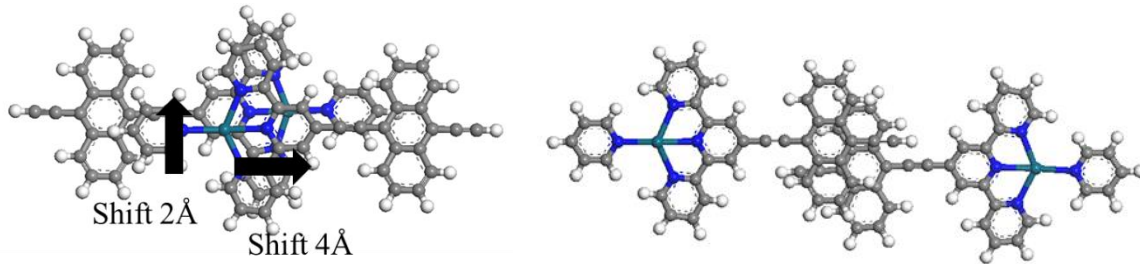


**Figure B4.** Slide between the two chains, as found after MM/MMD simulations, by 2 Å along the lamellae direction (vertical arrow) and by 4 Å along the molecular direction (horizontal arrow).

		Lamellae Pd-Pd	TI_holes (eV)	TI_electrons (eV)
1	2	1-3	1.64296e-04	5.00458e-05
	4	2-4	2.29483e-05	1.25300e-05
		Lamellae At-At	TI_holes (eV)	TI_electrons (eV)
3	1	1-3	1.76937e-04	2.50000e-04
	2	2-4	3.30578e-05	6.00000e-05

**Figure B5.** (left) Schematic representation of the four non-equivalent monomers present in the unit cell, labelled with numbers from 1 to 4. The arrow refers to the lamellae direction along which the TI is calculated. The table report the values of TI for both holes and electrons calculated along the lamellae direction for the overlap of the metal centers and for the overlap od the antracene groups of the ligand for cofacial packing.

Since in the packing geometry the two polymer chains are shifted apart, test calculations were made shifting the two monomer dimers towards a “cofacial” packing, to study the relation between the shift and the TI. As test case, only the  $\pi$ -stacking direction is considered (dimer 1-2). Three different directions toward cofacial are considered: two consecutive shifts along the lamellae direction (by 1 Å, vertical) followed by two shifts along the molecular direction (by 2 Å, horizontal) to reach the cofacial; two consecutive shifts along the molecular direction (by 2 Å, horizontal) followed by two shifts along the lamellae direction (by 1 Å, vertical) to reach the cofacial; a diagonal shift, moving twice along both

molecular and lamellae directions by 2 and 1 Å, respectively. Results for the overlap of metal centers are reported in figure B6.

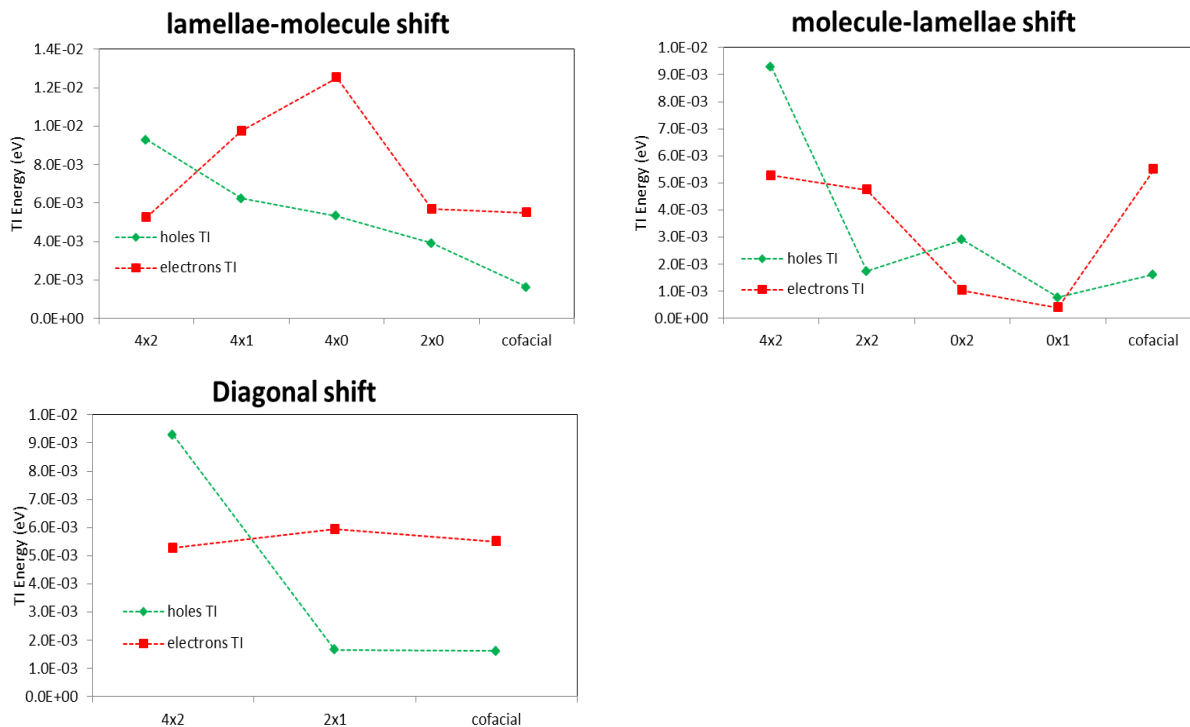


**Figure B6.** Evolution of the transfer integral going toward a cofacial packing for the metal centers overlap dimers along the p-stacking direction, with the three different shift directions.

In all the three studied cases, the holes transfer integral decreases by one order of magnitude, from  $\sim 10^{-2}$  to  $\sim 10^{-3}$  eV, while different behaviors are observed for the electrons transfer integral. It increases up to  $\sim 1.2 \cdot 10^{-2}$  eV for the 4x0 shift and then it decreases reaching the cofacial in the lamellae-molecule shift; it constantly decreases till 0x1 to increase again for the cofacial in the molecule-lamellae shift and it is almost constant for a diagonal shift.

Both the effects can be explained considering the localization of the frontier orbitals on different part of the monomer: the decrease in the transfer integral for holes derives from the localization of the HOMO on the antracene part, while the small increased transfer integral for

electrons is due to the localization of the LUMO on the metal center, hence the shift towards the cofacial slightly increase the overlap and as consequence the transfer integral.

A different scenario arises when the antracene-antracene overlap is considered, see Figure B7. By applying the same shift scheme, both the holes and the electrons transport are enhanced going towards a cofacial position, with stronger increase for holes (due to the strong HOMO orbitals overlap). In fact, passing from 4x2 to cofacial, the transfer integral is increased up to  $\sim 2.5 \cdot 10^{-1}$  eV with small fluctuations for the different paths followed. The increase of electron transfer integral is less sensible to the shift, increasing up to  $\sim 5 \cdot 10^{-2}$  eV when the two monomers are cofacial.

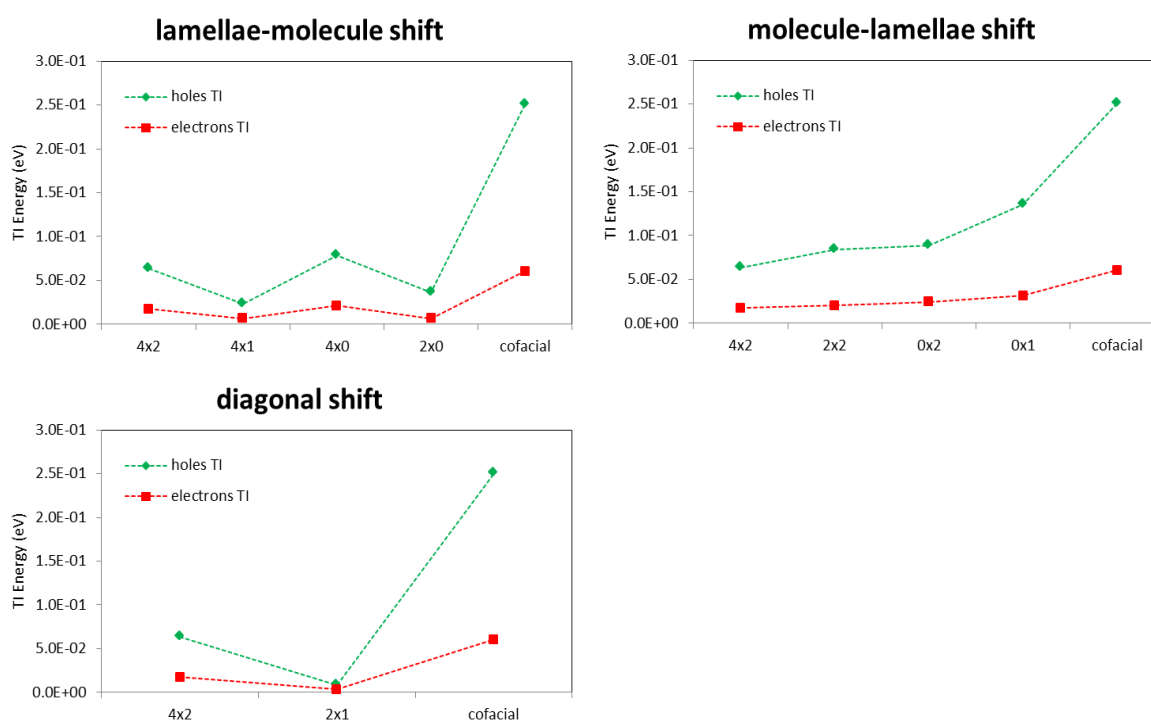


**Figure B7.** Evolution of the transfer integral going toward a cofacial packing for the antracene groups overlap dimers along the  $\pi$ -stacking direction, with the three different shift directions.



# SUPRAMOLECULAR ELECTRONICS: FROM MOLECULAR WIRES TO (SEMI)CONDUCTING MATERIALS

## Résumé

L'électronique supramoléculaires vise à construire et à étudier les propriétés optoélectroniques des architectures supramoléculaires à l'échelle nanométrique. L'objectif de cette thèse est d'obtenir le contrôle de l'organisation des systèmes moléculaires organiques et de corrélérer leur structure avec les propriétés électriques, avec une attention particulière sur les propriétés à l'échelle nanométrique.

Les stratégies exploitées nécessitent un design chimique adapté, un équilibre des interactions intermoléculaires et d'interface, un contrôle sur la cinétique des processus et, éventuellement, l'exploitation des forces extérieures.

Les résultats présentés montrent que la compréhension des propriétés locales d'un matériau sur une base à l'échelle nanométrique est un énorme défi fondamental vise à apporter des solutions à des questions scientifiques et technologiques, puisque les performances dans les appareils électroniques sont fortement dépendante de l'ordre au niveau supramoléculaire.

**Mots-clés:** électronique organique, électronique moléculaire, microscopie à force atomique à sonde conductrice C-(AFM), auto-assemblage, assemblage dirigé.

## Abstract

Supramolecular electronics aims to construct and investigate the optoelectronic properties of tailored supramolecular nanoarchitectures. The aim of this thesis is to get control over the organization of organic molecular systems and correlate their structure with the electrical properties, with particular attention at the nanoscale properties.

The exploited strategies require a focused molecular design, the balancing of intermolecular and interfacial interactions, a control on the kinetics of the processes and possibly the exploitation of external forces.

The presented results showed that understanding the local properties of a material on a nanoscale basis is a huge fundamental challenge to bring solutions to both scientific and technological issues, since in electronic devices the performances are strongly dependent on the order at the supramolecular level.

**Keywords:** Organic electronics, molecular electronics, Conductive Atomic Force Microscopy (C-AFM), self-assembly, directed-assembly.